Organization and function of signaling molecules in sperm

Dissertation

Zur

Erlangung des Doktorgrades (Dr. rer. nat.)

der

Mathematisch-Naturwissenschaftlichen Fakultät

der

Rheinischen Friedrich-Wilhelms-Universität Bonn

vorgelegt von

Hussein Hamzeh

aus

Brital

Bonn, 2017

Angefertigt mit Genehmigung der Mathematisch-Naturwissenschaftlichen Fakultat der
Rheinischen Friedrich-Wilhelms-Universitat Bonn

1. Gutachter: Prof. Dr. Dagmar Wachten
2. Gutachter: Prof. Dr. Thorsten Lang
3. Gutachter: Prof. Dr. Ulrich Benjamin Kaupp
4. Gutachter: Prof. Dr. Anton Bovier

Tag der Promotion: 29.06.2017

Erscheinungsjahr: 2017

In loving memory of my sister, Sarah

Zusammenfassung

Um die Eizelle zu befruchten, müssen die Spermien die Eizelle zunächst lokalisieren. Dabei helfen ihnen unterschiedliche chemische oder physikalische Signale auf dem Weg zur Eizelle, die dann das Schwimmverhalten der Spermien steuern. Externe Befruchter, wie z.B. der Seeigel *Arbacia punctulata*, geben ihre Ei- und Samenzellen in das Seewasser ab, worauf die Spermien den Weg zur Eizelle finden müssen. Um die Spermien auf ihrem Weg zu leiten, sekretiert die Eizelle ein kleines Peptid (resact), welches als Lockstoff für die Spermien dient. Die Spermien schwimmen stets auf höhere Resactkonzentrationen zu. Dieses Verhalten bezeichnet man als Chemotaxis. Resact bindet an einen Rezeptor auf dem Flagellum der Spermien, was zu einer Erhöhung der intrazellulären cGMP-Konzentration führt. cGMP steht am Anfang einer Signalkaskade, die schließlich zu einem Ca^{2+}-Einstrom und damit zu einer Änderung des Schwimmverhaltens führt. . Spermien von *Arbacia punctulata* sind in der Lage einzelne Resactmoleküle zu detektieren. Der molekulare Mechanismus, der sowohl der Einzelmolekülsensivität als auch der cGMP-Homöostase zugrunde liegt, ist nur unzureichend verstanden. Daher habe ich ein *in vivo* Verfahren entwickelt, mit dem es möglich ist, den zeitlichen Verlauf der cGMP-Konzentration während der Resactdetektion nachzustellen. Diesem liegt das sogenannte *reverse opto-chemical engineering* (ROCE) zugrunde. Meine Ergebnisse liefern quantitative Einblicke in die molekularen Mechanismen, mit der Spermien periodische Änderungen der Lockstoffkonzentration in Änderungen der intrazellulären Ca^{2+}-Konzentration und schließlich des Schwimmverhalten umsetzen. Des Weiteren ist die supramolekulare Anordnung der Signalkomponenten, die das Schwimmverhalten von Seeigel- sowie Säugetierspermien kontrollieren, weitgehend unbekannt. Daher habe ich eine Strategie entwickelt, den Resactrezeptor in Seeigelspermien zu markieren und so die supramolekulare Organisation zu untersuchen. In Säugetierspermienist der der Ca^{2+}-Kanal CatSper verantwortlich für den Ca^{2+}-Einstrom und steuert so das Schwimmverhalten. Mit Hilfe der *super-resolution-microscopy* konnte ich zeigen, dass CatSper bei Mäusen und beim Menschen in vier Reihen entlang des Flagellums angeordnet ist.

Während der Spermatogenese entwickeln sich Spermien mit Kopf und Schwanz aus runden Vorläuferzellen. Die nicht-lysosomale Glycosylceramidase GBA2 spaltet Glycosylceramid (GlcCer) zu Glukose und Ceramid. Ein erhöhte zelluläre GBA2-Konzentration führt zu *Globozospermie*,einem schwerwiegenden morphologischen Defekt in Mäusespermien. Wir konnten zeigen, dass diesen Defekten eine Fehlregulierung der zytoskelettalen Dynamiken zugrunde liegt, bedingt durch die Anreicherung von GlcCer in der Zelle. In meiner Arbeit habe ich neue Methoden entwickelt, die ermöglichen, den Einfluss der Lipidumgebung auf die Dynamik des Zytoskellets zu untersuchen und somit die physiologische Rolle von GBA2 in der Spermatogenese zu studieren.

Abstract

Successful fertilization depends on the ability of sperm to locate the egg. Sperm from different species rely on diverse signaling components to gather chemical and physical cues and transduce them into a behavioral swimming response. External fertilizers like the sea urchin *Arbacia punctulata* release their gametes into the sea water, where the sperm have to find the egg. Here, the oocyte secretes a chemoattractant – a small peptide called resact. Resact binds to chemoreceptor on sperm flagella, causing an elevation in the intracellular cGMP concentration, which results in a sequence of events that ends with Ca^{2+} influx. $[Ca^{2+}]_i$ modulates sperm flagellar movement, thereby allowing sperm to adjust their swimming direction up the concentration gradient and towards the egg in a process called chemotaxis. *A. punctulata* sperm are able to register the binding of a single resact molecule; however, the mechanism underlying single-molecule sensitivity and the ensuing cGMP homeostasis are not well understood. Therefore, I first established an *in vivo* assay to measure cGMP dynamics using reverse opto-chemical engineering (ROCE). My results provide insights into the molecular mechanism how sperm transduce a periodic change in chemoattractant concentration into a periodic change in the asymmetry of the flagellar beat. I also used ROCE to study the single-molecule response in sperm and provide a quantitative description of the molecular events underlying the single-molecule sensitivity in sperm. Moreover, the supra-molecular arrangement of the signaling cascade controlling sperm behavior in sea urchin and mammalian sperm are not known. Therefore, I developed a new labeling strategy to tag the chemoreceptor in sea urchin sperm to elucidate its supra-molecular organization. In mammals, and in particular in human sperm, the "chemoreceptor" is CatSper, the principal Ca^{2+} channel controlling sperm motility. Using super-resolution microscopy, I unraveled the quadrilateral arrangement of CatSper in mouse and in human sperm.

Before sperm are mature and able to navigate their way to the egg, they have to develop from a round cell into an elongated cell with a head and a tail during spermatogenesis. The non-lysosomal glucosylceramidase GBA2 degrades glucosylceramide (GlcCer) to glucose and ceramide. Lack of GBA2 results in a condition called globozoospermia - manifested with severe morphological defects in mouse sperm. GlcCer accumulation in the absence of GBA2 and the subsequent dysregulation of cytoskeletal dynamics is thought to underlie the defects in sperm shaping during spermatogenesis. I established methods to study the effect of lipid environments on cytoskeletal dynamics to reveal the physiological function of GBA2 during sperm development. My results suggest a novel role for GlcCer as a key regulator for cytoskeletal dynamics during sperm development.

Table of Contents

Abbreviations

°C	Degrees Celsius
3B	Bayesian analysis of blinking and bleaching
AC	Alternating current
ADU	Analog-digital-unit
AM	Acetoxymethyl
AOTF	Acousto-optical tunable filter
BeRST	Berkeley Red-based Sensor of Transmembrane potential
BME	2-Mercaptoethanol
BTB	Blood-testis-barrier
C (t)	Function describing $[Ca^{2+}]_i$ variation with time
cAMP	Cyclic adenosine -3´ , 5´ -monophosphate
CatSper	Cation channels of sperm
cGMP	Cyclic guanosine -3´ , 5´ -monophosphate
CHO	Chinese hamster ovary cells
CNBD	Cyclic nucleotide binding domain
CNG	Cyclic nucleotide–gated ion channels
CNGK	K^+-selective cyclic nucleotide–gated ion channels
Cryo-EM	Cryo-electronmicroscopy
DC	Direct current
DEACM	7- Diethylaminocoumarin- 4- yl)methyladenosine- 3', 5'- monophosphate
DMEM	Dulbecco's Modified Eagle Medium
DMEM-HS	Dulbecco's Modified Eagle Medium with human serum
DNA	Deoxyribonucleic acid
DNase	Deoxyribonuclease
DSS	Disuccinimidyl suberate
E_k	K^+ equilibrium potential
EMCCD	Electron multiplying charge-coupled device
ES	Ectoplasmic specialization
FRC	Fourier ring correlation
FRET	Förster resonance energy transfer

FWHM	Full width at half maximum
G (t)	Function describing [cGMP] variation with time
GBA2	non-lysosomal glucosylceramidase
GC	Guanylate cyclase
GlcCer	Glucosylceramide
GP	Generalized polarization
GPMV	Giant plasma membrane vesicles
GPU	Graphics processing unit
GSD	Ground-state depletion
HBSS	Hank's Balanced Salt Solution
HCN	Hyperpolarization activated Cyclic Nucleotide gated channel
HEK293	Human embryonic kidney cells 293
HEPES	N-2-hydroxyethyl peperazine-N´ -2-ethanesulfonic acid
HPLC	High-performance liquid chromatography
Hv1Sper	Human sperm proton channel Hv1
IBMX	3-Isobutyl-1-methylxanthin
K_D	Dissociation constant
M	Molar
MEA	2-mercaptoethylamine
MW	Molecular weight
NA	Numerical aperture
NBD-NJ	N-butyldeoxynojirimycin
NCKX	$Na^+/Ca^{2+}-K^+$ exchanger
NEM	N-Ethylmaleimide
NHA1	Na^+/H^+ antiporter 1
NHS	N-Hydroxysuccinimid
OD	Optical density
PAGE	Polyacrylamide gel electrophoresis
PALM	Photoactivated localization microscopy
PBS	Phosphate buffered saline
PDE	Phosphodiesterase

PEI	Polyethylenimine
PeT	Photoinduced electron transfer
PMT	Photomultiplier tube
PSD	Phase sensitive detection
PSF	Point-spread-function
ROCE	Reverse opto-chemical engineering
sACY	Soluble adenylyl cyclase
SDS	Sodium dodecylsulfate
SE	Succinimidyl ester
SML	Single molecule localization
sNHE	Sperm-specific Na^+/H^+ exchanger
SNR	Signal-to-noise-ratio
SOFI	Super-resolution optical fluctuation imaging
SRRF	Super resolution radial fluctuation
SSIM	Saturated structural illumination microscopy
SSNR	Spectral signal-to-noise-ratio
STED	Stimulated emission depletion
STORM	Stochastic optical reconstruction microscopy
THPTA	Tris(3-hydroxypropyltriazolylmethyl)amine
TIRF	Total internal reflection fluorescence
V_m	Membrane voltage
V_m (t)	Function describing membrane voltage variation with time
βCD	β-Cyclodextrin
ε	Molar absorption coefficient
λ	Wavelength

I. Introduction

1. Diversity in sperm

The success of fertilization in different species depends on the ability of sperm to locate the egg. While swimming, sperm from different species rely on diverse signaling components [1] to gather chemical and physical cues and transduce them into a behavioral swimming response. For instance, sea urchin sperm from *Arbacia punctulata* release their gametes into the sea water where the sperm has to find the egg. The sea urchin oocyte secretes a chemoattractant – a small peptide called resact. Sea urchin sperm bind resact and adjust their swimming direction up the concentration gradient and towards the egg in a process called chemotaxis [2]. In contrast, mammals are internal fertilizers - sperm are ejaculated into the vagina, from where they have to swim up the oviduct and towards the fallopian tube in order to meet the egg. During their journey, mammalian sperm, unlike sea urchin sperm, undergo a spatially constraint swimming behavior that is guided by long- and short-range cues to navigate by chemotaxis, rheotaxis, thermotaxis, or a combination of all three [1]. Chemotaxis, rheotaxis, and thermotaxis refer to the directed movement of sperm, in a chemical gradient, against a fluid flow, and in a temperature gradient, respectively. The molecular mechanisms underlying chemotaxis in sea urchin sperm are well defined; in fact, most of our knowledge on sperm chemotaxis originates from the study of marine invertebrates, notably sperm from the sea urchin *A. punctulata*. However, in mammals, none of the aforementioned mechanisms or their contribution to sperm guidance is well understood [3].

2. Sea urchin sperm

Oocytes from the sea urchin *A. punctulata* release a short, species-specific chemoattractant peptide called resact consisting of 14 amino acids. The chemoattractant binds to a receptor guanylate cyclase (GC) and, thereby, stimulates the synthesis of cGMP. In turn, cGMP opens K^+-selective cyclic nucleotide–gated (CNGK) channels [4], leading to membrane hyperpolarization. This hyperpolarization activates two other signaling components: a sperm-specific Na^+/H^+ exchanger (sNHE) and a hyperpolarization-activated cyclic nucleotide–gated

(HCN) channel. sNHE activity causes a rapid sperm alkalization [3], whereas opening of HCN channels leads to a Na^+ inward current that depolarizes the cell membrane [5]. The alkalization shifts the voltage dependence of the CatSper channel [6], thus allowing its opening during subsequent depolarization, leading to a Ca^{2+} influx. During the recovery phase, the resting $[Ca^{2+}]_i$ is restored by the action of a Na^+/Ca^{2+}-K^+ exchanger (NCKX) and hydrolysis of cGMP by a phosphodiesterase (PDE). Of note, upon resact binding, sea urchin sperm not only synthesize cGMP, but also cyclic adenosine monophosphate (cAMP), probably through activation of the soluble adenylate cyclase (sACY). The released cAMP could act on the HCN channels because their voltage-dependent opening has been shown to be modulated by cAMP [7], and also on sNHE (Figure 1). The signaling components involved in chemoattractant signal transduction are discussed in the following sections.

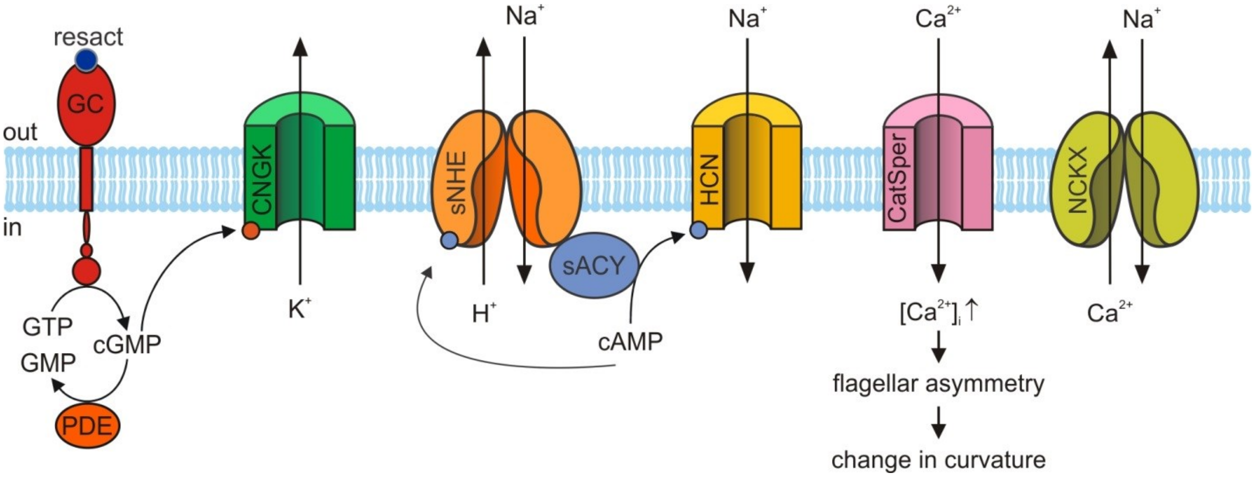

Figure 1. Signaling pathway in sea urchin sperm. The guanylate cyclase (GC) serves as the receptor for the chemoattractant resact. Resact binding activates the GC, resulting in cGMP synthesis. cGMP activates the K^+- selective cyclic nucleotide-gated channel (CNGK). Opening of CNGK hyperpolarizes the cell and activates a hyperpolarization-activated and cyclic nucleotide-gated (HCN) channel [5] and a sperm-specific Na^+/H^+ exchanger (sNHE). Opening of HCN channels depolarizes the membrane and restores the resting potential, whereas activation of sNHE increases the intracellular pH. Both events activate CatSper [6]. The alkalization shifts the voltage dependence of CatSper channel, thus allowing its opening during subsequent depolarization, leading to influx of Ca^{2+}. During the recovery phase, the resting $[Ca^{2+}]_i$ is restored by the action of a Na^+/Ca^{2+}-K^+ exchanger (NCKX) and hydrolysis of cGMP by a phosphodiesterase (PDE). Sea urchin sperm not only synthesize cGMP, but also cAMP, probably through activation of the soluble adenylate cyclase (sACY), which might bind to the HCN channel and sNHE, whose voltage-dependent opening is modulated by cAMP. Image adapted from [3].

2.1. Chemoreceptor Guanylate Cyclase

The GC is composed of three functional domains [8]: an extracellular domain that binds resact, an intracellular catalytic domain that synthesizes cGMP, and a single transmembrane domain that connects the binding and catalytic domain and, in turn, transduces the binding event to the cell interior. The flagellum expresses about 300,000 GC copies at a density of 9,500 GC molecules/μm^2 [9]. At very low receptor occupancy, the binding affinity of GC is in the picomolar range ($K_{1/2}$ = 90 pM), while at higher occupancy, the GC affinity is lowered ($K_{1/2}$ = 0.65 nM), thereby allowing the sperm to register chemoattractant concentrations over six orders of magnitude. The combination of high density and adjustable affinity provides the sperm with a broad concentration range to respond to the ligand. The exquisite capture efficacy allows sperm to operate at extremely low chemoattractant concentrations down to single molecules when being distant from the egg. At the same time, the adjustable affinity and high GC density allows sperm to operate in high chemoattractant concentrations prevailing near the egg. The turnover number of active GC is 72 cGMP molecules/active GC/second [9]. GC is initially phosphorylated and becomes dephosphorylated upon resact binding [10,11]. The activity ceases within 150 ms by multi-stage auto-dephosphorylation, where phosphate groups from six conserved serine residues of the GC are removed upon resact binding [9]. A sequential multi-stage dephosphorylation could allow for precise lifetime control of the GC and, thereby, resulting in reduction of 'molecule noise' that limits the ability to register single resact molecules [12]. Otherwise, an exponential probability distribution of the GC lifetime would produce variability in the single-molecule response, thereby, compromising the precision in measuring the chemoattractant at low concentrations. A similar mechanism to reduce noise and allow highly reproducible unitary responses has been proposed for rod photoreceptors [13], where a similar multi-stage deactivation mechanism of rhodopsin control its lifetime and, thereby, reduce photon noise [14].

2.2. K^+- selective cyclic nucleotide-gated channel (CNGK) channel

The hyperpolarization upon chemoattractant stimulation is mediated by CNGK channel. This channel is unique compared to classical CNG channels [4]: The large pore-forming polypeptide consists of four homologous repeats; each repeat carries the prototypical GYGD pore motif of K^+ channels in addition to a cyclic nucleotide-binding domain (CNBD). Binding of a single cGMP molecule to the third repeat is necessary and sufficient to activate the channel [4]. CNGK channels respond to small changes in cGMP in a non-cooperative fashion ($K_{1/2}$ = 25 nM, hill coefficient of 1), whereas CNG channels in photoreceptors and olfactory neurons operate in the micromolar range with cooperative binding of several ligands [15]. In fact, given the high input resistance of sperm cells, the CNGK channel ability to respond to minute changes in cGMP concentrations could explain how sperm are able to transduce the binding of a single molecule into a macroscopic electrical signal.

2.3. Na^+/H^+ exchanger (sNHE)

The sperm-specific Na^+/H^+ exchanger (sNHE) harbors a voltage-sensor domain (VSD) similar to voltage-gated K^+, Na^+, and Ca^{2+} channels. In addition, the sNHE carries a CNBD as in CNG channels. sNHE shares with other NHEs a membrane-spanning exchange domain that features at least 12 transmembrane segments [16]. sNHE is activated by voltage and it alkalizes the sperm – a crucial event for CatSper activation [6].

2.4. Hyperpolarization-activated and cyclic nucleotide-gated (HCN) channel

There are two isoforms (*SpHCN1* and *SpHCN2*) of the hyperpolarization-activated and cyclic nucleotide-gated (HCN) channel family expressed in sperm from the sea urchin *Strongylocentrotus purpuratus* and *A. punctulata* [5,17]. HCN channels are activated by hyperpolarization, carrying a depolarizing inward Na^+ current, and their open probability is enhanced by cAMP. Thereby, they initiate the recovery after a stimulus and allow sperm to encode a wide range of chemoattractant concentrations. In neurons and in the sinoatrial node of the heart, HCN channels control rhythmic electrical activity, and are, therefore, called pacemaker channels. In sperm, HCN channels might serve a similar function by allowing sperm to pace Ca^{2+} oscillations in response to stimulus patterns during periodic swimming [3].

2.5. CatSper channel

The CatSper channel in *A. punctulata* consists of four pore-forming α subunits (CatSper 1 – 4) and at least three auxiliary subunits (CatSper β, CatSper γ, and CatSper δ) [6]. CatSper channels are closed at resting membrane potential and are activated in a two-step process. The alkalization driven by sNHE shifts the voltage dependence of CatSper channels by ca. -30 mV, whereby

CatSper channels open during the recovery from hyperpolarization, resulting in a Ca^{2+} influx. The pH dependence of CatSper is very steep with a Hill coefficient of ca. 11, allowing CatSper to transduce small elementary changes in pH and membrane voltage (V_m) into a Ca^{2+} response.

2.6. Single-molecule response in sperm – lessons from photoreceptors

A. punctulata sperm are able to transduce the binding of one resact molecule into an elementary V_m and Ca^{2+} response. Another cell type that shows similar sensitivity is retinal rod photoreceptors. Signaling in sperm and rods relies on cGMP-signaling pathways to achieve single-molecule or single-photon sensitivity, respectively. The mechanism underlying single-photon sensitivity in rod photoreceptors has been extensively studied [13,14,18–20], making it a "gold standard" when studying other cell types that have high sensitivities towards an external stimulus, such as the response to resact in *A. punctulata* sperm. When comparing sperm to rod photoreceptors, we come across intriguing variations on a common signaling motif that allows each cell type to achieve high sensitivity.

2.6.1. Phototransduction in rods

The mammalian retina contains two types of photoreceptors, rods and cones. Rods are more abundant and more sensitive to photons than cones; therefore rods are more suited for low-light vision. Both rods and cones transduce captured photons into an electrical response that can be relayed across synapses to other neurons in the retina. The photosensory signaling cascade takes place in a specialized cylindrical part of rod a cell called the outer segment (Figure 2). The outer segment is a modified sensory cilium that is tightly packed with stacks of membrane disks, containing high densities of visual pigment protein called rhodopsin. Rhodopsin, the visual pigment is built from the protein opsin and the chromophore 11-cis-retinal. When light hits rhodopsin, the chromophore 11-*cis*-retinal isomerizes to all-*trans*-retinal, resulting in a conformational change and activation of rhodopsin. The quantum yield of isomerization is 50 %; in contrast, spontaneous isomerization in the dark occurs only once in 500-1000 years. Opsins are G protein-coupled receptors and the corresponding trimeric G protein is transducin (G_t), while the effector activated by G_t is a cGMP phosphodiesterase (PDE). In the dark, rhodopsin is inactive (Rh) and the outer segment maintains a high level of cGMP in the cytoplasm as a result of cGMP synthesis by GC, causing a small fraction of cGMP-gated CNG channels to be constantly opened. Therefore, a steady Na^+ inward current depolarizes the cell in the dark, which is why the current has been termed dark current. Upon light stimulation, rhodopsin is activated (Rh*), which, in turn, activates transducin by catalyzing a GDP/GTP exchange. GTP binds to the γ-subunit of its effector, the PDE. Activated PDE rapidly hydrolyzes cGMP and reduces its concentration in the cytoplasm. The drop of cGMP causes the closure of CNG channels, resulting in a transient hyperpolarization (Figure 2) [21]. The spread of hyperpolarization induces a decrease in the release of glutamate at the synapse and conveys the information to a downstream neuron.

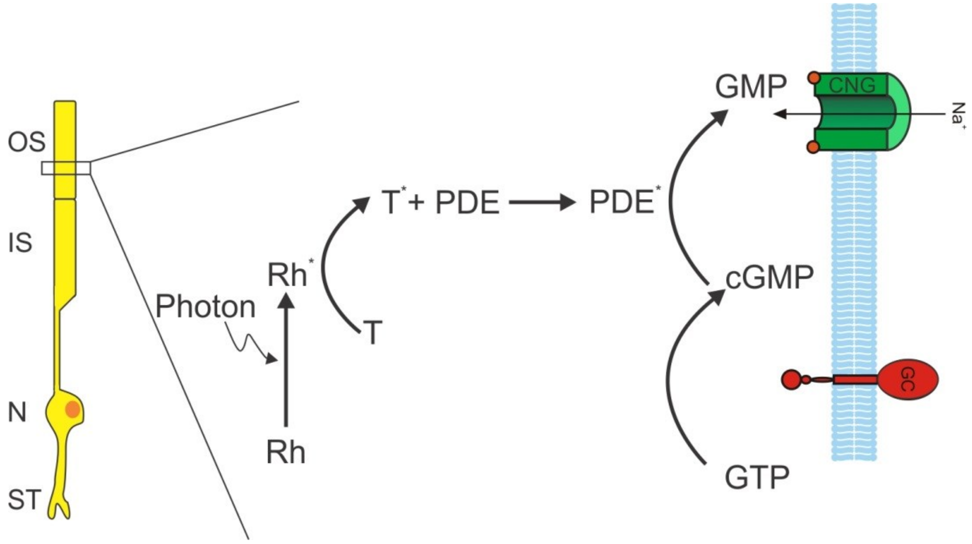

Figure 2. Phototransduction in rod photoreceptors. (Left) Schematic of the morphology of a rod photoreceptor: Outer segment (*OS*), inner segment (*IS*), nuclear region (*N*), and synaptic terminal (*ST*). (Right) Upon light activation, rhodopsin (Rh*) activates transducin (T*), which in turn activates the PDE*. In the dark, cGMP synthesis by the GC maintains a high level of cGMP, upon activation of PDE*, cGMP level drops, resulting in closure of the cGMP-gated CNG channels and a transient hyperpolarization. PDE activation persists until the GTP molecule bound to transducin is hydrolyzed to GDP. GTP hydrolysis is followed by the return of both transducin and PDE into their inactive states. Figure adapted from [18,22].

2.6.2. Mechanism underlying single-molecule / single-photon response

Rods can reliably detect light intensities over 3-4 orders of magnitude, down to a single photon [22]. Similarly, sea urchin sperm can encode chemoattractant concentrations over six orders of magnitude down to a single chemoattractant molecule [9]. Dark-adapted rods can detect and count single photon with reliability close to limits set by statistical fluctuations in the number of absorbed photons. Thus, rod photoreceptors act as nearly perfect photon counters [18]. For single-photon/single-molecule counting, light detection in the rods or molecule detection in sperm, just as light detection in a photomultiplier tube (PMT), must fulfil four requirements: 1) high capture efficiency (analogous to PMT quantum efficiency), 2) sufficient sensitivity to produce a macroscopic measurable response, 3) low dark noise to measure elementary responses above noise level, and 4) high reproducibility of the elementary response (low trial-to-trial variability) to be able to distinguish between 0 and 1 photon/molecule. By contrast to the solid-state reactions in a PMT, rods and sperm meet these requirements using biochemical reactions [18] and biophysical mechanisms:

High capture efficiency:

Sperm and rods harbor a high density of GC and rhodopsin, respectively, which results in a high capture efficiency of molecules in sperm and photons in rods. In fact, the two proteins are among the most densely packed membrane receptors [9], with a density of 9,500 GC molecules/μm^2 in sperm and 25,000 rhodopsin molecules/μm^2 in rods [12].

High sensitivity:

Both sperm and rods possess intriguing variations on a common signaling motif that allows each cell type to achieve high sensitivity.

For instance, rods rely on two enzymatic amplification steps (transducin and PDE activation), and a boost from the CNG channel cooperativity to achieve high sensitivity. The ability of rods to encode the absorption of single photons results from three amplification steps within the signal transduction cascade: activation of the G protein by rhodopsin, subsequent cGMP hydrolysis by the PDE, and cooperative gating of CNG channels. The absorption of a single photon by rhodopsin causes the activation of about 1000 transducin molecules. In turn, one transducin molecule activates a PDE molecule, which hydrolyzes cGMP at a rate near the diffusion limit ($k_{cat}/K_m \sim 10^8\ M^{-1}\cdot s^{-1}$) [23], with one PDE destroying about 2000 - 4000 cGMP molecules per second. The drop in cGMP concentration produces a threefold larger fractional change in the inward current due to the cooperative activation of the cGMP-gated channels (Hill coefficient ~3) [24] and eventually, at least one million cations fail to enter the outer segment [19].

Sperm do not rely on high-gain enzymatic amplification. However, the K^+-selective CNGK channel is exquisitely sensitive in a non-cooperative fashion to cGMP with $K_{1/2}$ = 20 nM. Binding of one cGMP molecule can open a channel [4]. During a single-molecule response, ca. 10 cGMP molecules are synthesized by the GC, thereby increasing the cGMP concentration by ca. 10 nM (assuming a flagellar volume of 1.6 femtoliter). There are about 15,000 CNGK channel in a sperm, therefore, at this low cGMP concentration, cooperative binding of cGMP would compromise the sensitivity. Thus, CNGK channels evolved to operate at extremely low ligand concentration. Because of the large input resistance, even a single CNGK channel might be sufficient to produce an elementary voltage response of 2 mV. By contrast, the CNG of rods is non-selective, about 500 to 1000 fold less sensitive to cGMP, and opens upon cooperative binding of more than one cGMP molecule. Moreover, a single photon response of 1 mV requires the closure of several hundreds of CNG channels [25]. In addition to CNGK, CatSper plays a crucial role in single-molecule sensitivity. CatSper in sea urchin sperm is activated by two events: alkalization shifts the voltage dependence by -30 mV, allowing CatSper to open during depolarization. The pH dependence of CatSper is very steep with a hill coefficient of ca. 11 [6]. This high cooperativity of pH_i control allows CatSper to accurately relay the elementary changes in pH_i and V_m into Ca^{2+} signals. Therefore, sperm rely on the exquisite sensitivity of CNGK and CatSper channels to minute changes in cGMP and pH_i during a single-molecule response. Consequently, high amplification might not be needed to produce a macroscopic measurable response.

Low dark noise:

A small amount of current flows in a PMT even when operated in a completely dark state. This dark current is referred to as dark noise. In order for a PMT to count photons, the single-photon response has to be detectable above the noise level. Similarly to a PMT, sperm and rods possess a certain level of dark noise that could come from spontaneous activation of signaling components. There are two potential sources that could contribute to the total variance of the dark noise [26]. The first source is the spontaneous activation of the receptor, resulting in discrete events that resemble the absorption of one photon in the case of rhodopsin, or the capture of one resact molecule in the case of GC. This is the case in rod cells where thermal isomerization of rhodopsin occur about once every 30 seconds in a toad rod at 20°C [26] and about once every 90 seconds in a mammalian rod at 37°C [27]. Toad rod contains 3 billion rhodopsin molecules, so each rhodopsin activates spontaneously only once every few thousand years. While mammalian rod contain about 100 million rhodopsins, so each rhodopsin activates about once every 300 years at 37°C [28]. For the GC in sperm, spontaneous activation rate is not known. The second source of dark noise is the continuous fluctuation of the cGMP basal level. The stability of cGMP basal level in sperm is not known. In rods the fluctuation in cGMP concentration originates from spontaneous activation of PDE through a process that does not involve transduction [29].

High reproducibility of the elementary response:

In rods, multiple phosphorylation sites on rhodopsin's C-terminus may provide a multi-step shutoff mechanism that in turn controls the lifetime of active rhodopsin. This was suggested to be the reason behind the almost uniform single-photon response [14]. Nevertheless, other mechanisms are still debated and might also explain the low variability [18]. In sperm, GC is inactivated in a similar mechanism via a multi-stage dephosphorylation, which could allow for precise lifetime control and, thereby, reduction of 'molecule noise' that limits the ability to register single resact molecules [12]. In rods, high reproducibility has been established and individual single-photon responses have highly reproducible amplitude and shape. Therefore, one photon can be clearly distinguished from either 0 or 2 photons [14]. However, high response reproducibility for the capture of single resact molecules by sperm is yet to be examined.

3. Mammalian sperm

Unlike sea urchin sperm, mammalian sperm have to navigate across the female genital tract to reach the egg. During this journey, sperm undergo capacitation and hyperactivation. Capacitation is a complex, ill-defined maturation process that is controlled by Ca^{2+} influx and an increase in the intracellular cAMP concentration. Hyperactivation also relies on Ca^{2+} influx and is initiated during capacitation. It is characterized by a whip-like beat of the flagellum, which allows sperm to penetrate the egg vestments [30]. Similar to sea urchin sperm, navigation in mouse and human sperm is triggered and controlled by changes in pH_i, V_m, and $[Ca^{2+}]_i$, which are in turn mediated by a set of ion channels and transporters that are unique to each species (Figure 3) [1,3].

3.1. The principal Ca^{2+} CatSper channel

CatSper is the principal Ca^{2+} channel in human and mouse sperm [31]. The heteromeric CatSper channel complex is made up of at least nine subunits. The four pore-forming α subunits (CatSper 1-4) [31,32] and the auxiliary subunits CatSper β, γ, δ, Ɛ, and ζ [33]. CatSper is localized in the principal piece of the flagellum in mouse and human sperm [31], forming a quadrilateral arrangement in three dimensions, which has been demonstrated to serve as a platform for Ca^{2+} signaling [34]. Lack of any one of the CatSper subunits compromises the organization of these signaling domains and, in turn, compromises hyperactivated motility [34]. Despite CatSper being the principal Ca^{2+} channel in human and mouse sperm, the properties of the channel in each species are different. For instance, mouse CatSper is less voltage-dependent and has higher pH sensitivity than human CatSper (Figure 3A-B) [35]. At resting membrane potential, mouse CatSper is partially opened, whereas human CatSper is mostly closed [36,37]. Human CatSper is activated by various ligands of the oviductal fluid (prostaglandin and progesterone) (Figure 3B) and even structurally diverse synthetic chemicals [38],[4]. Furthermore, human CatSper is inhibited by the endocannabinoid 2-arachidonoylglycerol (2-AG). Progesterone binds to alpha/beta hydrolase domain-containing protein 2 (ABHD2), which degrades 2-AG and relieves CatSper from inhibition (Figure 3B) [40]. Ligands in the oviductal fluid that activate CatSper in mouse are not known. Mammalian sperm swim against the direction of flow, when subjected to a gradient of flow velocities, suggesting that they perform rheotaxis [41,42]. Mouse sperm lacking CatSper fail to undergo rheotaxis and to travel through the oviduct [42], suggesting that CatSper might be responsible for shear-induced Ca^{2+} influx [1].

3.2. The human sperm proton channel Hv1

The proton channel Hv1 mediates a H^+ efflux in human sperm, resulting in intracellular alkalization (Figure 3B) [36]. Hv1 is expressed in the principal piece of sperm flagellum. The channel is a homodimer with a H^+-selective pore formed by four transmembrane segments [43]. Hv1 is activated by depolarization and is regulated by pH. Moreover, the channel is inhibited by Zn^{2+} [44]. Human sperm express an N-terminally cleaved Hv1 isoform, termed Hv1Sper, which carries both outward and inward H^+ currents [45]. Because capacitation requires cytosolic alkalization, Hv1 has been suggested to mediate this alkalization during capacitation (Figure 3B)

[36]. Human patients with mutations in Hv1 are yet to be identified and the role of Hv1 in human sperm remains ill-defined. In contrast to human sperm, mouse sperm do not express functional Hv1 channels [36].

3.3. Na^+/H^+ exchanger family

Eukaryotic Na^+/H^+ exchangers (NHE) and Na^+/H^+ antiporters (NHA) are two subfamilies of the exchanger family that maintain and regulate cellular pH by utilizing the Na^+ gradient across the plasma membrane to extrude H^+ ions [46]. Two NHEs, NHE1 and NHE5 and two NHAs, NHA1 and NHA2 are expressed in spermatozoa [47], [48]. Although the molecules have been attributed different names, as far as we know, they all catalyze Na^+/H^+ exchange.

3.3.1. Sperm-specific Na^+/H^+ exchanger (sNHE)

The atypical, sperm-specific Na^+/H^+ exchanger (sNHE) is expressed in the principal piece of mouse sperm [47]. sNHE harbors a voltage-sensor domain (VSD), similar to the one in voltage-gated K^+, Na^+, and Ca^{2+} channels. In addition, sNHE carries a CNBD similar to those in CNG channels. The function of these domains is still unknown, because, the sNHE molecule has not been functionally expressed. Neither has the physiological role of sNHE in mammalian sperm been identified. Mice lacking sNHE are infertile due to a defect in sperm motility as a result of the concomitant loss of sACY[47]. sACY is found in a signaling complex with sNHE (Figure 3A) and it is the predominant source of cAMP in sperm [49]. Loss of sACY in sperm results in defects in sperm motility [50].

3.3.2. Na^+/H^+ antiporter (NHA)

Two members of the Na^+/H^+ antiporter (NHA) subfamily, NHA1 and NHA2, are expressed in the principal piece of mouse sperm [51]. The NHA harbors 12 transmembrane segments and, unlike the sNHE, no VSD or CNBD. Mice lacking either NHA1 or NHA2 are sub-fertile, while mice lacking both proteins are infertile [48]. In mouse sperm, NHA1 has been shown to play an important role in the signaling events that allow the sperm to penetrate the oocyte's outer protective layer – the zona pellucida (ZP). NHA1 was shown to be responsible for the ZP-evoked alkalization, which is a crucial step for CatSper activation.

3.3.3. The principal K^+ channel Slo3

Slo3 is the principal K^+ channel in mouse and human sperm and it is the sperm-specific member of the Slo family of K^+ channels [52,53]. The membrane potential in mouse and human sperm is regulated by Slo3 and the channel is exclusively expressed in the principal piece of the sperm flagellum [54]. In mouse and human, the Slo3 channel complex contains the auxiliary subunit leucine-rich repeat-containing 52 (LRRC52) (Figure 3A-B) [55,56]. LRRC52 regulates the gating behavior of Slo3, allowing the activation of the channel at physiological pH_i and V_m [52]. Mouse Slo3 is activated at depolarized membrane voltages and alkaline pH_i and carries a hyperpolarizing outward current (Figure 3A). By contrast, in human sperm, Slo3 activity is controlled by Ca^{2+} rather than pH_i, and the K^+ current is inhibited by progesterone [54] (Figure 3B). In mouse sperm, the Ca^{2+} regulation of Slo3 is ill-defined and whether Slo3 is located up- or downstream from CatSper is unknown (Figure 3A). In human sperm, Slo3 is suggested to act downstream from CatSper on the recovery branch of Ca^{2+} signaling [54] (Figure 3B).

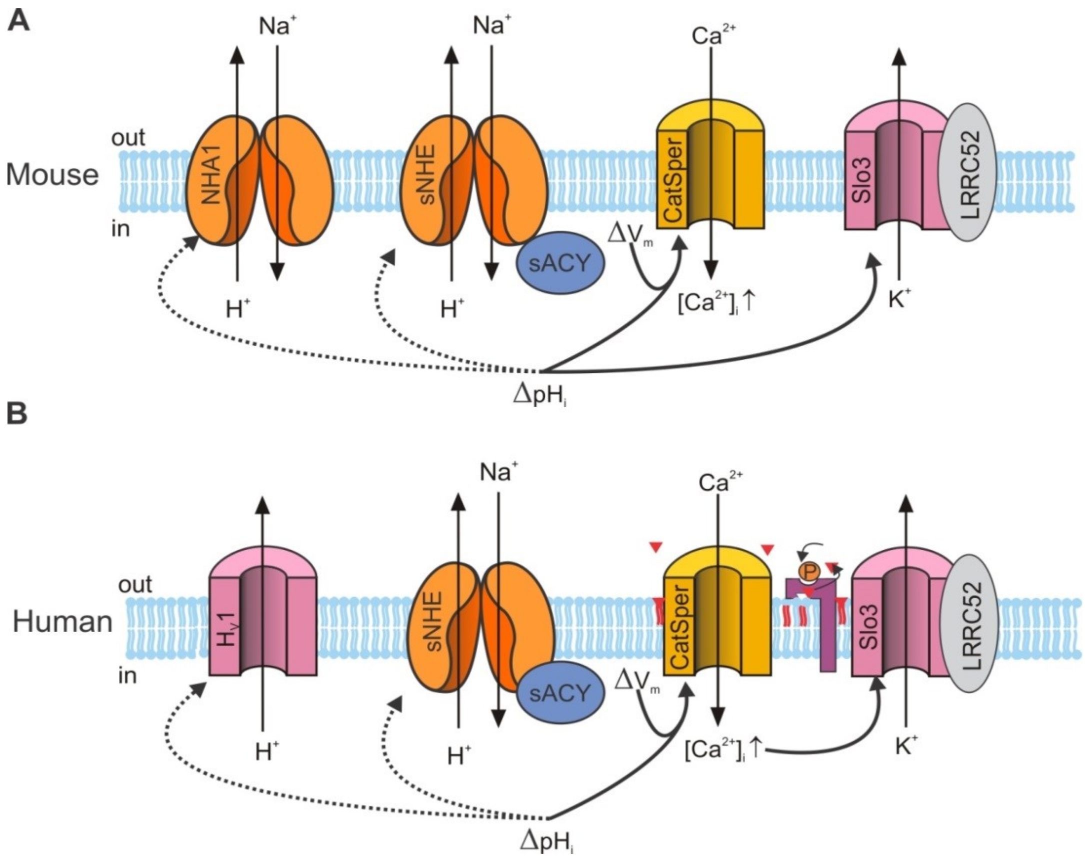

Figure 3. Signaling pathway in mouse and human sperm. **A.** In mouse sperm, the principal Ca^{2+} channel CatSper is regulated by changes in intracellular pH (ΔpH_i) and changes in membrane potential (ΔV_m) . The membrane potential is controlled by the pH-dependent Slo3 K^+ channel. The pH and voltage-dependent opening of Slo3 are controlled by its auxiliary subunit LRRC52. The activation of Slo3 during Ca^{2+} signaling is ill-defined. Prominent candidates for controlling the intracellular pH are two Na^+/H^+ exchangers, the sperm-specific sNHE and NHA1. sNHE is localized in a protein complex with the soluble adenylate cyclase (sACY). However, the role of sNHE and NHA1 in controlling the intracellular pH has yet to be confirmed. The recovery of the Ca^{2+} homeostasis after CatSper opening is not well understood. **B.** In human sperm, similar to mouse sperm, the principal Ca^{2+} channel is CatSper, which is also regulated by changes in pH_i and V_m. In addition, CatSper is activated by binding of progesterone (P) to the lipid hydrolase ABHD2, which hydrolyzes the endocannabinoid 2-arachidonoylglycerol (2AG) to arachidonic acid and glycerol. This relieves CatSper inhibition by 2AG and opens the channel. In human sperm, the principal K^+ channel is also Slo3; it is regulated by Ca^{2+} and by changes in pHi. Presumably, Slo3 is placed downstream from CatSper on the recovery branch of Ca^{2+} signaling. Human sperm contain an H^+ channel (Hv1), which carries an outward rectifying H^+ current. Hv1 and sNHE are the candidates to control pHi in human sperm. Dotted lines present hypothetical signaling pathways that have not yet been confirmed experimentally. (Figures modified from [3]).

4. Supra-molecular arrangements of sensory receptors

Sensory receptors and signalling components are often organized in supra-molecular complexes. Four hierarchical levels of organization have been identified for rhodopsin in dark-adapted mouse rod photoreceptors using cryoelectron tomography. Rhodopsin forms dimers and at least ten dimers form a row. Rows form pairs that are termed tracks, which are aligned parallel to the disk incisures (Figure 4) [20]. Incisures are typically aligned in consecutive disks, creating axial passageways that enhance the diffusion of soluble substances along the long axis of rods during phototransduction. It is thought that signal components like G_t proteins, transducin and PDE are pre-associated to the tracks at rest. Upon light activation, rhodopsin first activates transducin from its own track, and the recruitment of transducin from other tracks proceeds more slowly, as suggested by particle-based simulation. Therefore, rhodopsin sequentially interacts with several downstream signalling components, including transducin and other proteins that terminate rhodopsin activity. Therefore, rhodopsin organization might provide the structural platform that organizes the arrangement of these signalling molecules and coordinates their spatio-temporal interaction [20].

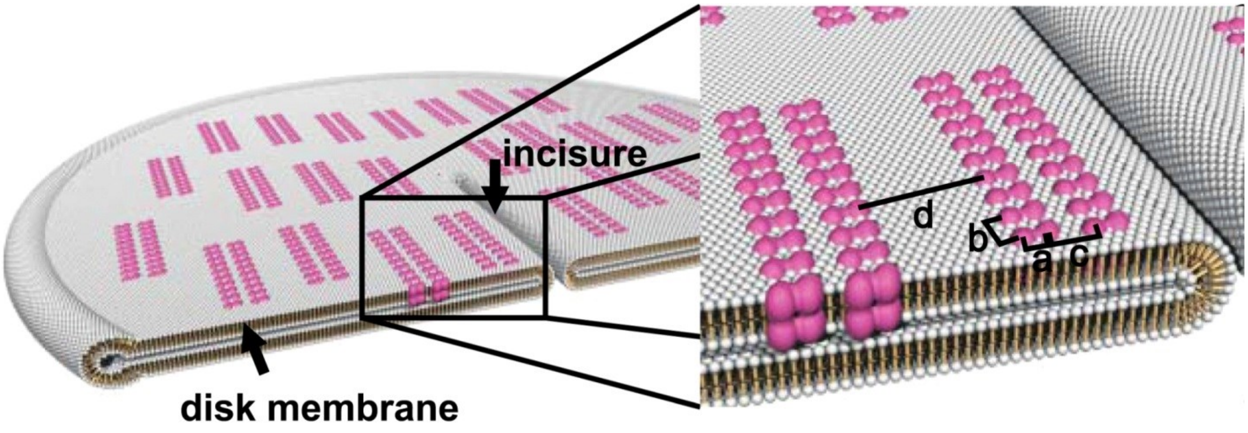

Figure 4. Model for rhodopsin organization in th disk membrane. Overview of rhodopsin organization (purple) in the intact disk membrane. Four hierarchical levels of organizations are shown: rhodopsin forms dimers with distance between monomers a = 4 nm. Dimers form rows with dimer to dimer distance b = 5 nm. Rows come in pairs with a separation distance c = 5 nm, and finally, two pairs of rows termed tracks are separated by a distance d = 15 nm. Image adapted from [20].

Bacterial chemoreceptors were found to be arranged in a highly conserved, 12-nm hexagonal array [57] (Figure 5). The chemoreceptors are key components regulating bacterial chemotaxis. They are localized in a cluster at the cell pole, where it is suggested that the organization of the receptors and high-order interactions among sensory components might contribute to the exquisite sensitivity, wide dynamic range, and precise adaptation [58].

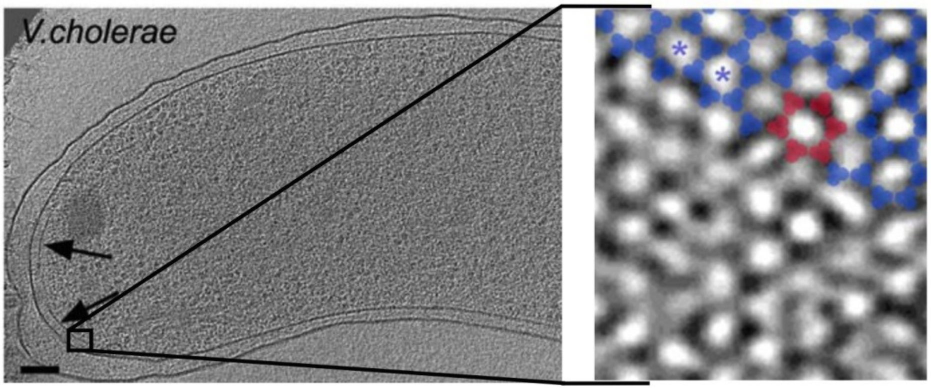

Figure 5. Organization of chemoreceptors in bacteria. (Left) Tomographic slices of cryo-EM in *V.cholerae* bacteria. Black arrow shows the localization of chemoreceptor complexes. (Right) Zoomed image showing trimers of dimers (blue) fit into the vertices of the hexagonal lattice in a chemoreceptor array. Six trimers of dimers (red) enclose one hexagon. The spacing from the center of one hexagon to the center of an adjacent one is 12 nm (blue asterisks). Images adapted from [57]. Scale bar : 100 nm.

The CatSper channel complex in mouse sperm forms a quadrilateral arrangement in three dimensions (Figure 6) that organizes structurally distinct Ca^{2+} signaling domains along the flagella [34]. Recently, it was shown that human CatSper channels form the same quadrilateral arrangements [33]. The Ca^{2+} signaling domains are disrupted in CatSper-deficient mice, suggesting that CatSper is crucial for organizing the signaling domain. Moreover, within a heterogeneous sperm population, only sperm with intact CatSper domains could hyperactivate and move efficiently. The quadrilateral arrangement of CatSper allows spatio-temporal control of tyrosine phosphorylation – an important process for capacitation [34]. The lack of CatSper ζ in mice sperm resulted in partial disruption of the Ca^{2+} quadrilateral arrangements, which was associated with the inability of sperm to undergo rheotaxis [33].

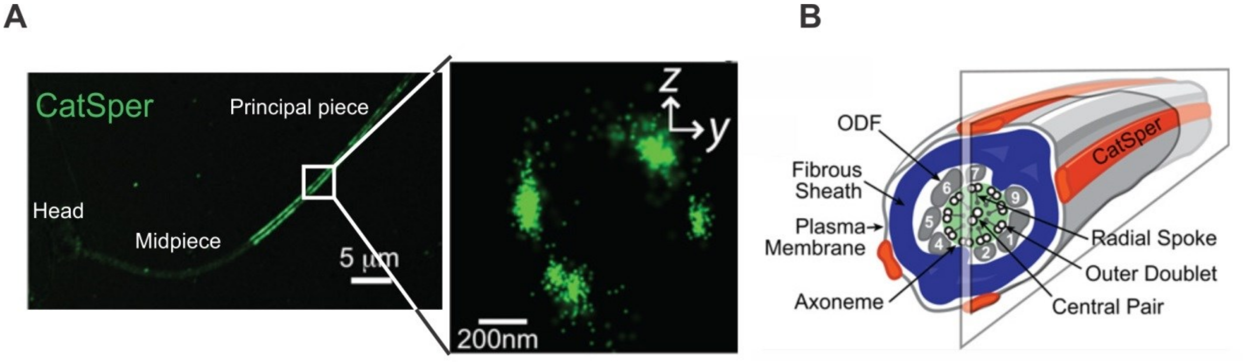

Figure 6. CatSper have a quadrilateral arrangement along the sperm flagellum. A. Confocal fluorescence image with CatSper1 in mouse sperm (green). 3D stochastic optical reconstruction microscopy (STORM) images of CatSper1 in y-z projection, with the four linear domains. **B.** Model of the sperm flagellum showing the quadrilateral arrangement of CatSper (red) relative to the underlying cytoskeletal structures. Images adapted from [34].

5. Sperm development – Role of non-lysosomal β-glucosidase GBA2

5.1. Glucosylceramide homeostasis

Glucosylceramide (GlcCer) is the simplest glycosphingolipid, forming a building block for more complex glycosphingolipids. Glycosphingolipids are anchored to the membrane by a two-tailed lipid anchor, the ceramide. Ceramide consist of a sphingosine and a fatty acid [59]. GlcCer is synthesized by the glycosylation of ceramide in the Golgi through the action of a glucosylceramide synthase (GCS) and GlcCer is degraded to glucose and ceramide by beta-glucosidases, which cleave the beta-1,4 glycosodic linkage between the terminal non-reducing residue and the ceramide backbone (Figure 7) [60,61]. Three beta-glucosidases that degrade GlcCer have been identified, namely glucocerebrosidase 1 (GBA1), the non-lysosomal beta-glucosidase (GBA2), and the cytosolic beta-glucosidase (GBA3) (Figure 7) [62–64]. Furthermore, GlcCer also functions as an intracellular messenger with implications on cell growth and differentiation [65], axonal growth in hippocampal neurons [66], and post-Golgi trafficking.

Figure 7. GlcCer metabolism. GlcCer is synthesized by glycosylation of ceramide. GlcCer is hydrolyzed to glucose and ceramide by any of the three beta-glucosidases (GBA1, GBA2, GBA3).

5.2. Role of GBA2 in spermatogenesis

GBA2 is a non-lysosomal beta-glucosidase with highest activity at an optimal pH of 6. GBA2 can be blocked with N-butyldeoxynojirimycin (NBD-NJ) [67]. It has been shown that GBA2 is membrane-associated at the ER and Golgi with the N and the C termini facing the cytoplasm [68], suggesting that the degradation by GBA2 occurs in the cytosol. GBA2 is ubiquitously expressed with high levels found in the testis and brain and lower levels found in liver, heart, spleen, and skin [69]. The lack of GBA2 in mice resulted in GlcCer accumulation in tissues that have high GBA2 expressions such as testis and brain. GBA2 knockout-mice are sub-fertile and GlcCer accumulation in the testis has been linked to defects in spermatogenesis, resulting in a condition called globozoospermia [69]. Globozoospermia is characterized by round-headed sperm and a severely deformed acrosome (Figure 8). Sperm heads of wild type mice are sickle-shaped with a well-formed acrosome, whereas the sperm head of GBA2 knockout-mice is round contains no or a malformed acrosome (Figure 8) [69]. Moreover, mitochondria in the sperm flagellum are displaced. In humans, mutations in the *GBA2* gene have been associated with bilateral testicular hypotrophy and sperm defects [70]. The molecular mechanisms underlying the role of GBA2 in sperm development leading to globozoospermia are ill-defined.

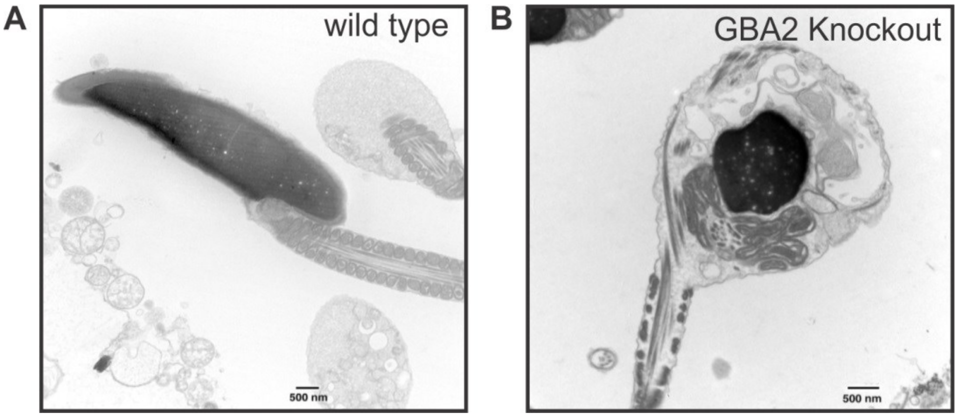

Figure 8. Head morphology of wild type and GBA2 knockout-sperm. A. Electron micrograph of sperm from a wild type mouse showing normal, sickle-shaped head. **B.** Electron micrograph of a GBA2 knockout sperm showing round-shaped head. Dark electron dnese region represents the sperm nucleus. Images taken from [69]. Scale bar: 500 nm.

Spermatozoa are produced from spermatogonial stem cells in a process called spermatogenesis. Spermatogenesis occurs in the testis in the seminiferous tubules. The basal ectoplasmic specialization (ES) at the site of blood-testis barrier (BTB) divides the seminiferous epithelium into the basal and the apical (adluminal) compartments. The ES is a testis-specific, actin-based hybrid anchoring and tight junction [71]. The BTB is a specialized junction made of Sertoli cells that are close to the basal membrane. The BTB restricts the flow of molecules from the basal to the adluminal compartment and acts as an immunological barrier by preventing entry of antibodies that could act on developing germ cells [72]. The first step of spermatogenesis starts at the basal lamina of the seminiferous epithelium with diploid spermatogonia. Mitotic division of spermatogonia results in primary spermatocytes, which cross the BTB in the preleptotene phase of meiosis I. Primary spermatocytes complete meiosis I and II upon reaching the adluminal compartment to form secondary spermatocytes. Secondary spermatocytes differentiate into round spermatids at puberty. The round haploid spermatids undergo dramatic morphological changes to form elongated sperm. During spermatid elongation, the sperm head is connected to the Sertoli cell via the ES and is shaped by two cytoskeletal processes: the F-actin at the ES and the microtubule manchette at the anterior end of the apical ES (Figure 9) [73,74]. The microtubule manchette consists of a perinuclear ring that is supported by numerous vertically arranged microtubules. The postacrosomal region of the sperm head is shaped by the constrictive downward movement of the manchette. The ES consists of F-actin that is supported by the ER and plasma membrane of Sertoli cells. F-actin forms hoops around the sperm head (Figure 9), where polymerization and depolymerization causes tread milling of the F-actin containing hoops. This movement generates constriction forces that shape the acrosomal region of the sperm head [75]. Members of the Rho family of GTPases, such as Cdc42 and Rac1, have been shown to regulate actin dynamics [76,77]. Lack of GBA2, which results in accumulation of GlcCer in the plasma membrane, could change the activity of Cdc42 and Rac1 associated with the plasma membrane of Sertoli cells (Figure 9) thereby, compromising the sperm-head shaping mechanism [78]. However, the cellular localizations of the membrane domains affected by GlcCer accumulation are not known and the direct effect of those domains on GTPase activity and cytoskeletal dynamics is yet to be determined.

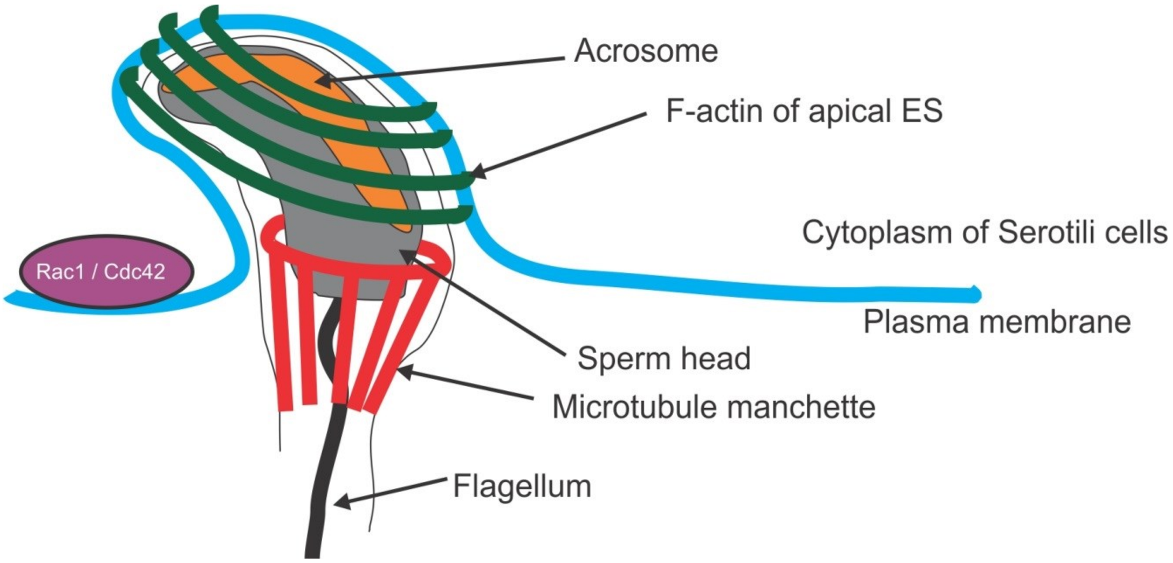

Figure 9. Shaping of the sperm head. Schematic representation of the ectoplasmic spezialisation (ES) between a wild-type spermatid head and Sertoli cell. F-actin of the Sertoli cell at the apical ES (dark green) and the microtubule manchette of the spermatid (red) shape the sperm head. As a result, sperm heads are sickle-shaped with a well formed acrosome (orange). The nucleus and the flagellum are indicated in grey and black, respectively. Proteins associated with the plasma membrane, such as GTPases Cdc42 and Rac1, could control actin and microtubule dynamics, thereby, controlling sperm-head shaping. Image adapted from [78].

II. Aim of my PhD thesis

The molecular mechanisms underlying chemotaxis in sea urchin sperm are extensively studied; and most of our knowledge on sperm chemotaxis originates from the study of marine invertebrates, notably sperm from the sea urchin *A. punctulata*. However, the mechanism underlying single-molecule sensitivity and cGMP dynamics is not well understood. To gain insights into the molecular mechanisms was the first aim of my PhD thesis. Moreover, the supra-molecular arrangement of the signaling cascade controlling sperm behavior in sea urchin and mammalian sperm are not known. Thus, my second aim was to address the supra-molecular structure of the chemoreceptor in sea urchin sperm and the signaling components underlying mammalian sperm navigation using super-resolution microscopy.

Before sperm are mature and able to navigate their way to the egg, they have to develop from a round cell into an elongated cell with a head and a tail during spermatogesis. Lack of GBA2 enzyme results in severe morphological defects in mouse sperm – a condition called globozoospermia. GlcCer accumulation in the absence of GBA2 enzyme and the subsequent dysregulation of cytoskeletal dynamics is thought to underlie the defects in sperm shaping during spermatogenesis. However, the underlying processes are not well understood; thus, unraveling the molecular mechanism was the third aim of my PhD thesis.

In detail, I addressed the following three questions:

1. How can sea urchin sperm register the binding of a single chemoattractant molecule? And what is the mechanism underlying cGMP dynamics following the activation of chemoreceptors?
2. How are the key signaling components organized in sea urchin and mammalian sperm? Namely, the GC chemoreceptor in sea urchin sperm and CatSper in human sperm?
3. What is the underlying mechanism behind the defects in spermatogenesis in mice lacking GBA2 enzyme? In particular, how accumulation of GlcCer dysregulates cytoskeletal dynamics, which in turn lead to dysregulation of sperm shaping during spermatogenesis?

III. Materials

1. Antibodies

1.1. Primary antibodies

Antibody	Host species	Used against	Dilution	Manufacturer
Polyclonal anti-CatSper3	Zabbit	Human sperm	1:100	D. Fusshoeller caesar
Polyclonal anti-CatSper 1 (D-17)	Goat	Mouse sperm	1:250	Santa Cruz (#sc-21180)
Monoclonal anti-Catsper3	Rat	Sea urchin sperm	Undiluted*	E. Kremmer (HZ München)
Monoclonal anti-GC (GCN 3D12)	Rat	Sea urchin sperm	1 : 100	E. Kremmer (HZ München)
Polyclonal anti-HA tag	Mouse	Transfected HEK293 cells	1:5000	Sigma (#H9658)
Polyclonal anti-tubulin	Mouse	CHO cells	1:1000	Sigma (#T5168)

* In addition to 0.5 % Triton X-100.

1.2. Secondary antibodies and markers

Conjugated dye	Host species	Used against	Dilution	Manufacturer
Alexa Fluo-488	Goat	Mouse	1:400	Life Technologies (#A11029)
Cyanine-5	Donkey	Mouse	1:100	Dianova (#715-175-151)
Cyanine-5	Donkey	Rabbit	1:400	Dianova (#711-175-152)
Alexa Fluo-647	Donkey	Goat	1:75	Life Technologies (#A21447)
Alexa Fluo-647	Donkey	Rat	1:150	Dianova (#712-605-153)
IRDye800	Goat	Rat	1:20000	Li-Cor Bioscience

Phalloidin-647 (Alexa Fluor 647 Phalloidin) for actin staining was, purchased from ThermoFisher Scientific (#A22287)

2. Fluorescent dyes

- Laurdan (6-Dodecanoyl-2-Dimethylaminonaphthalene) - Molecular Probes, #D250

Laurdan aliquots were prepared in DMSO at concentration of 2.5 mM.

- DAPI - Molecular Probes #D1306

- Cy5-azide – Sigma Aldrich #777323-1MG
- Coumarin-azide (7-Azido-4-Methylcoumarin) #L511455-10MG
- Dy654-N_3 (Dyomics 654 azide) - dyomics GmbH

Voltage sensitive dye Berkeley Red-based Sensor of Transmembrane potential (BeRST) was generously provided by Dr. Evan Miller (University of California, Berkley, USA) and prepared as 2 mM stock solution in DMSO and stored at -20°C. BeRST is a far-red voltage sensitive dye that make use of a photoinduced electron transfer (PeT) trigger for optical interrogation of membrane voltage [79].

Fluo-4 is a fluorescent Ca^{2+} indicator whose fluorescence quantum yield increases upon binding to Ca^{2+}. Fluo-4 is composed of a fluorescein-based fluorophore and a BAPTA-like Ca^{2+} chelator [80]. The affinity of Fluo-4 for Ca^{2+} (Kd of 345 nM) is appropriate for physiological Ca^{2+} levels [80]. Sperm were loaded with the acetoxymethyl (AM) derivative, Fluo-4-AM. The AM ester renders Fluo-4 insensitive to Ca^{2+}, but able to diffuse across the membrane [81]. Once internalized, the ester is hydrolyzed by cytosolic esterases; thereby, releasing the charged, Ca^{2+}-sensitive indicator. As a charged molecule, Fluo-4 is membrane impermeable and becomes trapped in the cytosol. Fluo-4 was purchased from ThermoFisher Scientific (Waltham, MA, USA) # F14201.

pHrodo™ Red, succinimidyl ester (pHrodo-red SE) was purchased from TherFisher Scientific # P36600. The ester modification allows the dye to diffuse across the membrane. Once internalized, the ester is hydrolyzed by cytosolic esterases, releasing the pH sensitive indicator. Since it is charged, the dye is impermeable and becomes trapped in the cytosol. The fluorescence of this dye increases as pH decreases, and is appropriate for use in the physiological range.

3. Caged compounds

DEACM 7-(diethylamino)-4-(hydroxymethyl)-coumarin-cGMP a caged derivative of guanosine 3',5'-cyclic monophosphate (cGMP) was used in stopped-flow experiments to record membrane voltage and Ca^{2+} signals in response to uncaging. Stock solutions of caged cGMP (10 mM) were prepared in anhydrous DMSO and stored at – 20°C. Dry sperm suspended in 1:6 (v/v) in ASW were loaded with the appropriate fluorescent dye and caged compound. Sperm were then diluted

1:20 in ASW and caged compound was added again in order to maintain a constant concentration in the external medium. The quantum yield of DEACM-cGMP is 0.25 and its extinction coefficient is $1.93 \times 10^7\ \mathrm{M}^{-1}\mathrm{m}^{-1}$ at 403 nm.

4. Plasmids

The following constructs were provided by Prof. Klaus Hahn

#	Construct	Obtained on
490	Ypet-C1 (390, Klaus Hahn)	14.04.2016
491	Cerulean3-C1 (1706, Klaus Hahn)	14.04.2016
492	Rac1FLARE CD1g (1287, Klaus Hahn)	14.04.2016
493	Cdc42FLARE CD1g (1204, Klaus Hahn)	15.04.2016

5. Solutions

Artificial Sea Water (ASW) was prepared according to Table 1. For K^+ fortified ASW with concentrations ranging from 30 mM to 100 mM, standard ASW (9 mM KCl) was mixed with high K+ ASW (51 - 191 mM KCl) in appropriate ratios to get a final 30 mM to 100 mM in the stopped-flow cuvette. The pH was adjusted to 7.8 with NaOH at room temperature.

Table 1. ES buffer composition

ASW (mM) - pH 7.8	
NaCl	423
KCl	9
$CaCl_2$	9.27
$MgCl_2$	22.94
$MgSO_4$	25.5
EDTA	0.1
HEPES	10

Extracellular solution (ES) was prepared according to Table 2. The pH was adjusted to 7.4 with NaOH at room temperature.

Table 2. ES buffer composition

ES (mM) - pH 7.4

NaCl	120
KCl	5
$CaCl_2$	2
$MgCl_2$	2
Glucose	10
HEPES	10

Phosphate buffer saline was prepared according to Table 3.

Table 3. PBS buffer composition

PBS (mM) - pH 7.4

NaCl	137
KCl	2.7
KH_2PO_4	1.5
Na_2HPO_4	6.5

Lysis buffer was prepared according to Table 4.

Table 4. Lysis buffer composition

Lysis buffer - pH 7.5

NaCl	10 mM
EDTA	2 mM
HEPES	25 mM
Triton X-100	1 % (V/V)
Protease-inhibitor (mPIC)	1 : 500

6. Multi-LED system

Cage:	#B1C	Thorlabs
	#SM1L03	Thorlabs
	#ACL2520U-A	Thorlabs
	#SM1V05	Thorlabs
	#SM1T2	Thorlabs
	#SM1CP2	Thorlabs
	#FFM1	Thorlabs
	#B4C	Thorlabs
	#C4W	Thorlabs
Light-guide coupler:	#B1C	Thorlabs
	#SM1L03	Thorlabs
	#ACL2520U-A	Thorlabs
	#SM1V05	Thorlabs
	#SM1T2	Thorlabs
	#SM1CP2	Thorlabs
	#FFM1	Thorlabs
	#B4C	Thorlabs
	#C4W	Thorlabs
LED filter mounts	#SM1L03	Thorlabs
LEDs:	#M455L3	Thorlabs
	#M490L3	Thorlabs
	#M530L3	Thorlabs
	#M660L4	Thorlabs
	#M660L4	Thorlabs
Dichroic filters:	#F48-600	AHF
	#F48-510	AHF
	#F48-470	AHF
	#DG10-600	Thorlabs

IV. Methods

1. Cell culture

GBA2 knockout-mice were generated as mentioned in [69]. All experiments performed with animals were in accordance with the relevant guidelines and regulations.

1.1. Isolation of dermal fibroblasts

Dermal fibroblasts were isolated from mice tails using collagenase digestion by Dr. Diana Raju. Tail pieces were incubated in fibroblast growth medium containing 0.1 mg/ml collagenase (Sigma) for 3h, 37°C, and 5 % CO2. After digestion, the supernatant was centrifuged for 5 min, 600 x g at room temperature. The cell pellet was re-suspended in fibroblast growth medium; cells were plated on cell culture plates, and cultured at 37°C, 5 % CO2. After 24 hours, the medium was changed.

Fibroblast growth medium: DMEM/GlutaMax containing 10% FCS, 100 mM sodium pyruvate, 200 mM L-glutamine, 70 IU/ml penicillin, 70 µg/ml streptomycin.

1.2. Isolation of cerebral neurons

Cerebral neurons were isolated by Dr. Sina Stern. In brief mouse brain was placed in a sterile 3 cm dish with Hank's Balanced Salt Solution (HBSS). The cerebellum was removed from the brain using fine forceps and transferred to a new 3 cm dish with HBSS. The meninges were removed and the clean cerebellum was transferred to a new 3 cm dish. After that the cerebellum was cut into small pieces and the tissue was collected in a 15 ml tube. Fresh HBSS was added in the tube with 1 ml trypsin-DNase solution and it was left at room temperature for 10 minutes. The trypsin solution was then replaced with DMEM-HS. Next, the tissue was triturated with 2 fire-polished Pasteur pipettes pre-coated with 4 % BSA to separate the cells. Cells were centrifuged at 800 x g for 5 minutes at 4°C, washed 2 times with HBSS and then re-suspended in HBSS. After counting, the cells were plated in DMEM-HS**. For drug treatment, neurons were incubated in presence of 5 µM NBD-NJ for 48 hours.

Table 5. Composition of Complete Neurobasal Medium (CNM)

CNM (50 ml)

Neurobasal Medium (GIBCO)10 B-	47 ml
27 Supplement	1 ml
Glutamine	0.5 ml
Pen Strep antibiotic	0.5 ml
FBS (Fetal Bovine Serum)	1 ml

Table 6. Composition of Trypsin-DNase

Trypsin-DNase solution (100ml)

Trypsin	1 mg
DNase*	100 mg
CMF-PBS	99.4 ml
MgSO4x7H2O	22.5 mg
1N NaOH	0.6 ml

*DNase (DNase grade II ref 104159 Roche) at 1mg/ml in 0.001 HCl . It was aliquoted in 500 µl batches and stored at -20°C for 100 ml of HBSS (Sigma Aldrich).

**DMEM-HS : (Dulbecco's Modified Eagle Medium) DMEM + 5 % Human Serum (HS) (Sigma Aldrich).

1.3. Immunocytochemistry

Cells were plated on 1.5H glass coverslip and fixed in 4 % paraformaldyhyde at room temperature for 10 minutes. For cytoskeletal imaging, Phem* buffer was used to preserve the cytoskeleton. After Phem fixing, cells were washed with PBS and then quenched in 0.1 % sodium borohydride for 10 minutes. Before blocking, all cells were washed 3 times with PBS. To block unspecific binding sites, cells were incubated for 1 hour with blocking buffer (0.5 % Triton X-100 and 5 % ChemiBLOCKER (Millipore) in 0.1 M phosphate buffer, pH 7.4). Primary antibodies were diluted in blocking buffer and incubated 1 hour at room temperature. For sperm in particular, primary antibodies were incubated overnight at 4 degrees. Fluorescent secondary antibodies were diluted in blocking buffer and incubated for 1 hour in the dark. For nuclear staining cells were incubated for 5 minutes in blocking buffer containing 0.5 µg/µl DAPI

(Invitrogen). For STORM imaging, cells were post-fixed with 4 % paraformaldyhyde for 10 minutes and kept in PBS buffer at 4 degrees until imaging.

Phem stock (pH 7.0)	*Phem buffer
2 mM MgCl2	1 x Phem buffer
10 mM EGTA	0.1 % (v/v) Triton X-100 (Roth)
25 mM HEPES	0.25 % (w/v) glutaraldehyde (Sigma)
60 mM PIPES	3.7 % (w/v) PFA/sucrose

1.4. Laurdan membrane staining

Laurdan staining of HEK293, fibroblasts and primary neurons was performed as follows:

1. Medium was removed from the cell culture dish and replaced with 2 ml of fresh, serum-free medium.
2. Cells were incubated with 20 µM Laurdan. Concentrations of up to 50 µM can be used to efficiently stain cells without affecting cell viability [82].
3. Cells were shaken gently to ensure good mixing.
4. Cells were then incubated at 37°C in a humified 5 % CO_2 atmosphere for 30 minutes.
5. Cells were then fixed in 4 % paraformaldehyde for 10 minutes at room temperature.
6. Finally, cells were washed 2 times with PBS and kept in PBS until imaging.

1.5. Isolation of GPMV

Giant plasma-membrane vesicles (GPMVs) have been isolated as described in [83] . In brief, dermal fibroblasts or HEK293 cells were incubated with GPMV buffer containing 2 mM NEM for 1-2 h at 37°C, 5% CO2. Cell plates were shaken every 30 minutes to increase vesicle yield. For imaging, the supernatant was transferred to 15 ml falcon tubes and left on ice for cell debris to settle. Supernatant was then transferred to another falcon and labeled with 20 µM Laurdan. Pure GPMV were needed for spectroscopy, therefore, the supernatant was centrifuged for 10 minutes at 2,000 x g and room temperature to pellet cell debris and intact cells. The resulting supernatant was subjected to high-speed centrifugation for 1 hour at 45,000 x g and 4°C to pellet the vesicles. The vesicle rich pellet was re-suspended in GPMV buffer.

1.6. Transfection of HEK293 cells

PEI transfection of HEK 293 cells in 4-well plates were performed as follows:

1. Cells were seeded to be 90-95 % confluent by the time of transfection.
2. 0.5 µg DNA were added to OptiMEM. 50 µl OptiMEM and 0.5 µg DNA per well.
3. Branched PEI* stock was added to the DNA suspension (1 µg/µl stock SIGMA 408727, 1 µg/well), then mixed.
4. Medium was removed from well and replaced with 200 µl/well of DMEM containing 2 % serum.
5. PEI/DNA suspension was then added to wells.
6. Cells were then incubated at 37 °C in a humified atmosphere with 5 % CO_2 for 1 to 3 days before imaging.

*Polyethylenimine (PEI) was purchased from Polysciences, (25kD linear from cat# 23966-2).

1.7. Transfection of mouse dermal fibroblasts

$1x10^6$ mouse fibroblasts were resuspended in 100 µl transfection buffer (Neon transfection system, Life technologies) and 4 µg of plasmid DNA was added. Using a microporator mini (Digital Bio Technology, MP-100), 100 µl of the cell suspension were subjected to two pulses (20 ms each) of 1000 V and afterwards transferred to glass-bottom dishes pre-coated with poly-L-Lysine. The cells were allowed to grow overnight at 37°C and 5% CO2 in medium.

1.8. Collection of sea urchin sperm from *Arbacia Punctulata*

Animals were purchased from the Marine Biological Laboratory (MBL) Woods Hole (Woods Hole, MA, USA). Sperm was obtained from male A*rbacia punctulata* sea urchin by injecting 500 µl of 0.5 M KCl into its body cavity [84]. The released sperm are very dense and referred to as ‘dry’ sperm. In dry sperm, sperm are immotile and show stunted responses to stimuli. Sperm become activated upon dilution in ASW by a minimal dilution factor of 1:20 (v/v). For stopped-flow kinetic measurements, sperm were used on the same day in Woods Hole. For imaging and biochemical assays, dry sperm were transferred and stored on ice during transport to Caesar research institute in Bonn, Germany. Sperm were on ice an average of 2-3 days prior to use.

2. Biochemical methods

2.1. SDS-PAGE and western-blot analysis

SDS-sample buffer (4x; 200 mM Tris/HCL pH 6.8, 0.04 % bromophenol blue, 4 % beta-mercaptoethanol, 8 % SDS, 50 % glycerine) was added to all samples (final 1x) and heated for 5 minutes at 95°C prior to loading onto SDS-PAGE (sodium dodecyl sulfate polyacrylamide gel electrophoresis). The SDS-PAGE was performed in running buffer (final 1x; 10x: 250 mM Tris, 1.92 M glycine, 1 % SDS) at 180 V and 120 mA. As protein standard the protein prestained protein marker VI (AppliChem # A8889, 0500) was used. For Western-blot analysis, proteins were transferred onto PVDF membranes (Immobilon-FL, Millipore), probed with antibodies, and analyzed using the Odyssey Imaging System (LI-COR).

2.2. In-gel-fluorescence analysis

SDS-PAGE with protein samples that contained fluorescence dye were performed in the dark. Gels were imaged directly in one channel using the LI-COR system or transferred onto PVDF membranes in the dark, probed with antibodies and then imaged in two channels using the LI-COR system.

2.3. Cell lysate preparation

Sperm lysate were prepared as follows:

1. Sperm suspension was centrifuged at 1000 x g for 10 minutes.
2. Supernatant was discarded and replaced with lysis buffer.
3. Sperm were then lysed for 60 minutes at 4°C.
4. Sperm lysate was then transferred to Eppendorf tubes (1.5 ml).
5. Lysate were then centrifuged at 8000 x g at 4°C for 30 minutes and pellet was discarded.

2.4. Sperm head and tail preparation

Sperm heads and tails were prepared by Dr. Diana Raju. In brief, 500 µl of dry sperm was re-suspended in 12 ml of ASW at pH 7.8. To remove the protease containing coelomycytes, sperm suspension was centrifuged for 7 minutes at 200 x g and the sperm-rich supernatant was transferred to a new falcon. Next, the sperm suspension was centrifuged at 300 x g for 15 minutes and the pellet was re-suspended in 5 ml ASW. After counting, the sperm suspension was sheared 20 times with a 24G needle in order to separate the sperm heads from the flagella. Next, the sperm suspension was centrifuged at 2000 g for 10 minutes to pellet the sperm heads, and the flagella-rich supernatant was transferred to a new falcon tube. The application of shear forces on sperm suspension was repeated until no sperm heads were observed under the microscope in the flagella-rich supernatant.

2.5. Photo-crosslinking, chemical crosslinking and click chemistry

Photo-crosslinking of photoresact and photosperact to sea urchin sperm from *A. Punctulata* and *S. Purpuratus,* respectively, were performed as follows:

1. Dry sperm was suspended in ASW for a final $4x10^8$ sperm in 500 µL in low bind Eppendorf.
2. 5 µL photoresact/photosperact was added (aliquot 1 mM, final concentration 10 µM).
3. Sample was crosslinked under UV lamp (Maglite-UV-lamp 1.25 A Diode centered at 360 nm) for 2-5 minutes.
4. Sample was then washed in ASW (Centrifuged for 10 minutes at 700 x g at room temperature). Supernatant was discarded and then we proceeded for click chemistry.

Chemical crosslinking protocol of chemresact to sperm from *A. Punctulata* was performed as follows:

1. Dry sperm was suspended in ASW for a final $4x10^8$ sperm in 500 µL in low bind Eppendorf.
2. 5 µL photoresact/photosperact was added to sperm suspension (aliquot 1 mM, final concentration 10 µM).
3. DSS cross-linker was added and reaction was allowed to proceed for 10 minutes at room temperature.
4. Reaction was quenched with 100 mM Tris-HCl buffer.
5. Samples was then washed in ASW (Centrifuged for 10 minutes at 700 x g at room temperature). Supernatant was discarded and then we proceeded for click chemistry.

Click chemistry reaction was performed as follows:

1. The following was added to sperm pellet after either photo- or chemical-crosslinking:

a. Buffer: 455 µL ASW

   b. Ligand: 5 µL THPTA
      aliquot 50 mM – final concentration 500 µM
   c. Fluorophore: 10 µL Dyomics 654-azide
      aliquot 1 mM – final concentration 20 µM
   d. Catalyst: 10 µL Cu(I)
      aliquot 25 mM – final concentration 500 µM
2. Suspension was mixed gently and kept in dark for 30 minutes at room temperature.
3. Suspension was then washed 3 times in ASW by centrifugation at 700 x g for 10 min at room temperature and sperm were then plated on 1.5H coverslips for fluorescence imaging. Alternatively for SDS-PAGE analysis, suspension was centrifuged at 1000 x g. Supernatant was aspirated and pellet re-suspended in loading buffer.

2.6. Protein enrichment with cleavable azide-beads

After photoresact was photo-crosslinked to sea urchin sperm, the sperm preparation was centrifuged at 400 x g for 10 minutes. Supernatant was discarded and replaced with lysis buffer. Cleavable azide beads were added to the sperm lysate in the presence of 0.5 mM THPTA. 0.5 mM Cu (I) was then added to the lysate and the reaction was allowed to proceed for 30 minutes on a magnetic stirrer. Finally, beads were washed extensively and transferred to a new Eppendorf tube. SDS-sample buffer (4x; 200 mM Tris/HCL pH 6.8, 0.04 % bromophenol blue, 4 % beta-mercaptoethanol, 8 % SDS, 50 % glycerine) was added to the beads (final 1x) and heated for 5 min at 95°C prior to loading onto SDS-PAGE (sodium dodecyl sulfate polyacrylamide gel electrophoresis).

2.7. Sample preparation for mass spectrometry

SDS-PAGE gels were stained overnight in Colooidal Coomassie (Table 7) at room temperature. They were then destained with 1 % Acetat for 30 minutes. Destaining was repeated three times. After that, gels were placed on a clean glass plate and protein bands of interests were cut into slices. Each slice was then chopped to 2 x 2 mm and transferred to a clean 1.5 ml Eppendorf tube with 150 µl 50 % (v/v) methanol. Methanol was then replaced with destaining solution (40 mM NH_4HCO_3 in 50 % Acetonitril) and incubated for 20 min at 37°C while shaking. Destaining was repeated until the gel pieces became clear. Finally, destaining solution was discarded and the remaining solvent was removed using a centrifugal vacuum concentrator. The destained gels were then shipped for mass spectrometry analysis.

Table 7. Colloidal Coomassie recipe

Colloidal Coomassie	
G-250 Coomassie	0.1 % (w/v)
Phosphoric acid	1.6 % (v/v)
Ammonium sulphate	8 % (w/v)
Methanol	20 % (v/v)

2.8. Conjugation of dye to antibodies

To aliquot the Alexa Fluo dyes, 1 mg was dissolved in anhydrous DMSO and aliquoted again into tubes for a final 0.02 mg amount of dye per tube. DMSO was then removed using an evaporator and the aliquots were stored at -20°C. For labeling unconjugated antibodies, one aliquot of Alexa Fluo-647 was dissolved in 10 µl anhydrous DMSO and then 1.5 µl of dye solution was added to 50 µl of antibody (1.25 mg/ml in PBS) and 6 µl of $NaHCO_3$. The reaction was allowed to proceed in the dark for 30 minutes at room temperature. NAP-5 columns were then used to separate the labeled antibodies from the free dye molecules. Finally, antibody-dye ratio was measured with UV/Visible spectrophotometer.

2.9. Determination of antibody-dye ratio

The labeling ratio was calculated by measuring the absorption of antibody and dye molecules at 280 nm and 647 nm. The concentrations were calculated using Beer-Lambert's law. The antibody absorbance ($A_{280\ (measured)}$) was measured at 280 nm and corrected for dye absorbance at this wavelength and then the concentration of antibody and dye was determined according to the following formulas:

$$A_{280\ (actual)} = A_{280\ (measured)} - CF_{280,Alexa647}A_{647\ (measured)} \qquad \text{(IV.1)}$$

where $CF_{280,\ Alexa647}$ is the correction factor of Alexa Fluo-647 at 280 nm.

$$\text{Antibody concentration} = \frac{A_{280\ (\text{actual})}}{\varepsilon_{f280}} \tag{IV.2}$$

ε_{f280} is the extinction coefficient of the antibody at 280 nm

$$\text{Dye concentration} = \frac{A_{647\ (\text{actual})}}{\varepsilon_{f647}} \tag{IV.3}$$

ε_{f647} is the exctinction coefficient of the dye at 647 nm.

3. Peptide synthesis

All peptides were synthesized by Biosyntan GmbH (Berlin, Germany) using Fmoc-based SPPS and purified by preparative HPLC.

3.1. Photoresact

Resact was modified with a diazirine to introduce a photocrosslinker functionality and two terminal alkynes to render it accessible via click chemistry. To this end, V9 was substituted by photoleucine [85], which has almost identical sterical bulk, and two terminal alkynes were introduced. The N-terminal alkyne was attached by means of amidation with 5-hexynoic acid, whereas the C-terminal alkyne was introduced as the unnatural amino acid propargyralanine. Both being only minor modifications to the overall peptide structure.

3.2. Photosperact

The design of photosperact followed a similar approach as for photoresact. L4 was substituted by photoleucine, again introducing the photocrosslinker functionality with minimal structural perturbation. This time only one terminal alkyne was introduced to account for the smaller size of speract, compared to resact. It was attached to the N-terminus by amidation with 5-hexynoic acid.

3.3. Chem-resact

For chemical crosslinking, utilizing Bis-N-hydroxysuccinimide reagents, a free amino group is required. Therefore amidation of the N-terminus was omitted. Nevertheless, to keep the two terminal alkynes for click chemistry that proved successful in photoresact we substituted both V2 and L14 by propargyralanine.

3.4. Azide-beads

In brief, reductively cleavable azido-beads were synthesized as follows: The bis-NHS-ester of 3,3′-dithiodipropionic acid (1) was treated with 11-Azido-3,6,9-trioxaundecan-1-amine (2) to obtain mono-NHS-ester (3). The remaining NHS-functionality was reacted with amino modified Tentagel-beads (4) to obtain the reductively cleavable azide-beads (5) that were treated with acetic anhydride for capping of unreacted amino groups (Figure 10). Beads were purchased from Rapp-polymere (Tentagel® MB NH_2; Particle size: 200-250 µm; Loading: 0.23 mmol / g).

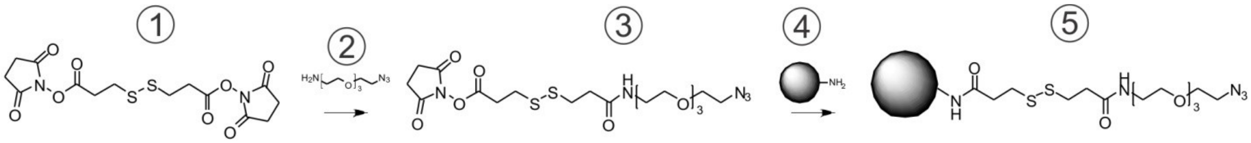

Figure 10. Synthesis of cleavable azide-beads

4. Spectroscopy and fluorescent kinetic studies

4.1. Fluorescence spectroscopy

All fluorescence spectroscopy measurements were performed in a quartz cuvette using the FluoroMax-3 spectrofluorometer from Horiba Jobin Yvon.

4.1.1. Laurdan fluorescence spectroscopy in GPMV

Laurdan molecule possesses a dipole moment due to a partial charge separation between the 2-dimethylamino and the 6-carbonyl residues. Upon excitation this dipole moment increases and may cause reorientation of the surrounding solvent dipoles. The energy required for solvent reorientation decreases the excited state energy of the probe, which is reflected in a continuous red shift of the probe’s emission spectrum. Laurdan Naphtalene moiety locates in the membrane at the level of the glycerol backbone of the phospholipids. The red shift observed in different phases of lipids is due to the rearrangement of water molecules localized around the Laurdan dipole [86].

Laurdan fluorescence spectroscopy in GPMV isolated from HEK293 cells and primary fibroblasts were performed on two steps. First, GPMV concentration was normalized across all samples as follows: Isolated GPMV samples were suspended in GPMV buffer and the emission spectrum was recorded from 400 nm to 500 nm at 385 nm excitation. The lipid resonance-peak was detected at 425 nm for each sample in the absence of Laurdan. All samples were normalized to the sample that had the lowest amplitude at the lipid resonance-peak. Next, GPMVs were labeled with 5 μM Laurdan for 20 minutes at 23°C. Measurements were performed at 350 nm excitation and fluorescence emission was recorded from 400 to 600 nm. All measurements were done at 23°C. GP value was calculated according to the following equation:

$$\mathrm{GP} = \frac{\sum_{i=420}^{460} I_i - \sum_{i=470}^{510} I_i}{\sum_{i=420}^{460} I_i + \sum_{i=470}^{510} I_i} \qquad \text{(IV.4)}$$

4.2. Stopped-flow fluorescent measurement

Rapid mixing experiments were performed using a stopped flow set-up (SFM-400; Biologic, Claix, France).

4.2.1. Principle of stopped-flow technique

Th SFM-400 sopped flow instrument (Biologic, Claix, France) is a rapid mixing device used to kinetically investigate biochemical processes in the time regime of milliseconds to seconds [87]. Solutions are rapidly mixed and pushed into an observation cuvette, where optical, calorimetrical or electrical measurements are performed. The delay time until the reaction can be monitored depends on the flow rate (f) of the reactants and the volume (V) of the apparatus. Thus the delay time (t) can be calculated as:

$$t = \frac{V}{f} \qquad \text{(IV.5)}$$

The principle and operation has been explained in detailed in previous works [88]. The core piece of the stopped-flow apparatus contains four 10 ml syringes (S1, S2, S3 and S4) (Figure 11B). The syringes can be filled through a valve accessible from the outside. The pistons of the syringes are moved by a step motor which are computer-controlled by the MPS-60 module (BioLogic) through the BioKine software (v. 4.45; Biologic). The syringes, flow lines, mixing chambers, and the observation-head housing the cuvette are enclosed in a water jacket to allow temperature regulation. For sea urchins sperm experiments, the temperature was set at 18°C. Each syringe can hold up to 10 mL and is filled through a valve accessible from the outside. The volume in the syringe is precisely controlled by a plunger; the movement of which, is driven by microprocessor-controlled (MPS-70, Biologic, France) stepping motor. The instrument is operated with Bio-Kine software (version 4.6x, Biologic, France). An overview of the flow lines in our setup is shown in Figure 11B. Three mixing chambers (M1-M3) are available for mixing. M3 resides immediately before a 31 µl quartz cuvette (model: FC-15, Biologic, France). The volume between the mixing chamber and cuvette determines the lag time between the onset of stimulation (i.e. mixing) and observation at the cuvette, referred to as the dead-time. In rapid mixing experiments with sperm, mixing chamber M3 is employed to minimize the dead-time. The volume between M3 and the cuvette is 36.6 µl. For a flow rate of 4 ml/sec the resulting dead-time is 9.1 ms. The liquid column is immobilized by the hard-stop valve, which is controlled with the Bio-Kine software. This minimizes the fluctuation of liquid flowing to cuvette and thereby lower noise in fluorescence measurement. The closing of the hard-stop valve is synchronized with the halting of the syringe motors to prevent overpressure and marks the onset of fluorescence recording at the cuvette.

Sperm loaded fluorescent indicators and caged compounds were incubated inside the syringe for 10 minutes prior to measurement to allow the activation process initiated by dilution to take place. Syringe 4 was filled with either stimulus solution or ASW. The mixing protocol in the stopped-flow was divided into 4 phases. First phase consisted of 50 ms phase for electronic synchronization of stepping motors. Second phase consisted of 200 ms flush of the system with 400 µl ASW from S1. Third phase consisted of 300 ms pause and the final phase consisted of 62.5 ms for mixing 120 µl of sperm suspension from S3 and 120 µl of stimulus solution from S4 that were driven into mixing chamber M3 and then into the cuvette. Total flow rate = 4 ml/sec was used for voltage and pH recording and total flow rate = 1 ml/s was used for Ca^{2+} recording. After 62.5 ms, the hard-stop valve closed, immobilizing the liquid column and marking the onset of fluorescence recording at the cuvette.

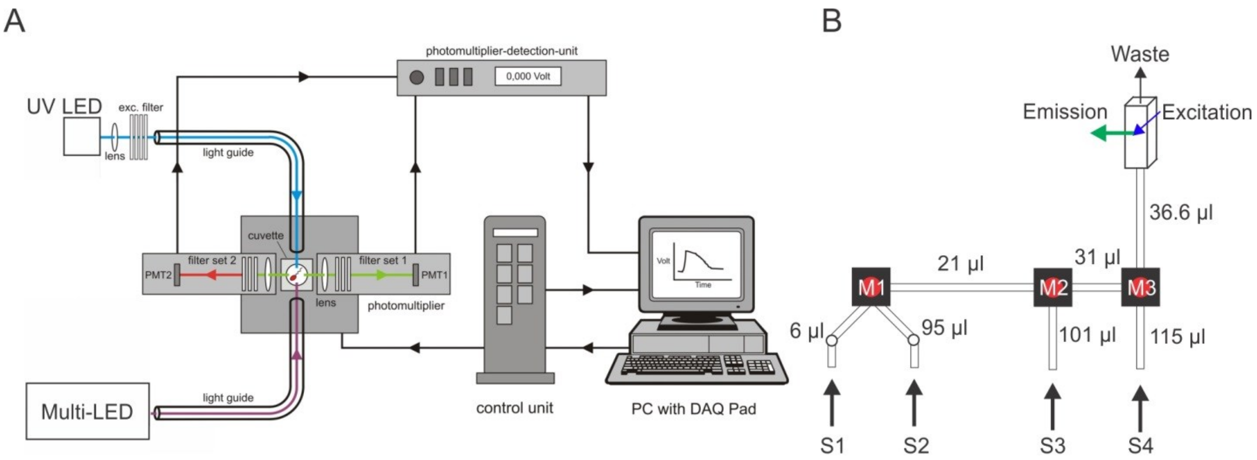

Figure 11. Schematic of a Stopped Flow Module. A. Schematic of a Stopped Flow Module (SFM-400) for simultaneous recording of two fluorescence emission. See details in text above. **B.** Schematic of flow paths in SFM-400 stopped-flow device. The apparatus consist of four independently controlled syringes (S1-S4), three mixing chambers (M1-M3) and an observation cuvette. The volumes of flow lines separating the various components are shown beside the lines. In a typical experiment with sea urchin sperm suspension, dye-loaded sperm suspension from syringe S3 is mixed with stimulus solution from syringe S4 in mixing chamber M3. The mixture is then pushed into the cuvette for fluorescence recording. The dead volume between M3 and the cuvette is 36.6 µl.

Table 8. Loading conditions for sea urchin sperm

Dye	Concentration	Excitation	Emission	Incubation	Indicator	Flow rate
Fluo-4	10 µM	494/20	536/40	45 min	Calcium	1 ml/s
BeRST	10 µM	650 / 10	675/67	10 min	Voltage	2 ml/s
pHrodo-red SE	10 µM	565 / 20	628 / 20	40-45 min	pH	2 ml/s

Table 9. Conditions for simultaneous voltage and calcium recordings in sea urchin sperm

Dye	Concentration	Excitation	Emission	Incubation	Indicator	Flow rate
Fluo-4	10 µM	494/20 – 3 kHz	536/40	45 min	Calcium	2 ml/s
BeRST	10 µM	650 / 10 – 2.5 kHz	675/67	10 min	Voltage	2 ml/s

Table 10. Conditions for simultaneous pH and calcium recordings in sea urchin sperm

Dye	Concentration	Excitation	Emission	Incubation	Indicator	Flow rate
Fluo-4	10 µM	494/20 – 3 kHz	536/40	45 min	Calcium	1 ml/s
pHrodo-red SE	10 µM	565 / 20 – 2.5 kHz	628 / 20	40-45in	pH	1 ml/s

4.2.2. Multi-LED system for excitation and lock-in detection

Fluorescence was recorded using digital lock-in amplifiers (Model 7230, Signal Recovery, Oakridge, TN, USA). Lock-in amplifiers enhances the signal-to-noise ratio of fluorescence recordings by detecting the signal at a given reference frequency and rejecting noise and other fluorescence contributions that are modulated at different frequencies. Lock-in amplifiers were employed in our setup as follows: the light output from either the Lumencor (Lumencor, Inc., USA) or our custom-made multi-LED (Figure 12A) system was modulated at a reference frequency of 10 kHz or 1-100 kHz, respectively. The resulting fluorescence was an alternating current (AC) signal also modulated at the reference frequency. The lock-in amplifier uses a phase-sensitive detector (PSD) to extract and amplify the AC signal modulated at the reference frequency. The PSD achieves this by multiplying all signals reaching the detector by the reference frequency. In general, the products of this multiplication are AC signals at various frequencies. The multiplication yields a direct current (DC) signal that is proportional to the amplitude of the fluorescence signal if its frequency is equal to the reference frequency. The output of the PSD is then passed through a low pass filter with a variable time constant τ; upon which, the AC signals are attenuated and the DC signal passes through unaffected. Thus, noise at frequencies different than that of the reference is eliminated at the PSD output by the low pass filter. In digital lock-in amplifiers, multiplication and filtering are performed by a digital signal processing chips. The signals detected by the lock-in amplifier were recorded with the Bio-Kine software. The multi-LED system and the simultaneous fluorescence detection via lock-in amplifiers is shown Figure 12A for up to four channels using two PMTs. The multi-LED system allow for the use of three LEDs at any time. The spectra of the used LED is shown in Figure 12B.

Fluo-4 and BeRST were used for recording of simultaneous Ca^{2+} and voltage signals. The two dyes can be spectrally separated as shown in Figure 12C. For exciting FLuo-4 we used an LED centered at 490 nm that was equipped with 485/25 nm excitation filter. BeRST was excited with LED centered at 660 nm that was equipped with 658/10 nm filter. Fluorescence emission was recorded with two separate photomultiplier tubes (PMTs), one equipped with a 695/50 filter for BeRST emission and another equipped with 536/40 nm filter for Fluo-4 emission. We used lock-in amplifiers to maximize the signal-to-noise ratio and filter out the contribution from the UV

LED that was used for uncaging. Both LEDs were modulated with a 25 kHz reference frequency. We also used a pH dye called pHrodo-red SE simultaneously with Fluo-4. Figure 12D shows their separable excitation and emission spectra. pHrodo-red SE was excited with 560 nm LED and collected through a PMT equipped with 600/20 nm filter. We modulated both LEDs in this case with different frequencies (3 kHz and 2.5 kHz) in order to minimize cross-talk since the spectra of Fluo-4 and Phrodo-red are not completely separable. We tested the setup using sperm loaded with Fluo-4 and BeRST that were stimulated with resact. Then we tested sperm loaded with Fluo-4 and Phrodo-red under the same conditions. Fluo-4 was used as a common dominator and allowed us to align the three signals.

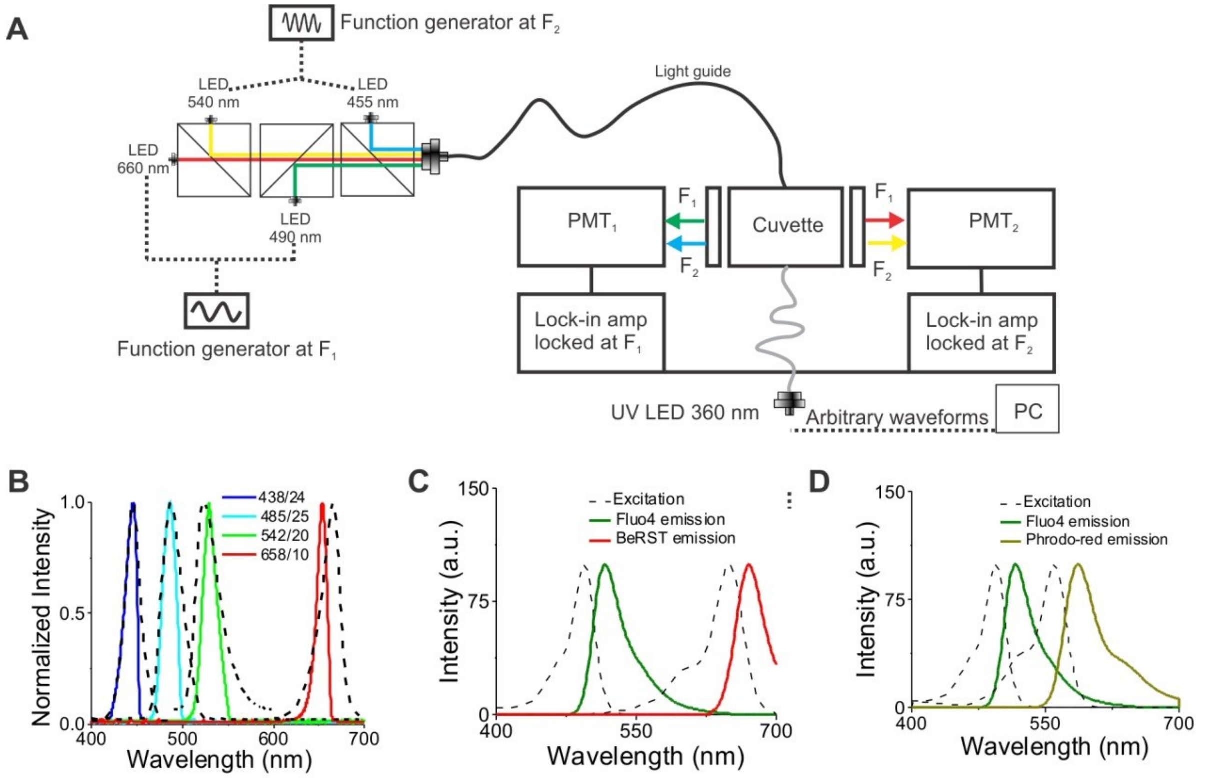

Figure 12. System used for multiplexed fluorescence detection A. On the left a Multi-LED system is used for excitation via a light guide. On the right, an overview of the configuration that can be used for multiplexed fluorescence detection. **B.** Spectra recorded from the multi-LED system. **C.** Normalized excitation and emission spectra of Fluo-4AM and BeRST. **D.** Normalized excitation and emission spectra for Fluo-4 and pHrodo-red SE.

4.2.3. Photolysis using flash and arbitrary waveforms

The UV LED was triggered by a program written in LabView 8.0 (developed by Dr. Luis Alvarez). The power level was adjusted between 5 % and 100 % according to a calibrated lock-up table. And neutral optical density filters (ODs) were used for power levels lower than 5 %. The neutral optical density filters were fitted in a slot located between the UV LED and the light guide.

4.2.4. Data analysis

MATLAB GUI (The MathWorks Inc., Natick, MA, 2000) was written for data evaluation and analysis. Further processing and representation were done in OriginPro 9 (OriginLab, Northampton, MA, USA). Fluorescence signals recorded in single emission mode are reported as the change in fluorescence with respect to the mean of the first 3-5 data points of the recording ($\Delta F/F_0$). The control (ASW) signal was subtracted from $\Delta F/F_0$. Time courses of fluorescence signals were adjusted for the dead-time.

4.3. Fluorescence Microscopy

4.3.1. Principle

Fluorescence microscopy includes two categories: 1) widefield microscopy, where a large field of view within the sample is illuminated with a broad collimated beam and the fluorescence is collected by a camera to form an image, without optical sectioning. 2) Confocal microscopy where only fluorescence from a confined confocal volume is collected and an image is obtained by scanning the sample with a focused beam. One photon confocal microscopy relies on the use of pinhole to reject out of focus light while two photon microscopy is confocal by principle. Nevertheless, widefield microscopy offers a higher photon detection efficiency and fast acquisition, which makes it more suitable for STORM imaging. The principle behind fluorescence microscopy is simple. A biological sample is labeled with a fluorescent dye and then it is excited with a light source that has a wavelength matching with its absorption spectrum. Dichroic filters reflect well defined regions of the electromagnetic spectrum and let others pass, thereby allowing the separation of emission light and excitation light (Figure 13). Lasers can be used as monochromatic, collimated and coherent light sources. Otherwise, a lamp with excitation filters and a collimator could be used. In widefield microscopy, the light beam is focused onto the back focal plane of the objective lens. A collimated beam leaves the objective and illuminates the sample. The fluorescence emitted by the sample is collected by the same objective which results in a collimated beam that can be separated from the excitation beam by the use of dichroic filters (Figure 13). Additionally, emission filters are used to allow only a specific region of the spectrum to reach the camera. The filters can also filter out stray light and Raman scattering.

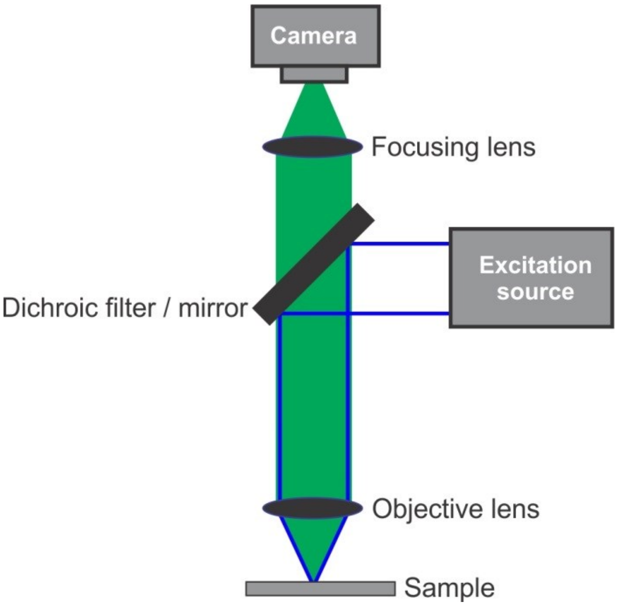

Figure 13. Basic scheme of fluorescence microscope. Excitation light is shown in blue and emission light is shown in green.

Resolution in fluorescence microscopy is limited by the diffraction of light at the aperture of the microscope objective. Due to diffraction, an object that has a size less than the resolution limit can be considered a point light source and, thereby produce a finite intensity distribution at the image space called point-spread-function (PSF). The imaging system is characterized by its PSF which can be defined as the intensity distribution of an image generated by a point light source. The PSF Full Width at Half Maxima (FWHM) is used to define the resolution of an optical microscope. The width of the PSF is related to Rayleigh criterion and is determined by the numerical aperture (NA) of the microscope objective and the wavelength of light (λ). Therefore, we can define the lateral $\Delta_{x,y}$ and axial Δ_z resolution by:

$$\Delta_{x,y} = 0.61\frac{\lambda}{NA} \quad \text{and} \quad \Delta_z = \frac{2\lambda n}{NA^2} \qquad \text{(IV.6)}$$

$\Delta_{x,y}$ specifies the minimum separation between two sources that can still be resolved into two distinct objects as shown by the Rayleigh criterion in Figure 14B.

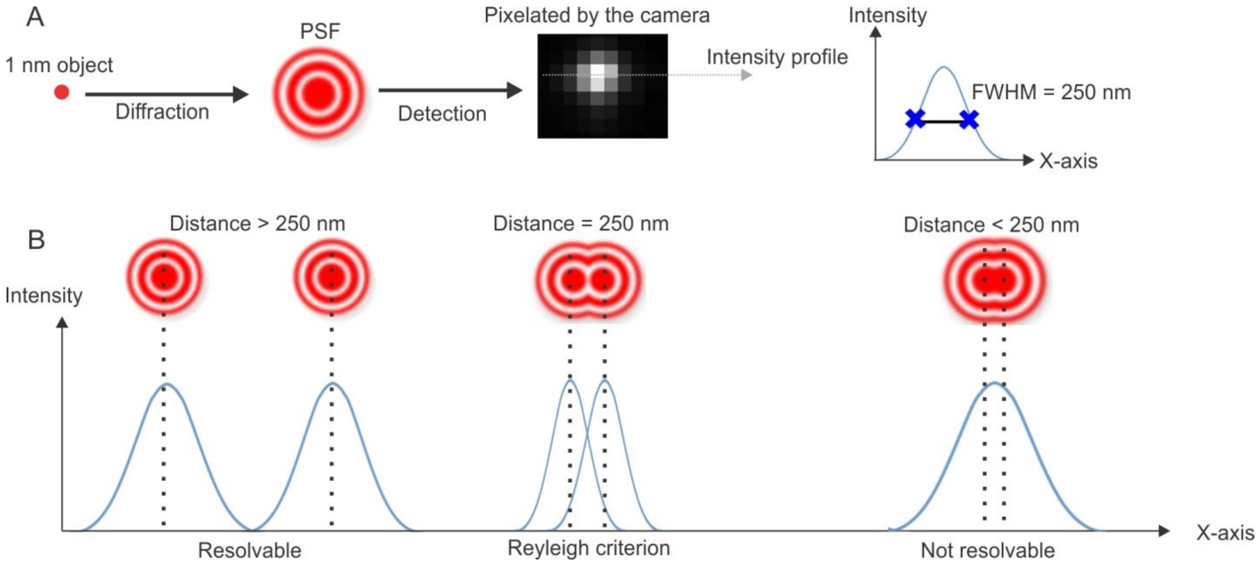

Figure 14. Diffraction limit of resolution. A. An object smaller than the resolution limit produces an image with a finite intensity distribution called point spread function (PSF) due to diffraction. The image is digitized by the camera. The lateral intensity profile produces a Gaussian intensity distribution with a FWHM ~ $\Delta_{x,y}$. The FWHM = 250 nm for objective with NA = 1.49 and λ = 600 nm. **B.** Depiction of the Rayleigh criterion where only objects with a separation distance larger or equal than $\Delta_{x,y}$ are resolvable.

C. M. Sparrow presented another definition of the resolution limit called Sparrow-criterion which is defined as the distance from which on the dip between two peaks are not observed any more. It is ca. 20 % smaller than the Rayleigh-criterion. However, Rayleigh criterion can be used as an upper limit of resolution.

4.3.2. Total internal reflection microscopy

Total internal reflection fluorescence (TIRF) microscopy (TIRFM) is an advanced optical technique that allows the excitation of fluorophores to be confined to an extremely thin axial region. Depending on the excitation wavelength, and NA used, the excitation depth can be less than 100 nm from the glass interface (Figure 15B). Confocal image section is approximately 500 nm which makes TIRFM more powerful for studying processes and structures at the cellular membranes. The small illumination volume offers many advantages. For instance, there is virtually no out of focus fluorescence collected (Figure 15B) and therefore, background is significantly minimized compared to widefield microscopy, which results in a high signal-to-noise ratio. Moreover, cells are exposed to significantly smaller amount of light, thus, making it more suitable for live cell applications. The critical angle for total internal reflection (Figure 15A) is obtained from Snell's law when $\theta_r = 0$, then:

$$sin\theta_r = \frac{n_i}{n_r} sin\theta_i \quad \rightarrow \quad sin\,\theta_{critical} = \frac{n_r}{n_i} = 65.22\,° \tag{IV.7}$$

for a typical coverslip where $n_r = 1.38$ for cell cytosol and $n_i = 1.52$ for glass-immersion.

An electromagnetic wave in vector space that is constant in (x,y) and propagating in z can be described by:

$$\vec{E} = \vec{E}(k_x, k_y, 0)e^{\pm ik_zZ} = \vec{E}(k_x, k_y, 0)e^{\pm iZ\sqrt{k^2-{k_x}^2-{k_y}^2}} \tag{IV.8}$$

Where the wave vector k of a given wave with wavelength λ is defined by: $k = \frac{2\pi}{\lambda}$ and $k^2 = {k_x}^2 + {k_y}^2 + {k_z}^2$. If ${k_x}^2 + {k_y}^2 \geq k^2$ then k_z is imaginary and the propagation in + z is determined by the term $e^{\pm i|k_z|Z}$ that describes an evanescent wave undergoing an exponential decay with z (Figure 15C).

The evanescent wave varies exponential with z according to the following formula:

$I_z = I_0 e^{\frac{z}{d}}$ where I_z is the intensity at depth z and I_0 is the intensity at z = 0 at the interface. Where penetration d is given by:

$$d = \frac{\lambda}{(4\pi n_r)\times\sqrt{((sin^2\theta/sin^2\theta_{critical})-1)}} \tag{IV.9}$$

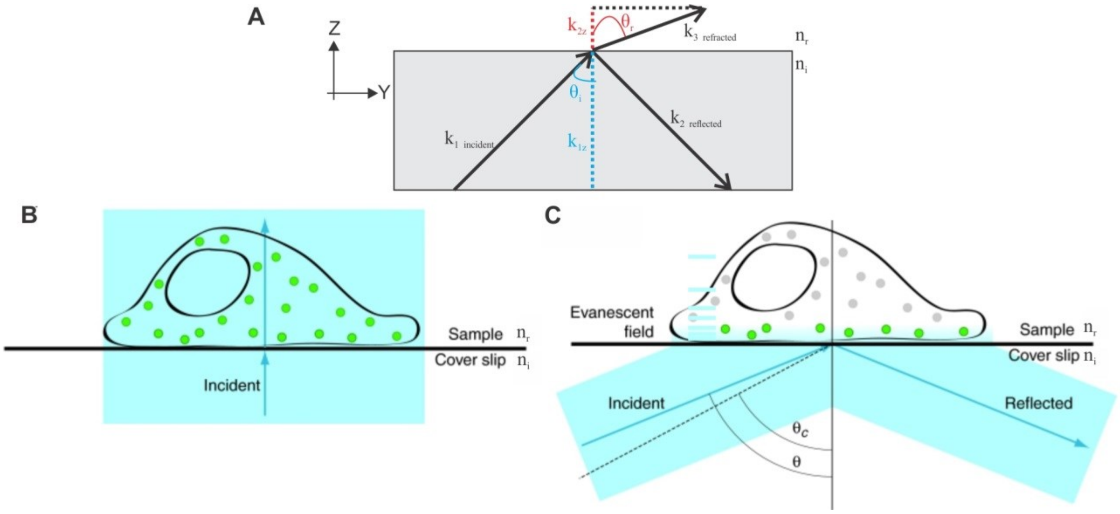

Figure 15. Basic principle of TIRFM. A. Overview of total internal reflection between two surfaces of refractive indices n_i and n_r. $k_{1,incident}$ denotes the wave vector of incident wave, $k_{1,refracted}$ denotes wave vector of refracted wave with z-projection k_{1z}. And $k_{2,reflected}$ denotes wave vector of reflected waves with z-projection k_{2z}. θ_r denotes the angle between the normal and the reflected wave vector while θ_i denotes the angle between the normal and the incident wave vector. **B.** In widefield ilumination, the excitation beam travels directly through the coverslip-sample interface. All of the fluorophores in the sample are excited. **C.** In TIRF, the excitation beam enters the sample at an angle θ, which is greater than the critical angle θ_c . The beam is reflected off the coverslip-sample interface and an evanescent field is generated on the sample side of the interface. Therefore, only fluorophores in the evanescent field are excited, as indicated by the green color. The refractive index of the sample n_r must be smaller than the index of refraction of the coverslip n_i in order to achieve total internal reflection.

4.3.3. FRET imaging and analysis

FRET imaging was performed on an inverted Nikon Ti microscope. Live cells were imaged in ES buffer at 24°C. 405 nm laser was used for donor excitation, while 488 nm laser was used for acceptor excitation. Donor was acquired with a 480/20 emission filter and FRET and acceptor emission were acquired with a 560/40 emission filter. The microscope has two filter cube stages that can be controlled automatically. Excitation filters were installed in the first stage and emission filters were installed in the second stage. This allowed multicolor imaging in three channels using the same camera. Channel misalignment was corrected using image registration in MATLAB. To correct for bleedthrough and excitation cross-talk, HEK293 cells expressing either Cerulean alone or Citrine alone were imaged in three channels. The bleedthrough was measured by either calculating the slope from the colocalization between the respective channel and FRET channel or by finding the average ratio of the respective channel and FRET channel. A MATLAB GUI was written to perform the required image processing which include photobleaching correction, bleedthrough correction, ratio calculation, background subtraction and generation of a mask for each channel and finally image visualization of FRET images/movies.

4.3.4. Two photon Generalized polarization (GP) imaging

Laurdan GP measurements in the microscope were done using two-photon excitation, because one photon confocal excitation can induce severe photo-bleaching of the dye; thereby, making it impossible to collect images for more than few seconds [19]. Two-photon excitation can minimize this problem due to the confined two photon absorption volume, thus reducing the extent of probe photo-bleaching. Two photon also offers an intrinsic sectioning (confocal) effect allowing the collection of images from different focal planes with low background [86]. Two photon GP imaging were performed on TriM Scope II from LaVision BioTec GmbH. The two photon source used was a Titanium:Sapphire laser pumped by an Argon:ion laser, with an excitation wavelength at 800 nm. The beam enters the microscope through the epifluorescence port and focuses into the sample through an objective (Olympus XLUMPlanFl 20x/0.95 water immersion objective). The red and blue components of the fluorescence were split into two channels by using a dichroic beam splitter (465LP #F32-165A AHF). Interference filters were placed in the appropriate emission paths to further isolate the 440 and 490 region of the emission spectrum (490/20 and 440/20). In order to compensate for photoselection effect in vesicles an adjustable quarter wave-plate was added in the beam path before the scan head. Two simultaneous images with 256x256 pixels were obtained from the sample and processed by applying the GP formula (equation IV.10) to each pixel using ImageJ. A calibration GP image was obtained using a highly concentrated Laurdan suspension. The GP calibration image is calculated from the blue and red channel emission with $g = 1$.

$$GP\ (i,j) = \frac{I_o(i,j) - g(i,j)I_d(i,j)}{I_o(i,j) + g(i,j)I_d(i,j)} \qquad \text{(IV.10)}$$

Where I_0 and I_d are the ordered and disordered channels, respectively. While g is the GP calibration image and i and j represent the position of image pixels.

5. Stochastic Optical Reconstruction Microscopy (STORM)

Ernst Abbe (Abbe, 1873) and Lord Rayleigh (Rayleigh, 1896) formulated what is now known as the diffraction limit for optical microscopy in the end of the nineteen century. However, a lot of progress has been made in the last decade to indirectly bypass this limitation. Many methods were developed to accomplish this task; we can summarize them into these categories:

1. Saturation: Methods like stimulated emission depletion (STED) [89], saturated structural illumination microscopy (SSIM) [90] or ground-state depletion (GSD) [91]. These methods use strong irradiation to saturate the fluorescence process and differentiate between fluorophores that are near each other. The emission from the remaining fluorophores help to reconstruct the image and therefore no computational post-processing is needed.
2. Ensemble localization: Methods like super-resolution optical fluctuation imaging (SOFI) [92], Bayesian analysis of blinking and bleaching (3B) [93] and super resolution radial fluctuation (SRRF) [94]. These methods rely on modeling the natural or modified stochastic blinking and bleaching of fluorophores to compute likely fluorophore distributions. Computation in these methods is very costly and requires powerful processors or GPUs.
3. Single molecule localizations: Methods like stochastic optical reconstruction microscopy (STORM) [95,96], photoactivated localization microscopy (PALM) [97] and many others that are based on same principle. These methods modify the blinking rates of fluorophores to isolate individual fluorophore emissions. In other words, they try to separate fluorophores in time rather than in space. The isolated emission from individual fluorophores can be fitted to a model point PSF with very high precision. Computation and post-processing is necessary for image reconstruction but they come at a lower cost in comparison to ensemble localization methods.

STORM bypasses the diffraction limit by separating molecules in time rather than in space. Using fluorophores that can be switched *on* and *off* so that only a few spatially-separated molecules are active at any one time, STORM can build an image molecule by molecule. The molecules need to be switched rapidly so that thousands of frames can sample the underlying structure with sub-diffraction precision. STORM has been demonstrated to work with commercially available organic dyes [98]. Best dyes for STORM are chosen based on four important criteria, namely the detected photons per switching event, the *on-off* duty cycle (this defines the contrast between o*n* and *off* states of the dye, for dense structures *on-off* duty cycle has to be very low), survival fraction (low photo-bleaching rate) and finally, the number of switching cycles. Number of switching cycle is defined by the number of blinks per fluorophore. A high number can enhance localization precision and density, but is not recommended for protein counting. Generally, *on-off* duty cycle varies with imaging laser power, activation laser power and thiol concentration in imaging buffer. Therefore, all these factors can be used to control the *on-off* duty cycle and thereby the density of *on* molecules per frame.

Sample preparation, image acquisition and image processing, analysis and interpretation have to be well established for a successful implementation of this technique. Unlike conventional fluorescence imaging, the size of the antibody used in immunolabeling can introduce an offset between the protein of interest and the fluorophore, thereby, compromising the resolution. In case of microtubule STORM imaging, antibody offset results in apparent diameters of 40-50 nm compared with actual microtubule diameter of 25 nm. Moreover, the labeling density has to be sufficient enough to meet the Nyquist criterion in order to generate high quality images [99]. The achievable resolution is dependent on the localization accuracy and is given by [100]:

$$\sigma_{xy} = \sqrt{\frac{\sigma^2{}_{PSF}}{N} + \frac{a^2/12}{N} + \frac{8\pi\sigma^4{}_{PSF}b^2}{a^2N^2}} \tag{IV.11}$$

where σ_{PSF} is the standard deviation of the PSF, a is the pixel size, b is the background noise and N is the number of photons.

The structural resolution R is given by [99]:

$$R = \sqrt{\left(2.35\bar{\sigma}_{xy}\right)^2 + \left(2\bar{d}\right)^2} \tag{IV.12}$$

where $\bar{\sigma}_{xy}$ is the mean localization accuracy for all molecules in a dataset and $\bar{d}$ is the mean of the pairwise nearest neighbor distance of the molecules.

5.1. Point Spread Function

PSF of an imaging system is the intensity distribution of an image generated by a point incoherent light source. A single molecule emitter can be treated as an incoherent point source in single molecule data. The theoretical PSF is an Airy disk (Figure 16) due to the diffraction of light and can be defined as:

$$PSF(x) = I_0 \left(\frac{2J_1(x)}{x}\right)^2 \tag{IV.13}$$

Where I_0 is the maximum intensity of the pattern at the Airy disk center, J_1 is the Bessel function of the first kind of order one. The radius of the airy disk in the image plane is given by:

$$R_{airy} = 0.61\frac{M\lambda}{\mu NA} \quad (in \;\; pixels) \tag{IV.14}$$

Where M denotes the magnification, λ denotes the detection wavelength, NA denotes the numerical aperture of the imaging system and μ denotes the pixel size of the camera in the image plane. The convolution operation can mathematically model imaging of objects. It can be seen as the application of the PSF to every point in the specimen**:** light emitted from each point in the object is convolved with the PSF to produce the final image. Convolution is given by the following equation:

$$\text{Image} = \text{PSF} * \text{object} \tag{IV.15}$$

$$I(x) = \int P(\tau)PSF(t-\tau)d\tau \tag{IV.16}$$

$I(x)$ denotes the intensity at distance x from the position of the point light source in the image plane, and P is the object. The smaller the PSF the higher the resolution of an optical system (Figure 16).

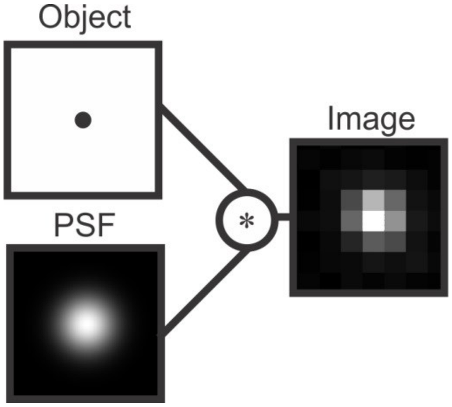

Figure 16. Image formation.

Bessel function is very computationally intensive for computing and fitting [101] therefore a Gaussian function that approximates the Besselian PSF is used [102]. A common approximation of the real PSF is a symmetric two-dimensional Gaussian function given by the formula [103]:

$$PSF_G(x,y|\theta) = \frac{\theta_N}{2\pi{\theta_\sigma}^2} exp\left(-\frac{(x-\theta_x)^2+(y-\theta_y)^2}{2{\theta_\sigma}^2}\right)+\theta_b \qquad \text{(IV.17)}$$

Where $\mathrm{PSF_G}(x,y|\theta)$ gives the expected photon count at the integer pixel position (x,y) for a vector of parameters $\theta = [\theta_x, \theta_y, \theta_\sigma, \theta_N, \theta_b]$. Where θ_x and θ_y are the sub-pixel molecular coordinates, θ_σ is the imaged size of the molecule, $\theta_N$denotes the total number of photons emitted by the molecule, and $\theta_b$corresponds to the background offset. 3D STORM was established using a weak cylindrical lens which was introduced into the imaging path to create slight astigmatism. The resultant PSF of the molecules will have different ellipticity depending on molecule's axial position. When a molecule is in focus, its image appears symmetrical and round. Molecules above or below the focal plane will have an ellipsoidal PSF. A commonly used PSF model for astigmatisc 3D STORM is a rotated, elliptical Gaussian function given by the following formula:

$$PSF_G(x,y|\theta,\phi) = \frac{\theta_N}{2\pi\sigma_1(\theta_z)\sigma_2(\theta_z)} exp\left(-\frac{x'^2}{2(\sigma_1(\theta_z))^2}-\frac{y'^2}{2(\sigma_2(\theta_z))^2}\right)+\theta_b \qquad \text{(IV.18)}$$

where $\mathrm{PSF_G}(x,y|\theta,\phi)$ provides the expected photon count at the integer pixel position (x,y)for the parameters $\theta = [\theta_x, \theta_y, \theta_z, \theta_N, \theta_b]$ and $x' = (x-\theta_x)\cos\phi - (y-\theta_y)\sin\phi$ and $y' = (x-\theta_x)\sin\phi - (y-\theta_y)\cos\phi$. θ_x, θ_y, and θ_z are the sub-pixel molecular coordinates. $\sigma_1(\theta_z)$ and $\sigma_2(\theta_z)$ are the imaged widths of the molecule along two perpendicular axes rotated by the angle ϕ with respect to xy coordinates. θ_N denotes to the total number of photons emitted by the molecule and $\theta_b$denotes the background offset.

5.2. EMCCD

Electron Multiplying Charged-Coupled Devices (EMCCD) camera offer a high photon detection efficiency and signal-to-noise ratios. The detection area is an array of photodiodes (Figure 17) with a finite size. After a photon impinges on one of the pixels, an electron-hole pair is generated. The electron is shifted to an opaque area of the array after exposure (grey part of the array in Figure 17) in a process called frame-transfer. This allows parallelized data acquisition and read-out, which results in a faster frame rate. Next, the stored charges in the frame transfer array are read out row by row by shifting to a serial register which sequentially shifts each row of the image to the output node. EMCCD camera has an extended multiplication register which is located between the serial register and the output node, and allows the amplification of the charge before reading. The amplification factor is called Gain. Finally, the charge is digitalized and the EMCCD displays the data in the form of image counts and not number of photons per pixel. The calibration determines the camera gain which converts the detected photon numbers to camera output signal for a given configuration.

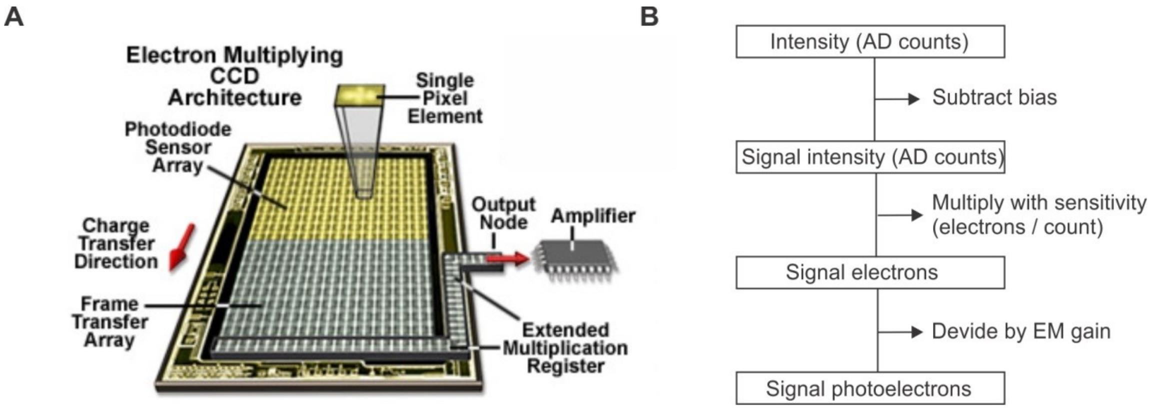

Figure 17. EMCCD operation. A. EMCCD architecture taken from (http://micro.magnet.fsu.edu). **B.** Overview of procedure to estimate the number of photoelectrons.

There are many sources of noise in the EMCCD camera such as dark count noise, readout noise, spurious charge and shot noise. Shot noise originates from statistical fluctuations in the number of detected photons and can be described by a Poissonian distribution. For a CCD, the variance of the detected photons can be defined as ${\sigma_P}^2 = N_{photon}$. While for an EMCCD, an additional noise factor called multiplicative noise occurs as the gain factor is also subject to a distribution around a mean value. Therefore, the formula has to be corrected by a factor F which tends to 2 when the number of amplification steps is infinite and amplification probability for a single step is low. Therefore, for an EMCCD camera ${\sigma_P}^2 = 2N_{photon}$

The EMCCD adds I_{offset} counts for each pixel in order to display positive count number at all times. For our camera from Andor iXON, this offset is set at 100. Hence the effective signal intensity I_{eff} can be deduced by subtracting the bias offset from intensity of each pixel I. This is explained by the following equation:

$$I_{eff} = \begin{cases} I - I_{offset}\,, & I \geq I_{offset} \\ 0, & I < I_{offset} \end{cases} \tag{IV.19}$$

Let $\mathrm{n}_{\gamma\mathrm{e}^-}$ be the number of photoelectrons after photon conversion to photoelectrons. Let $\mathrm{n}_{\mathrm{e}^-}$ be the number of electrons after charge multiplication and $\mathrm{G}_{\mathrm{ccd}}$ be the EMCCD camera gain then we get:

$$n_{e^-} = G_{ccd} n_{\gamma e^-} \tag{IV.20}$$

Now if G_a denotes electrons/AD count then the conversion of electron to digital signal is governed by the following equation:

$$I_{eff} = \frac{n_{e^-}}{G_a} \tag{IV.21}$$

We now can estimate the number of the signal photoelectrons by substituting equation (3.3) in equation (3.2) and defining a new constant $\mathrm{G}_{\mathrm{eff}} = \frac{\mathrm{G}_{\mathrm{ccd}}}{\mathrm{G}_{\mathrm{a}}}$ then we can define photoelectrons as:

$$n_{\gamma e^-} = \frac{I_{eff}}{G_{eff}} \tag{IV.22}$$

So far all the above equations are free from noise sources. However, for an accurate calibration we have to estimate statistical noise within the conversion process. The noise is comprised of multiplicative noise (shot noise), read-out noise and dark current. The total noise σ can be modeled using the following equation:

$$\sigma = \sqrt{F^2\left(n_{\gamma e^-} + \sigma_{dark}{}^2\right) + \left(\frac{\sigma_{read}}{G_{ccd}}\right)^2} \tag{IV.23}$$

We operate the EMCCD at a temperature of -70°C. Under this condition the dark current noise can be neglected. Moreover, the read-out noise can also be neglected when using high gain, therefore total noise can now be estimated by:

$$\sigma = F\sqrt{n_{\gamma e^-}} \tag{IV.24}$$

F denotes the excess noise factor of the camera. F was shown to converge to $\sqrt{2}$ when the gain is larger than 100 [104]. Using substitution we arrive to the following linear relationship:

$$\sigma = (\frac{2}{G_{eff}})I_{eff} \tag{IV.25}$$

Equation (3.7) is of the form y=ax where $\frac{2}{\mathrm{G_{eff}}}$ is the slope of the straight line describing the relationship between noise and mean count. The Gain was measured by plotting the variance of counts against the mean number of counts from an image stack obtained using Tetraspeck beads. The gain was derived from the slope $\frac{2}{\mathrm{G_{eff}}}$.

For multicolor SORM imaging a calibration was necessary. An imaging chamber plated with 100 nm sized TetraSpeck microspheres was used. The 647, 561, and 488 nm excitation lasers were assigned for the red, yellow, and green channel, respectively. The bead coordinates were calculated with subpixel precision in the three channels and the red channel was set as reference. Mapping consisted of producing a transformation matrix, relating the coordinates of the reference channel to the coordinates in other channels. A custom written MatLab code was used to assign the coordinates to individual channels then apply a third order polynomial transformation matrix that relates the coordinates x,y in the reference channel to x',y' in the other channel according to:

$$\binom{x\prime}{y\prime} = (\,1\; x^2\; y^2\; yx^2\; xy^2\; x^3\; y^3\,).P_{transform} \tag{IV.26}$$

5.3. Image acquisition

a. STORM imaging buffer

All STORM imaging experiments were performed in an imaging buffer (50 mM Tris, pH 8, 10 mM NaCl) with an oxygen scavenging system (0.5 mg/mL glucose oxidase (G2133; Sigma-

Aldrich), 40 µg/mL catalase (106810; Roche Applied Science or C100–50MG; Sigma-Aldrich), and 10% (w/v) glucose), and either 143 mM 2- hydroxy-1-ethanethiol (βME; Fluka) or 10-100 mM 2-aminoethanethiol (MEA; Fluka), unless otherwise indicated. MEA was stored as a solid at 4°C and prepared as a 1 M stock solution in water with pH adjusted to 8 with 1 M aqueous KOH. This stock solution was kept at -20°C. βME was stored as a liquid at 4°C. For experiments, the thiol solutions were diluted immediately before imaging to the final concentrations as described above. The preparation protocol was adopted from [98]. Typically, imaging times up to 5-6 hours were possible when the sample chamber was sealed in order to reduce permeation of oxygen.

b. Image acquisition

10,000 – 60,000 frames were acquired per data set using 647 nm excitation at 100 mW at the sample plane unless mentioned otherwise. 405 nm laser was used to maintain an adequate number of localizations per frame. A cylindrical lens was introduced in the detection path for 3D STORM acquisition. Perfect focus system from Nikon was used to minimize axial drifting and vibration isolation table was used to minimize lateral drifting.

5.4. Image reconstruction

STORM movies were analyzed as described previously using either the Nikon software package based on a technology developed by Dr. Xiaowei Zhuang [105], software described in [103] or GDSC (http://www.sussex.ac.uk) from ImageJ. Briefly, fluorescence peaks corresponding to individual molecules were identified in each frame and fit using least-squares fitting or maximum-likelihood estimator with a two-dimensional Gaussian to determine the (x,y) position of each molecule. For 3D imaging, the ellipticity of the Gaussian was used to assign a z coordinate as described in [105]. Briefly, single-molecule images were fit to an elliptical Gaussian to obtain the centroid position coordinates (x and y) and the Gaussian widths ($\sigma_1(\theta_z)$ and $\sigma_2(\theta_z)$). Molecules that were within a distance of one pixel or 160 nm in successive frames were linked together and the mean position of the molecule in successive frames was used to report the position of that molecule. To calculate experimental localization precision molecules were not linked together.

5.5. Three dimensional STORM

5.5.1. Calibration

Calibration for astigmatic 3D STORM is performed by introducing a weak cylindrical lens into the imaging path (NSTORM system, Nikon Ti microscope) to create slight astigmatism in the image. The resultant PSF of molecules will have different ellipticity depending on their axial position. Therefore, if a molecule is in the focal plane, its image appears round while a molecule above and below the focal plane will appear ellipsoidal. Calibration of the imaging system determines the orientation angle ϕ of the imaged ellipsoids since the EMCCD chip might not be perfectly aligned with the cylindrical lens and it also determines the relationship between the axial position z of the molecules and their imaged widths $\sigma_1(\theta_z)$ and $\sigma_2(\theta_z)$.

In brief, Tetraspeck multicolor beads from ThermoFisher Scientific #T7279 were diluted 1:5000 in distilled water and sonicated before they were plated in chambers on 1.5H coverslip. The chamber was stored in PBS buffer at 4°C. Next, images at different axial positions were acquired on STORM setup with cylindrical lens placed in detection path. Each bead image was then fit to an elliptical Gaussian to obtain the Gaussian widths, $\sigma_1(\theta_z)$ and $\sigma_1(\theta_z)$ and their average values from many beads at different z positions were used to create the calibration curve. Protocol adopted from [106].

5.5.2. Wobble calibration and correction

Similar to 3D calibration, the beads were used to acquire images at different z positions. After reconstruction, the position (x,y) for individual beads was plotted as function of z position. The values from many beads at different z positions were used to create the calibration curve. Calibration was applied to 3D datasets to correct for the depth dependent lateral distortions [107].

5.6. Drift correction

Lateral and axial drift in the sample during acquisition was corrected computationally using Nikon software and it relied on image cross-correlation as described in [108] . Briefly, the STORM movie was segmented into non-overlapping, 2,000–5,000 frame segments, and the

STORM image reconstructed from each segment was correlated to the first one in the series to monitor sample drift. The magnitude of the drift is calculated from the image cross-correlation according to equation IV.27. This approach depends on having a sufficient density of localizations from each set of frames to ensure the accuracy of the correlation. 405 nm activation intensity was gradually increased to maintain an adequate density. However, in the case of imaging low dense structures then fiducial markers (TetraSpeck beads), were used to track and correct sample drift.

$$G_{np}(x,y) = \frac{\sum_i \sum_j (I_n(i,j) I_p(i+x,j+y))}{\left[\sum_i \sum_j (I_n(i,j))^2 \, \sum_i \sum_j (I_p(i+x,j+y))^2\right]^{1/2}} \qquad \text{(IV.27)}$$

Where $G_{np}(x,y)$ is the normalized cross-correlation function of reconstructed images from two non-overlapping frame segments n and p.

5.7. Visualization

STORM images were typically rendered with each localization plotted as a Gaussian with a width that is weighted by the inverse square root of the number of detected photons. Images were filtered to reject molecules with low photon number (below 500 photons). Molecules with aspect ratio higher than 1.5 for 2D and 2.5 for 3D datasets were rejected. Moreover, molecules that appear for >10 consecutive frames were rejected. Non-specifically bound antibodies can give background in the STORM images which appears as scattered localizations at low local densities. This background noise was removed by a local density filter. Low-density localizations were filtered out by removing a molecule if it was surrounded by fewer than 10 localizations in the 80 nm × 80 nm region surrounding the localization. The density filter was adjusted according to each dataset. 3D datasets were extracted from Nikon software and adjusted so that they are compatible with ViSP software [109]. ViSP software was mainly used visualization.

5.8. Quantitative analysis

5.8.1. Cluster analysis

Pair correlation function was used to quantify organizations in STORM datasets. The method was adopted from [110,111]. Let $g(r)$ be the pair auto-correlation function that show the increased probability of finding a second localized molecule a distance r away from a given localized molecule then the measured auto-correlation function can be expressed by the following formula:

$$g_{measured(r)} = \frac{e^{\left(\frac{-r^2}{4\sigma^2}\right)}}{4\pi\sigma^2\rho} + g(r > 0) * g_{psf}(r) \qquad \text{(IV.28)}$$

where ρ is the average density, σ is standard deviation of the PSF and $g_{psf}(r)$ describes the distribution of molecules within the resolution limit imposed by the average PSF and it can be modeled by the following equation:

$$g_{psf}(r) = Ae^{\left(\frac{-r^2}{4\sigma^2}\right)} \qquad \text{(IV.29)}$$

for a random distribution we get:

$$g_{measured(r)} = \frac{g_{psf}}{\rho}(r) \qquad \text{(IV.30)}$$

and for a clustered distribution we get:

$$g_{measured(r)} = \frac{e^{\left(\frac{-r^2}{4\sigma^2}\right)}}{4\pi\sigma^2\rho} + \left(Ae^{\left(\frac{-r}{\xi}\right)} + 1\right) * g_{psf}(r) \qquad \text{(IV.31)}$$

5.8.2. Single particle tracking

Typically, single particle tracking consist of the following steps:

1. Image filtering
2. Identification of particles and localizations (Two dimensional Gaussian fitting is used to calculate coordinates)
3. Linking coordinates that belong to the same particle to generate tracks
4. Analysis of tracks to extract dynamics

STORM datasets consist of localization coordinates from millions of molecules. Therefore, we only need to identify coordinates that belong to the same particle within the dataset. Generally, if some molecules remained *on* for several frames, their coordinates can be tracked and molecular dynamics can be extracted. Tracking was performed by connecting particle positions in consecutive frames for a given maximum displacement. Maximum displacement is the distance that a particle moves in a single time interval. To account for blinking, we can specify the number of frames that a particle can disappear before being considered a new particle.

The dynamics can be measured by mean square displacement (MSD) and the lag time τ, and is characterized by diffusion coefficient D. MSD is defined as:

$$MSD(\tau) = \langle (x(t) - (x(t+\tau))^2 + (y(t) - (y(t+\tau))^2 \rangle \tag{IV.32}$$

Random diffusion was identified by fitting the following model:

$$MSD(\tau) = 2dD\tau \tag{IV.33}$$

where d denotes the dimension. While Random diffusion with a flow was fit with the following model:

$$MSD(\tau) = 2dD\tau + (v\tau)^2 \tag{IV.34}$$

v is the flow velocity. The velocity autocorrelation is another method to detect type of dynamics and it is defined over a time delay domain by:

$$V_{corr}(dt) = \langle V(t_2).V(t_1) \rangle \tag{IV.35}$$

where $dt = t_2 - t_1$, and (.) denotes a dot product. For a Brownian motion, the displacements are uncorrelated and therefore the velocity autocorrelation should be zero for every delay, except at dt = 0.

5.8.3. Tracing of sperm flagellum

To trace sperm flagella and plot average cross-sectional profile an algorithm from [112] was used. The tracing algorithm was given an initial position P_0 in the middle of a flagellum, a desired direction with a search radius r that matches the radius of flagella and a step size s. The algorithm searches around the initial position for all points within the search radius. Then it calculates their orientation by calculating the principal components of the covariance matrix (green ellipse in Figure 18). It then sets the geometrical mean of the point cloud as the first point in the trace (green point) and moves along the strongest component (green arrow) for a distance

s. It repeats this process with unvisited points until there are not enough points along the trace (less than 20).

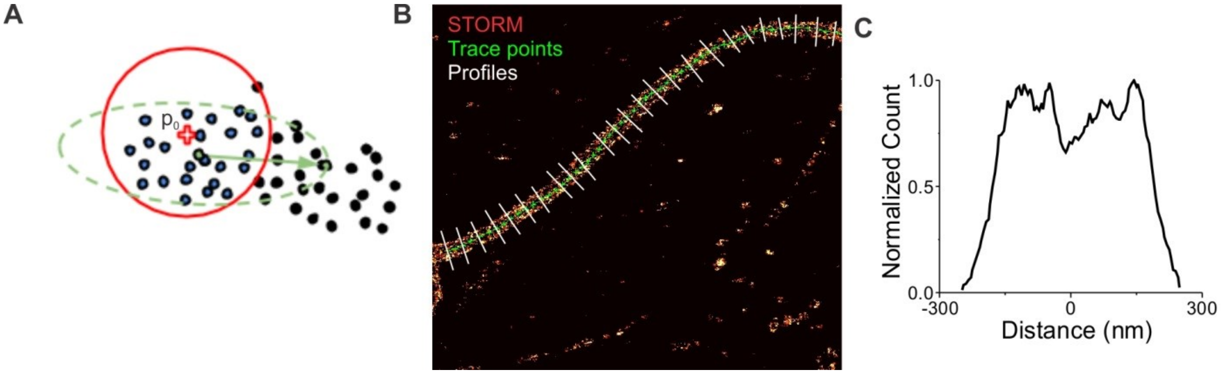

Figure 18. Scheme for the tracing algorithm obtained from [112]**. A.** Overview of the tracing algorithm with an initial point P_0 (red) and covariance matrix (green ellipse). **B.** Tracing algorithm applied on STORM image of sperm flagella showing the traced points and a representation of the profiles collected along the flagella. White lines represent the normal to the flagellum. **C.** Average profile produced from the sum of all the profiles in (B). Scale bar 1 µm.

5.8.4. Colocalization analysis

Coordinate based colocalization analysis was adopted from [113]. In brief, using MATLAB, the coordinate-based colocalization (CBC) histogram was calculated from single-molecule localization data observed in two channels. In order to calculate CBC for a localization A_i of channel A, the distribution of localizations from both channels A and B around Ai was calculated. Then a CBC value is assigned to each single localization A_i within channel A. The CBC is calculated as follows:

First distance distributions were calculated as:

$$D_{A_i,A} = \frac{N_{A_i,A}(r)}{N_{A_i,A}(R_{max})} \cdot \frac{R^2{}_{max}}{r^2} \qquad \text{(IV.36)}$$

$$D_{A_i,B} = \frac{N_{A_i,B}(r)}{N_{A_i,B}(R_{max})} \cdot \frac{R^2{}_{max}}{r^2} \qquad \text{(IV.37)}$$

where $\mathrm{N}_{\mathrm{A_i,A}}(\mathrm{r})$ is the number of localizations of channel A within distance r around Ai, $\mathrm{N}_{\mathrm{A_i,B}}(\mathrm{r})$ is the number of localizations of channel B within distance r around $\mathrm{A_i}$ and $\mathrm{R_{max}}$ is the largest observed distance.

From the above two distributions, the rank correlation coefficient based on Spearman is calculated. Let $\mathrm{O}_{\mathrm{D}_{\mathrm{A_i,A}}}$ denote the rank of $\mathrm{D}_{\mathrm{A_i,A}}$ and $\overline{\mathrm{O}}_{\mathrm{D}_{\mathrm{A_i,A}}}$ denote the arithmetic average of $\mathrm{O}_{\mathrm{D}_{\mathrm{A_i,A}}}$. Similarly, let $\mathrm{O}_{\mathrm{D}_{\mathrm{A_i,D}}}$ denote the rank of $\mathrm{D}_{\mathrm{A_i,B}}$ and $\overline{\mathrm{O}}_{\mathrm{D}_{\mathrm{A_i,A}}}$ denote the arithmetic average of $\mathrm{O}_{\mathrm{D}_{\mathrm{A_i,D}}}$. Then:

$$S_{A_i} = \frac{\sum_{r_j}^{Rmax}\left(o_{D_{A_i,A}} - \bar{o}_{D_{A_i,A}}\right)\left(o_{D_{A_i,B}} - \bar{o}_{D_{A_i,B}}\right)}{\sqrt{\sum_{r_j}^{Rmax}\left(o_{D_{A_i,A}} - \bar{o}_{D_{A_i,A}}\right)^2}\sqrt{\sum_{r_j}^{Rmax}\left(o_{D_{A_i,B}} - \bar{o}_{D_{A_i,B}}\right)^2}} \tag{IV.38}$$

The CBC value becomes:

$$C_{A_i} = Se^{\left(-\frac{E_{A_i,B}}{R_{max}}\right)} \tag{IV.39}$$

Where $\mathrm{E}_{\mathrm{A_i,B}}$ denotes the distance from $\mathrm{A_i}$ to the nearest neighbor from channel B. $\mathrm{C}_{\mathrm{A_i}}$ is calculated for every localization $\mathrm{A_i}$ within a channel A and its value range from -1 to +1 [113].

5.8.5. Resolution estimation

5.8.5.1. Fourier ring correlation (FRC)

Fourier Ring Correlation (FRC) can be computed directly from experimental data. FRC is centered on the spectral signal-to-noise-ratio (SSNR) method commonly used in the field of cryo-electronmicroscopy to assess single particle tomographic reconstructions of macromolecular complexes [114]. To calculate FRC, STORM localizations that constitute an image were divided into two statistically independent sub-sets, yielding two sub-images. Subsequent statistical correlation of their Fourier transforms over the pixels on the perimeter of circles of constant spatial frequency magnitude *q* gives FRC (Figure 19).

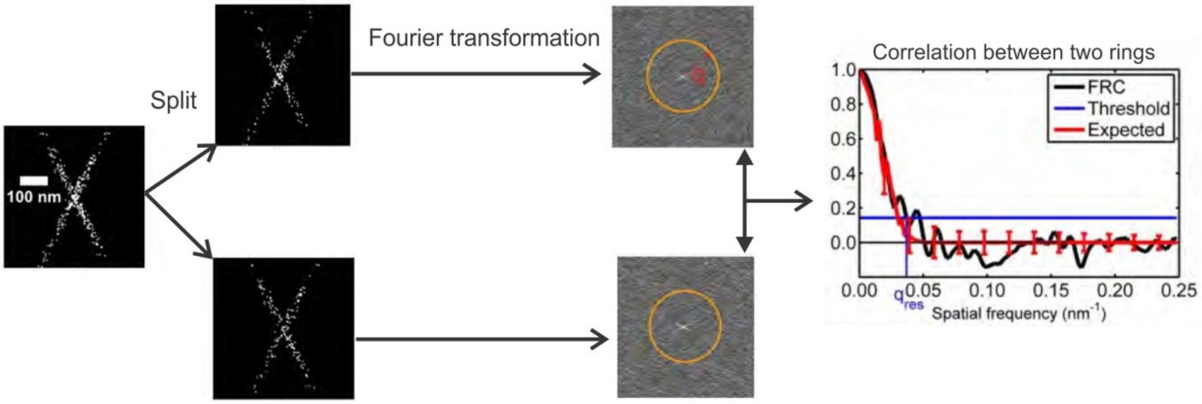

Figure 19. Fourrier Ring Correlation (FRC) principle. Localizations are divided into two halves, the correlation of their Fourier transforms over the perimeter of circles in Fourier space of radius q is calculated, resulting in an FRC curve indicating the decay of the correlation with spatial frequency. The image resolution is the inverse of the spatial frequency for which the FRC curve drops below the threshold $1/7 \approx 0.143$. In the above example FRC curve crosses threshold at $q = 0.04\ \text{nm}^{-1}$ corresponding to 25 nm resolution. Image adopted from [114].

5.8.5.2. Experimental localization precision – Tracing single molecules

To determine the precision experimentally, we used a custom made MATLAB code to group molecules which remained *on* for several frames based on nearest neighborhood distance. Next, a standard deviation was calculated from each group belonging to a single molecule. Standard deviation from all the molecules within the dataset gave the histogram for the experimental localization precision. A similar method is described elsewhere [115].

5.9. Simulation of STORM data

5.9.1. Simulation of microtubules

STORM images of microtubules in CHO cells were used as a mask for the simulation. Simulation was performed using a software from [116]. Localization precision was fixed at 10 nm and label size was set to 20 nm for indirect labeling. Microtubule radius was set to 12.5 nm and fluorophore per label was set to 4 in order to match the fluorophore-label ratio from experiments. Pixel size in simulation was set to 160 nm to match the pixel size in experimental data.

5.9.2. Protein distributed on sperm flagellum

For the protein randomly distributed on sea urchin sperm flagellum simulation was performed using a software from [116] similar to microtubules. Localization precision was fixed at 10 nm. Flagellum radius was set to 125 nm and the label size was adjusted to 20 nm for antibody labeling and 1 nm for photoresact labeling.

For simulation of the GC helical distribution on sperm flagellum, the coordinates were set as follows:

$\mathrm{X} = \mathrm{R} \times \cos\left(\frac{2\pi\mathrm{Y}}{\mathrm{P}}\right) + \mathrm{n} \times \mathrm{S}$, $\mathrm{Z} = \mathrm{R} \times \sin\left(\frac{2\pi\mathrm{fY}}{\mathrm{P}}\right) + \mathrm{n} \times \mathrm{S}$ and Y was chosen to be an array with increasing numbers. R denotes the radius of the flagellum, n denotes a normally distributed random noise, S denotes a factor related to label size and P denotes the pitch as shown in Figure 20. P was set to 6 nm in accordance with cryo-electronmicroscopy data.

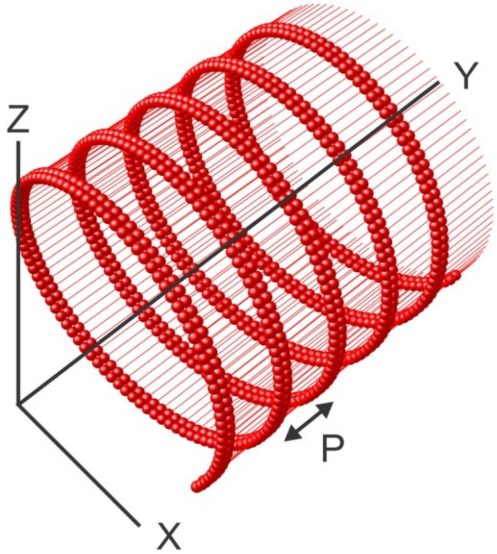

Figure 20. Guanylate cyclase (GC) helical organization as used in the simulation. Functional unit is GC dimers. Each red sphere represents a GC molecule. Pitch P set to 6 nm. Radius = 125 nm.

V. Results

1. Establishing STORM

Optical microscopy has provided deeper understanding of many biological processes at the cellular level. However, the resolution provided by optical microscopy is limited by diffraction of light at the microscope aperture. Under Rayleigh criterion ($R = \frac{0.61\lambda}{NA}$; R being the shortest distance at which two point emitters can be distinguished as separate objects), the resolution reaches a limit of around 200 nm for a numerical aperture (NA) of 1.49 in the visible range. A method named stochastic optical reconstruction microscopy (STORM) has been developed to bypass this limitation [95,96]. It works by modifying the blinking rates of fluorophores in order to isolate individual fluorophore emissions. In other words, it separates fluorophores in time rather than in space. The isolated emission from individual fluorophores can be fitted to a model point-spread-function (PSF) with very high precision. Computation and post-processing is necessary for image reconstruction but they come at a lower cost in comparison to ensemble-based localization methods [92]. I established this technique in order to study the 3D supra-molecular arrangement of proteins on sperm flagella; a tiny structure of a diameter that ranges from 250 nm to 800 nm depending on the species. The method was first tested on microtubules in CHO cells and its potential has been explored with simulation and experimentation.

1.1. Instrumentation and optimization

STORM was established on a Ti-E microscope from Nikon (Figure 21). The system was calibrated and optimized on two levels: 1) the instrumentation, including the objectives and camera, and 2) the imaging conditions and post-processing algorithms.

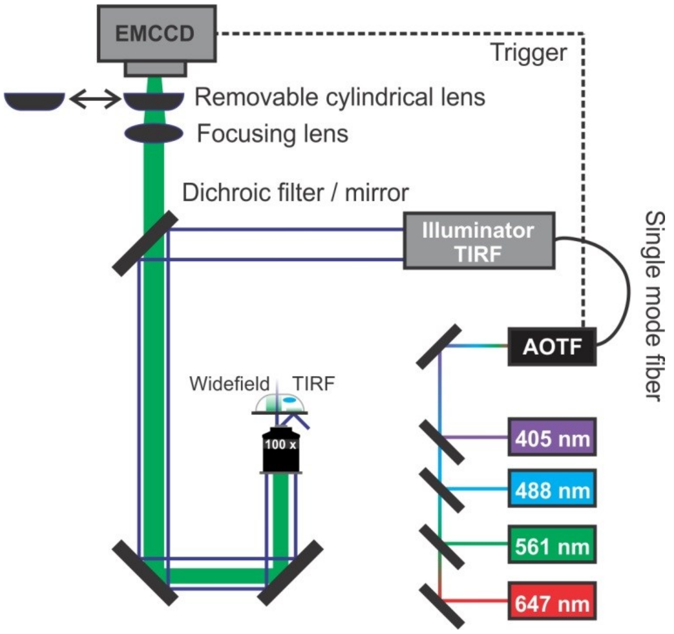

Figure 21. 3D STORM setup with multicolor configuration. AOTF: acoustic optical tunable filter used for fast switching between four laser lines with intensity modulation. The trigger synchronizes the EMCCD camera exposure and excitation duration. The TIRF illuminator allows switching between widefield and TIRF modes.

1.1.1. EMCCD calibration

An electron multiplying charge-coupled device (EMCCD) camera is crucial for STORM because of its high photon detection-efficiency and superior signal to noise ratio, two factors that are essential for single-molecule-localization (SML). In order to implement this camera in our analysis, two calibration steps are necessary for accurate image reconstruction: 1) conversion of camera counts into photons, and 2) color mapping for accurate multicolor imaging.

1.1.1.1. Photon collection and conversion

The EMCCD displays data as image counts and not as number of photons per pixel. However, knowing the number of photons is required for calculating the localization precision in SML methods since localization precision of an emitter depends on the number of photons collected from that emitter (precision $\approx \frac{s}{\sqrt{N}}$, where s is the standard deviation of the Gaussian fit to the PSF and N is the number of photons) (Figure 23H). The calibration determines the camera gain, which converts the detected photon number to camera output signal for a given configuration.

The gain can be obtained from the slope ($\frac{\mathbf{2}}{Gain}$) of a straight line describing the relationship between noise variance and mean count. Hence, I designed an experiment, where I measured the mean and variance from a set of images containing 100 nm fluorescent beads. The variance versus mean was fitted to a straight line and the gain was extracted from the slope (Figure 22). The EMCCD gain was 0.108 e^-/ADU, where ADU is the Analogue-Digital Unit. The read-out noise was 0.8 e^- for the EMCCD, which is 10 times lower than that obtained with CCD camera. The bias was estimated to be around 104 counts, which matched the 100 value provided by the company.

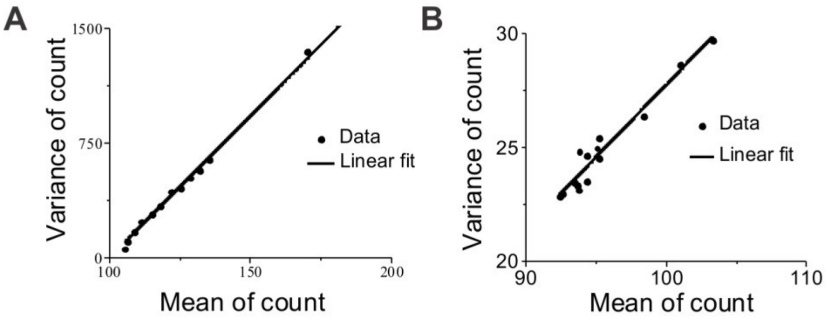

Figure 22. Mean variance plot. A. Mean variance plot of the EMCCD working as a normal CCD. **B.** Mean variance plot of EMCCD.

Next, I optimized the photon collection and PSF sampling with two objective lenses, namely a 60 x objective and a 100 x objective, each with NA = 1.49. To increase the sampling frequency for proper Gaussian fitting of the PSF, I added an additional 1.5 x magnification lens to the 100 x objective, thereby obtaining a smaller pixel size. A weak cylindrical lens was introduced into the imaging path to create two slightly different focal planes for the *x* and *y* directions that allow 3D STORM imaging. Therefore, photon detection efficiency was measured in the presence or absence of an additional cylindrical lens. However, the cylindrical lens did not compromise the photon collection efficiency (Figure 23G). The PSF profile of each objective (Figure 23D-F) revealed that the 150 x magnification provided a better Gaussian fit to the PSF, because photons collected from one molecule are distributed over a larger number of pixels. However, it gave the lowest photon collection efficiency (Figure 23G). Typically, magnification has to be high enough to avoid that all photons fall on the same pixel, and photon count has to be sufficient for precise localization (Figure 23H). Therefore, I decided to use mainly the 100 x objective as a compromise between photon collection efficiency and sampling frequency.

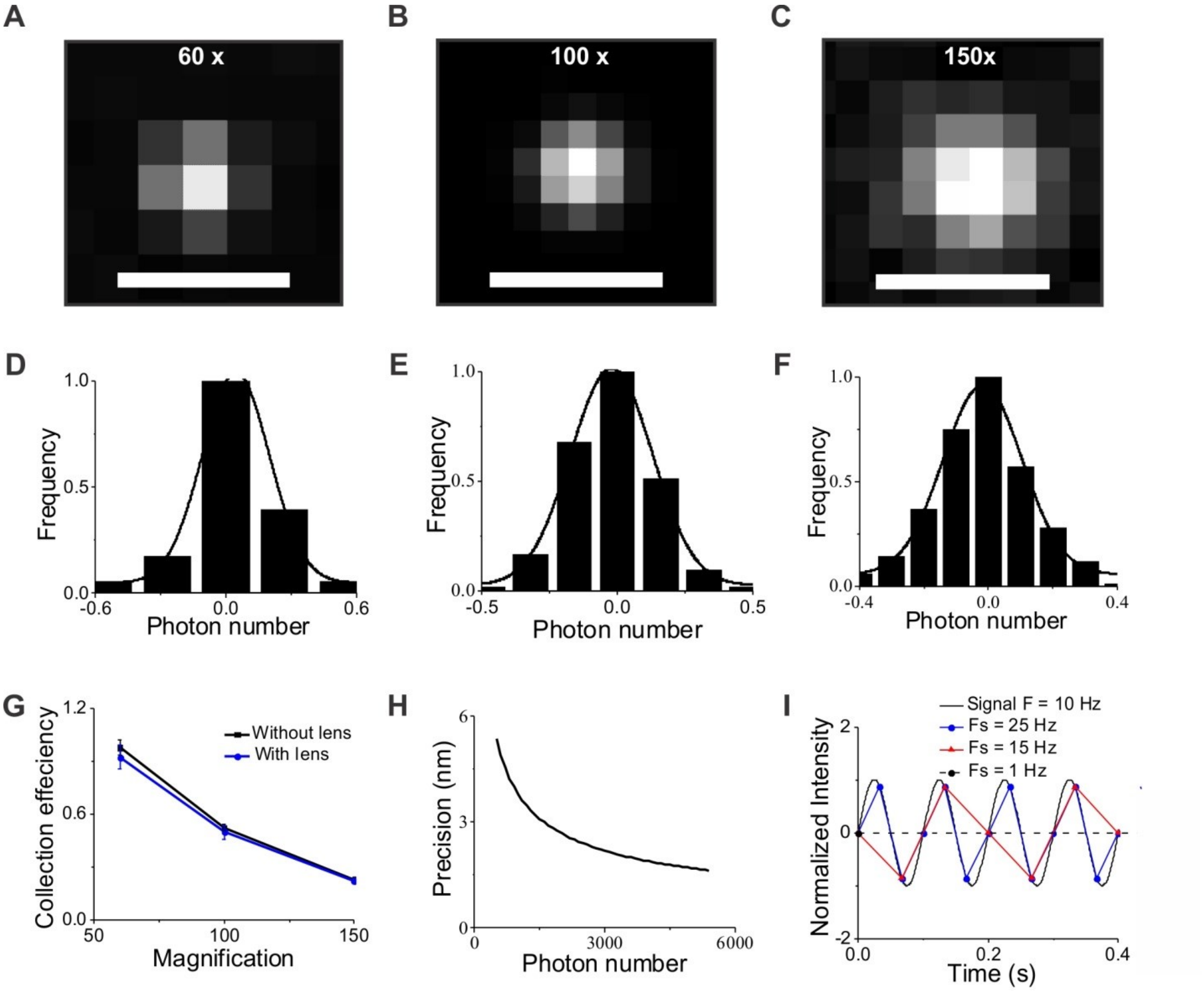

Figure 23. Magnification and localization precision. A-C. Image of sub-resolution bead obtained with three different magnifications. **D-F.** Plot with Gaussian fit for the intensity profile obtained from images in (A-C). **G.** Plot showing variation of photon collection efficiency with magnification in presence (blue) or absence (black) of cylindrical lens. **H.** Plot showing how localization precision varies with photon number. **I.** Plot summarizing the result of a simulation demonstrating Nyquist criterion for sampling. When Nyquist criterion is not met, the signal (black) is not properly reconstructed (red). Scale bar is 1 µm.

1.1.1.2. EMCCD mapping – multicolor imaging

To be able to visualize different proteins simultaneously, I implemented multicolor imaging in our microscope. The EMCCD camera measures photons regardless of the wavelength. Therefore, multicolor imaging requires the addition of emission filters to allow a specific wavelength range to reach the camera. In turn, multiple cameras or two halves/four quarters of the same camera have to be used. This approach suffers from a large chromatic shift and misalignments which might be difficult to correct. Therefore, I used multi-laser stroboscopic illumination, where the same optical path for detection and the same camera were used for all emission wavelengths, thereby keeping aberration to a minimum. I introduced a quadband dichroic filter and a quadband emission filter that allowed four different laser lines to be reflected toward the sample and four different emission channels to be directed toward the camera (Figure 24A). The four different channels were assigned by the corresponding imaging laser using the trigger between the camera and the AOTF (Figure 24C). Whereby switching can be as fast as 1 ms per channel.

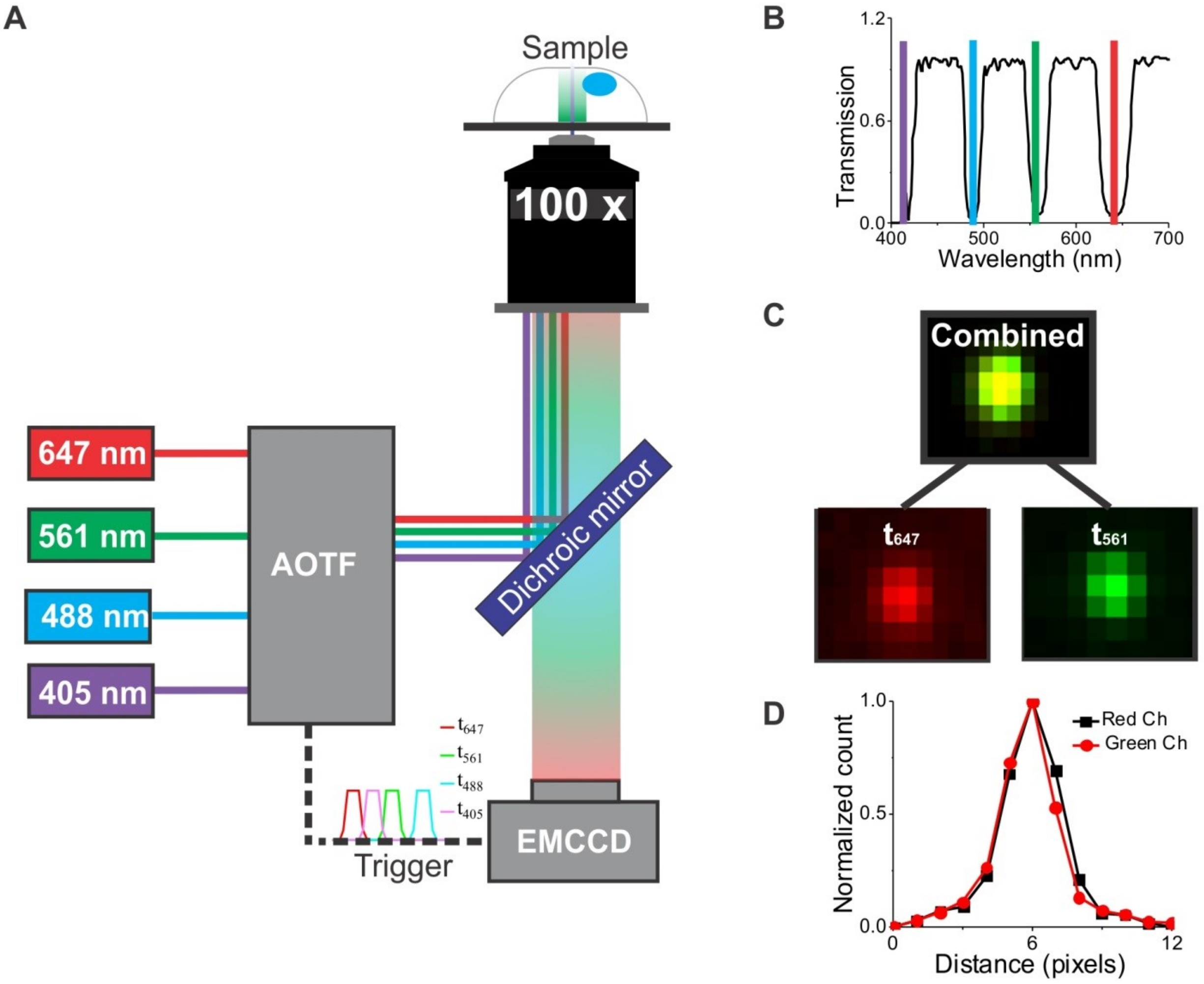

Figure 24. Multiplexing four different spectra with one camera. A. Overview of the multicolor setup where the trigger coupled to EMCCD camera and AOTF, assign the channel. Four laser lines are coupled to the microscope through an ATOF. The AOTF and the EMCCD camera are synchronized with a common trigger; therefore four pulses at different time delays can be used where each pulse is used to trigger a laser line. **B.** Dichroic filter transmission profile showing four different emission spectra and four different excitation lines. **C.** Overlap of a multicolor sub-resolution bead imaged in two channels. **D.** Intensity profile of the multicolor beads in (C) showing a subpixel shift.

For calibration, an imaging chamber plated with 100 nm TetraSpeck microspheres was used. I assigned the 647, 561, and 488 nm excitation lasers for the red, yellow, and green channel, respectively. The bead coordinates were calculated with subpixel precision in the three channels and the red channel was set as reference. Mapping consists of producing a transformation matrix, relating the coordinates of the reference channel to the coordinates in other channels. I wrote a

MATLAB code to assign the coordinates to individual channels then apply a third order polynomial transformation matrix that relates the coordinates x,y of a chosen channel to x',y' in the reference channel (equation V.1). The chromatic shift between red and yellow channel on the EMCCD FOV is represented using a vector plot (Figure 25A); each vector is calculated from coordinates of a single bead obtained from two channels. The chromatic shift has a spatial dependence and hence it is important to sample as much pixels as possible.

$$\begin{pmatrix} x' \\ y' \end{pmatrix} = (\,1\; x^2\; y^2\; yx^2\; xy^2\; x^3\; y^3\,).P_{transform} \qquad \text{(V.1)}$$

P denotes the transformation matrix used to transform the coordinates (x,y) from one channel onto the reference channel. I tested this method using STORM images of individual beads in all three channels and the subpixel localizations of the same bead were initially misaligned (Figure 25B). However, applying the transformation matrix corrected for this chromatic shift between the channels (Figure 25B-C).

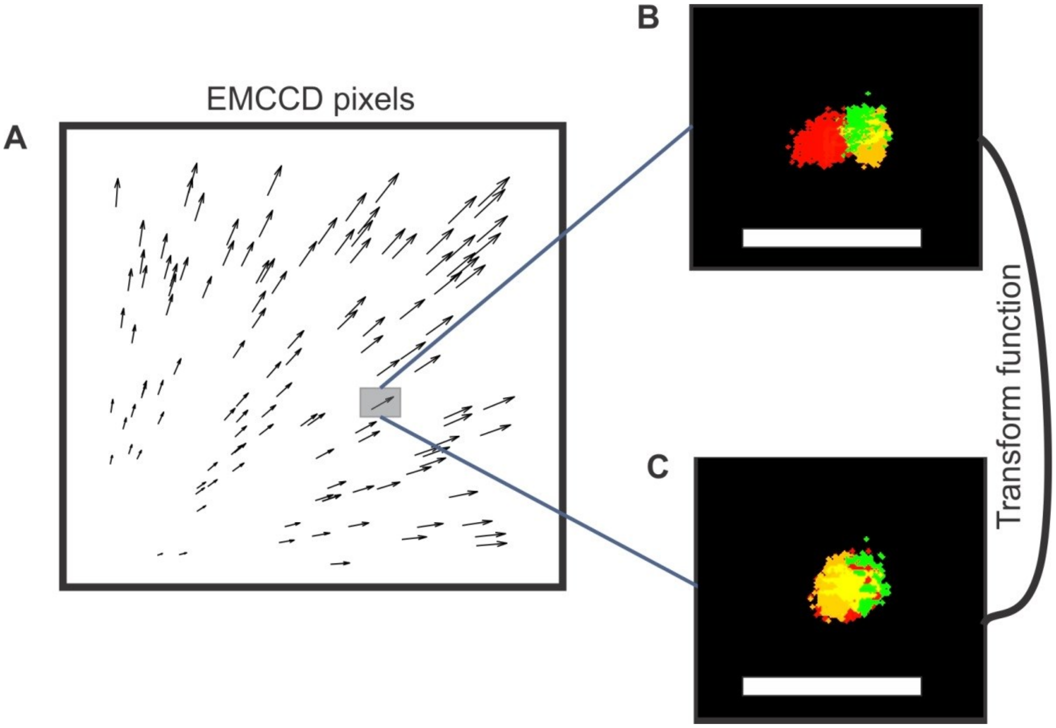

Figure 25. EMCCD color mapping using multicolor fluorescent beads. A. Vector plot showing color mapping between red and yellow channels across the EMCCD pixels. It was obtained using multicolor subresolution beads. **B.** Subpixel localization of one bead before chromatic correction in three excitation channels. Red: 647 nm, yellow: 561 nm, green: 488 nm. **C.** Subpixel localization of the bead

after correction. Localizations of the same bead obtained with 647 nm, 561 nm and 488 nm excitation channels are shown in red, yellow and green color respectively. Scale bar 100 nm.

To demonstrate the method using a biological sample, I used microtubules in CHO cells labeled with a primary antibody and two secondary antibodies, one secondary antibody conjugated to Alexa-647 and another to Alexa-488. The buffer system was optimized for both dyes and the samples were imaged using a sequence consisting of 9 frames at 647 nm excitation followed by 9 frames at 488 nm excitation. Initially, images contained a small offset between the channels, which was corrected after applying the polynomial transformation matrix (Figure 26C). The correction routine was assessed using coordinate-based colocalization analysis [113]. A colocalization index of 1 represents perfect colocalization, whereas -1 represents complete delocalization. The average colocalization index of the microtubules shifted to 1 after correction (Figure 26D) suggesting good alignment. Of note, the 488 nm laser bleached Alexa-647, and thereby reduced the number of acquired localizations. This is not a problem for microtubules, because of the high abundance of the protein. In other samples, it is better to use other dyes or to use sequential imaging where Alexa-647 dataset is acquired first, and Alexa-488 dataset acquired last.

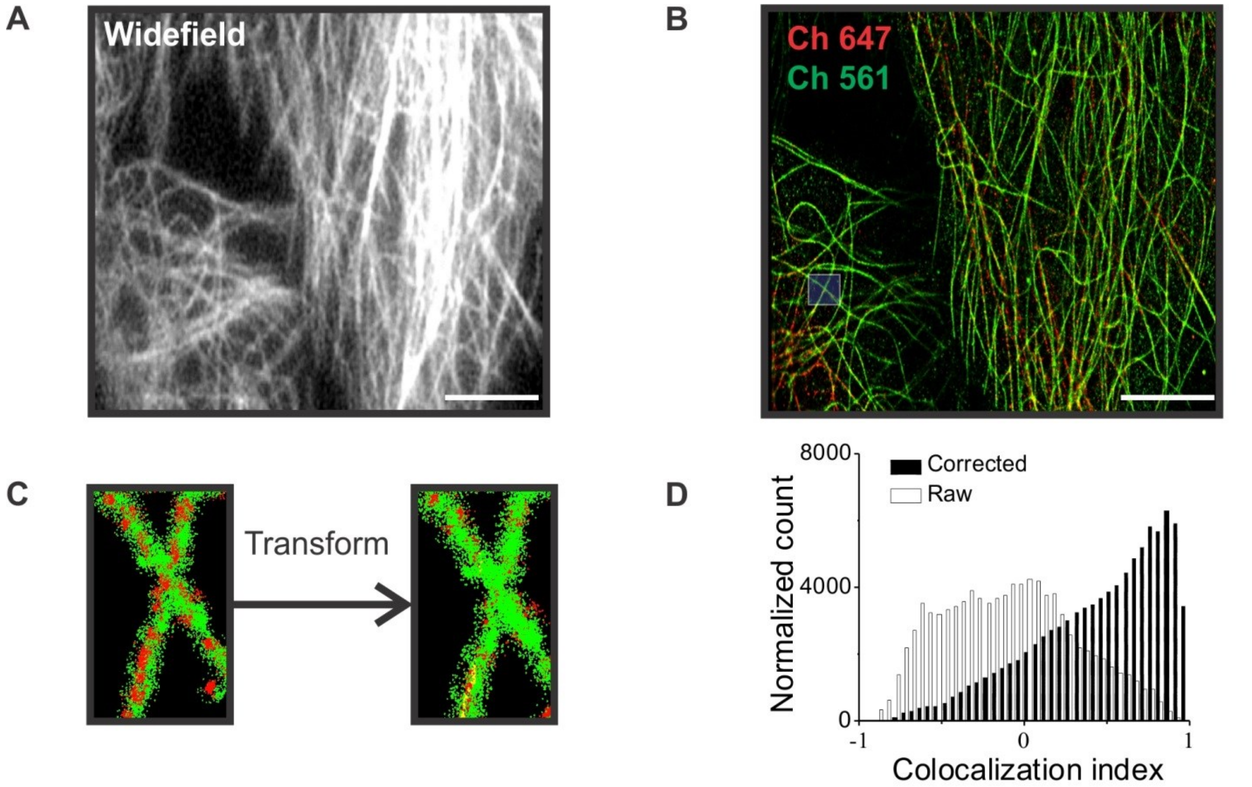

Figure 26. Testing the chromatic shift transformation on microtubules in CHO cells. A. Widefield image of immunostained microtubules in CHO cells, labeled with two secondary antibodies that were conjugated to Alexa-647 and Alexa-488 respectively. Image shows the sum of the two channels. **B.** Multicolor STORM image after correction showing proper alignment of microtubules in two channels. **C.** A zoom-in showing before and after correction STORM image of two crossing microtubules. **D.** Coordinate based colocalization [113] applied to the STORM data in (B) before and after correction. Colocalization index of 1 shows a complete colocalization. Scale bar 10 μm.

1.1.2. Improving image quality

1.1.2.1. Factors affecting image quality

I used a fluorescence calibration slide and adjusted the fiber angle at the TIRF illuminator to obtain a Gaussian illumination profile centered in middle of Field Of View (FOV) (Figure 27A). Then I focused the beam at the back aperture of the objective to get a collimated beam at the sample position. This way I could ensure a proper TIRF alignment for high quality STORM acquisition. The system was tested using fluorescent beads and the absence of the out of focus and freely diffusing beads from the image, was taken as an indication that TIRF has been attained (Figure 27B). Thereby, I determined the critical angle experimentally as a reference point for future experiments. TIRF provided a significant enhancement in SNR compared to widefield when tested with fluorescent bead sample and actin labeled CHO cells (Figure 27C-E). Of note, SNR can still be improved while keeping a deep depth of field when using angles that are at the intermediate between TIRF and widefield [117].

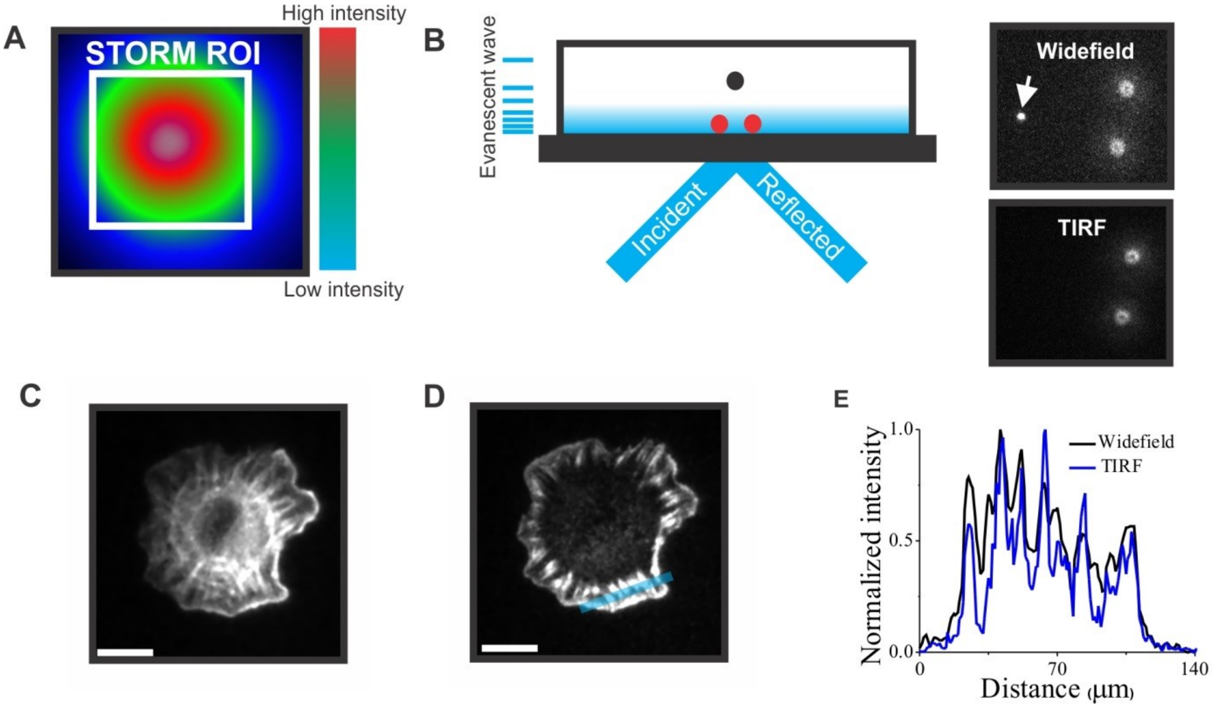

Figure 27. Adjusting illumination profile for proper TIRF imaging. A. Illumination profile across FOV widefield. **B.** Diagram showing TIRF penetration depth. Focusing above the coverslip shows no out of focus bead (arrow) in TIRF. **C.** Widefield image of actin CHO cell labeled with phalloidin-647. **D.** Image of same cell in (C) in TIRF mode. **E.** Intensity profile along the blue line in (D) for the images taken in widefield (black) and TIRF (blue). Scale bar 10 µm.

The next step is the sample preparation. My experiments demonstrated that ultrastructures like microtubules were better preserved in Phem fixation solution compared to 4% PFA (Figure 28A-B). To improve specificity and labeling density, the antibody concentration and incubation time was varied to achieve adequate density (Figure 28B-D). It has been reported that adding Cyclooctatetraene (COT) to the STORM imaging buffer increases the number of photons emitted during one cycle, without altering the blinking behavior of the dye or the achievable localization density [118]. Thus, I tested a buffer containing 2 mM COT and 50 mM Cysteamine (MEA) with immunostained microtubules in CHO cells. A secondary antibody conjugated to Alexa-647 was used. I obtained 10,000 frames for each condition using the same settings and repeated this on 3 samples. Adding COT resulted in a 70 % increase in photon count (Figure 28F). In addition, I estimated the influence of antibody size on resolution using simulation of directly and indirectly labeled microtubules (Figure 28H-I). From the image and profile in Figure 28I-J, I was able to assess how antibodies enlarged the observed structure. Taking a precision of 10 nm for both cases, I estimated an enlargement of around 20 nm in the size of microtubule when using antibodies.

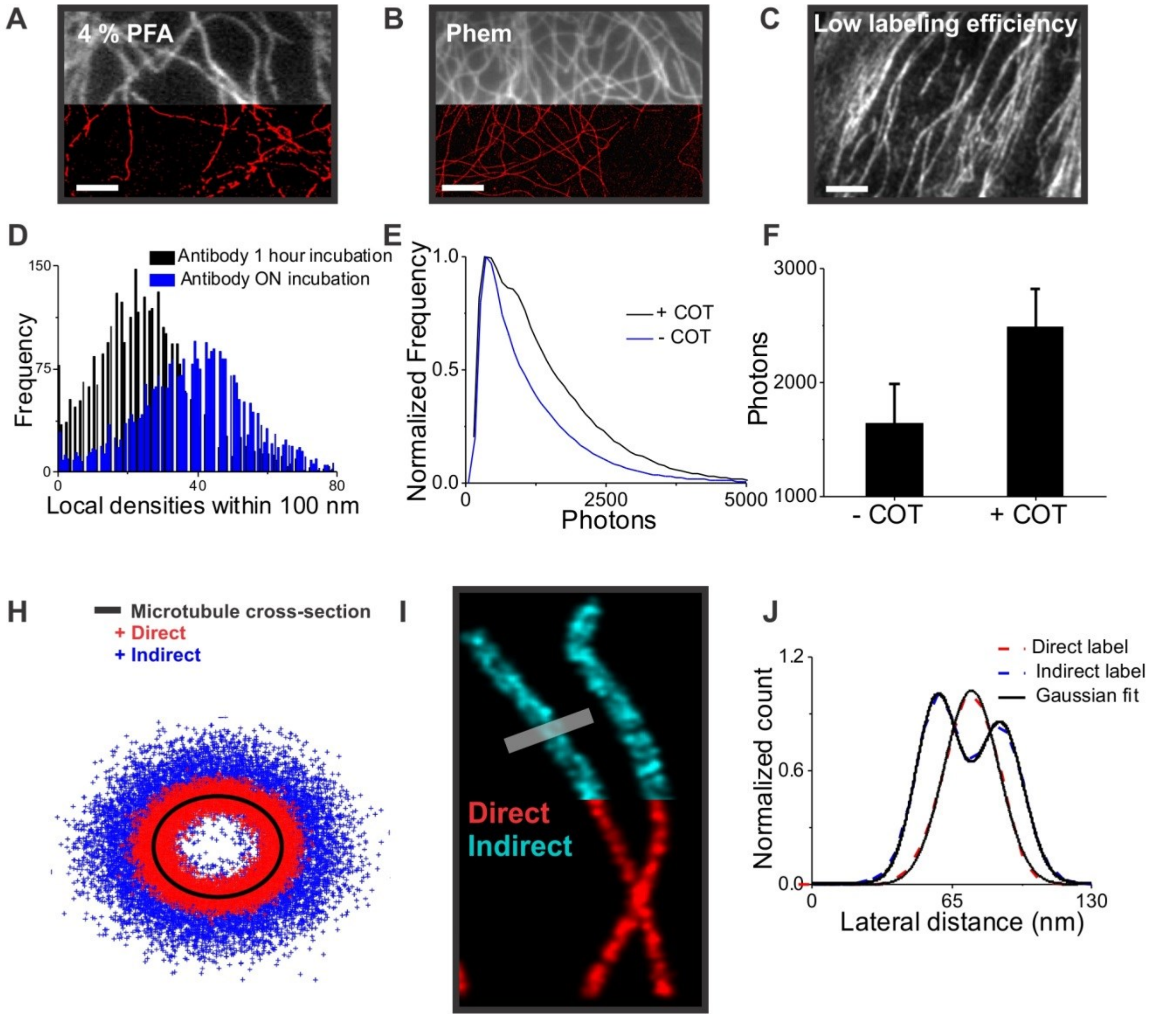

Figure 28. Effect of fixation and labeling on ultrastructures. A. Immunostained microtubules fixed with 4% PFA. **B.** Immunostained microtubules fixed with Phem solution. **C.** Fluorescence image showing microtubules with low labeling efficiency. **D.** Histogram showing the quantification of local densities STORM images of microtubules for 1 hour (black) and overnight (ON) antibody incubation. **E.**

Photon histogram with (black) and without (blue) COT. **F.** Bar graph showing average photon count per molecule with and without COT. Bar graph shows average ± SD (n = 3). **H.** Cross-section from a simulation with microtubule cross-section (black), fluorophore localizations originating from direct labeling of tubulin proteins (red), and fluorophore localizations originating from primary and secondary antibody labeling (blue). **I.** Rendered STORM image of the simulation with direct antibody labeling (red) and indirect antibody labeling (cyan). **J.** Profile plot showing normalized density distribution across the line in (I). Scale bar 10 µm.

To show the evolution of structural resolution with acquisition time, I produced STORM images from a microtubule dataset at different time points (Figure 29). I measured the size of an individual microtubule by plotting a density profile at different acquisition times (Figure 29D). However, I was not able to quantitatively define a threshold for what is considered to be enough number of localizations per experiment. Whereas, Fourier Ring Correlation (FRC) can provide a more convenient measure of this resolution. I used FRC to measure how resolution evolves with time (Figure 29E). In one example (Figure 29A-C), I was able to conclude that there is no structural resolution gain after 75 seconds and hence the experiment can be stopped at this point. The achievable resolution converged with time to a value that is comparable to the size of one microtubule and it approached this value after 75 seconds of acquisition (Figure 29F).

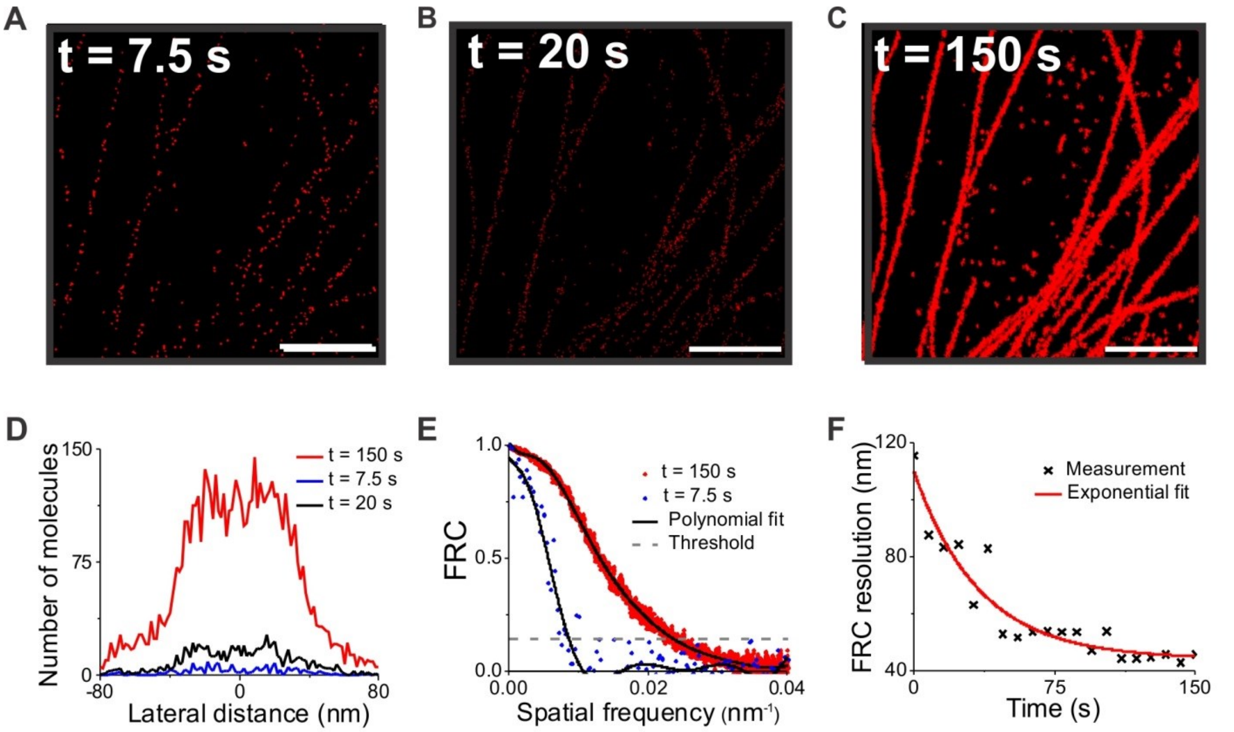

Figure 29. Structural resolution evolves with acquisition time. A-C. STORM image of microtubules at different acquisition times. **D.** Profile plot of one microtubule at different acquisition times. **E.** FRC plot at different acquisition times. **F.** Plot shows how resolution evolves with acquisition time. Plot shows FRC resolution as a function of acquisition time (black x). Data was fitted to an exponential (red). Scale bar 10 µm.

In brief, two properties of the dyes are important for high image quality, the number of photons per cycle and the *on*/*off* duty cycle or the fraction of time a fluorophore spends in the *on* state [98]. I optimized the imaging procedure on our set-up accordingly and produced suitable conditions for high imaging quality. The majority of emitters can be forced to an *off* state using a high power 647 nm laser until they achieve equilibrium (Figure 30A), where single molecules can be identified and fitted. I could tweak the duty cycle by using one of the two activation lasers, 405 nm and 488 nm. Using the same power, the activation response was higher for the 405 nm laser (Figure 30B). Thereby, a high dynamic range of activation can be achieved by varying this laser power (Figure 30C). Moreover, the 647 nm imaging laser can be tuned to achieve a desirable ON fraction per frame (Figure 30D). In addition to the activation laser wavelength/power and imaging laser power, the buffer composition played an important role in the production of high quality STORM datasets. I varied the concentration of MEA between 10 mM for high number of localizations per frame to 100 mM for low number of localization per frame (Figure 30E-G). Finally, imaging laser, activation laser and buffer composition could be tweaked and varied from experiment to experiment depending on available labeling density and desired acquisition duration.

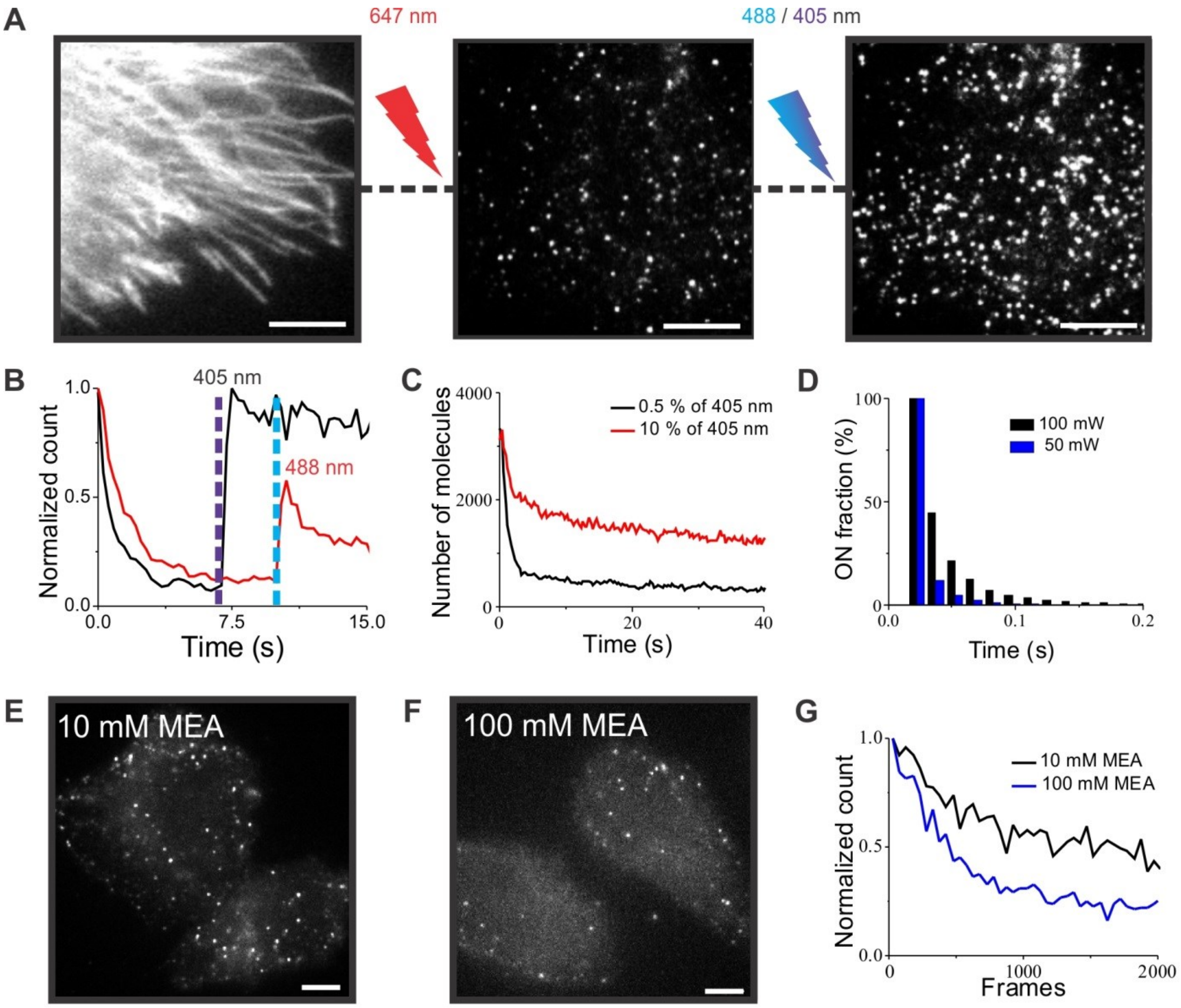

Figure 30. Selection of proper activation laser wavelength and imaging laser power. A. STORM imaging cycle. Initially, all molecules are on, after 647 nm imaging laser illumination majority of molecules switch off and only a sparse number of molecules can be seen at any time point. The density of on molecules per frame can then be adjusted with the use of either 488 nm or 405 nm activating lasers. **B.** Plot showing molecule count with acquisition time. Laser activation by 405 nm (black) or 488 nm (red) was performed after few seconds (violet and cyan dotted lines). **C.** A plot showing how 405 nm lasers control the number of molecules per frame. **D.** Plot shows distribution of the duration during which a molecule remained on with two imaging laser power. **E.** Fluorescence image showing molecules that are spontaneously on at equilibrium with 10 mM MEA. **F.** Same as in (E) with 100 mM MEA. **G.** Plot shows effect of MEA concentration on molecule (fluorescent molecules) density per frame. Scale bar 20 μm.

1.1.2.2. Drift correction

Temperature and mechanical perturbation lead to drift; thereby, decreasing image resolution (Figure 31H). I used two different methods to compensate for this drift. The first method required the addition of fluorescent beads to the sample and it relied on particle tracking of fluorescent beads that remain *on* throughout the whole experiment. The tracks of particles in 3D were then subtracted from the STORM data (Figure 31D). The second method relied on the STORM data itself to extract the drift [119]. Drift here, was extracted from the spatial cross-correlation function between image subsets chosen at consecutive times (Figure 31E-F). Both methods resulted in similar results. However, the cross-correlation method required an adequate number of localizations within each subset and it worked only on fixed samples, whereas for sparser and dynamic samples, bead tracking had to be used.

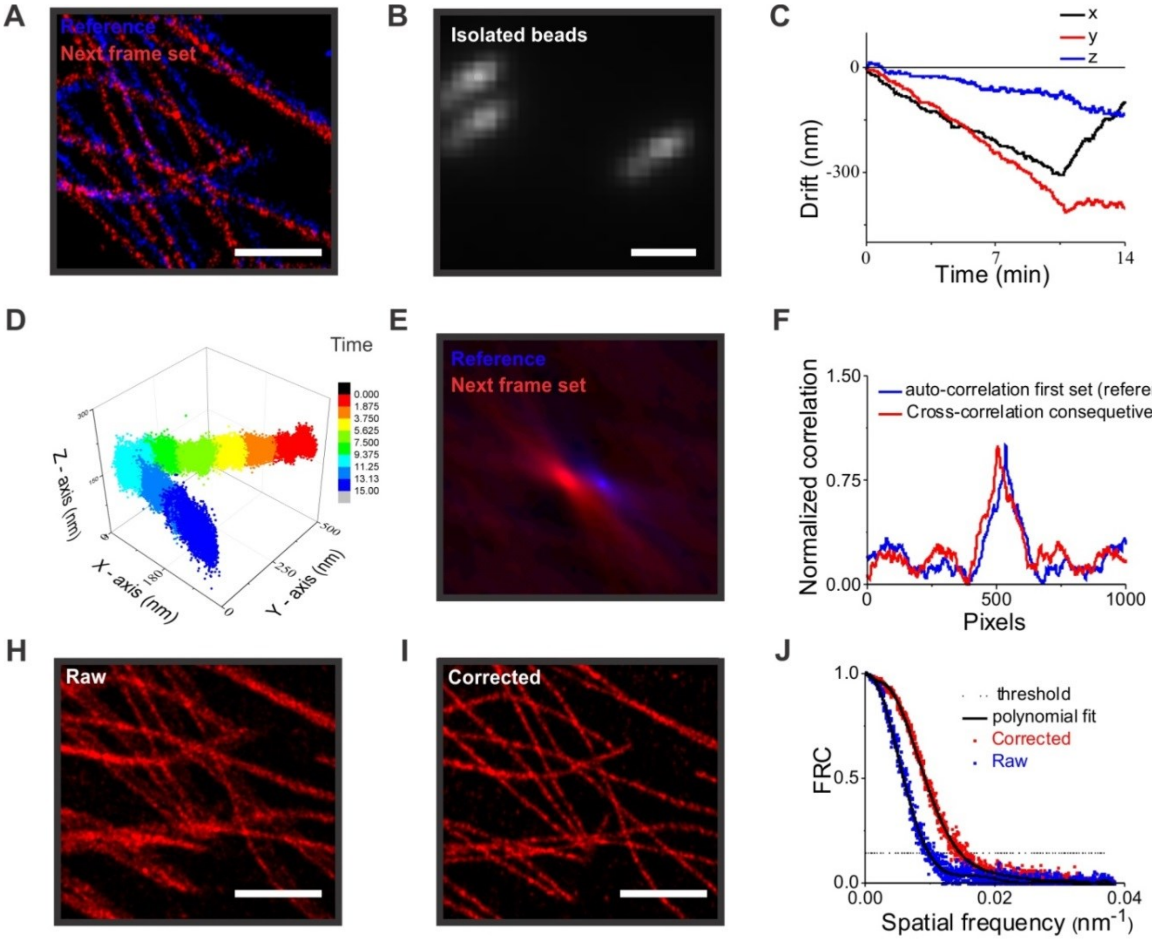

Figure 31. Testing drift correction algorithms. A. STORM image showing two subsets of one datasets demonstrating sample drift with initial subset (blue) and subsequent subset (red). **B.** Time

projection image of isolated beads. (C) Plot shows the 3D drift, extracted from cross-correlation method. **D.** Plot shows 3D drift, extracted from tracking of beads. **E.** Autocorrelation images of the two subsets in (A). **F.** Horizontal profile of the images in (E). The drift can be estimated from the shift in the peak. **H.** Uncorrected STORM image. **I.** Drift corrected STORM image. **J.** Plot shows FRC resolution before (red) and after drift correction (blue). After correction FRC decayed below threshold at higher spatial frequencies. Scale bar 10 µm for microtubules, 1 µm for beads

1.1.2.3. Calibration for three dimensional imaging – astigmatism

The next step was to extend the method to three dimensions using an astigmatism-based approach [105]. A weak cylindrical lens was introduced into the imaging path to create two slightly different focal planes for the x and y directions that allow 3D STORM imaging. The system was calibrated to assign a specific PSF shape to the corresponding z-coordinates (Figure 32A). I used 100 nm fluorescent beads that were plated on a 1.5H coverslip and imaged them in STORM imaging buffer. Images were acquired at different z-positions which covered a range of 1000 nm using 10 nm steps. The width of the PSF in x and y was extracted then plotted as a function of z, resulting in a calibration curve (Figure 32C). The data was fitted with a polynomial which was later used to determine the z positions in STORM datasets.

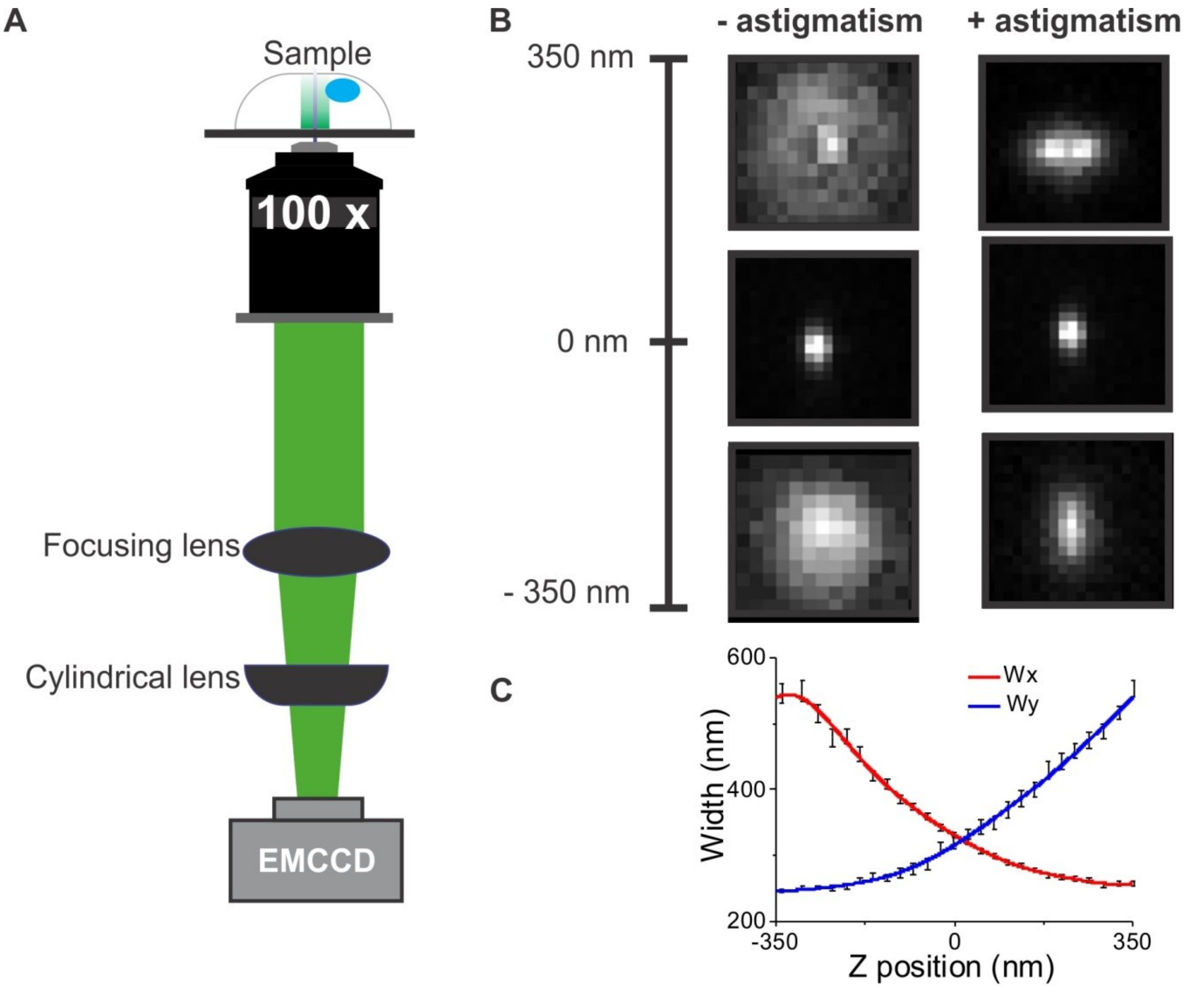

Figure 32. 3D calibration with astigmatic lens. A. Simplified diagram showing the position of the cylindrical lens in the imaging system. **B.** Images showing how PSF shape varies with z position in the presence and absence of astigmatism. **C.** Calibration curve obtained by plotting PSF width in x and y as function of z.

Furthermore, I detected depth-dependent lateral distortion (Figure 33A). To correct for it, I measured this distortion using fluorescent beads and a similar method to 3D calibration. Instead of lateral width I measured the lateral position as a function of z (Figure 33B).

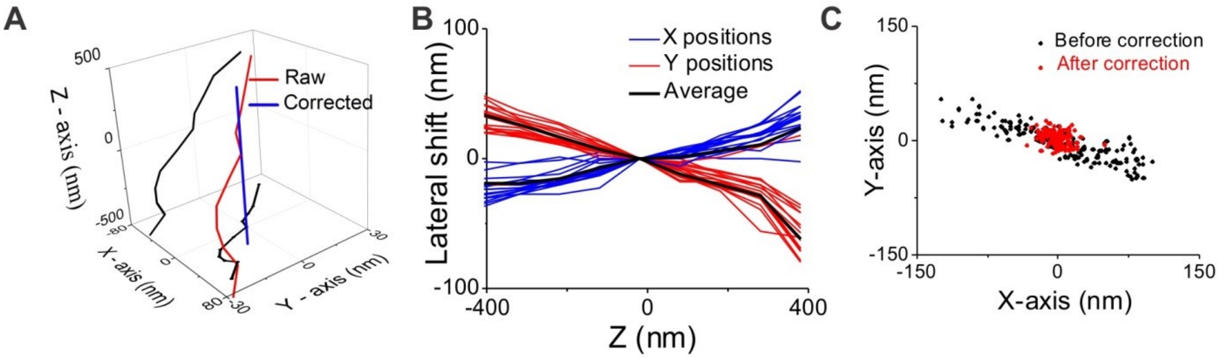

Figure 33. Correction of the depth-dependent lateral shift. A. 3D plot showing how localizations from the same molecule vary as function of z before and after correction. **B.** Calibration curve of the lateral shift obtained by measuring lateral position of a bead sample as function of z. **C.** Localization obtained from an isolated cluster before and after correction.

Finally, I tested the 3D calibration and 3D reconstruction using microtubules in CHO cells that were labeled with an antibody against tubulin and a secondary antibody coupled to Alexa-647 (Figure 34). Image quality was high enough that I could extract the course of a single microtubule filament in 3D and its relative axial position to other filaments (Figure 34B). Experimental localization precision was 15 nm (lateral) and 25 nm (axial). In addition, precision could also be extracted from isolated clusters that did not belong to any structures. These clusters represent localizations from single antibodies that were non-specifically adsorbed to the coverslip. I collected around 30 of such clusters and aligned them according to their center of mass and then I produced a 3D localization map (Figure 34E). The profile of these localizations was fitted to a Gaussian function and the resolution was extracted from the width of the Gaussian fit – estimated to be 45 nm (Figure 34F). Furthermore, resolution could also be extracted directly from the microtubular structure. I plotted the localization density profile across one isolated microtubule and extracted the structural resolution from its width (Figure 34H). The profile was fitted to a double Gaussian function, resulting in a width of 50 nm. Thus, the 25 nm microtubule was enlarged to 50 nm due to the finite localization precision and antibody size. Finally, I applied the FRC method to our dataset to extract the resolution (Figure 34I). In summary, all the methods gave similar results, except the one where we estimated the resolution theoretically from the number of photons (Figure 34J). This is mainly due to the fact that precision estimation from photons does not take into consideration all the imaging artifacts and background levels, hence it is far from a realistic representation of our resolution limit.

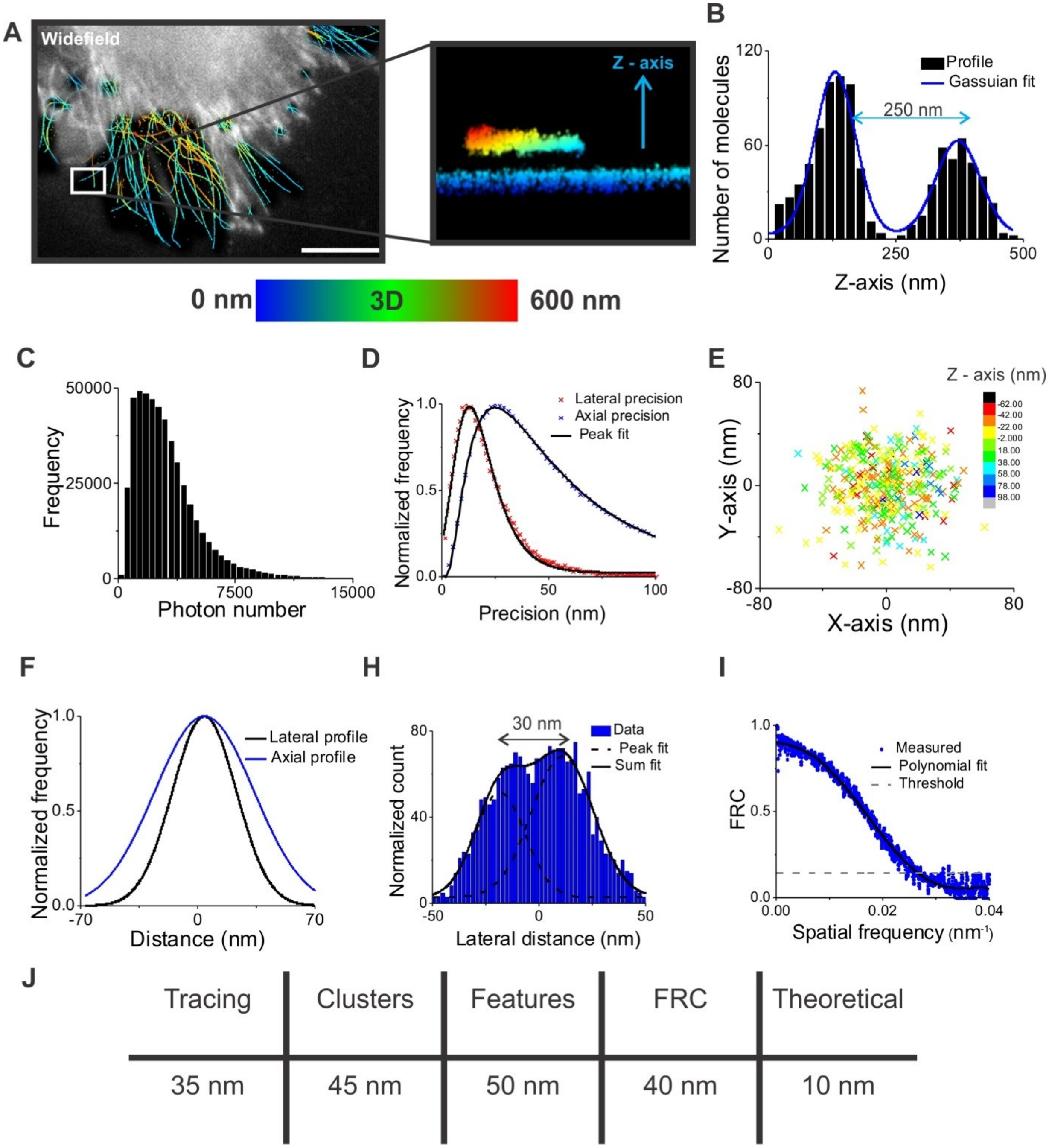

Tracing	Clusters	Features	FRC	Theoretical
35 nm	45 nm	50 nm	40 nm	10 nm

Figure 34. 3D STORM of microtubules in CHO cells. A. 3D color coded STORM image of microtubules. Widefield image shown in gray scale, 3D STORM is color coded for z. (Right) Zoomed in axial cross-section image showing two microtubules crossing above each other. Z RGB color code is shown below images. **B.** Profile plot of the microtubules in (A) showing a sub-resolution axial separation distance. **C.** Histogram of photon number from the STORM dataset in (A). **D.** Experimental lateral and axial precision (see methods). **E.** 3D plot of isolated and aligned clusters (n=30). Localizations are color coded for z. **F.** Gaussian fit of the clusters in (E) in lateral (black) and axial (blue) direction. **H.** Density

profile of one microtubule that was averaged over a distance of 5 µm with double Gaussian fit. **I.** FRC plot of the image in (A). **J.** Summary of resolution extracted from the same image with different methods. Scale bar 20 µm.

The depth of field in 3D STORM is limited to around 800 nm. I extended this range by combining astigmatism and z-scanning. The experiment was performed as follows: At z = 0 nm, a 3D STORM dataset, comprising thousands of frames, is acquired. The objective is moved to a second position at z = 400 nm to allow for some structures to overlap in the final image. Here, another 3D STORM dataset is acquired. This procedure is repeated at different z positions until the sample is completely out of focus (Figure 35A). Finally, the datasets are analyzed and the resulting STORM images are concatenated to form an extended 3D STORM image. This method allowed the reconstruction of the whole microtubule network of one CHO cell (Figure 35B). This method suffers from depth-dependent aberration, such as coma and spherical aberration, which are enhanced as we go deeper into the sample. Choosing a 400 nm steps allow for structures to overlap and, thereby, allowing the drift correction in 3D to correct for sample drift and aberration. 3D drift correction was applied using cross-correlation on the final concatenated image.

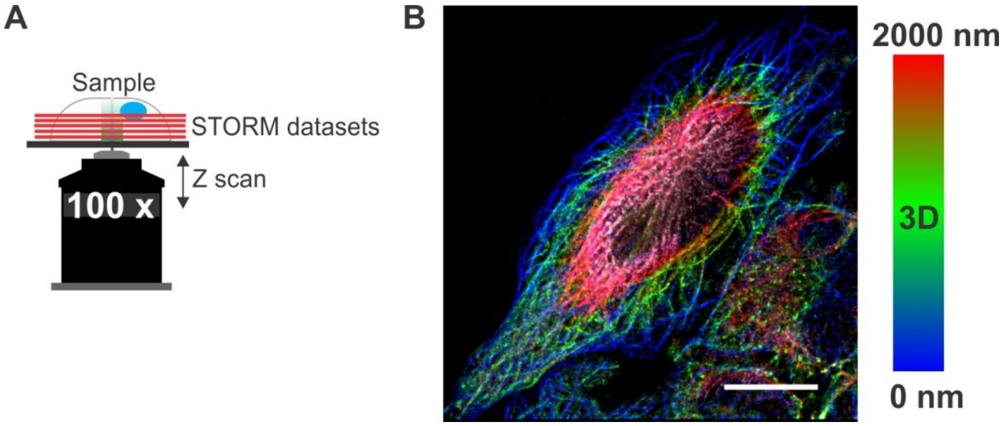

Figure 35. Extending the depth of field for 3D STORM. A. Overview of the concept used to extend the depth of field for 3D STORM. Each red line represents a STORM dataset obtained in the presence of an astigmatic lens. **B.** 3D STORM image of microtubules in CHO cells with an extended depth of field. Image is color coded for z. Scale bar 10 µm.

1.2. Quantification of data – Cluster analysis and high density particle tracking

The characteristic of STORM data makes the method quantitative by nature. Distribution of proteins in subcellular compartments can be extracted using pair correlation analysis [12,13]. I verified that pair correlation analysis [110] could be used on our set-up to quantify protein organizations in heterogeneous samples and I showed that it can be easily applied to STORM pointillistic datasets. I tested this method on STORM images of commercial antibodies, where each antibody had an average of 4 fluorophores. The measured auto-correlation function $g(r)$ of data containing overcounting can be used to extract the effective resolution. First, correction was done by tracing and combining all the localizations that belonged to a single molecule and then creating one averaged localization for each molecule. Then, I obtained a total $g(r)$ from raw data, and $g(r)$ from corrected data. The $g_{psf}(r)$ is the difference of the two and it can be fitted by a model describing the contribution of the PSF (see method) (Figure 36A). The fitting gave an effective PSF of 18.26 nm. Furthermore, I fitted the data with two models, one representing a random distribution and a second representing a clustered distribution (see method). And as expected from a sample of antibodies conjugated to multiple fluorophores, the clustered distribution fitted best and I derived a cluster size of 35 nm containing an average of 3.2 molecules. The size agrees with the isolated clusters (Figure 33E) and the number of molecules per cluster agrees with the degree of labeling provided by the company which I later validated using absorption spectroscopy (see method).

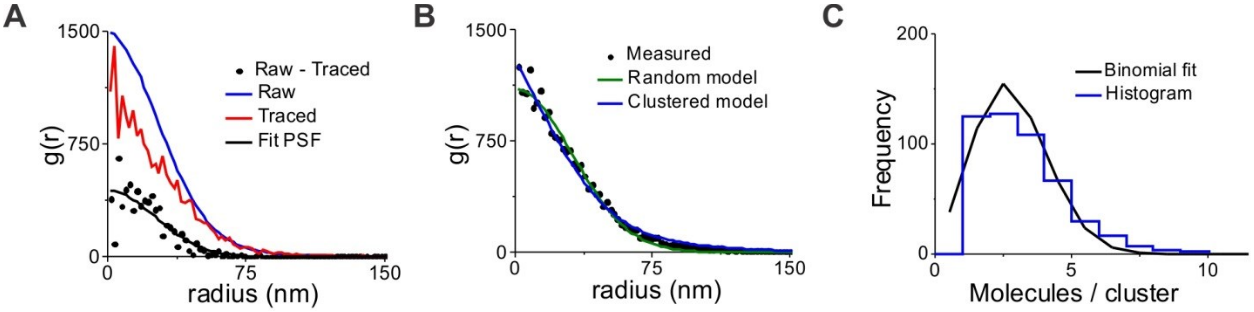

Figure 36. Correlation function quantifies resolution and clustering. A. Correlation functions of raw and traced data. The difference is fitted to PSF model to extract resolution. **B.** Correlation function can be fit to either clustered or random model. In this case a clustered model seem to be a good fit and then cluster sizes and number of molecules per cluster can be extracted from the model. **C.** Histogram showing manually obtained number of molecules per cluster from isolated antibodies in a STORM image.

Given an adequate frame rate and *on*-time (duration during which molecules remain *on*) molecules can be tracked. I tested how we could extract dynamics from two simulated datasets containing molecules undergoing Brownian motion. One sample consisted of molecules in absence of flow (D = 1 μ^2/s) and another of molecules subjected to flow (D = 0.1 μ^2/s). After STORM reconstruction, I tracked the localizations (Figure 37A-B) using a homemade matlab code which allowed me to extract the mean square displacement (MSD). For the pure Brownian motion case the MSD I obtained showed a linear variation with time lag as expected (Figure 37C) while the molecules subjected to flow showed a nonlinear variation. The diffusion in both cases was derived from fitting the data to a model describing either a pure Brownian motion or Brownian motion in presence of a flow (see methods), and diffusion was 0.9 μ^2/s and 0.08 μ^2/s respectively. Moreover, I applied image fluctuation analysis on the first dataset for comparison [120]. This method analyzes the fluctuation of the ensemble and still extracts information about single-molecule dynamics. I recovered the same diffusion coefficient from the dataset using a fit of the published 2D diffusion model [120] to the time evolution of the autocorrelation function (Figure 37E). In addition, I could detect flow from raw STORM data using velocity autocorrelation. Molecules undergoing pure Brownian motion are characterized with a velocity autocorrelation that is equal to zero everywhere except at a delay time of zero , unlike molecules that were subjected to flow which showed a non-zero velocity autocorrelation (Figure 37H).

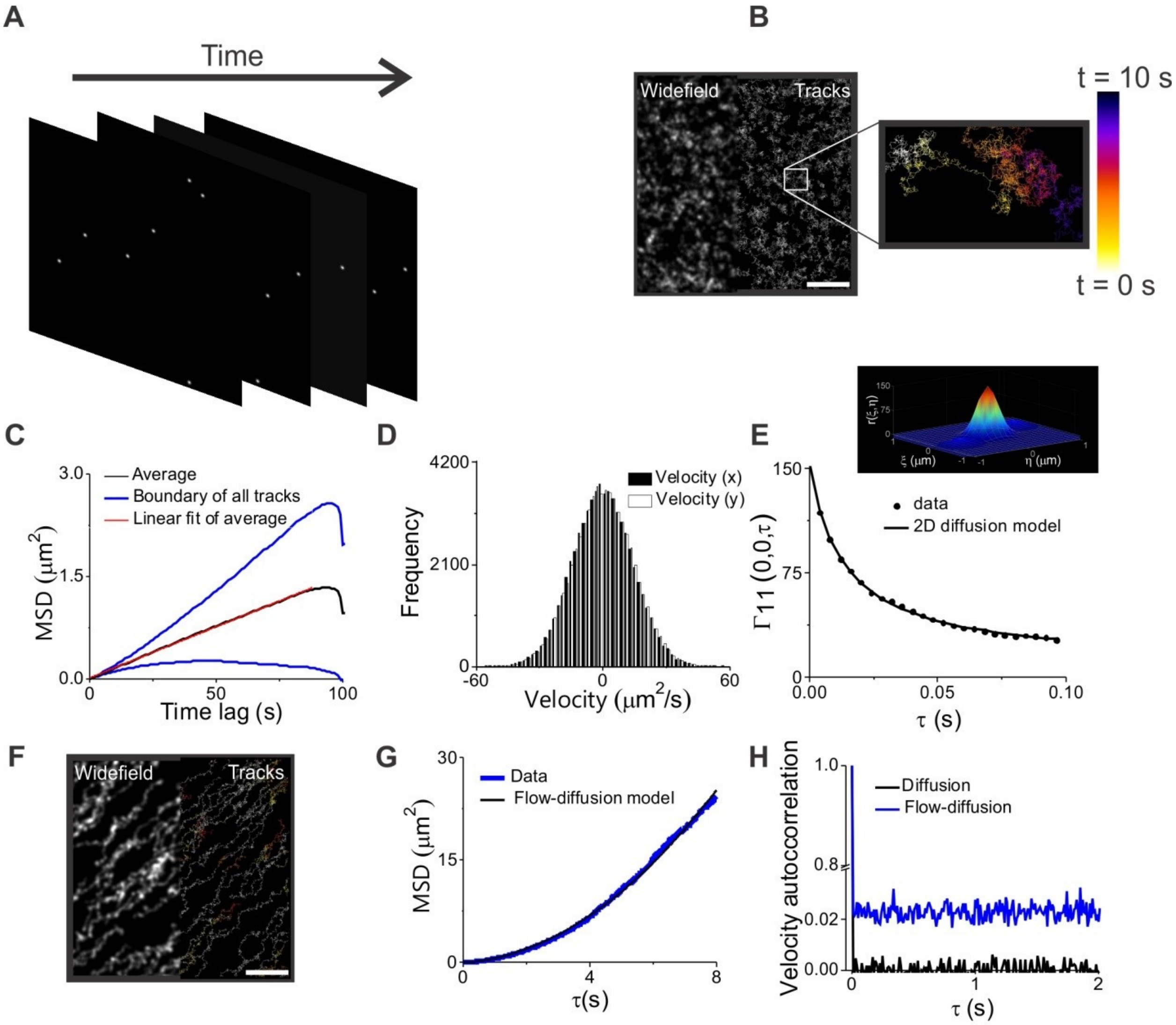

Figure 37. Extracting dynamics from STORM data using single particle tracking. **A.** Images showing simulated frames of diffusing particles at different time points. **B.** Widefield projection overlayed with the extracted tracks. Boxed region contain isolated track of one molecule, color coded for time. Color code of time is shown on the right. **C.** Plot showing average MSD (black) with a linear fit (red). Boundary of all tracks is shown in blue. **D.** Velocity histogram of the molecules from (B) showing symmetric distribution. **E.** Top part: Plot showing autocorrelation plot of the initial frame of the dataset that was fit to a 2D Gaussian function. Bottom part: correlation curve showing the time evolution of the autocorrelation function. **F.** Widefield projection overlayed with tracks of molecules subjected to flow. **G.** Average MSD (blue) fitted with a nonlinear model (black) (see method). (H) Velocity autocorrelation for freely diffusing particles in the presence (blue) and absence of flow (black). Scale bar 2 μm.

2. Elucidating the single-molecule response and cGMP dynamics in sea urchin sperm

A single resact molecule, impinging on the sea urchin sperm flagellum, is transduced into a Ca^{2+} signal that mediates the swimming trajectory in a chemoattractant gradient. The single-molecule response comprises the rapid synthesis of cyclic guanosine monophosphate (cGMP) by a single guanylate cyclase (GC) receptor (Figure 38). In turn, cGMP opens K^+-selective cyclic nucleotide–gated (CNGK) channels, leading to membrane hyperpolarization. This hyperpolarization activates two other signaling components: an Na^+/H^+ exchanger (sNHE) and a hyperpolarization-activated and cyclic nucleotide–gated (HCN) channel. sNHE activity causes a rapid intracellular alkalization, whereas opening of HCN channels leads to a Na^+ inward current that depolarizes the cell membrane. The alkalization shifts the voltage dependence of CatSper channel, thus enabling CatSper to open during subsequent depolarization leading to Ca^{2+} influx. Recovery from stimulation involves restoration of resting $[Ca^{2+}]_i$ by a Na^+/Ca^{2+}–K^+ exchanger (NCKX) and hydrolysis of cGMP by a phosphodiesterase (PDE) [2]. Resact single-molecule sensitivity and the ensuing cGMP dynamics are still not fully understood.

All the results in this chapter were done on sperm of the sea urchin *Arbacia punctulata* by Prof. U.B. Kaupp and me at the MBL laboratory in Woods Hole, Massachusetts, USA.

2.1. Experimental design – Simultaneous recording of signaling events

In a stopped-flow device, a sperm suspension loaded with fluorescent dyes (to record Ca^{2+}, voltage, or pH) is rapidly mixed with resact and the resulting fluorescence changes are monitored over time. In addition, sperm were loaded with (7-diethylaminocoumarin-4-yl)methoxycarbonyl (DEACM)-caged cGMP that has an absorption maxima at 405 nm. The excitation LED was triggered at a reference frequency that was set between 1 and 100 kHz. The resulting signal from the PMT was an alternative current (AC) signal modulated at the reference frequency. A lock-in amplifier was used to filter out any fluorescence or noise that is not modulated at this reference frequency. For uncaging, a UV LED centered at 360 nm is triggered by either single pulses or arbitrary waveforms of up to 5 Hz. Any fluorescence from the released cage is filtered out using phase sensitive detection (see methods). To record Ca^{2+}, voltage, or pH changes, we used the following indicators:

1. Fluo-4 AM as a Ca^{2+} indicator [80].
2. pHrodo-red SE as a pH indicator.
3. Either, FluoVolt, di-8-anepps, or BeRST were used as voltage sensitive indicator [79].

1.1.1. Resact-evoked responses: Voltage, Ca^{2+}, and pH_i

First, sperm loaded with BeRST were mixed with various concentration of resact, resulting in membrane hyperpolarization. The amplitude of hyperpolarization increased and its rise time decreased with increasing resact concentrations. Moreover, the recovery from hyperpolarization became faster with increasing resact concentration (Figure 38C). Next, sperm loaded with pHrodo-red SE were stimulated with resact. This dye shows a decrease of fluorescence with increasing pH; therefore, the traces were multiplied by -1 to present alkalization as an increase in fluorescence. Resact stimulation increased the intracellular pH (pH_i) in a dose-dependent manner. The amplitude increased and its rise time decreased with increasing resact concentration (Figure 38D). Lastly, sperm loaded with Fluo-4 AM were stimulated with resact, resulting in a dose-dependent transient increase in the intracellular $[Ca^{2+}]_i$. The Ca^{2+} signal delay time and its rise time both decreased with increasing resact concentration (Figure 38E). The delay is caused by binding of resact to the receptor, followed by synthesis of cGMP, and opening of CNGK channels. The ensuing membrane hyperpolarization, which opens HCN channels, causes a membrane depolarization, opening of CatSper channels, and, thereby, Ca^{2+} influx. Next, I measured simultaneously resact-evoked voltage, pH_i, and Ca^{2+} signals with BeRST, pHrodo-red SE, and Fluo-4 AM, respectively. The experimental set-up used is explained in details in the methods section. The multiplexed signals revealed the time delay between the three signaling events (Figure 38F): 1) upon stimulation with resact, sperm hyperpolarized. 2) sNHE was activated during membrane hyperpolarization, causing sperm alkalization. 3) Finally, upon depolarization, CatSper channel opened, resulting in Ca^{2+} influx.

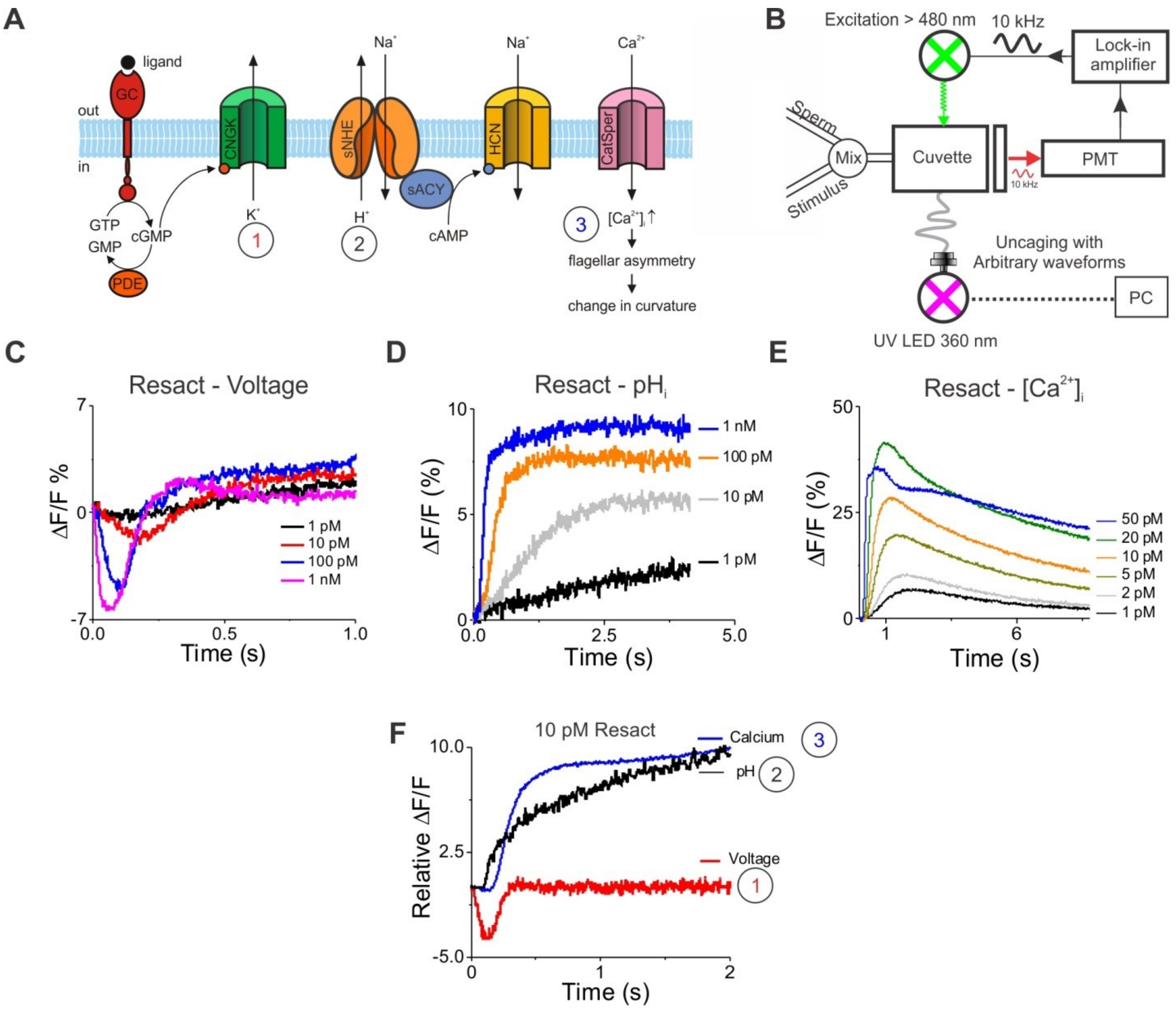

Figure 38. Resact-evoked responses. A. Chemotactic signaling pathway in sea urchin sperm. Resact, the chemoattractant peptide, binds to receptor GC and, thereby, stimulates the rapid synthesis of cGMP. The ensuing surge in cGMP opens K^+-selective cyclic nucleotide–gated (CNGK) channels to produce a brief hyperpolarization of the cell membrane. This hyperpolarization activates two other signaling components: an Na^+/H^+ exchanger (sNHE) and a hyperpolarization-activated cyclic nucleotide–gated (HCN) channel. sNHE activity causes a rapid sperm alkalization. Upon opening of HCN channels, the ensuing Na^+ inward current depolarizes the cell and leads to the opening CatSper Ca^{2+} channels. Figure modified from [6]. **B.** Scheme showing stopped-flow apparatus with excitation and uncaging LED light sources, where sperm loaded with an indicator are rapidly mixed with a stimulus. The fluorescence change over time is recorded by a PMT. The PMT is coupled to a lock-in amplifier that is locked at the excitation frequency (10 kHz), whereby UV stimulation is filtered out. **C.** Dose-dependency of resact-evoked voltage responses using BeRST dye: 1 pM (black), 10 pM (red), 100 pM (blue), and 1 nM (pink).

D. Dose-dependent resact-evoked pH responses using pHrodo-red SE: 1 pM (black), 10 pM (red), 100 pM (blue), and 1 nM (pink). **E.** Dose-dependent resact-evoked Ca^{2+} responses using Fluo-4-AM: 1 pM (black), 2 pM (gray), 5 pM (olive), 10 pM (orange), 20 pM (green), and 50 pM (blue). **F.** Multiplexed voltage, Ca^{2+}, and pH signals upon 10 pM resact stimulation. Signals are numbered 1 to 3 in sequential order and they are associated with the numbers in (A): 1) cGMP synthesis upon resact activation of the GC induces a K^+ efflux, leading to hyperpolarization. 2) Then sNHE is activated, resulting in alkalization, and 3) finally, CatSper channel open, leading to Ca^{2+} influx.

1.1.2. cGMP-evoked voltage and calcium responses

Next, I used sperm loaded with caged-cGMP (Figure 39A), BeRST, and Fluo-4 AM to measure voltage and Ca^{2+} signals, respectively. Upon UV light stimulation, uncaging cGMP inside sperm activated the CNGK channel directly, resulting in membrane hyperpolarization and, finally, a Ca^{2+} influx (Figure 39B). Thus, we can bypass resact stimulation and study the signaling cascade using a reverse opto-chemical engineering (ROCE) approach. Upon UV stimulation with 10 ms square pulses, sperm hyperpolarized due to the cGMP release, and the absolute value of the signal amplitude increased and its rise time decreased with increasing light levels (Figure 39C). Moreover, the recovery from hyperpolarization became faster with increasing light levels. The signals were similar to those obtained with resact (Figure 38C). The depolarization, however, was more pronounced for cGMP-evoked voltage signals. The amplitude of cGMP-evoked Ca^{2+} signals (Figure 39D) increased, while the corresponding delay time decreased with increasing light levels, similar to those evoked by resact (Figure 38E). Nevertheless, cGMP-evoked Ca^{2+} signals displayed a more distinct second Ca^{2+} peak, which is a result of Ca^{2+} oscillations in sperm that are averaged out in a population measurement. The UV-triggered release of cGMP is more synchronized between different cells of the population compared to resact-triggered cGMP synthesis, which leads to the visible Ca^{2+} oscillations or peaks upon synchronized uncaging of cGMP. Finally, as a proof of principle, I measured simultaneously cGMP-evoked voltage and Ca^{2+} signals using BeRST and Fluo-4AM, respectively (Figure 39E). The delay between voltage and Ca^{2+} signals can be explained by the following sequence of events: upon stimulation, sperm hyperpolarized, triggering alkalization by the sNHE thereby, shifting CatSper voltage dependence. During depolarization, CatSper channels open resulting in Ca^{2+} influx (Figure 39E).

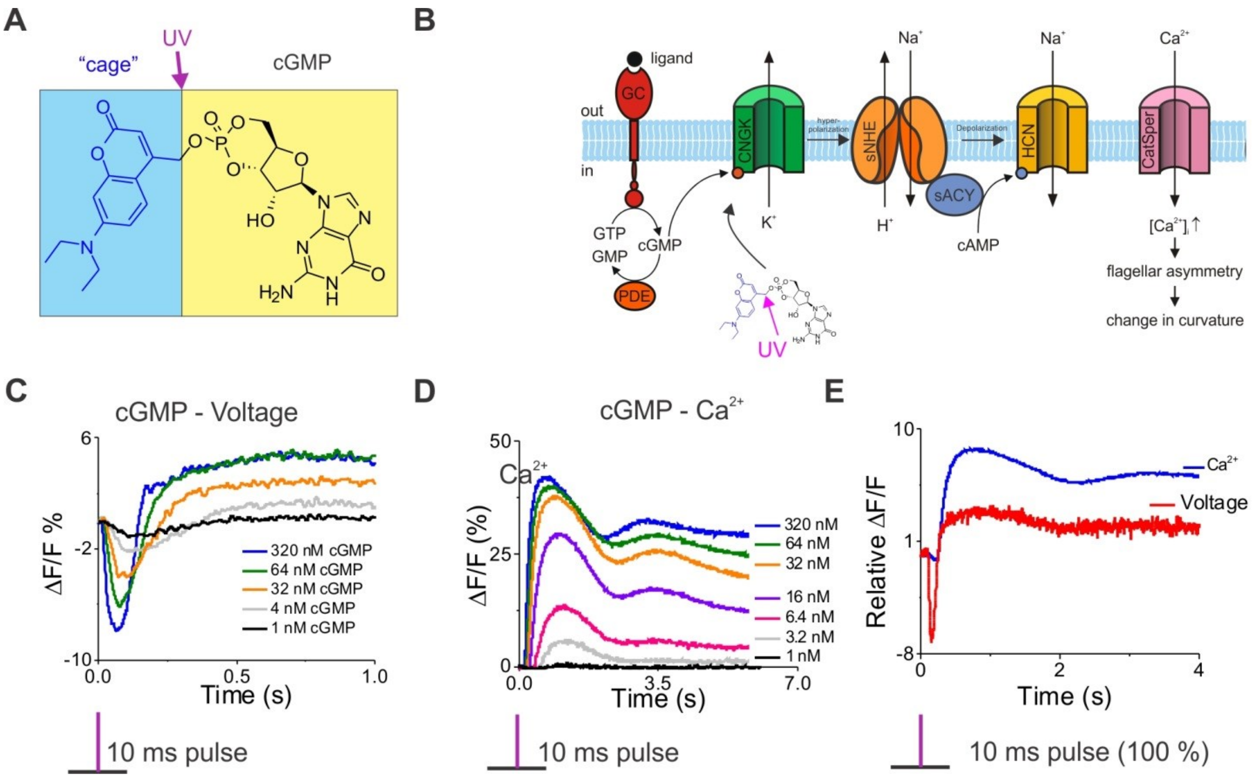

Figure 39. cGMP evoked responses in sea urchin sperm. A. Structure of DEACM caged cGMP. The cage (blue) is photolysed upon UV illumination and cGMP (black) is released. **B.** Signaling cascade showing how uncaging cGMP inside the sperm can act directly on the CNGK channel, thereby inducing K^+ efflux and a hyperpolarization that results eventually in a Ca^{2+} influx. Figure modified from [6]. **C.** cGMP-evoked voltage responses using 10 ms pulses with various light levels. Cumulative released cGMP is shown on the right side. **D.** cGMP-evoked Ca^{2+} responses using 10 ms pulses with various light levels. Cumulative released cGMP is shown on the right side. **E.** Multiplexed voltage and Ca^{2+} signals evoked by cGMP obtained with 10 ms pulse at 100 %. Cumulative cGMP released is estimated at 130 nM.

1.1.3. Calibration of membrane potential with BeRST

I used external $[K^+]_o$ null-point calibration to convert fluorescence changes of BeRST into changes in membrane voltage (V_m). Compared to other cells, sea urchin sperm are relatively depolarized at rest with V_m = - 52 mV [6]. Stimulation with either resact or cGMP opens K^+-selective CNGK channels. This hyperpolarizes the cell towards the K^+ equilibrium potential (E_k). The amplitude of the hyperpolarization increases with cGMP concentration (Figure 39C) and saturates when V_m reaches E_k. Using the $[K^+]_o$ null-point calibration, the external $[K^+]_o$ was changed and the V_m was measured at each concentration. The membrane potential depolarized gradually with increasing $[K^+]_o$ (Figure 40A). Plotting the amplitude of cGMP-evoked voltage signal as a function of the logarithm of the $[K^+]_o$ revealed a linear relationship, as predicted by the Nernst equation (Figure 40B). The fit yielded a slope of 0.109 that corresponds to 10.9 % change per 57.7 mV or 1.9 ± 0.2 % per 10 mV (n = 4). Extrapolating the linear fit to identify $[K^+]_{o,}$ at which cGMP does not change $V_{m,}$ and then substituting this value in the Nernst equation resulted in a resting membrane potential of -57 mV, which is in line with the resting membrane potential of – 52 mV reported in [6].

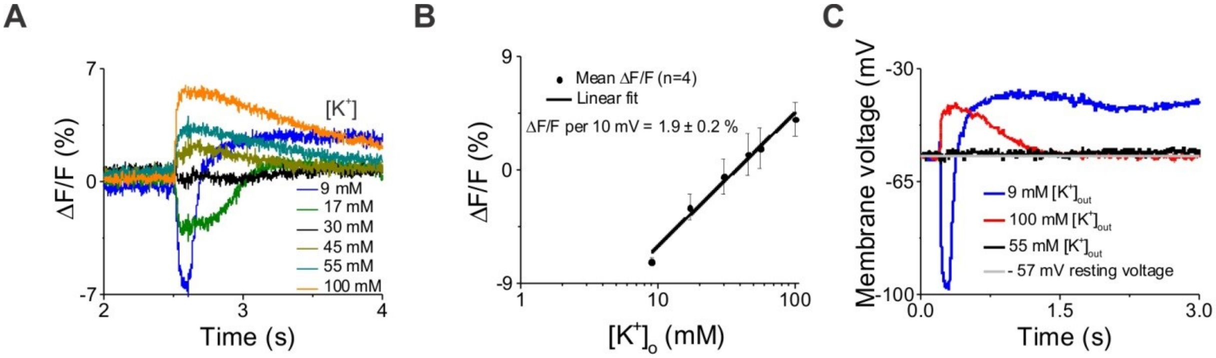

Figure 40. $[K^+]_o$ null-point calibration of BeRST voltage sensitive dye. A. cGMP-evoked voltage responses in presence of varying extracellular K^+ concentrations. $[K^+]_o$ is given on the bottom right of the plot. **B.** Plot of the voltage amplitude as a function of $[K^+]_o$. The slope of the linear fit gives the change per 10 mV. Bars represent SD (n = 4). **C.** Plot shows the voltage calibration applied to cGMP-evoked voltage responses with maximal hyperpolarization in blue (normal ASW) and maximal depolarization in red (at 100 mM $[K^+]_o$). $[K^+]_o$ is given on the bottom of the plot.

2.2. Single-molecule voltage and Ca^{2+} responses in sperm

2.2.1. Calibration of cGMP release rate

I used caged cGMP-loaded sperm to compare Ca^{2+} and voltage signals evoked by a single molecule of resact to cGMP-evoked responses. The purpose was to determine how many cGMP molecules are required for a single-molecule response. To calibrate the cGMP release by uncaging, I first obtained an accurate measure of the effective caged-cGMP concentration in suspension using LC-MC analysis. Here, a 15 μM solution contained an effective concentration of 10 μM. For calibration, I relied on the fact that the DEACM cage is only weakly fluorescent when bound to cGMP, but becomes fluorescent upon photolysis. I measured the increase in fluorescence upon UV excitation at increasing light levels (Figure 41A, B). The change in fluorescence with time, at which less than 10 % of the cage has been released, is linear (Figure 41C). These curves were fit with a straight line of equation y = ax, where a is the slope. I plotted the extracted slopes (µM x s^{-1}) as a function of UV power in %, which resulted in a linear relationship that has a zero intercept. From n = 4 experiments, I calculated a change of 130 ± 2 nM x s^{-1} x P^{-1}, where P is the power level in % or mW (Figure 41D). The average power at the light guide output of the UV LED was measured to be 12 mW at 100 %. Assuming that the concentration of the caged cGMP inside the sperm is equal to its concentration outside, I estimated the upper limit of cGMP released inside the sperm for a given pulse duration at a fixed power level. The calibration was used only when the estimated release is less than 10 % of the total caged cGMP concentration.

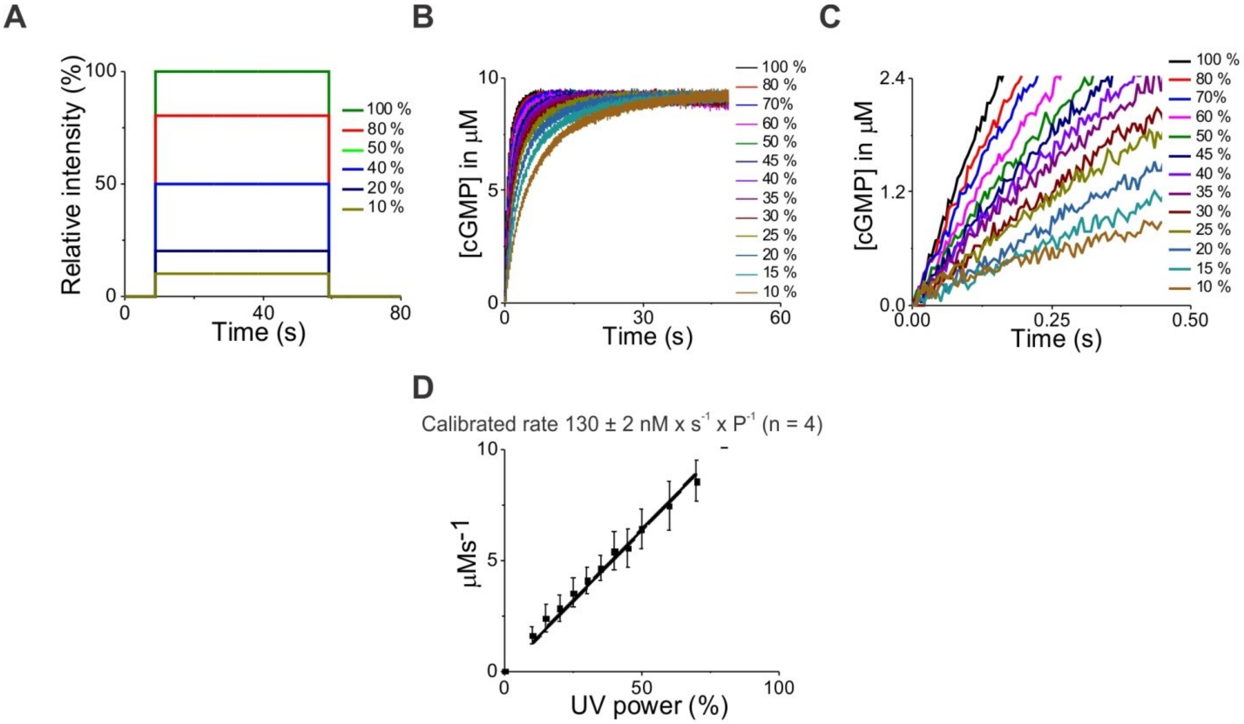

Figure 41. Calibration of cGMP release during uncaging. A. UV pulses with varying light levels used for calibration. **B.** Fluorescence recording from 10 µM cGMP suspension. The cage shows an increase in fluorescence upon uncaging. Light levels are shown on the right. (C) Plot showing the first 200 ms of the traces at which less than 10 % of the total amount have been released. Corresponding light levels are shown on the right. **D.** Plot showing the variation of cGMP release rate as a function of UV power level. The change in nM per second per power unit is calculated from the linear fit (n = 4). P denotes power level.

2.2.2. Single-molecule response

Next, I compared the amplitude of cGMP-evoked Ca^{2+} and voltage signals to those evoked by a single resact molecule. For a sperm suspension of 3×10^8 cell/ml, mixing with 0.5 pM of resact delivered on average one molecule of resact per sperm cell. Using the stopped-flow technique, I mixed sperm loaded with Fluo-4 AM and caged cGMP with 0.5 pM of resact. After the Ca^{2+} signal had recovered to resting levels, I used a 10 ms UV pulse to release the caged cGMP (Figure 42B). The UV power level was varied to obtain different cGMP levels (Figure 42A), whereby the response evoked by cGMP could be matched to Ca^{2+} response evoked by resact (Figure 42C). For instance, the amplitude of the Ca^{2+} response evoked by 5.1 nM cGMP matched the amplitude evoked by 0.5 pM resact (Figure 42D). I repeated this experiment with sperm from four different animals and I obtained a value of 6 ± 2 nM of cGMP per resact molecule per sperm. Assuming a flagellum volume of 1.6×10^{-15} liter, 1 nM of cGMP corresponds to 1 cGMP molecule. Thus, ca. 6 cGMP molecules are released in a single-molecule response. I repeated the same experimental procedure on BeRST-loaded sperm. Using the voltage calibration, I estimated a 2 mV change in membrane potential evoked by a single molecule of resact (Figure 42G). This value agrees with the reported 1 – 2 mV range for the single-molecule voltage response [121]. The superposition of single-molecule-evoked voltage response with an equivalent cGMP-evoked voltage signal (Figure 42G) revealed a slower rise time for the resact-evoked signal. This is due to the cGMP synthesis rate of a GC upon resact stimulation [9], which is slower than the release rate obtained by the 10 ms pulse.

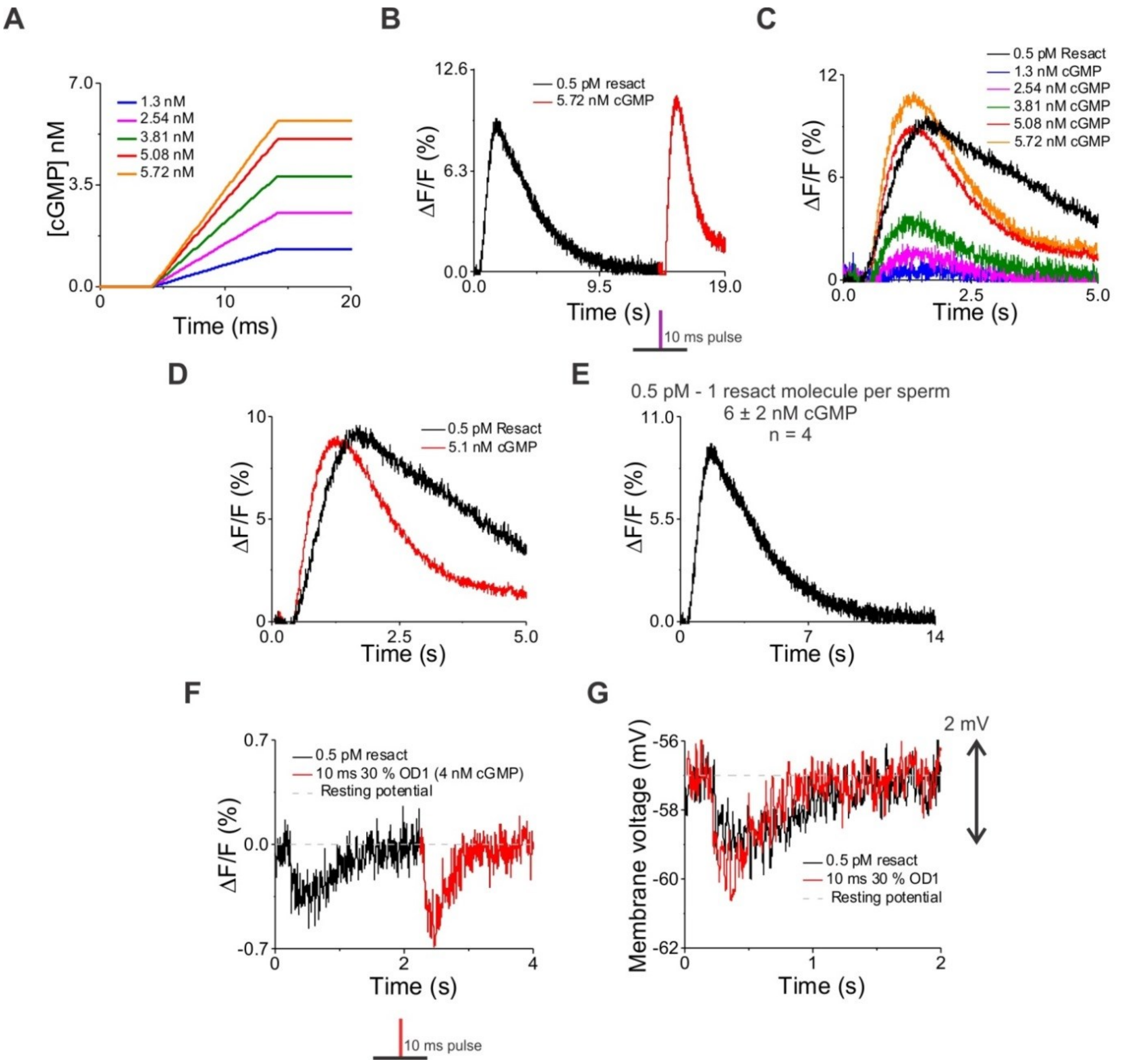

Figure 42. Single-molecule Ca^{2+} and voltage responses. **A.** Plot showing cumulative cGMP release for pulses with different light levels. The integrated [cGMP] is shown on the left of the plot. **B.** Single-molecule-evoked Ca^{2+} response (black) with cGMP-evoked Ca^{2+} response (red). Resact-evoked response (black) was allowed to recover before a 10 ms pulse was used to evoke another Ca^{2+} response (red). **C.** Overlay of Single-molecule-evoked Ca^{2+} response and cGMP-evoked responses. **D.** Plot showing an overlay of Ca^{2+} response by a single molecule of resact per sperm compared to the response evoked by 5.1 nM cGMP per sperm. (E) Representative single-molecule Ca^{2+} response. Average released [cGMP] released in a single-molecule response is shown on top as average ± SD (n = 4). **F.** Single-molecule-evoked voltage response (black) was allowed to recover to resting levels before a 10 ms pulse was used to evoke a second voltage response (red). (G) Superposition of single-molecule response and cGMP evoked response. The hyperpolarization amplitude is ca. 2 mV.

2.3. cGMP homeostasis during chemotaxis

The signaling events and molecules underlying resact stimulation include: 1) Binding of resact to GC, and triggering of cGMP synthesis. 2) Hyperpolarization evoked by the binding of cGMP to CNGK channels. 3) Recovery from hyperpolarization due to opening of HCN channels and PDE that breaks down cGMP. However, PDE regulation and cGMP dynamics during chemotaxis is not well characterized. Here, I tried to disentangle the role of the PDE from the HCN channel in order to obtain a better understanding for cGMP dynamics.

2.3.1. HCN and PDE role in recovery from hyperpolarization

I used a strong stimulation equivalent to 130 cGMP molecules and a weak stimulation equivalent to 13 cGMP molecules to induce hyperpolarization in sperm loaded with BeRST and caged cGMP (Figure 43A). The strong stimulation produced a hyperpolarization, which returned to resting levels in 90 ms. The weaker stimulation resulted in a hyperpolarization that recovered in 240 ms. These results suggests that HCN channel opening determines the recovery from hyperpolarization, because at large negative V_m values, HCN channels have a high opening probability [5]. Nevertheless, PDE activity might still contribute to the recovery by hydrolyzing cGMP, which leads to the dissociation of cGMP from CNGK channels and, thereby, closure of the channels. To analyze the contribution of PDE-dependent hydrolysis of cGMP to the recovery from hyperpolarization, I compared sperm loaded with either caged cGMP or caged 8-Bromoguanosine-cGMP (8-bromo-cGMP) - a non-hydrolysable analogue of cGMP (Figure 43B). The recovery from hyperpolarization was similar for both 8-bromo-cGMP and cGMP, suggesting that PDE-dependent hydrolysis does not play a role in the initial recovery. However, the depolarization beyond the resting levels is more prominent for the cGMP- compared to 8-bromo-cGMP-dependent response. The HCN open probability decreases towards more positive membrane potential, suggesting that PDE activity might regulate the membrane potential at a later stage of the response: HCN channels open first, and then PDE-dependent cGMP hydrolysis occurs, which triggers the dissociation of cGMP molecules from the CNGK channel resulting in further depolarization.

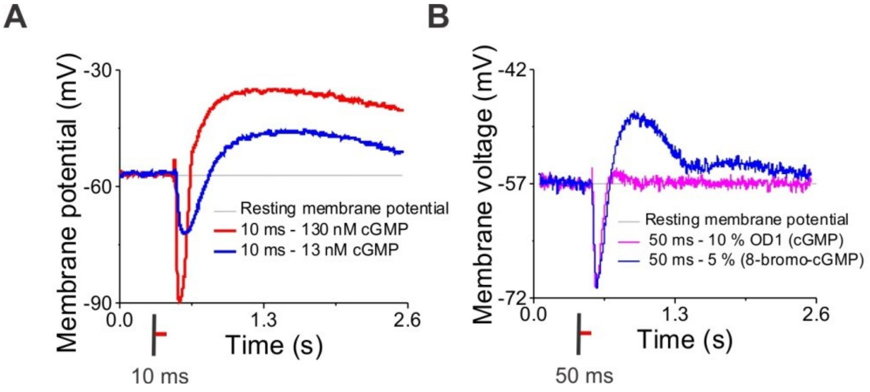

Figure 43. Recovery from hyperpolarization. A. cGMP-evoked responses evoked by 10 ms pulses. The voltage signal shown in red is evoked by 10 fold more cGMP molecules than the voltage signal shown in blue. Schematic of used UV pulse is shown on bottom of plot. **B.** cGMP- (blue) and 8-bromo-cGMP-evoked (magenta) voltage responses. Schematic of used UV pulse is shown on bottom of plot.

2.3.2. In vivo assay for monitoring cGMP regulation through CNGK activity

To disentangle the contribution of PDEs and HCN channels, we designed an *in vivo* assay to monitor CNGK channel activity in sperm uncontaminated by HCN activity. At 100 mM extracellular K^+ (K^+-fortified ASW), the reversal potential of K^+-selective channel at -36 mV is more positive than the resting voltage at -57 mV. Therefore, activating CNGK channel by cGMP would produce a depolarization rather than hyperpolarization, during which the HCN channel opening probability and electrochemical driving force are lowered [5]. Sperm were loaded with caged cGMP in normal ASW ($[K^+]_o$ at 9 mM) and rapidly mixed with medium containing 191 mM K^+ which resulted in a 100 mM K^+ in the cuvette. A short 10 ms UV pulse resulted in a rapid depolarization (Figure 44A red curve) compared to a rapid hyperpolarization in normal ASW (Figure 44A blue curve). Whereas the rise time of the depolarization and hyperpolarization were identical (Figure 44B), the recovery to resting levels from depolarization was much slower than from hyperpolarization. The maximal cGMP-evoked depolarization in K^+-fortified ASW is -36 ± 7 mV (n = 4), which is consistent with the reversal potential of CNGK. HCN channels are closed at membrane potential that are more positive than - 40 mV [5]. Additionally, at high extracellular K^+ levels, changes in pH and Ca^{2+} are abolished [6]. Thus, the depolarization evoked in this assay seems to be mainly due to opening of CNGK channel. The question now arises: Do PDEs control the recovery from depolarization when HCN channels are closed, and can we monitor cGMP hydrolysis by measuring CNGK activity?

To answer this question, I loaded sperm with either caged cGMP or caged 8-bromo-cGMP in combination with the PDE inhibitor IBMX. The recovery rate was slower for caged-cGMP in the presence of IBMX (Figure 44C blue and red) while the recovery was completely abolished for caged 8-bromo-cGMP (Figure 44C black), demonstrating that cGMP hydrolysis by PDEs is responsible for the decay after depolarization to resting levels. The decay provides kinetic information of two processes: cGMP dissociation from CNGK channel and a cGMP hydrolysis by the PDE. However, the rate limiting step, among the two processes, still needs to be unraveled.

Next, I explored how sperm respond to different caged cGMP release rates over a set of different pulse durations, ranging from 10 ms up to 4 s (Figure 44E). Of note, all pulses resulted in the same cumulative cGMP release of ca. 130 nM. All the observed voltage signals could be characterized by three phases. The first phase was characterized by the rise time, followed by a steady-state second phase, and a third phase during which voltage recovered to resting levels. The third phase started after the pulse was turned off (Figure 44F). Both hyperpolarization and depolarization are essential to evoke a Ca^{2+} signal, therefore, the voltage steady-state shown in this experiment for pulses longer than 1 second suggests that sperm attain equilibrium between cGMP release and hydrolysis that keep the CNGK channels constantly opened. This phase can be associated with adaptation [122]. The rapid recovery to resting levels once the cGMP is fully released indicates that sperm can respond to a decrease of cGMP levels. The ability of sperm to respond to a decrease of cGMP or resact stimulation was first reported in [123], where it was termed the *off* response. I verified this *off* response using cGMP-evoked Ca^{2+} and voltage responses. The typical *on* response produced by the 10 ms pulse was characterized by a rapid hyperpolarization that was followed by Ca^{2+} influx (Figure 44G), whereas the *off* response was observed when a 2 s UV pulse was used. The start of the 2 s UV pulse evoked a rapid hyperpolarization followed by a small Ca^{2+} influx and depolarization to below resting levels that was maintained at a steady-state until the pulse was stopped. When photolysis ceased at the end of the UV rectangular pulse, sperm produced a large second depolarization, which was followed by a larger Ca^{2+} signal. Our observation that cGMP hydrolysis is responsible for depolarizing the sperm beyond resting levels (Figure 43B) and the rapid recovery from depolarization, observed once the cGMP release has been ceased (Figure 44F), suggest that the PDE activity allow sperm to sense a decrease in cGMP level, which results in an *off* response (Figure 44H).

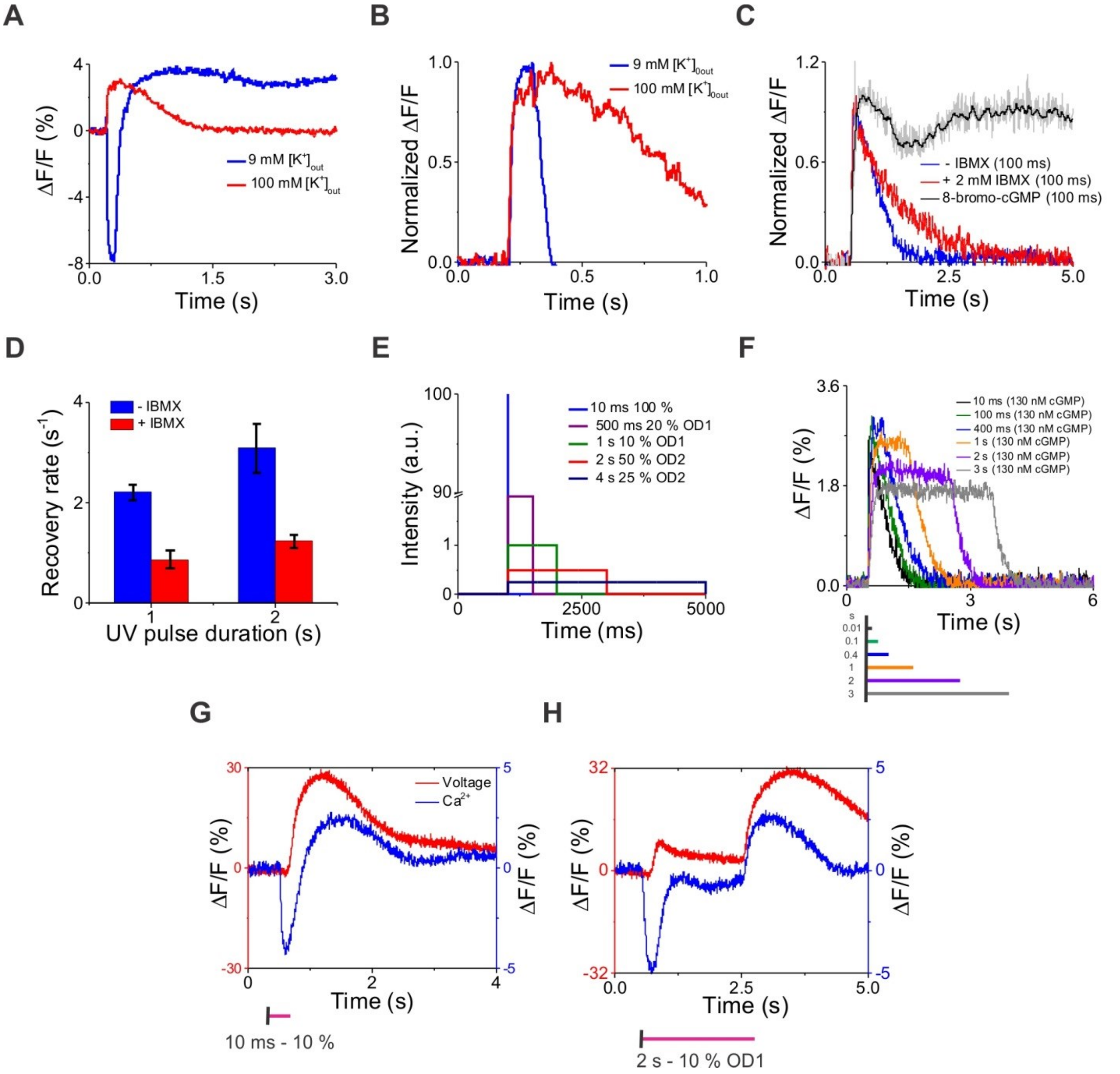

Figure 44. Kinetics of the cGMP hydrolysis by the PDE. A. cGMP-evoked voltage responses recorded with BeRST voltage-sensitive dye. Maximum response was achieved with a 10 ms pulse at 100% in either normal ASW (blue signal) or K^+-fortified ASW (red). **B.** Superposition of the rise phase during hyperpolarization and depolarization signals from (A). Both signals were normalized to unity. **C.** cGMP evoked voltage response in K^+-fortified ASW in presence (red) and absence (blue) of 2 mM IBMX, in addition to the 8-bromo-cGMP evoked responses (black). **D.** Average recovery time from depolarization for 1 s and 2 s pulses in the presence and absence of 2 mM IBMX. The recovery phase was fitted with a single exponential to estimate the decay rate. Data is presented as average ± SD (n = 3). **E.** UV protocols used for the integration experiment. The integrated intensity or cumulative cGMP

concentration is the same in all pulses. **F.** cGMP evoked response in K$^+$-fortified ASW, obtained using the UV protocols shown in (E). Schematic of UV pulses are shown on bottom of plot. **G.** Multiplexed Ca^{2+} and voltage cGMP-evoked responses with a 10 ms pulse. Schematic of UV pulses are shown on bottom of plot. **H.** Multiplexed Ca^{2+} and voltage *on* and *off* responses evoked with 2 s pulse. Schematic of UV pulses are shown on bottom of plot.

2.3.3. Integration is limited by cGMP hydrolysis

Here, I studied how cGMP hydrolysis sets a limit on sperm's ability to integrate individual responses within a duration longer than 300 ms - the GC inactivation time [124]. First, I verified integration of cGMP-evoked responses within duration of less than 200 ms. I accomplished this by measuring voltage and Ca^{2+} signals upon stimulation with UV pulse that range in lengths between 5 ms and 150 ms. All pulses resulted in the same cumulative cGMP release (Figure 45A). The resulting voltage signals had the same amplitude, suggesting that the sperm integrated the cGMP molecules that were released over the 150 ms duration and produced a summed response (Figure 45B). Also the amplitudes of the Ca^{2+} signals were similar (Figure 45C). Because the Ca^{2+} signal is directly associated with a motility response [6], my data suggest that sperm are able to sample the surrounding for up to ca. 200 ms before producing a Ca^{2+} response that controls its trajectory. The latency of the resact-evoked Ca^{2+} response is up to 500 ms, therefore, the integration time could be even longer.

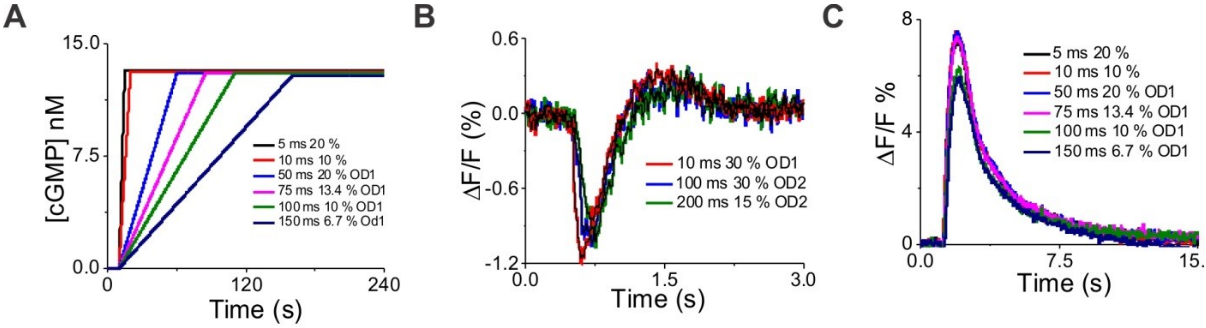

Figure 45. Integration of cGMP molecules in sperm. A. Cumulative caged cGMP release using UV pulses that have different lengths and same integrated intensity. **B.** Voltage signals evoked by three pulses: 10 ms (red), 100 ms (blue), and 200 ms (green). **C.** Ca^{2+} signals evoked by different UV pulses with width ranging from 5 ms to 150 ms. Signals are color coded according to the used UV pulse width and power level.

To investigate how cGMP hydrolysis sets a limit on integration, I applied pulses with length between 10 ms and 500 ms that have the same integrated intensity. I hypothesized that sperm would only respond if the cGMP release rate is higher than the PDE hydrolysis rate. To test this hypothesis, I measured voltage signals in normal $[K^+]_o$ levels with a cGMP release rate of 6.5 nM per second to test if sperm can still integrate the responses. Sperm integrated the signal up to 200 ms, but it dropped significantly at 500 ms when the cGMP release was 6.5 nM per second (60% OD3) (Figure 46A). However, when I increased the rate by two fold to 13 nM per second with a 500 ms pulse (12% OD2), I observed a hyperpolarization amplitude matching the result from the 10 ms pulse (Figure 46B). Similar results were obtained for the Ca^{2+} response (Figure 46C). This experiment suggests that the rate of cGMP hydrolysis by the PDE sets the limit on the ability of the sperm to integrate responses beyond the GC inactivation time.

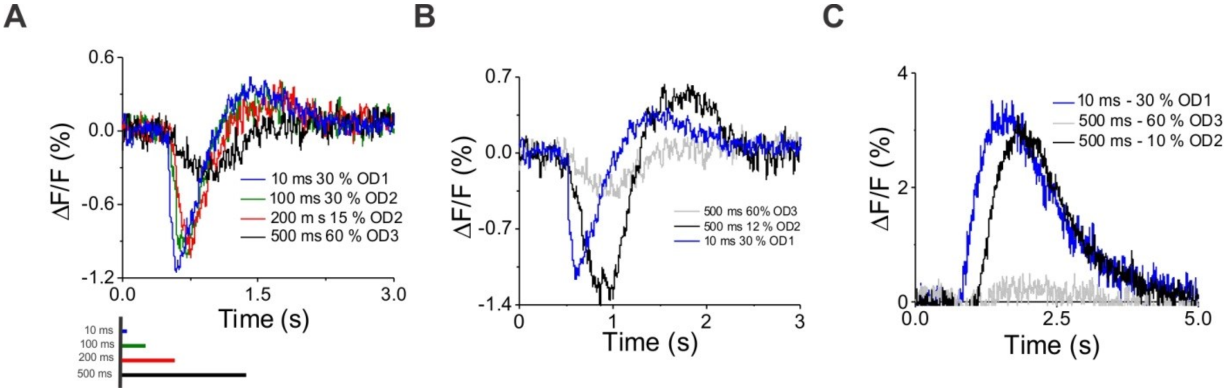

Figure 46. cGMP hydrolysis rate. A. cGMP-evoked voltage responses obtained in ASW with different pulses that resulted in the same cumulative cGMP concentration. **B.** cGMP-evoked voltage responses in ASW using the following pulses: 10 ms resulting in 6.5 cGMP/s (blue), 500 ms resulting in 6.5 nM/s (gray), and 500 ms resulting in 13 nM/s (black). **C.** Ca^{2+} signals evoked by the following pulses: 10 ms resulting in 6.5 cGMP/s (blue), 500 ms resulting in 6.5 nM/s (gray), and 500 ms resulting in 13 nM/s (black).

2.4. Sperm respond to periodic stimulation

A quantitative theory of chemotactic steering by [125] describes navigation along periodic paths: a cellular signaling system transforms the periodic stimulation (chemoattractant binding) into a periodic intracellular signal (Ca^{2+} bursts) that, in turn, modulates the swimming path curvature. In a chemical gradient, sperm are periodically stimulated with the angular frequency of its 2D circular swimming path of ca. 1 Hz [126]. I emulated this periodic stimulation by a sinusoidal periodic UV waveform of the form $(\sin(2\pi f t) + k)$ where f is the frequency and k is a constant (Figure 47A red), which resulted in a cumulative [cGMP] that change with time (G (t)) of the form $\left[\int\left(\sin\left((2\pi f t)\right) + k\right)\right]$ (Figure 47A blue). To explore if sperm encode such a periodic stimulation in their voltage and Ca^{2+} response, sperm loaded with Fluo-4 AM, BeRST, and caged cGMP were used. Interestingly, Voltage V_m (t) did not follow the cumulative cGMP increase (which is a cosine function + a ramp) (Figure 47B), but rather the first derivative of G (t) (Figure 47C). Therefore, V_m was proportional to $\frac{dG(t)}{dt} \propto sin(2\pi f t)$ rather than $\int\left(\sin\left((2\pi f t)\right) + k\right)$. The UV sinusoidal waveform triggered a $[Ca^{2+}]_i$ sinusoidal signal C (t) which was phase-locked to the first derivative of G (t) or V_m (t) with a phase shift φ (Figure 47D-E). Therefore, C (t) was proportional to $sin(2\pi f t + \varphi)$. I tested UV waveforms varying from 0.3 Hz up to 5 Hz and applied a Fourier transform to detect the Ca^{2+} and voltage frequency response in sperm. Fourier amplitude (FA) of Ca^{2+} and voltage signals showed that sperm are able to follow changes as fast as 5 Hz (Figure 47F-G).

Two signaling components are responsible for the fast rise and drop in Ca^{2+} , CatSper channel and NCKX. Upon stimulation, the Ca^{2+} influx is evoked by a transient hyperpolarization; during recovery from the hyperpolarizing peak which is initiated by HCN, CatSper channels open and Ca^{2+} enters the cell. The subsequent stimulation hyperpolarizes the cell membrane thereby closing CatSper channels. A shift to more negative membrane potentials caused by the hyperpolarization increases the activity of NCKX and Ca^{2+} is rapidly extruded out of the cell, thereby clearing $[Ca^{2+}]_i$ and preparing the cell for the second stimulus. The alternating activation/deactivation in CatSper and modulation in NCKX activity allows the sperm to encode a periodic stimulus and produce Ca^{2+} oscillation.

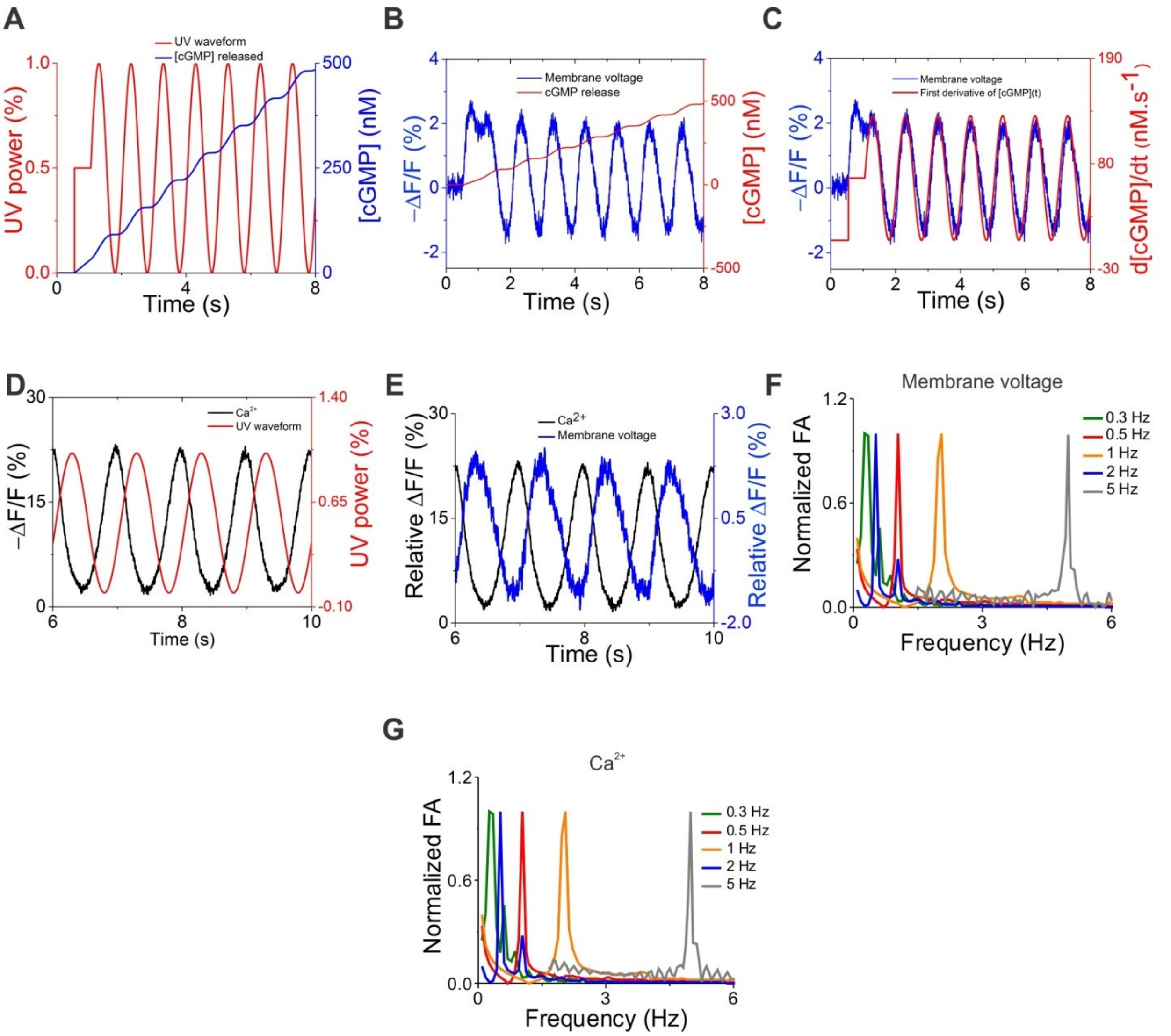

Figure 47. Sperm responds to periodic stimulus. **A.** Plot showing UV LED waveform (red) and cumulative cGMP release expected inside sperm (blue). **B.** Voltage oscillations (blue) in response to the cGMP cumulative release (red). **C.** Voltage oscillations (blue) superimposed with the first derivative of the cGMP cumulative release (red). **D.** Ca^{2+} oscillations (black) in response to the first derivative of the cGMP cumulative release (red). **E.** Multiplexed voltage and Ca^{2+} oscillations in response to the periodic UV waveform from (A). **F.** Fourier amplitude (FA) plots where the frequency at the peak represent the frequency at which voltage signals oscillated in response to sinusoidal UV pulses with frequency varying between 0.3 and 5 Hz. **G.** FA plots showing the frequency at which Ca^{2+} signals oscillated in response to sinusoidal UV pulses with frequency varying between 0.3 and 5 Hz. Voltage signal was multiplied with -1.

3. Supra-molecular arrangement of the chemotactic receptor in sea urchin sperm

Sensory receptors in eukaryotic and prokaryotic cells often form highly organized supramolecular complexes. For instance, chemoreceptors in bacteria are organized together with other signaling components into a hexagonal array [57]. The visual pigment rhodopsin is organized in densely packed rows of dimers located in the disk membrane of mammalian photoreceptors [20]. Finally, CatSper, the sperm Ca^{2+} channel, forms a quadrilateral arrangement along the flagellum of mouse [34] and human sperm (Chapter 4), [33] that organizes structurally distinct Ca^{2+} signaling domains. However, the supra-molecular architecture of chemoattractant receptor GC in sea urchin sperm is not known. The sea urchin sperm flagellum is ca. 250 nm in diameter, making it difficult to obtain supra-molecular arrangement of flagellar proteins using diffraction-limited optical microscopy, which is why I applied STORM to resolve the structure (Chapter 1).

3.1. STORM imaging using antibodies

I first tested the antibodies that are available against key components of the sea urchin signaling cascade, the chemoreceptor GC and the CatSper channel (Figure 48A). I used a primary antibody against the respective proteins and a secondary antibody conjugated to a fluorophore. The antibody against GC displayed a specific staining in the flagellum and some unspecific staining in the head that might result from the secondary antibody (Figure 48B-C). The antibody against CatSper did not show any specific labeling (Figure 48D), which could be due to the low copy number of the protein in sea urchin sperm. Thus, I proceeded with the antibody against the GC for STORM analysis.

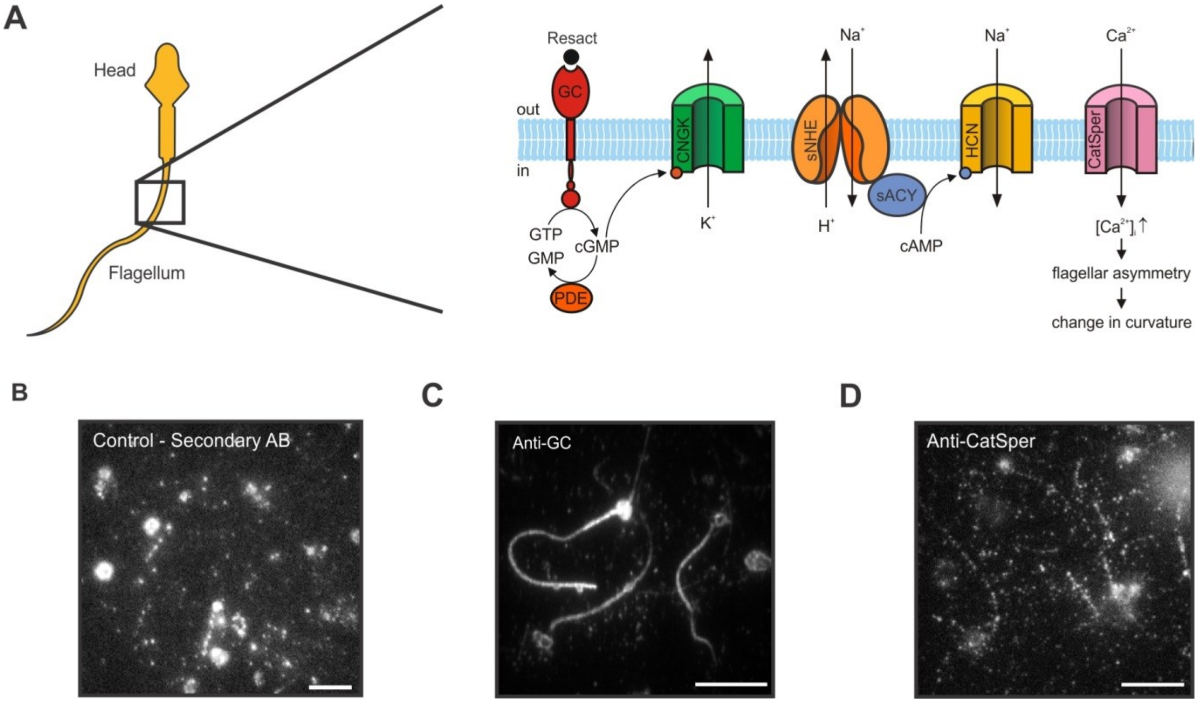

Figure 48. Localization of key proteins controlling sea urchin sperm chemotaxis. A. Chemotactic signaling pathway in sea urchin sperm. Resact, the chemoattractant peptide, binds to receptor GC on sperm flagella (See Figure 38). Figure modified from [6]. **B.** Fluorescence image of sperm after immunocytochemistry using a fluorescently-labeled secondary antibody as control. **C.** Fluorescence image of sperm after immunocytochemistry using a fluorescently-labeled secondary antibody and an antibody against GC. **D.** Fluorescence image of sperm after immunocytochemistry using a fluorescently-labeled secondary antibody and an antibody against CatSper. Scale bar: 20 µm.

The overlay of STORM image of the GC-labeled sperm with an epifluorescence image reveal the enhancement in resolution (Figure 49A). Plotting an intensity profile across the flagellum for both images at the same position revealed one large peak for epifluorescence and two smaller and distant peaks for STORM. The 3D cross-section of the sperm flagellum showed high localization density around a virtual cylinder with almost no molecules in the center, demonstrating that the GC is localized in the plasma membrane (Figure 49B). However, when zooming into one part of the flagellum, no distinctive structural organization of the GC was observed (Figure 49C). To investigate the supramolecular structure in more detail, I obtained an average cross-sectional density profile from a 5 µm section of the flagellum (Figure 49D). The peaks in the plot correspond to clusters of localizations, and the measured width of these peaks was close to the structural resolution that can be obtained by STORM (40-80 nm). Resolution was estimated by Fourier Ring Correlation (FRC) (Figure 49E) to be ca. 45 nm. The experimental localization precision was estimated using tracing of single molecules, (see methods) and it was ca. 15 nm (Figure 49F).

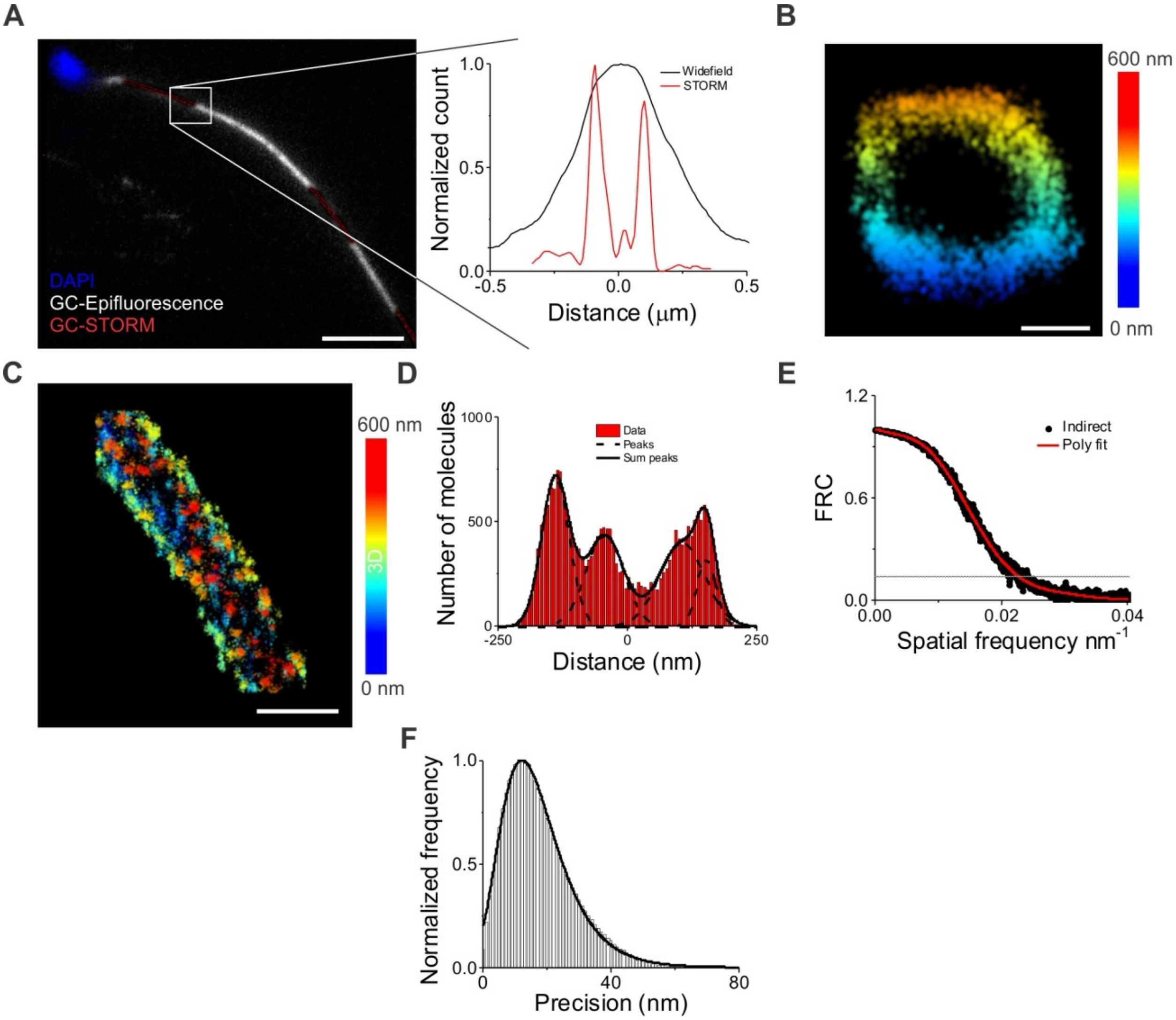

Figure 49. STORM imaging of sea urchin sperm. A. Overlay of STORM image in red and epifluorescence image in grayscale obtained using GC antibody and Alexa-647 conjugated secondary antibody. DAPI is shown in blue. Plot on the right shows intensity profile across the boxed region in both imaging modalities. Scale bar 10 µm. **B.** Axial cross-section of sperm flagellum color coded for depth. Depth color code is shown on the right. Scale bar 0.1 µm. **C.** Zoomed-in section of the flagellum. Scale bar 0.5 µm. Depth color code is shown on the right. **D.** Average profile of the STORM image in (C) obtained by plotting molecule distribution on a line that is perpendicular to the sperm (see tracing sperm

flagella in methods). **E.** FRC resolution of STORM image in (C). **F.** Experimental localization precision obtained by tracing single molecules within the dataset (see methods).

Antibodies are a powerful tool for protein labeling because of its high binding affinity and specificity. However, antibody size can add an offset of 10 nm when using direct labeling of the primary antibody or 15-20 nm when using a combination of primary and secondary antibodies [127]. This does not create major problems when using diffraction-limited imaging, but with STORM characterized by a 10-15 nm localization precision, the antibody size becomes a problem (Chapter 1).

3.2. Photoaffinity-labeling of the chemoreceptor

To allow direct labeling of the GC and, thereby, reduce the offset between the fluorescent dye and the GC, I developed a new strategy based on a modified resact that can be directly labeled with a fluorophore. Resact features a picomolar affinity to the chemoreceptor and it has a size of less than 0.5 nm compared to 10-20 nm for antibodies. I relied on photo-crosslinking to covalently couple resact to the receptor. Photo-crosslinking allows a light controlled reaction between the desired receptor protein and a ligand that has a diazarine group. Therefore, two modifications were applied to the natural resact: First, diazarine photoaffinity label was added to allow photo-crosslinking of resact to the receptor. (Figure 50B). Second, two alkyne groups were added to the N-terminus and C-terminus of the peptide (Figure 50B) to allow tagging the peptide with a fluorophore using click chemistry [128]. We added two alkyne groups to increase the chances that the reactive group is still accessible by the fluorophore after the peptide has bound to the chemoreceptor. I refer to this modified analogue of resact as photoresact.

To characterize photoresact in detail, I addressed the following questions:

1. Is photoresact active? Is the affinity compromised by the modification?
2. How long do I need to expose the sample to UV light to obtain a high crosslinking yield?
3. Is click chemistry efficient in ASW at pH of 7.8? Which dye can be used?
4. Is the labeling specific? Are we labeling the GC?

.

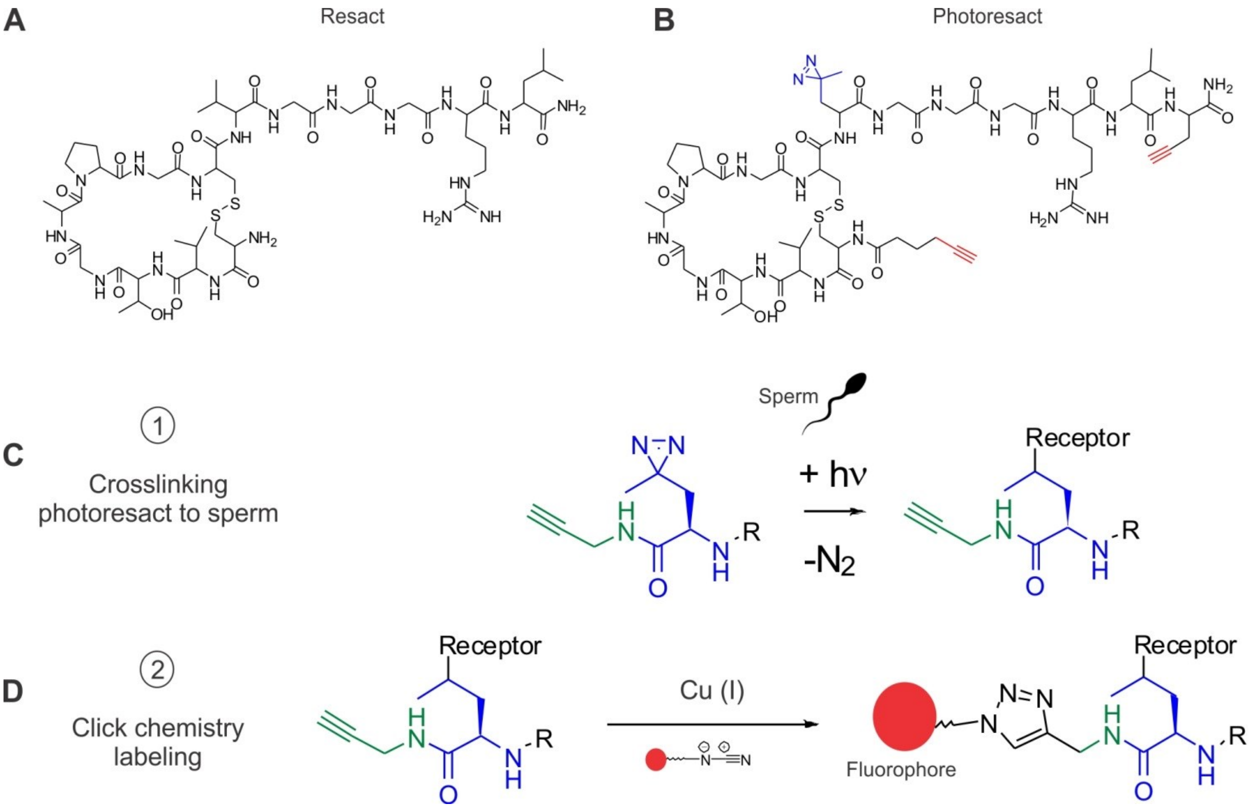

Figure 50. Resact as a photo-affinity label for imaging. A. Resact structure. **B.** Photoresact structure. Resact has been modified with a diazarine in blue and two alkyne groups in red. **C.** Photo-crosslinking. The photoaffinity label is crosslinked to sperm upon UV illumination. The end product consists of the resact receptor and the alkyne group. **D.** Overview of click chemistry labeling: The receptor with alkyne group in the presence of a fluorophore that has azide group reacts in the presence of Cu (I) as a catalyst to produce a complex containing the desired receptor, labeled with the fluorophore.

To measure the affinity of photoresact for the chemoreceptor, I used the kinetic stopped-flow technique. Sperm were loaded with Fluo-4 AM, and the evoked Ca^{2+} signals were recorded at varying photoresact concentration (Figure 51A-B). The dose-response relation was plotted and fitted using a logistic function (Originlab). Photoresact had $EC_{50} = 22.7 \pm 6.4\,pM$ (n = 3) compared to resact with $EC_{50} = 5 \pm 2\,pM$ (n = 2) (Figure 51C), demonstrating that photoresact still has a very high affinity.

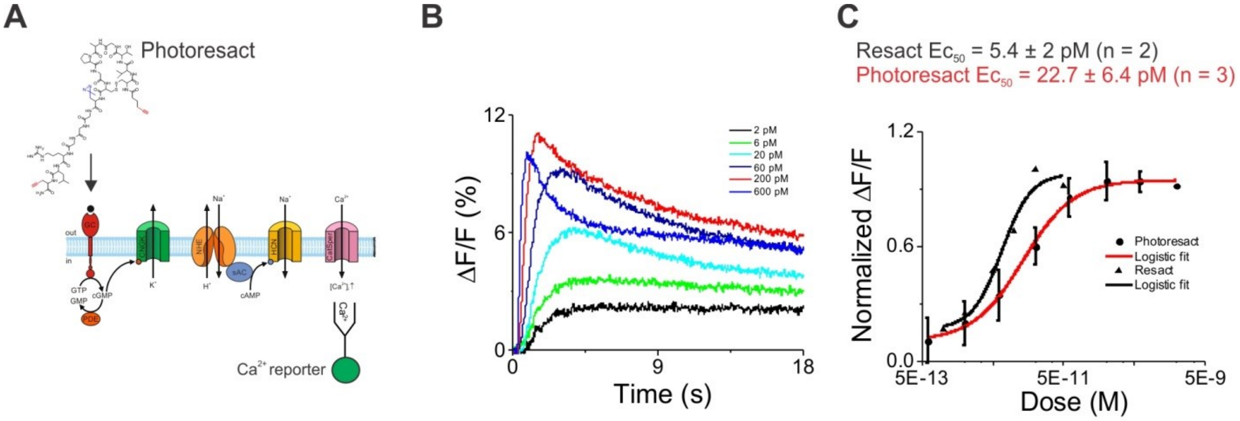

Figure 51. Photoresact activity in sperm. A. Schematic presentation of the assay used to verify photoresact activity. Photoresact is mixed with sperm and the Ca^{2+} influx is reported using a Fluo-4 AM. **B.** Stopped-flow recordings of Ca^{2+} signals with increasing photoresact concentration. **C.** Dose-response relationship of photoresact compared to resact, derived from stopped-flow experiments. Photoresact : $EC_{50} = 22.7 \pm 6.4\, pM$ (n = 3), resact: $EC_{50} = 5 \pm 2\, pM$ (n = 2).

To test the photoaffinity label, I used a 360 nm UV source to illuminate a sample containing 100 µM of photoresact in distilled water for 30 sec after which almost complete conversion was observed. The sample was analyzed by liquid-chromatography-mass spectrometry (LC-MS). Theoretically, two products can result from irradiation. The first is a result of an elimination reaction (Figure 52A green) and the second is a highly reactive carbine that reacts with water and nearby proteins (Figure 52A red). In the chromatogram, one peak was observed in the control sample, corresponding to the presence of only photoresact, whereas two new peaks appeared in the irradiated sample (Figure 52B). These two peaks were assigned with the expected products according to the masses determined by spectrometry (Figure 52B), using the following formula:

$$Exact\ mass = 2 \times observed\ mass - \ mass\ (\ 2H^{+}) \qquad (V.2)$$

The peaks are color coded to match the chemical structures in Figure 52A,C. Integration of the peaks gave us an estimate of 40 % for the reactive product and 60 % for the eliminated product (Figure 52C).

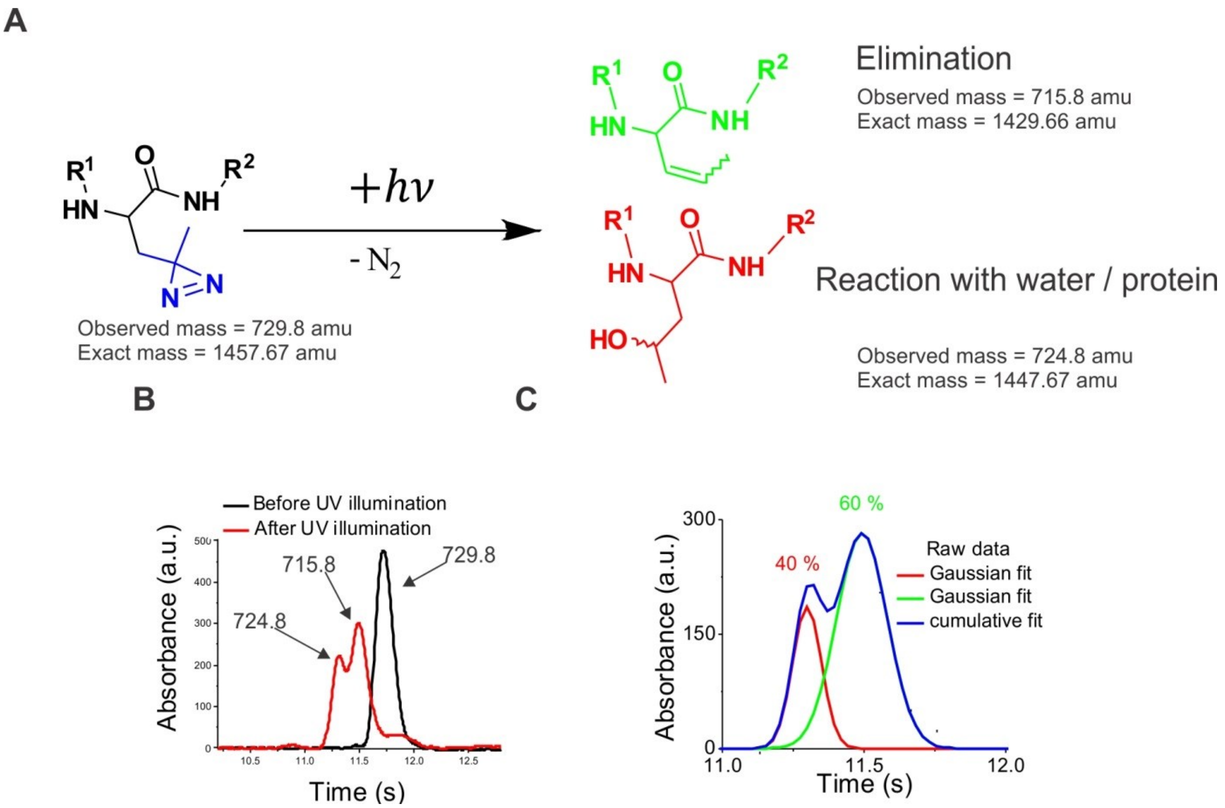

Figure 52. Verification of photo-crosslinking using LC-MS. A. Structure representing photoresact before illumination. The calculated mass obtained in LC-MS is related to exact mass by the formula in equation V.2. Photoresact was illuminated for 30 seconds and then analyzed in LC-MS along with a non-illuminated control sample. Structures on the right represent the derived fractions. Structure in green is one that underwent the elimination reaction, while the structure in red is the one that reacted with water. **B.** Absorption profile of the elution showing one peak for the control that was not illuminated and two peaks for the sample that was illuminated. The peaks were correlated with the structures in (A) using the calculated masses obtained in LC-MS. **C.** Double peak fit of the absorption profiles in (B) which gave an estimate of 40 % for the reactive product and 60 % for the eliminated product.

Click chemistry can be monitored and tested using 3-azidocoumarin. 3-azido-coumarin is initially weakly fluorescent and becomes brighter after click chemistry due to the formation of 1,2,3-triazole (Figure 53A). Photoresact was added to the click solution containing 3-azidocoumarin and Cu (I) as a catalyst and the fluorescence was recorded over time in a cuvette using fluorescence spectrometer. The emission intensity increased over time after the addition of the catalyst (Figure 53A). Thirty minutes were chosen for the click reaction with sperm based on this experiment. Increasing the Cu (I) concentration from 0.5 mM to 4 mM did not increase the efficiency of the reaction significantly (Figure 53B).

Choosing the optimal dye for fluorescence microscopy is very important, because water-soluble organic fluorophores are known to interact with lipid bilayers, resulting in unspecific labeling [129]. In addition, the dye's photophysics has to meet conditions for STORM imaging. Based on a recent study [129], we chose Dyomics-654 (Dy654) for testing. The dye is bright and performed very well in STORM imaging [98]. Intact sperm were incubated with 1 µM of either Dy654 or Cyanine-5 (Cy5), which is known to bind to membranes. Subsequently, sperm were washed extensively with ASW. After incubation and washing, the sperm pellet at the bottom of an Eppendorf tube was clearly labeled with Cy5, whereas no labeling was observed for Dy654 (Figure 53C). This was also confirmed by imaging (Figure 53D-E). Therefore, Dy654 was chosen to be used for the click reaction due to its low unspecific labeling.

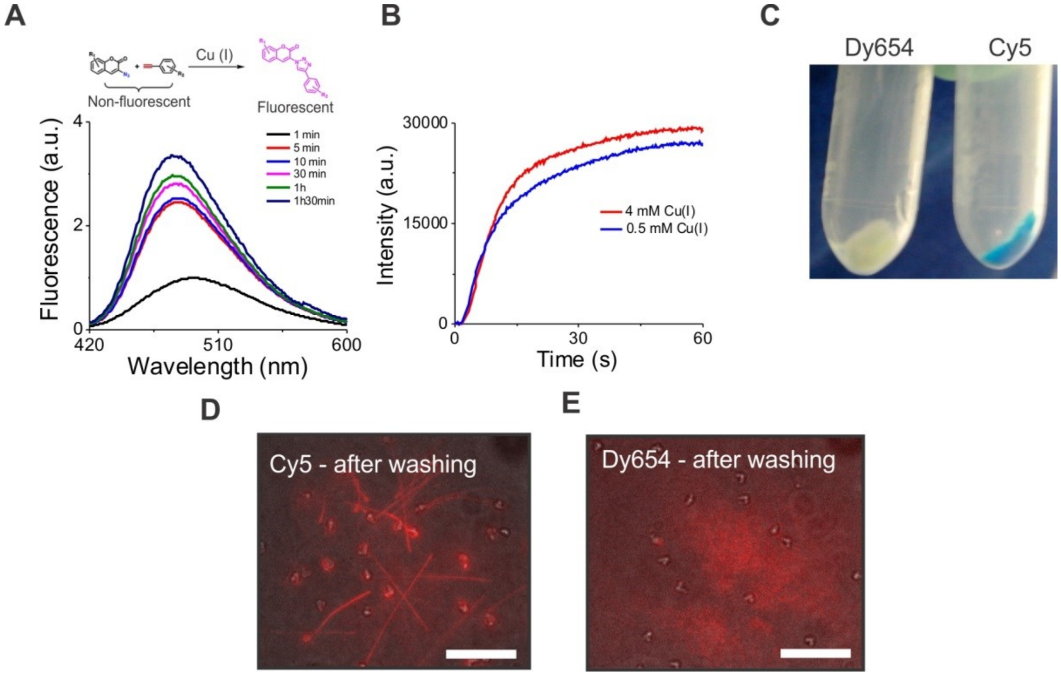

Figure 53. Verifying click chemistry and choice of dye. A. Top structures show azido-coumarin as a nonfluorescent molecule, which becomes fluorescent upon the formation of the triazole moiety. Bottom plots show the change in fluorescence with time upon the addition of Cu (I) to photoresact and azido-coumarin. **B.** Time traces obtained in a plate reader of photoresact and azido-coumarin in presence of two different Cu (I) concentrations. **C.** Pellet of sperm that were incubated with either Dy654 or Cy5. Pellet of sperm that was labeled with Cy5 is clearly labeled, whereas no labeling was observed for Dy654 **D.**

Fluorescence image of sperm that were washed after incubation with 1 μM Cy5. **E.** Fluorescence image of sperm that were washed after incubation with 1 μM Dy654. Scale bar 20 μm.

The next question that I tried to address is, whether the GC is specifically labeled by this approach. To this end, I used in-gel fluorescence and immunoblotting to explore the identity of the labeled protein. The sperm sample was incubated with photoresact and irradiated with UV light for crosslinking. After washing, the sample was resuspended in the click solution containing azido-Dy654 (Dy654-N_3) for 30 minutes. The resulting sample was reduced, denatured in SDS loading buffer, and loaded on an acrylamide gel. The resulting Western blot was labeled with an antibody against GC and a secondary antibody conjugated to a fluorophore that can be spectrally separated from Dy654 (Figure 54A). If both would label the same protein, the photoresact complex that is clicked to Dy654 should appear at the same height as the GC after antibody labeling (Figure 54B). Whereas, the band from the antibody labeling appeared at the expected height of 135 kDa, the photoresact-labeled protein (photoresact band) appeared at a height slightly above 63 kDa (Figure 54C), which was absent in the negative control lacking the catalyst Cu (I) in the click reaction. I repeated the experiment with a photoresact concentration ranging from 100 pM up to 10 μM. The photoresact band intensity increased with concentration, and it was detectable starting from 10 nM (Figure 54D).

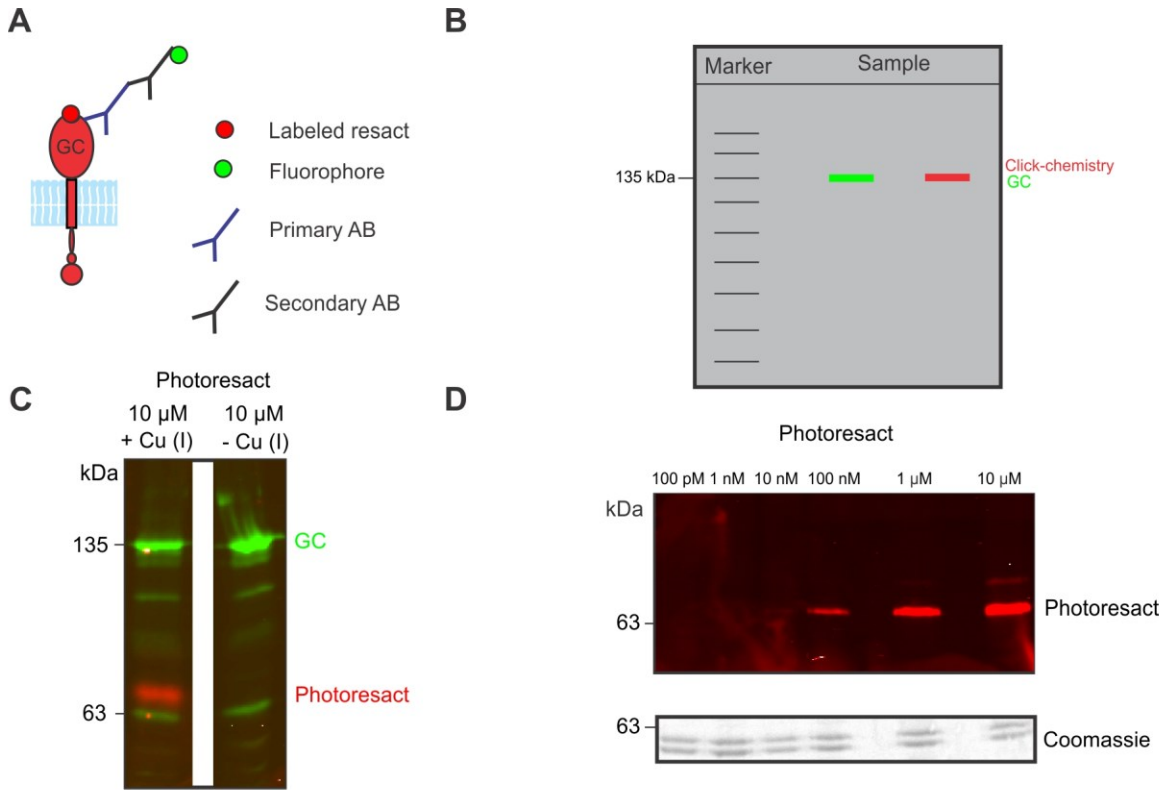

Figure 54. Revealing the identity of the resact receptor. A. Schematic overview of the labeling assay. The GC is supposed to be targeted with both, an antibody and photoresact using two spectrally distinct fluorophores. **B.** Western blot analysis shows both fluorophores and an overlapping signal indicates that the GC is labeled by both, the antibody and photoresact. **C.** Western blot of sperm labeled with photoresact (red) and antibody against GC (green). GC appeared at ca. 135 kDa, while the photoresact-coupled protein appeared at ca. 63 kDa. As a negative control, Cu (I) was omitted from the experiment. **D.** In-gel fluorescence of sperm that was labeled with varying concentration of photoresact. Bottom figure shows Coomassie staining as a loading control.

To verify the specificity of the approach, I used a non-related compound AR-451 as a negative control. This compound can be photo-crosslinked to proteins using a diazarine group and also clicked to Dy654-N_3 via its alkyne group (Figure 55A). Western blot analysis revealed that the “photoresact band” was only visible with photoresact and not AR-451 after photo-crosslinking (Figure 55B). In addition, I performed a competition experiment, where a constant photoresact concentration was competed with an increasing resact concentration. Western blot analysis showed that the photoresact labeling of the 63 kDa band could be competed using resact in a dose-dependent manner (Figure 55C), indicating that photoresact binding is specific. Furthermore, when I replaced intact sperm with frozen sperm, in-gel fluorescence showed that the "photoresact band" was still present. In addition, more bands appeared at molecular weight lower than 63 kDa, because the membrane integrity of frozen sperm is lost. This experiment suggests that binding of photoresact can occur in dead sperm. Competition experiment showed that only the band at 63 kDa was competed, while the other "nonspecific bands" remained, suggesting that the band at 63 kDa is specific while the other bands are not (Figure 55D).

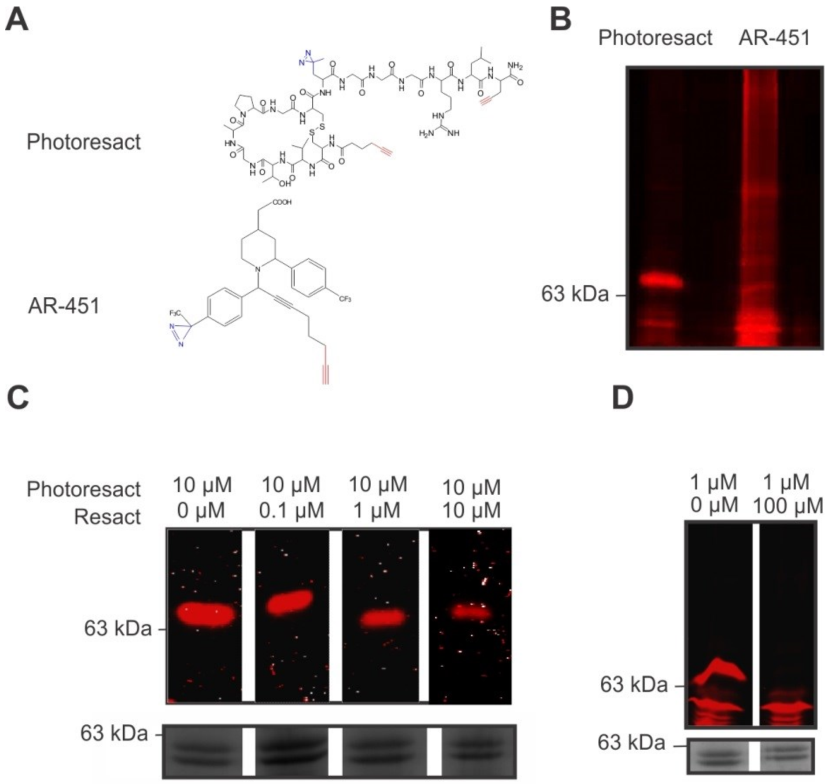

Figure 55. Testing the specificity of photoresact. A. Photoresact structure with diazarine in blue and alkyne groups in red compared to non-related AR-451 compound containing diazarine and alkyne groups. **B.** In-gel fluorescence of sperm labeled with either photoresact or AR-451. **C.** In-gel fluorescence of fresh sperm labeled with photoresact and varying concentration of resact for competition. **D.** In-gel fluorescence of frozen sperm labeled with photoresact in presence or absence of an excess of resact. Bottom gel shows Coomassie staining used as loading control.

The GC is localized in the flagellum [4] (Figure 56A), but where is the 63 kDa protein localized, which binds photoresact? To answer this question, I imaged sperm after labeling them with photoresact and Dy654-N_3: labeling was observed for both, head and flagellum (Figure 56B). Thus, I performed the labeling on samples that contained either heads only, flagella only, or intact sperm. Western blot analysis revealed that the protein of interest is localized mainly to the flagella (Figure 56C). Of note, the GC was present in all samples, which might be due to the fact that the method used to separate heads from tails is not very efficient, considering the high abundance of the GC in sperm.

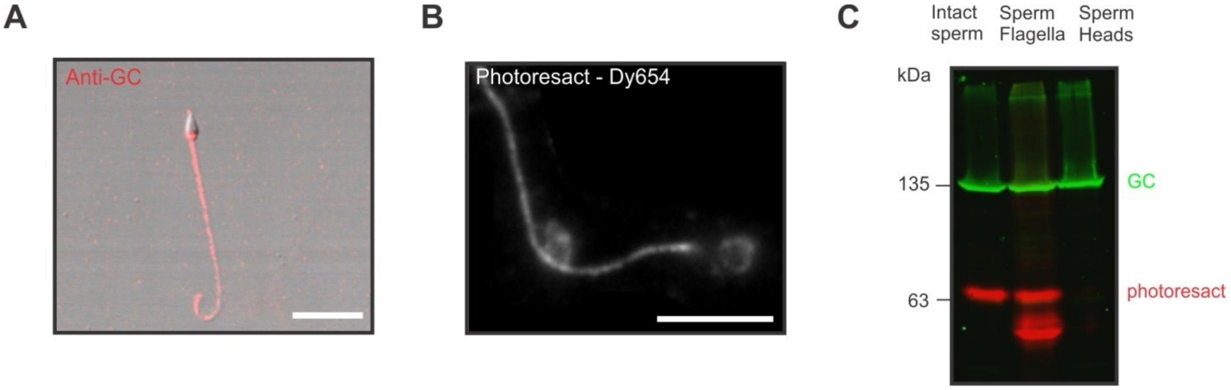

Figure 56. Localization of the target protein. A. Fluorescence image with primary antibody against GC and fluorescently-labeled secondary antibody (obtained from [4]). Scale bar 10 µm. **B.** Fluorescence image of sperm labeled with photoresact and Dy654-N_3. Sperm were first photo-crosslinked with photoresact and then click chemistry was performed using Dy654-N_3. Scale bar 20 µm. **C.** Western blot and in-gel fluorescence of intact sperm, isolated flagella, and isolated heads. Bands labeled with GC antibody are shown in green, while bands labeled with photoresact are shown in red.

3.2.1. Comparison of our labeling approach to other approaches done on related species

Early experiments on sea urchin sperm from *A. punctulata* and *S. purpuratus* in the 1980s [10] reported an elevation in intracellular [cGMP] and dephosphorylation of a major membrane protein when sperm was incubated with egg jelly of its own species. The major protein in both species was identified as GC and the dephosphyrlation resulted in loss of its enzymatic activity. Two peptides were identified in egg jelly of both *A. punctulata* and *S. purpuratus* and were named resact and speract respectively. Both peptides increased sperm intracellular [cGMP] in a species-specific manner [10]. In order to identify the resact and speract receptor in both species, radioiodinated chemically synthesized analogues of resact and speract were developed. Chemical-crosslinking was used for covalent coupling between the peptide and the target receptor and subsequent SDS-PAGE and autoradiography allowed the visualization of the protein bands coupled to the peptides in each species. In *A. punctulata*, a 150 kDa protein was identified using this method as GC while in *S. purpuratus,* the same method with speract analogue resulted in a predominant band at 70-80 kDa. The 70-80 kDa protein was reported as the receptor and it was suggested to be an adaptor associated to the GC and was called speract receptor [130]. The binding in all these experiments was done at pH of 6.6. When binding of speract analogue to *S. locentrotus* sperm was done at pH 8.2, a new band appeared at 140 kDa which is approximately the same molecular weight as the GC identified in *A. punctulata* [130]. It is unclear whether these crosslinking methods identified the putative receptor or a closely associated protein. The "photoresact band" that I identified at 63 kDa has approximately the same molecular weight as the speract receptor identified in *S. purpuratus.* Interestingly, the identified speract receptor in *S. purpuratus* has an ortholog in *A. punctulata* sperm, suggesting that the protein crosslinked to photoresact is the ortholog of speract receptor in *A. punctulata*.

I performed chemical cross-linking and photo-crosslinking on sperm incubated with photoresact in order to unravel an interaction between the GC and the protein coupled to photoresact. The concentration of the chemical cross-linking agent dissuccinimidyl suberate (DSS) (Figure 57A) was varied from 0 to 10 mM in five different conditions, while photoresact was kept constant at 10 µM. First, photoresact was photo-crosslinked to sperm under UV illumination. Then after click chemistry with Dy654-N_3, DSS was added for 10 minutes and then the reaction was quenched with 50 mM Tris buffer. Finally, samples were lysed in 1 % Triton X-100, centrifuged, and the resultant supernatant was reduced, denatured, and loaded on a gel. Western blot analysis using an antibody against GC in combination with in-gel fluorescence was performed (Figure 57B). The colocalization between the GC and the photo-crosslinked proteins was not observed in all conditions (Figure 57B), suggesting that the protein crosslinked to photoresact and the GC do not interact. Further investigation is needed to to identify the binding site of resact.

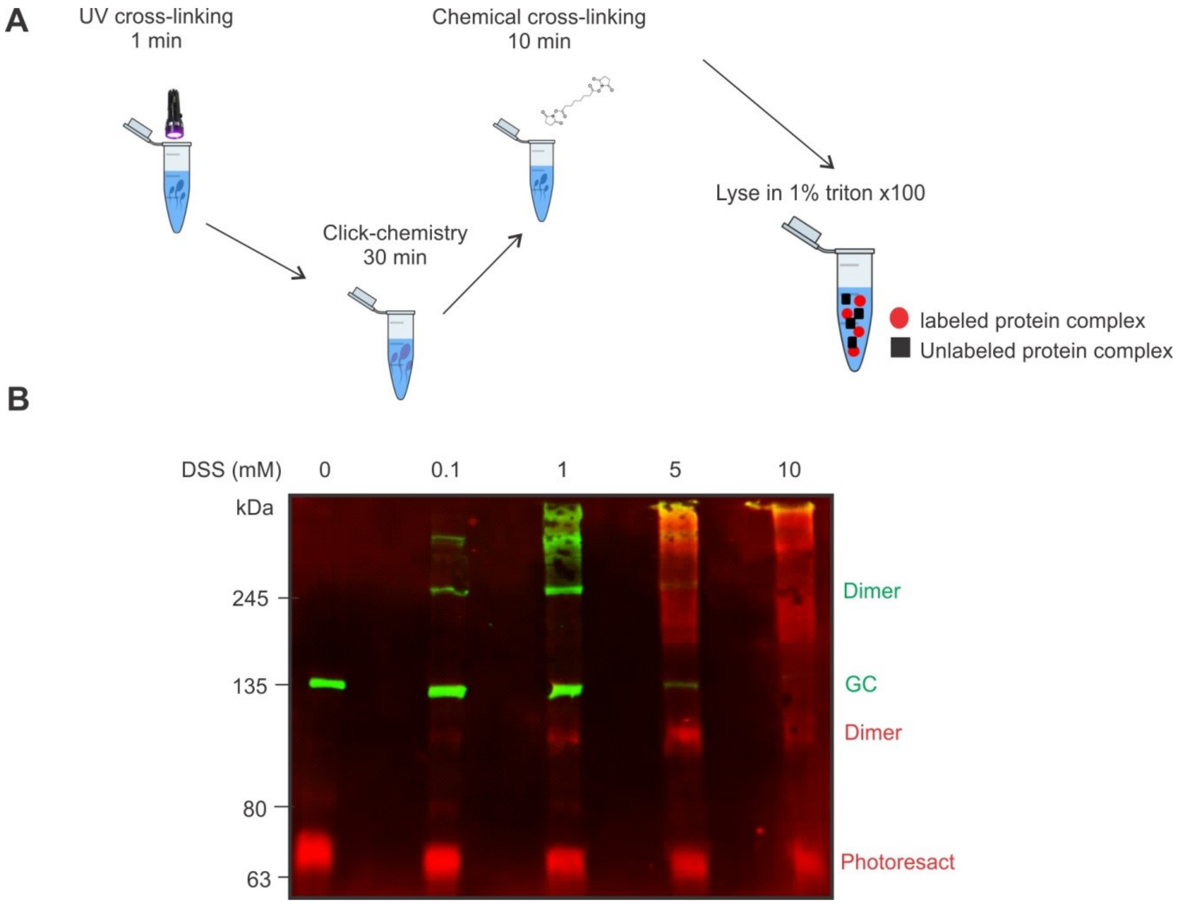

Figure 57. Exploring protein-protein interaction with chemical crosslinking. A. Overview of the photo- and chemical-crosslinking assay. Sperm, photo-crosslinked to photoresact, and then clicked to a fluorophore undergo chemical-crosslinking and then were lysed prior to SDS-PAGE analysis. **B.** Western blot and in-gel fluorescence showing photoresact labeled bands and GC monomer and dimers that are formed with chemical-crosslinking. GC monomer is at ca. 135 kDa, while the dimer is shown more clearly in the presence of 1 mM DSS at ca. 260 kDa. No colocalization between photoresact bands (red) and GC bands (Green) was observed.

The question arises: Why my photo-crosslinking approach in *A. punctulata* resulted in a 63 kDa protein while the GC was identified in [131], using a chemical-crosslinking approach? And why would the two sea urchin species, *A. punctulata* and *S. purpuratus* that share most of their signaling cascade components and functions have different chemoreceptors?

I obtained my results using photo-crosslinking, while the published results were obtained by chemically crosslinking resact to sperm (Figure 58A). Despite the fact that photo-crosslinking is a cleaner and a more specific method, the discrepancy could originate from our different crosslinking approaches.

Thus, I went one step back and tried to reproduce the results from the literature [130,131]. We designed a new resact analogue that was based on photoresact, but this time the N-terminus was kept free; thereby, making it available for chemical-crosslinking. We called this analogue chemresact. Chemresact was in fact highly active and the affinity was still in the low pM range (Figure 58C). Incubating the sperm with chemresact and DSS (Figure 58B) followed by click chemistry resulted in a single band when using 0.1 mM of DSS. The band appeared at ca. 75 kDa and, thereby, did not resemble the MW of the GC. Furthermore, the band could be competed using resact (Figure 58E). The experiments in the literature [130,131] were performed in ASW at pH 6.8 instead of the physiological pH of 7.8 that I used in my experiments. I performed the experiments at pH 6.8 and pH 7.8 and compared the resultant in-gel fluorescence from both conditions. The data did not show a band at the height of the GC, however, a band was present higher than 135 kDa that did not appear with pH 7.8 (Figure 58F). The pH variation did not explain the discrepancy but it suggests that pH is an important factor to be taken into account when trying to identify a receptor.

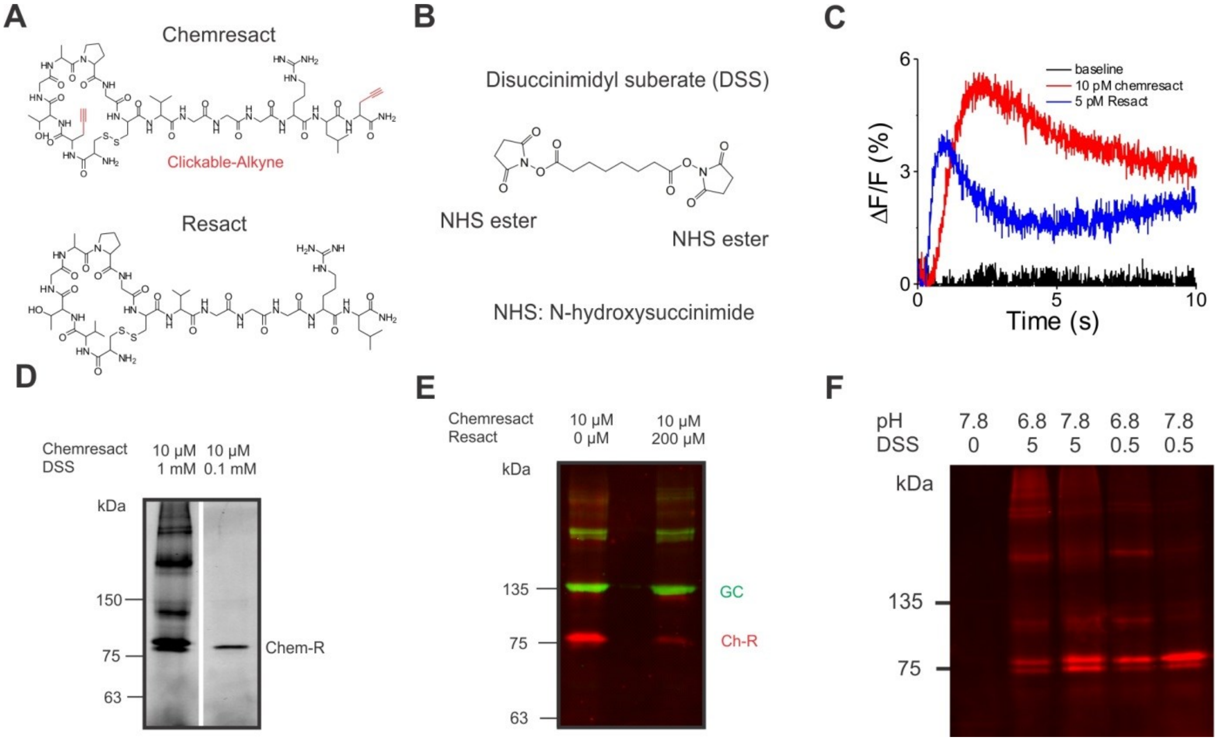

Figure 58. Targeting the receptor with chemical crosslinking. A. Chemresact structure that allows to perform chemical-crosslinking and click chemistry. **B.** Chemical structure of DSS crosslinker. **C.** Stopped-flow Ca^{2+} signals obtained with 10 pM chemresact (red) and 5 pM resact (blue), and ASW as baseline (black). **D.** In-gel fluorescence of chemresact labeled sperm in the presence of two different DSS concentrations. **E.** Western blot and in-gel fluorescence of sperm that were labeled with chemresact and Dy654-N_3 in absence or presence of resact for competition. **F.** In-gel fluorescence of sperm chemically crosslinked to chemresact and clicked to Dy654-N_3. Binding and chemical crosslinking was performed either at pH 6.8 or 7.8 while click chemistry was performed at 7.8 in all conditions.

I tried to validate my experimental design and method on *S. purpuratus* sperm. *S. purpuratus* sperm react only to speract, but not to resact. We designed a speract derivative that has a diazarine group and an alkyne group using a similar approach as for photoresact (Figure 59A). Photosperact evoked a Ca^{2+} response with an EC_{50} that was 16 fold higher than that of the natural speract (Figure 59B-C). Incubating *S. purpuratus* sperm with photosperact in the presence or absence of resact and speract showed a specific band at around 63 kDa that was competed with speract but not resact (Figure 59D). This result is in line with the literature [130], showing a 70-80 kDa band after chemical cross-linking.

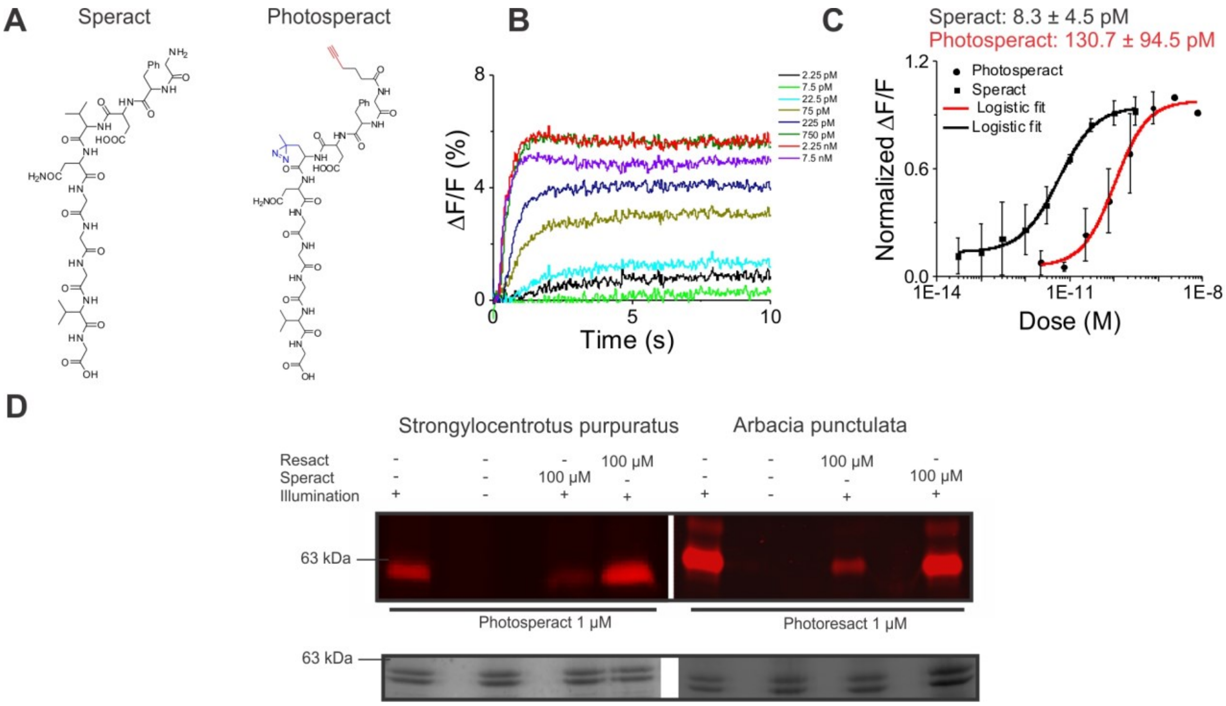

Figure 59. Targeting the receptor in *S. purpuratus* sperm using photo-crosslinking. A. Structure of speract and modified speract (photosperact) with diazarine (blue) and alkyne (red). **B.** Ca^{2+} responses of *S. purpuratus* sperm evoked by increasing concentrations of photosperact, measured using the stopped-flow technique. **C.** Dose-response relation of photosperact (red) and speract (black). Logistic fit was used to obtain the EC_{50}. The average EC_{50} ± SD (n = 3) is shown on top of the plot. **D.** In-gel fluorescence of *S. purpuratus* and *A. punctulata* sperm. Resact, speract and illumination conditions are summarized on top of the lanes. Left image shows in-gel fluorescence from *S. purpuratus* sperm. Labeled band appears at a height slightly lower than 63 kDa only when UV illumination was used. Band was significantly competed when using speract, but not resact. Right image shows in-gel fluorescence from *A. punctulata* sperm. Photoresact band appears slightly above 63 kDa and it disappeared in absence of UV illumination. The band intensity was reduced in presence of an excess of resact but not speract. Lower image shows Coomassie as a loading control from the above two plots.

A. punctulata sperm have been shown to absorb resact with high efficacy [9]. Therefore, I tested whether *S. purpuratus* sperm are able to absorb photosperact. Sperm are incubated with high pM concentration of a ligand and the supernatant containing free ligand was tested whether it still evoked a Ca^{2+} response. I adjusted the sperm dilution to a final GC concentration of 500 nM and used 100 pM resact, 100 pM speract, 100 pM photoresact, or 500 pM photosperact. Ca^{2+} signals were recorded using the stopped-flow technique and the responses were compared to a control ligand that has not been incubated with sperm. The experiment was split in two parts. In one part, *S. purpuratus* sperm were used as readout, while *A. punctulata* and *S. purpuratus* sperm were used for absorption (Figure 60A). Speract and photosperact were added to *S. purpuratus* sperm and the supernatant was used as a stimulus for Fluo-4 AM-loaded *S. purpuratus* sperm and compared to a speract- and photosperact-evoked signals. *S. purpuratus* sperm absorbed both speract and photosperact, because the signal amplitude was significantly decreased compared to control, speract-induced signals (Figure 60B). In a second step, speract and photosperact were added to *A. punctulata* sperm and the supernatant was used as a stimulus (Figure 60C) for *S. purpuratus* sperm and compared to the control, speract/photosperact-evoked signals. *A. punctulata* sperm did not absorb either speract or photosperact, because the signal amplitude remained unchanged compared to control, speract and photosperact-induced signals (Figure 60D).

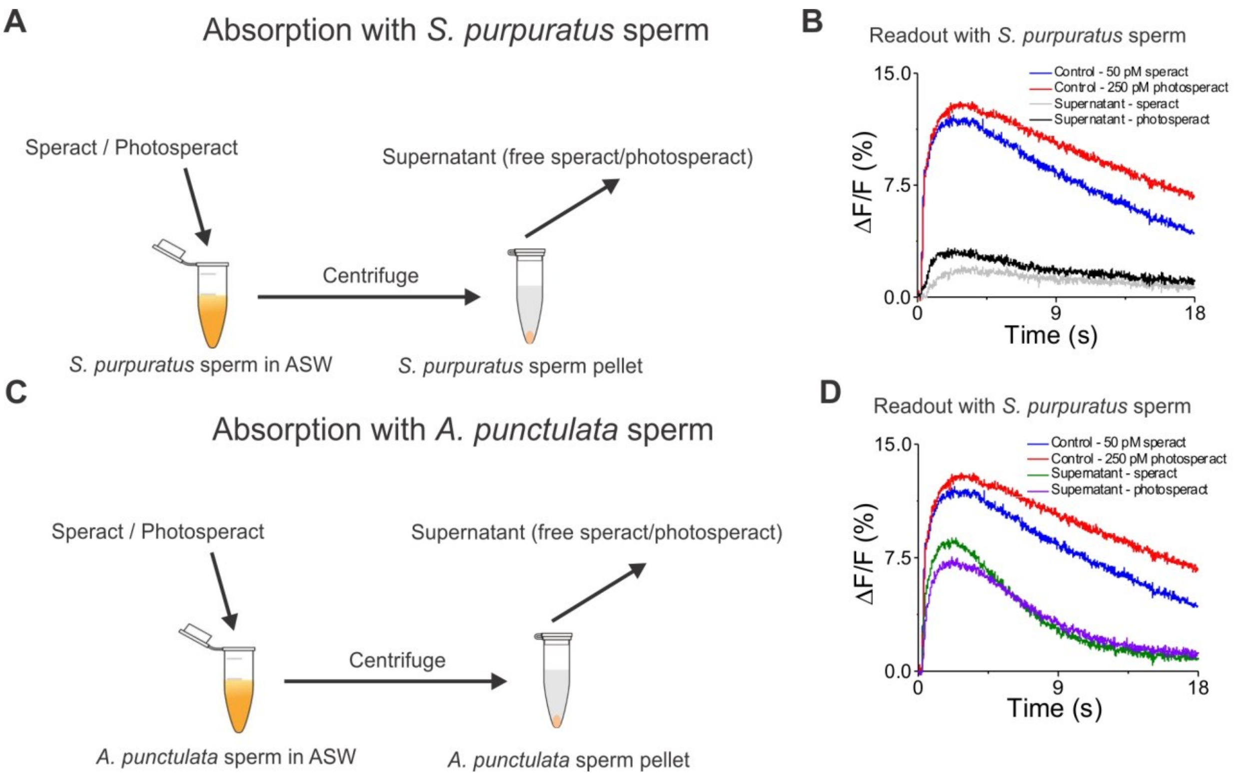

Figure 60. Speract and photosperact are absorbed only by *S. purpuratus* sperm. A. Overview of the binding test of speract and photoresact to *S. purpuratus* sperm. 100 pM speract and 500 pM photosperact were added to two separate vials containing *S. purpuratus* sea urchin sperm suspension. Suspension was adjusted to have 500 nM GC. After equilibration, samples were centrifuged at 1000 x g and the supernatant containing the free peptide was mixed with Fluo-4AM loaded *S. purpuratus* sea urchin sperm in the stopped-flow setup. **B.** Plot showing Ca^{2+} signals obtained in *S. purpuratus* sperm and

evoked by the supernatant containing free speract (gray) and free photosperact (black). 50 pM speract (blue) and 250 photosperact (red) was used as a control. **C.** Overview of the binding test of speract and photoresact to *A. punctulata* sperm. 100 pM speract and 500 pM photosperact were added to two separate vials containing *A. punctulata* sea urchin sperm suspension. Suspension was adjusted to have 500 nM GC. After suspensions were allowed to equilibrate, they were centrifuged at 1000 x g and the supernatant containing free peptide was mixed with Fluo-4 AM loaded *S. purpuratus* sea urchin sperm in stopped-flow setup. **D.** Plot showing Ca^{2+} signals obtained in *S. purpuratus* sperm and evoked by the supernatant containing free speract (green) and free photosperact (violet). 50 pM speract (blue) and 250 photosperact (red) was used as a control.

In the second experiment, *A. punctulata* sperm were used as readout, and *A. punctulata* and *S. purpuratus* sperm were used for absorption test (Figure 61). First, resact was added to *A. punctulata* sperm, the sperm suspension was centrifuged down (Figure 61A), the supernatant was used as a stimulus for *A. punctulata* sperm, and the Ca^{2+} response was compared to the resact evoked signals. *A. punctulata* sperm absorbed resact as demonstrated by the decrease in the Ca^{2+} response compared to resact-evoked response (Figure 61B). Next, resact and photoresact were added to *S. purpuratus* sperm, the sperm suspension was centrifuged down, and the supernatant was used as a stimulus for *A. punctulata* sperm and compared to the resact/photoresact evoked signals (Figure 60C). *S. purpuratus* sperm did not seem to absorb either resact or photoresact because the Ca^{2+} response evoked by the supernatant containing free resact/photoresact was similar to the control of resact- and photoresact-evoked response when using *A. punctulata* as a readout (Figure 61D).

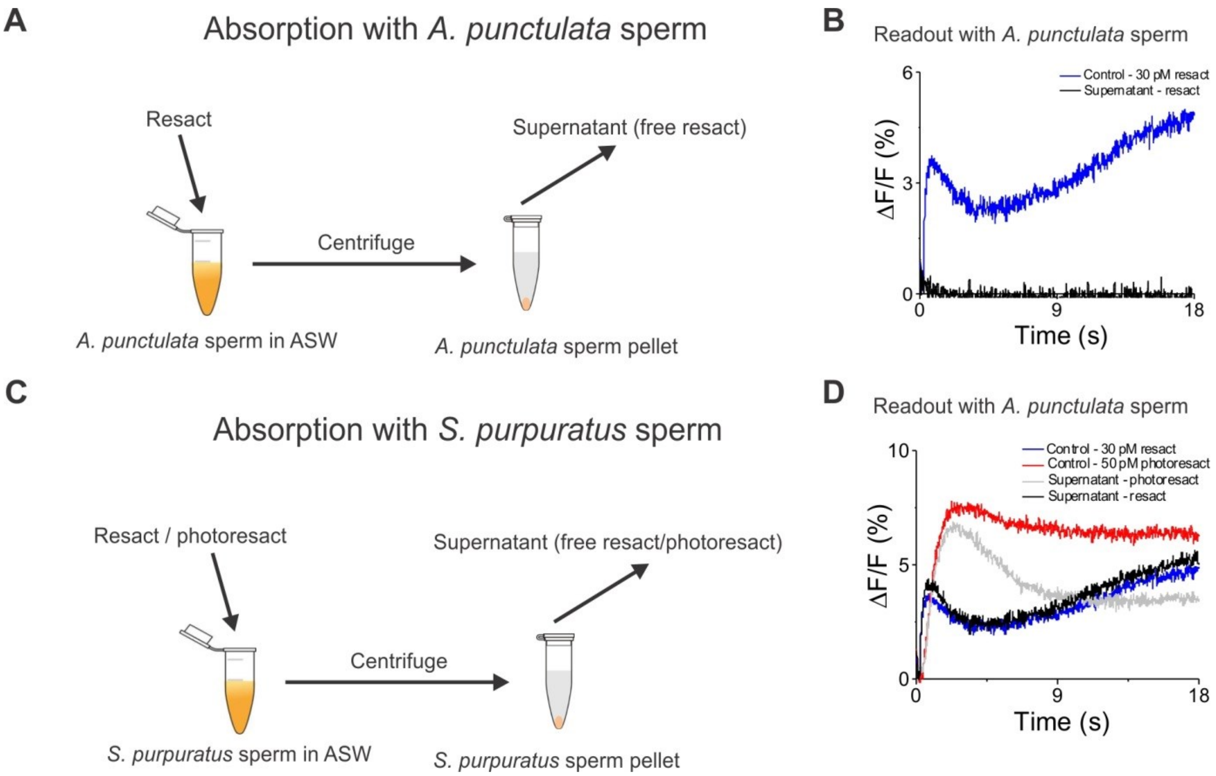

Figure 61. Resact and photoresact are absorbed only by *A. punctulata* sperm. A. Overview of the binding test of resact to *A. punctulata* sperm. 100 pM resact was added to a vial containing *A. punctulata* sperm suspension. Suspension was adjusted to have 500 nM of GC. After equilibration the samples were centrifuged at 1000 x g and the supernatant containing free peptide was mixed with Fluo-4AM loaded *A. punctulata* sperm in stopped-flow setup. **B.** Plot showing Ca^{2+} signals obtained in *A. punctulata* sperm and evoked by the supernatant containing free resact (black). 30 pM resact (blue) was used as a control. **C.** Overview of the binding test of resact and photoresact to *S. purpuratus* sperm. 100 pM resact and 500 pM photoresact were added to two separate vials containing *S. purpuratus* sea urchin sperm suspension. Suspension was adjusted to have 500 nM GC. After equilibration, the samples were centrifuged at 1000 x g and the supernatant containing the free peptide was mixed with Fluo-4AM loaded *A. punctulata* sea urchin sperm in stopped-flow setup. **D.** Plot showing Ca^{2+} signals obtained in *A. punctulata* sperm and evoked by the supernatant containing free resact (black) and free photoresact (gray). 30 pM resact (blue) and 50 photoresact (red) was used as a control.

The size of the labeled protein in *S. purpuratus* sperm matched the results from the literature [130]. *A. punctulata* sperm harbors an ortholog of speract receptor called speract-receptor-like with a molecular weight that matches the “photoresact band” at 63 kDa. To reveal whether this ortholog can bind photoresact, I expressed it in HEK293 cells. It is important to note that the physiological conditions for HEK293 cells are different from *A. punctulata* sperm in ASW regarding pH, divalent ion concentration, and osmolarity. Thus, I first tested the photoaffinity labeling on sperm in either ASW or extracellular solution (ES) that is suitable for HEK293 cells. In-gel fluorescence analysis revealed that the 63 kDa band was present when photo-crosslinking occurred in ASW, but not in ES, while other bands appeared in both conditions (Figure 62A). In a second experiment, the osmolarity and divalent ion concentration in ES was varied (Figure 62E). In-gel fluorescence analysis revealed again that only the 63 kDa band was sensitive to these changes. The band was only present when either osmolarity was increased or divalent ion concentration was adjusted to match that of ASW (Figure 62B). This experiment shows that the binding at the 63 kDa "photoresact band" is influenced by osmolarity and the divalent ion concentration. Now that we know the conditions, at which binding occurs, we tested the photoaffinity labeling on transfected HEK293 cells (Figure 62C) using buffer ES-2 (Figure 62E). In-gel fluorescence of proteins isolated from transfected cells that were photo-crosslinked to photoresact and clicked to Dy654-N_3 did not reveal any specific interaction between photoresact and the transfected protein (Figure 62D).

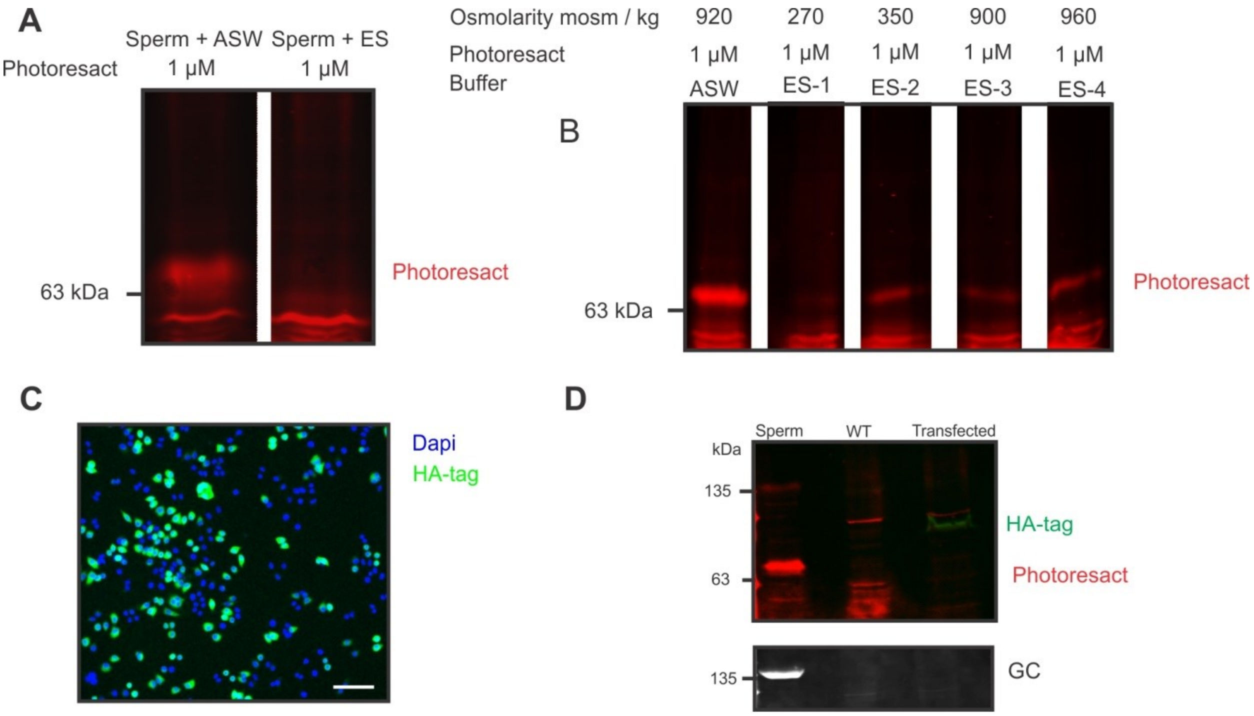

E

Buffer Chemicals	ASW	ES-1	ES-2	ES-3	ES-4
NaCl (mM)	423	120	120	120	120
KCl (mM)	9	5	5	5	5
MgCl$_2$	22.94	2	22.94	2	22.94
CaCl$_2$	9.27	2	9.27	2	9.27
MgSO$_4$ (mM)	25.5	0	25.5	0	25.5
HEPES (mM)	10	10	10	10	10
Glucose (mM)	0	10	10	600	600

Figure 62. Binding of photoresact. A. In-gel fluorescence of protein from *A. punctulata* sperm. Binding and photo-crosslinking was done either in ES or ASW solution. **B.** In-gel fluorescence of protein from *A. punctulata* sperm, where binding and photo-crosslinking was done in various buffer conditions. **C.** HEK293 cells transfected with the ortholog of speract receptor in *A. punctulata*. **D.** In-gel fluorescence of protein lysate from HEK293 cells that were labeled with photoresact. *A. punctulata* sperm was used as a control. First lane shows photoresact band from *A. punctulata* sperm (red) at ca. 63 kDa. Second lane shows a band (red) from WT HEK293 cells at ca. 100 kDa and the last lane shows band labeled with HA tag at ca. 90 kDa (green) and band labeled with photoresact (red) at ca. 100 kDa. **E.** Composition of buffers used for the experiment in (B). adjusted values are shown in blue. ES stands for extracellular solution.

3.2.2. Photo-affinity purification and enrichment

The identity of the photo-crosslinked protein is still unknown. Thus, I performed experiments to enrich the photo-crosslinked protein and reveal its identity using mass spectrometry. The photo-crosslinked protein contains a free alkyne group, which can be coupled to beads using click chemistry (Figure 63A). To verify the enrichment using SDS-PAGE and Coomassie staining, we designed and synthesized cleavable azide-beads. The beads contained a disulphide bond, separating the azide group from the beads. The desulphide bond allowed a controlled elution of the photo-crosslinked protein from the beads under reducing conditions (Figure 63A). First, sperm had to be incubated with photoresact and then crosslinked under UV illumination. After washing the excess photoresact, sperm had to be lysed in buffer containing 1% Triton X-100, and the cleavable azide-beads had to be added together with the click solution (Figure 63B). After washing, the suspension would be reduced and denatured, loaded onto an SDS-PAGE, and the SDS-gel would be labeled with colloidal Coomassie. Finally, the band of interest would be excised and sent for mass spectrometry (Figure 63C).

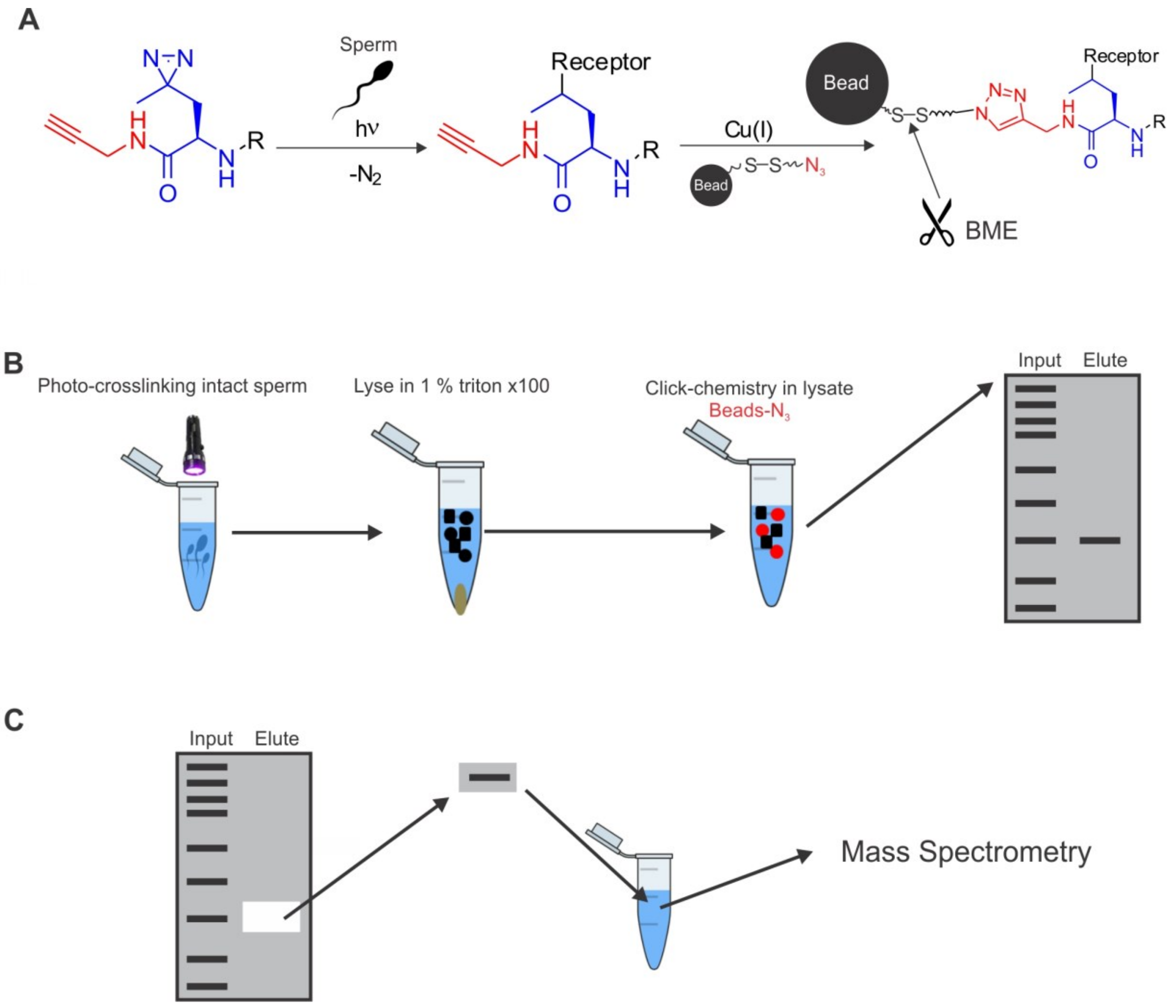

Figure 63. Homemade cleavable beads for protein enrichment using click chemistry. A. Working principle of the cleavable azide-beads. Photoaffinity label is photo-crosslinked to sperm and then the beads are added to the resultant sperm with a receptor-alkyne complex. Upon addition of Cu (I), the click-reaction occurs between the beads and the protein complex. The beads can be cleaved off using a reducing agent like beta-mercaptoethanol (BME), which acts on the bisulphate bond. **B.** Schematic overview of the enrichment experiment. Sperm in suspension are being photo-crosslinked, lysed in a buffer containing 1% Triton X-100, and then click chemistry occurs in the presence of the azide-beads and Cu (I). The suspension is then reduced, denatured, and loaded onto an SDS-PAGE. **C.** Protein bands labeled by Coomassie staining are excised and destained then sent for mass spectrometry.

Before I performed the actual experiment, I verified the experimental approach using Dy654-N_3 instead of the beads to test whether the lysis buffer containing 1 % Triton X-100 interferes with the reaction. Sperm were incubated with photoresact, photo-crosslinked under UV illumination, and the resultant suspension was split into two fractions: 1) The click reaction with Dy654-N_3

was performed on intact sperm, followed by click reaction in sperm lysate. Click reaction occurred in both conditions (Figure 64A). 2) Sperm were lysed first and the click reaction was performed in the lysate in the presence of Dy654-N_3. Analysis of the in-gel fluorescence demonstrated that the click reaction occurred in lysate without major changes compared to intact sperm. Thus, I proceeded using the cleavable azide-beads. Sperm were incubated with photoresact, photo-crosslinked, lysed, and then the beads were added to the lysate in presence or absence of Cu (I). Omitting Cu (I) in the reaction served as a control for nonspecific interactions of the proteins with the beads themselves. The photo-crosslinked band was enriched using this protocol and no non-specific interaction was observed after colloidal Coomassie staining (Figure 64B). Furthermore, the photo-crosslinked band after bead purification ran at a similar height compared to the band of sperm labeled with Dy654-N_3 (Figure 64C). The bands of interest were sent for mass spectrometric analysis and preliminary results were inconclusive. Thus, further experiments are needed.

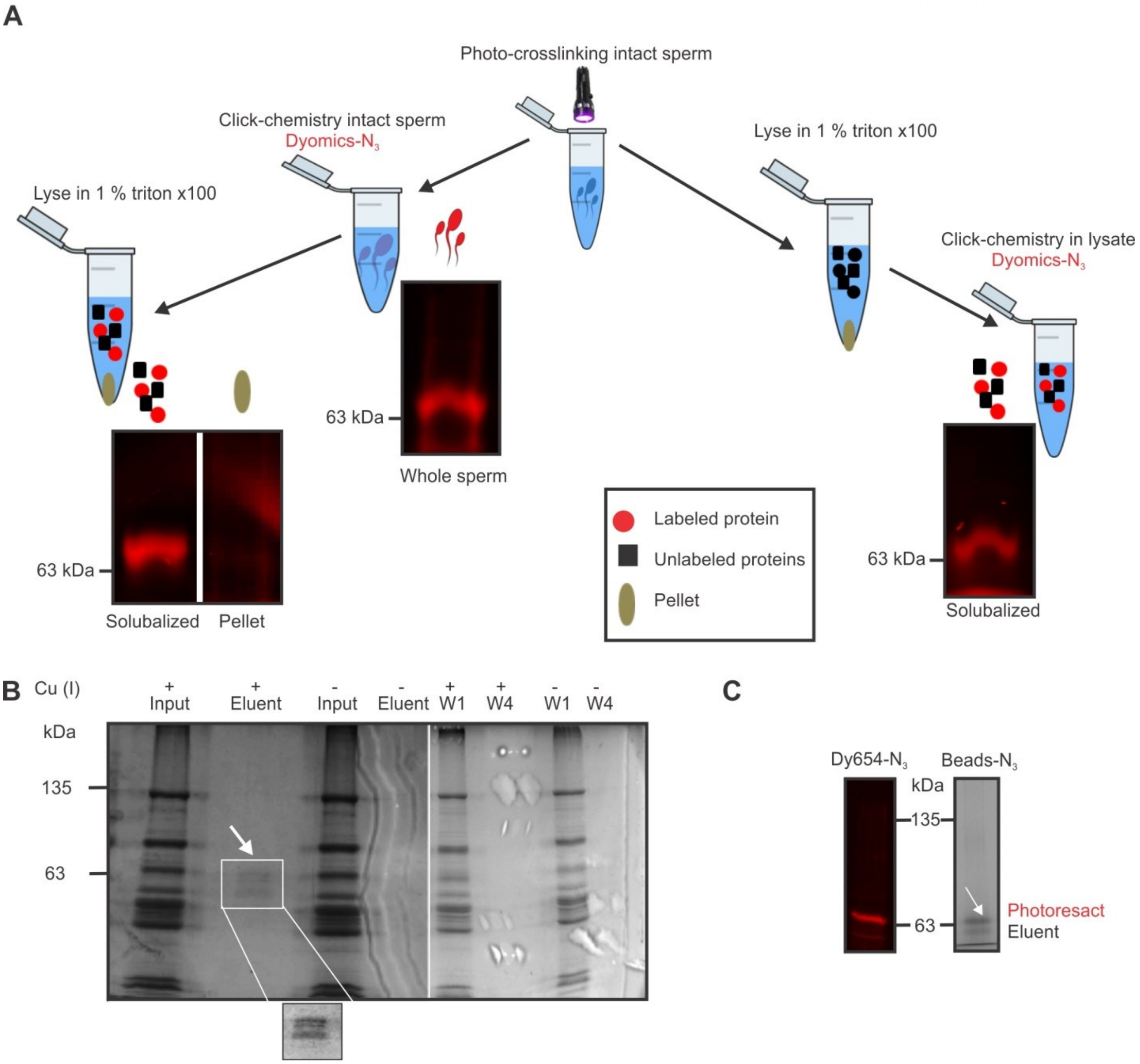

Figure 64. Establishing a protocol for protein purification using the cleavable beads. A. Overview of the experiment used to establish photo-affinity purification with the cleavable azide-beads. Sperm were photo-crosslinked to photoresact then split in half. The left section of the figure shows the first in-gel fluorescence of the first half that underwent photo-crosslinking and click chemistry on intact sperm. The rest of the sample was lysed and then loaded in a SDS gel along with the non-soluble pellet. The right half depicts assay for sperm that was lysed first then click chemistry occurred in lysate with Dy654-N_3. The lysate was then loaded in gel. **B.** SDS gel stained with Colloidal Coomassie, showing bands of sperm lysate that has been photo-crosslinked to photoresact and then clicked to Beads. Cu (I) was omitted from the negative control. Contrast was enhanced in the boxed region. **C.** Colloidal

Coomassie stained SDS-gel (right) and in-gel fluorescence (red) of sperm sample that was split between click chemistry with beads and dye.

3.3. Supra-molecular arrangement of GC revealed by cryo-EM

Although I could not unequivocally verify the identity of the protein being labeled by photoresact, I performed STORM imaging using photoresact labeled *A. punctulata* sperm. STORM imaging did not reveal a distinct supra-molecular structure along the flagellum – the membrane seemed to be rather uniformly labeled (Figure 65A). The resolution measured with FRC ranged between 40 and 50 nm (Figure 65C). The broadening effect of the antibody was decreased using photoresact as seen in the profile plots (Figure 65B). However, the question arises, whether the molecular arrangement of the chemoreceptor complex is beyond the resolution achieved by STORM. This was answered by my colleague Dominica Farci using cryo-electronmicroscopy (Cryo-EM). Her analysis revealed a helical organization of the GC along the entire flagellum with a helix pitch of 6 nm (Figure 65D). When incorporating these findings in a STORM simulation (Figure 65E), I can show that with a localization precision of 1 nm and a very small label size, we should be able to elucidate the structure (Figure 65F). However, in reality, STORM localization precision is difficult to push beyond 10 nm, with current fluorophores and techniques [132]. Simulating the STORM image with a 10 nm localization precision showed no distinct structures (Figure 65G). Thus, it was not possible to verify the helical arrangement of the GC along the flagellum using current STORM imaging technology.

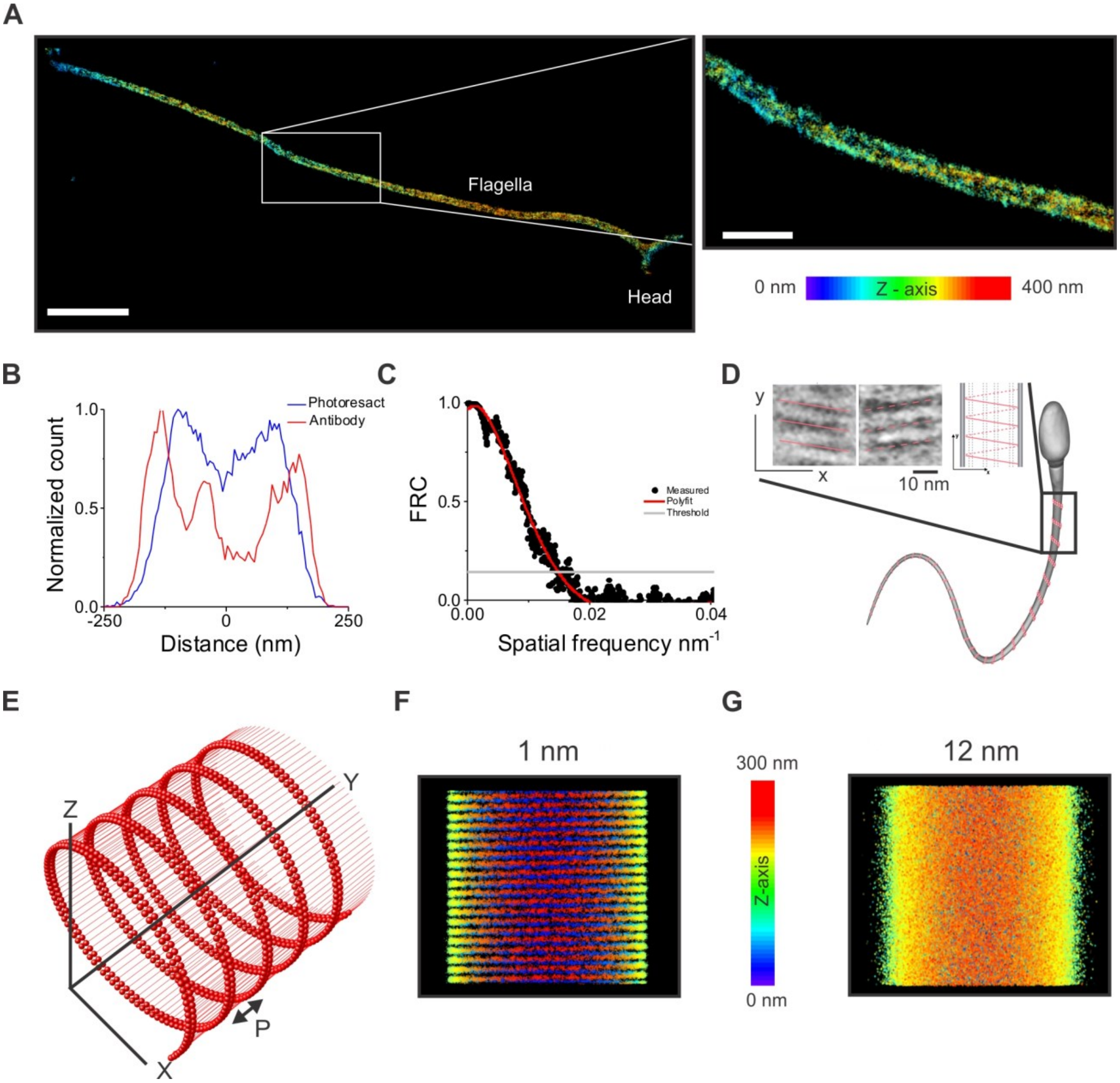

Figure 65. Organization revealed by cryo-EM beyond the scope of STORM imaging. A. Left - 3D STORM image of photoresact labeled sea urchin sperm showing photoresact distribution in sperm flagellum. Right – zoom-in STORM image of the boxed region. Z color code is shown on the right. **B.** STORM density profile across flagellum obtained from images with either antibody (red) or photoresact (blue). **C.** FRC plot of the dataset shown in (A), showing a resolution of 50 nm. **D.** Cryo-EM showing helical GC distribution along sperm flagella with a 6 nm pitch. Data obtained by Domenica Farci. **E.** Image depicts the GC organization. GC organization was modeled in accordance with cryo-EM data. Pitch (P) is 6 nm and diameter is 250 nm. **F.** STORM image rendered from the simulated GC distribution with 1 nm localization precision. **G.** STORM image of the simulated GC distribution with 12 nm localization precision. Scale bar in order of appearance 1 µm, 0.5 µm.

4. Supra-molecular arrangements of CatSper in mammalian sperm

Mammalian sperm must undergo a process in the female reproductive tract called capacitation to be able to fertilize the egg. This is manifested by an influx of Ca^{2+} that elevates intracellular cyclic adenosine monophosphate (cAMP) levels and, thereby, triggering hyperactivated motility. Hyperactivation requires CatSper, a channel complex that encompasses at least 9 different subunits (*CatSper1–4*, β, γ, δ, *ε,* and *ζ*). The CatSper-channel complex in mouse sperm forms a quadrilateral arrangement in three dimensions that organizes structurally distinct Ca^{2+}-signaling domains along the flagellum [34]. Here, I used STORM super-resolution microscopy to verify the spatial organization of CatSper in mouse sperm (Chapter 1). In order to check if the lack of other signaling molecules can disrupt CatSper organization, I analyzed the the CatSper supra-molecular organization in sperm lacking the testis-specific Na^+/H^+ antiporter 1 (NHA1). Finally, I determined the spatial organization of CatSper in human sperm.

4.1. Verification of CatSper supra-molecular arrangements in mouse sperm

First, I performed STORM imaging on mouse sperm labeled with an antibody against CatSper1 subunit. To verify its specificity, I tested the antibody on WT and CatSper-KO sperm. Fluorescence microscopy of WT sperm labeled with primary antibody against CatSper1 and secondary antibody conjugated to Alexa-647 showed that CatSper1 was localized in the principal piece. In addition, also the acrosome was labeled, which, however is unspecific, as demonstrated by labeling of CatSper-KO sperm (Figure 66A-B). Here, also the midpiece was unspecifically labeled. Next, I performed STORM imaging on WT sperm. 3D STORM reconstructions revealed quadrilateral arrangements of CatSper1 along the principal piece (Figure 66C-D). This observation is in line with the reported CatSper1 spatial organization [34]. To see if CatSper domain remained intact in sperm lacking the testis-specific NHA1, I determined the spatial organization of CatSper1 in NHA1-knock-out (KO) mice sperm. 3D STORM imaging of NHA1-KO sperm revealed that CatSper1 domains maintained the quadrilateral structure that was observed in WT sperm cells (Figure 66E-F), demonstrating that loss of NHA1 does not affect the organization of the CatSper complex. The resolution obtained by Fourier Ring Correlation (FRC) varied between 40-50 nm and the experimental localization precision varied between 15-25 nm.

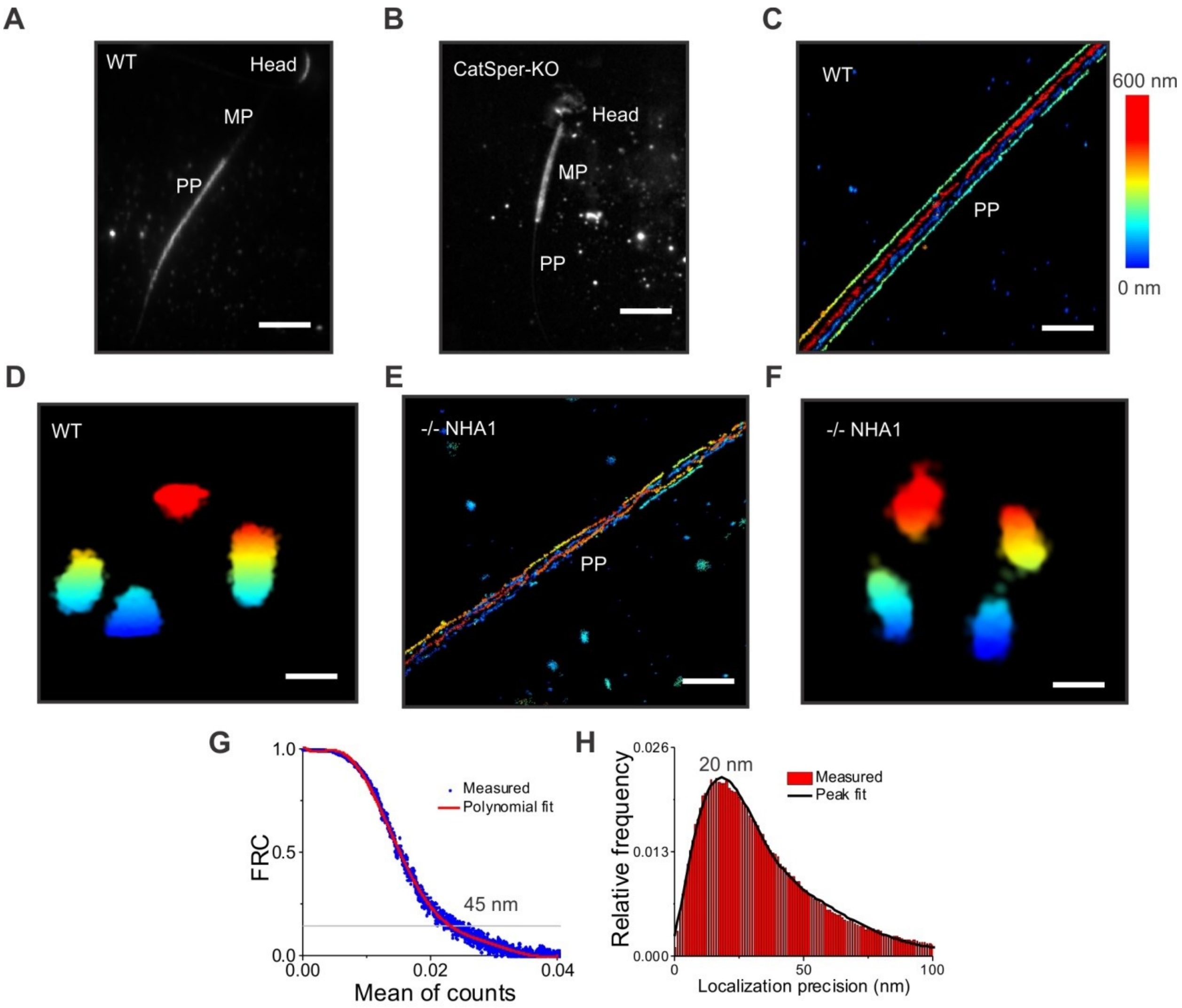

Figure 66. CatSper quadrative arrangement in mouse sperm. A. Fluorescence image of WT mouse sperm labeled with CatSper1 primary antibody and Alexa-647 conjugated secondary antibody. **B.** Fluorescence image of CatSper-KO mouse sperm labeled with CatSper 1 primary antibody and Alexa-647 conjugated secondary antibody. Scale bar: 10 µm. **C.** Color coded 3D STORM image of CatSper3 in WT mouse sperm at the principal piece. Scale bar: 200 nm. **D.** Axial cross-section showing the four CatSper domains in WT mouse sperm. Scale bar: 1 µm. **E.** Color coded 3D STORM of tNHA1-KO sperm showing the CatSper quadrilateral arrangements. **F.** Axial cross-section showing the four CatSper domains in the testis-specific NHA1-KO mouse sperm. Scale bar: 200 nm. **G.** FRC resolution of the image in (C), revealing a resolution of ca. 45 nm. **H.** Experimental localization precision of the image in (C) obtained with tracing of single molecules (see methods). Scale bar: 250 nm. Z color code shown in (C) applies to all 3D STORM images shown here.

4.2. CatSper is organized in four linear domains along the flagellum in human sperm

After verifying the spatial organization of CatSper in mouse sperm, I proceeded to perform STORM imaging on human sperm. I used an antibody against the CatSper3 subunit. Overnight incubation of the primary antibody and one hour incubation with an Alexa-647 conjugated secondary antibody nicely labeled CatSper3 in the principal piece (Figure 67A). I performed 2D STORM imaging on the CatSper-labeled sperm and the subsequent analysis revealed multiple domains of CatSper3 subunit in the principal piece of human sperm (Figure 67C). 3D STORM imaging along the principal piece demonstrated four quadrilateral domains, labeled 1 to 4, at the start of the principal piece in a virtual axial cross section (Figure 67G). Similar results were obtained by others, while writing this thesis [133]. Finally, the resolution measured with FRC varied between 40-50 nm, while experimental localization precision varied between 15-25 nm.

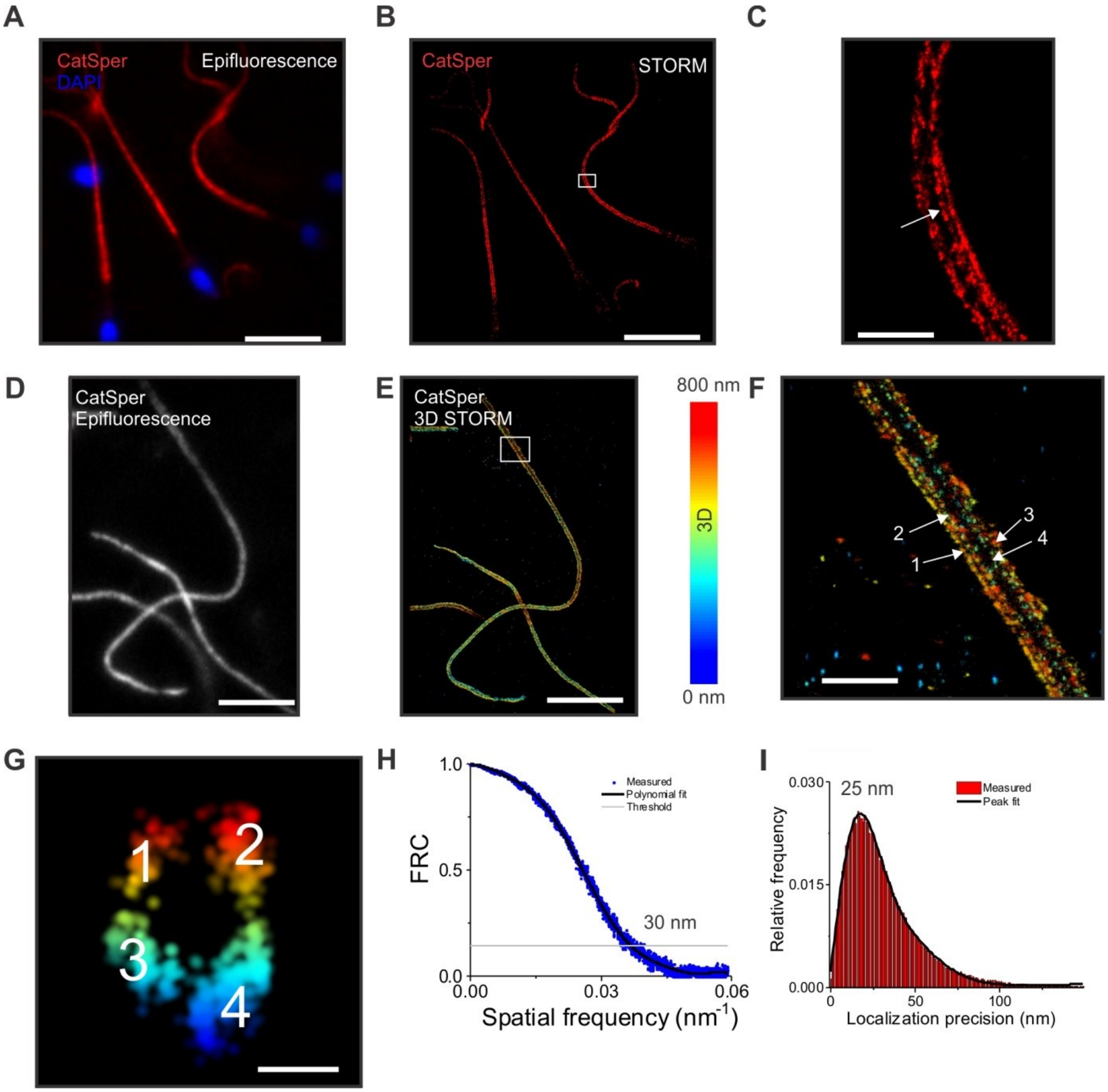

Figure 67. Catsper3 quadrilateral arrangement revealed along the flagellum in human sperm. A. Fluorescence image of human sperm labeled with DAPI (blue), an anti-CatSper3 primary antibody and Alexa-647 conjugated secondary antibody (red). **B.** 2D STORM image of the sperm in (A). Scale bar: 20 µm. **C.** Zoom-in and rotated image of the boxed area in B shows multiple linear domains along the flagella. Scale bar: 2 µm. **D.** Fluorescence image showing CatSper staining in grey scale. **E.** Color coded 3D STORM of the sperm in (D). **F.** Zoom-in of the boxed area in (E) showing quadrilateral arrangements along the principal piece. Scale bar: 10 µm. **G.** Axial cross-section of the principal piece shows the four CatSper domains, labeled 1 to 4. Scale bar: 250 nm. **H.** FRC resolution of the image in (E) revealing a resolution of 30 nm. **I.** Experimental localization precision of the image in (E) revealing an average of 25 nm (see methods).

5. Elucidating the molecular mechanism underlying globozoospermia

Defects in sperm development result in male infertility. The beta-glucosidase GBA2 plays an important role during sperm development. Lack of GBA2 leads to globozoospermia, which is characterized by severe sperm morphological defects [69]. GBA2 degrades the glycosphingolipid glucosylceramide (GlcCer) to glucose and ceramide. It has been suggested that accumulation of GlcCer in GBA2 knockout-mice causes the severe morphological defects and, thereby, globozoospermia [68]. Recently, our group revealed that the lack of GBA2 enzyme alters the cytoskeletal dynamics in developing sperm and Sertoli cells, which supports sperm development [78]. To study the molecular mechanisms how GlcCer accumulation dysregulates cytoskeletal dynamics, we moved to a cellular model system – dermal fibroblasts from wild-type and GBA2 knock-out mice. These cells show a similar phenotype as observed in the male germ line – accumulation of GlcCer leads to dysregulation of the cytoskeletal dynamics and, thereby, to a change in cell morphology and function [78]. However, the underlying mechanism is ill-defined. GlcCer can be incorporated into the inner leaflet of the plasma membrane. Moreover, glycosphingolipids are shown to organize in microdomains within the membrane, resulting in membrane domains with specialized functions [59]. We hypothesized that accumulation of GlcCer alters the membrane properties, which in turn dysregulates cytoskeletal dynamics. To test this hypothesis, I used Laurdan and FRET (Förster Resonance Energy Transfer) imaging to investigate the relationship between GlcCer accumulation and cytoskeletal dynamics at the molecular level. Laurdan is an environmentally sensitive dye that is used to investigate lipid order [86]. Members of the Rho family of GTPases, such as Cdc42 and Rac1, have been shown to regulate cytoskeletal dynamics [76,77] and, in particular, the formation of filopodia and lamellipodia, respectively. Therefore, cytoskeletal dynamics was studied using Rac1 and Cdc42 FRET biosensors. We focused mainly on Rac1 and Cdc42 because of their role in lamellipodia and filopodia formation, which were affected by GlcCer accumulation [78].

5.1. Investigating membrane order

5.1.1. Ensemble measurement – GPMV Laurdan spectroscopy

To analyze differences in lipid stacking between WT and GBA2 knock-out (KO) primary fibroblasts, I first used Laurdan spectroscopy on isolated giant-plasma-membrane-vesicles

(GPMVs) (Figure 68A). Laurdan is a fluorescent dye that is sensitive to the polarity of the environment due to its dipolar relaxation effect. The resulting dipolar relaxation effect causes a shift in the dye emission spectrum. This can be quantified by calculating the generalized polarization (GP) index [86]. In a highly packed lipid membrane, Laurdan emission peaks at 440 nm, whereas in a fluidic membrane, it peaks at 490 nm. I determined the GP index of GPMVs isolated from WT and KO fibroblasts and WT fibroblasts that were treated with 2 µM NBD-NJ - a GBA2-specific blocker. The unlabeled GPMVs were normalized across samples according to the scattering peak at 420 nm (Figure 68C-D). After normalization, I labeled the isolated GPMVs with Laurdan and measured the emission spectrum at 350 nm excitation. The GP value for GBA2 KO-fibroblasts and WT-fibroblasts treated with NBD-NJ were significantly higher than that of control WT-fibroblasts: 0.24 ± 0.03 and 0.27 ± 0.07 compared to 0.15 ± 0.06, respectively (Figure 68F). The GP was calculated from the measured spectra using equation V.3. Thus, the accumulation of GlcCer in the absence of GBA2 results in a highly ordered lipid stacking in the plasma membrane. However, these results do not provide any spatial information about the cellular localization of these highly ordered membrane regions.

$$GP = \frac{I_{420-460} - I_{470-510}}{I_{420-460} + I_{470-510}} \tag{V.3}$$

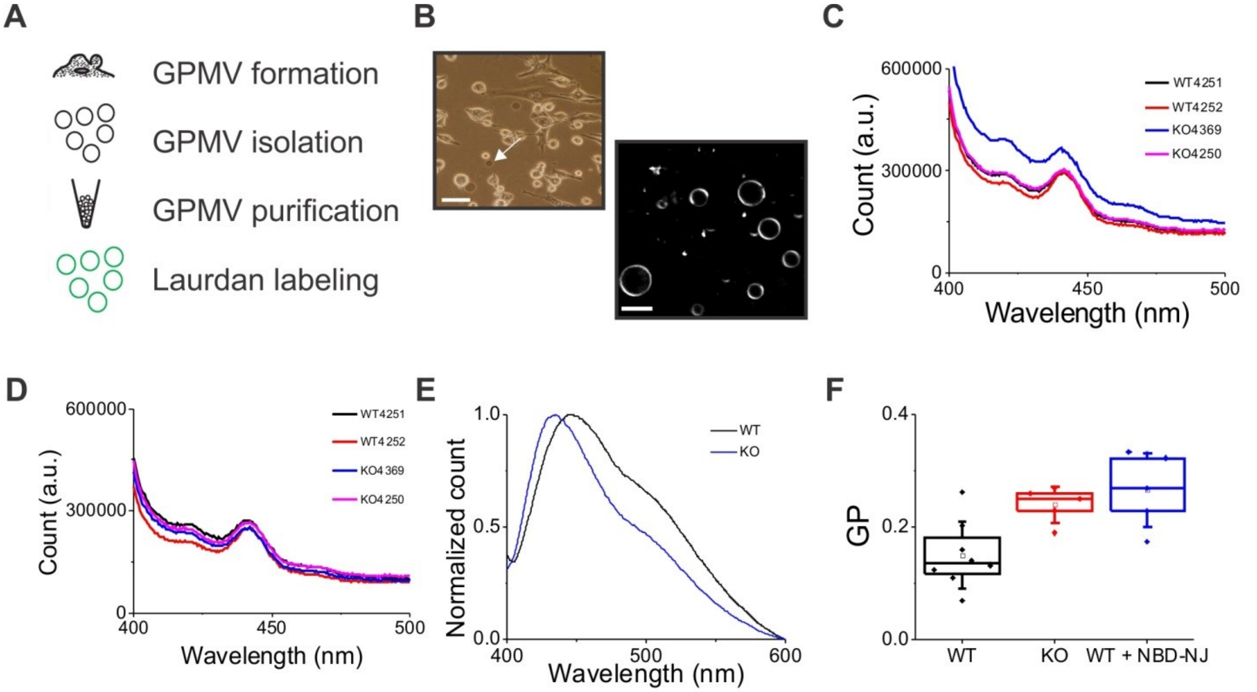

Figure 68. Laurdan spectroscopy - GPMV ensemble measurement. A. Scheme of GPMV isolation from adherent dermal fibroblasts. **B.** Top image shows adherent fibroblasts, releasing vesicles into the supernatant; image was taken with phase contrast optics. Bottom image shows fluorescence image of the isolated and Laurdan-stained vesicles. **C.** Scattering curve recoded at 385 nm excitation of purified vesicles from four different animals before normalization. **D.** Scattering curve of the same vesicles in (C) after normalization. **E.** Representative Laurdan emission spectrum recorded from KO and WT GPMVs. **F.** Whisker plot shows GP average ± SD (n = 4), obtained using WT and KO cells, as well as WT cells that has been treated with 2 µM NBD-NJ blocker. Scale bar 10 µm.

5.1.2. GP imaging

To reveal the cellular localization of GlcCer accumulation, I used two-photon laurdan imaging. The emission was split between two photomultiplier tubes (PMTs) using a low-pass dichroic filter centered at 460 nm (Figure 69A). To compensate for photoselection effect in vesicles, I added an adjustable quarter-wave plate in the beam path before the scan head. First, a calibration image was obtained using a highly concentrated Laurdan suspension. The GP calibration image was calculated from the blue and red channel emission using equation V.4 with g set to 1.

$$\mathrm{GP}\ (\mathrm{i},\mathrm{j}) = \frac{\mathrm{I_o}(\mathrm{i,j}) - \mathrm{g}(\mathrm{i,j})\mathrm{I_d}(\mathrm{i,j})}{\mathrm{I_o}(\mathrm{i,j}) + \mathrm{g}(\mathrm{i,j})\mathrm{I_d}(\mathrm{i,j})} \qquad (\mathrm{V}.4)$$

Where I_0 and I_d are the ordered (blue) and disordered (red) channels, respectively. While g is the GP calibration image and i and j represent the position of image pixels. Following calibration, data from cells or vesicles were analyzed as follows (Figure 69B):

1. A constant threshold was applied on both channels to remove background. The GP image was calculated according to equation V.4.
2. GP image was converted into binary and a mask was generated after removing connected regions that had a size smaller than a vesicle or a cell. This helped to remove small features in the field-of-view not belonging to structure of interest.
3. After applying the mask on the GP image, the image was converted to RGB.
4. The resultant RGB image was split into three channels Red, Green and Blue. Each of the channels was multiplied with the sum of both channels and combined to form a new RGB image, which is termed Hue-saturation-brightness (HSB) image. This step served to map the GP information onto the structures of cells.

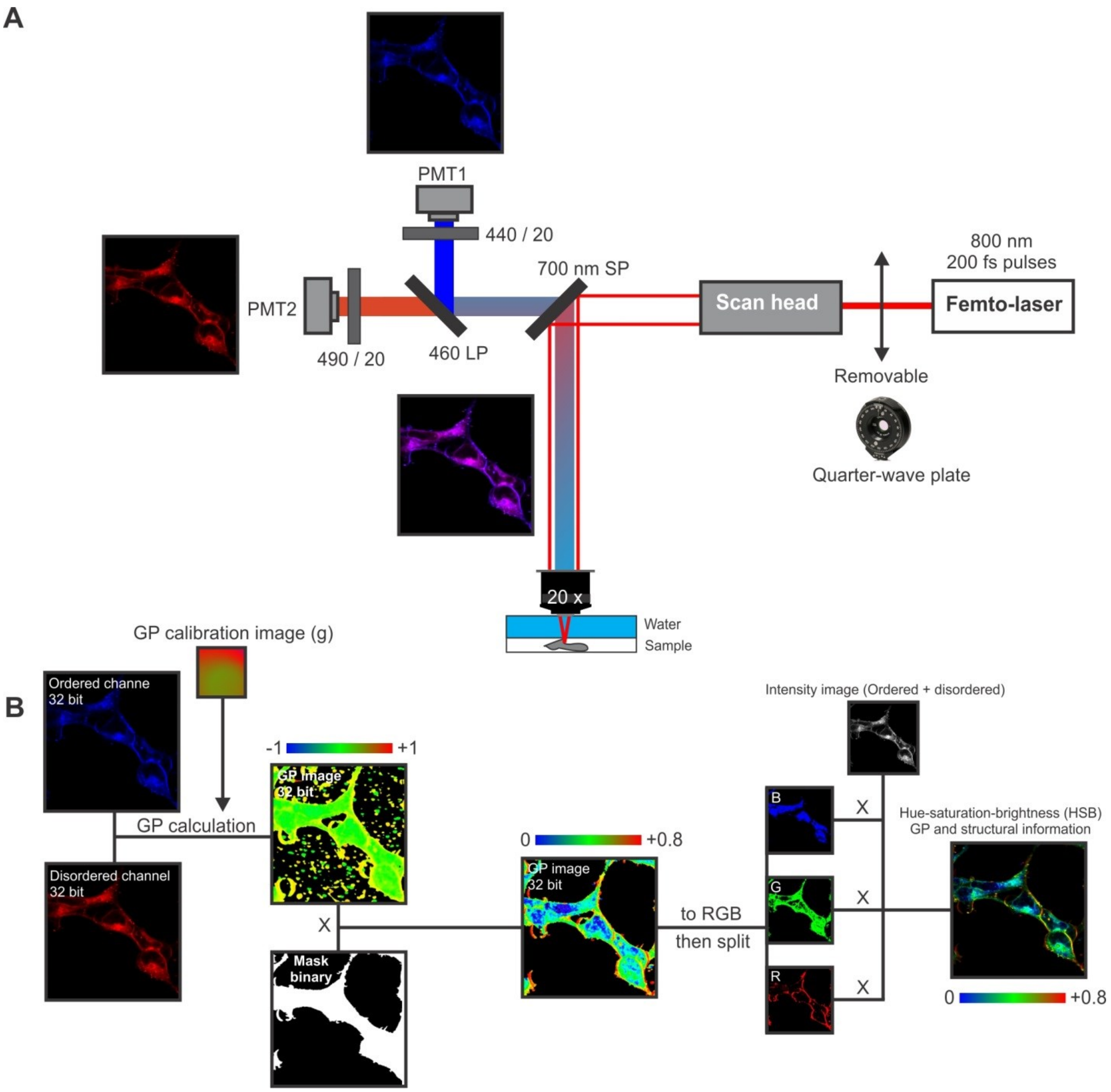

Figure 69. Two photon GP imaging. A. Two photon setup for GP imaging. Emission signal is split between two PMTs using a 460 long pass dichroic filter (460LP). Quarter-wave plate is inserted in the excitation laser beam path to compensate for photoselection effect when imaging vesicles. LP stands for long pass and SP stands for short pass. Images were collected using a water immersion 20x objective with NA = 0.95. **B.** Procedure for GP image processing. A constant threshold was applied on both channels to remove background. The GP image was calculated according to equation V.4, with g being the GP calibration image. GP image was converted into binary and a mask was generated after removing connected regions that had a size smaller than a vesicle or a cell. This helped to remove small features in the field-of-view not belonging to structure of interest. After applying the mask on the GP image, the

image was converted to RGB. The resultant RGB image was split into three channels Red, Green and Blue. Each of the channels was multiplied with the sum of both channels and combined to form a new RGB image, which is termed Hue-saturation-brightness (HSB) image. This step served to map the GP information onto the structures of cells.

An important technical aspect to be considered when imaging Laurdan using two photon microscopy is the photoselection effect [86]. This photoselection effect stems from the orientation of Laurdan inside the membrane (Figure 70A). The transition dipole of Laurdan in phospholipid bilayers is aligned parallel to the acyl chain of the phospholipids. If the lipids are in fluid disordered phase, then the chance of Laurdan dipole moment being parallel to the electric field of excitation light is higher and thereby photoselection is diminished. On the other hand, if the lipids are ordered, then the dye would have a restricted orientation. In this case less dye molecules would be excited (Figure 70B). Using linearly polarized light to image vesicles result in a strong excitation at the plane parallel to excitation electric field (Figure 70C). I imaged vesicles labeled with Laurdan on our two photon set-up with linearly polarized light, and I observed that only two sides of the vesicles are strongly excited (Figure 70D). This effect is even more evident with ordered membranes due to the lower flexibility of Laurdan orientation. We can decrease photoselection effect using circular polarized excitation light. Linear polarized light can be transformed into circular polarized light using a quarter-wave plate (Figure 70E). Imaging the Laurdan-labeled vesicles after adjusting and aligning the quarter-wave plate, showed a decrease in photoselection effect (Figure 70F).

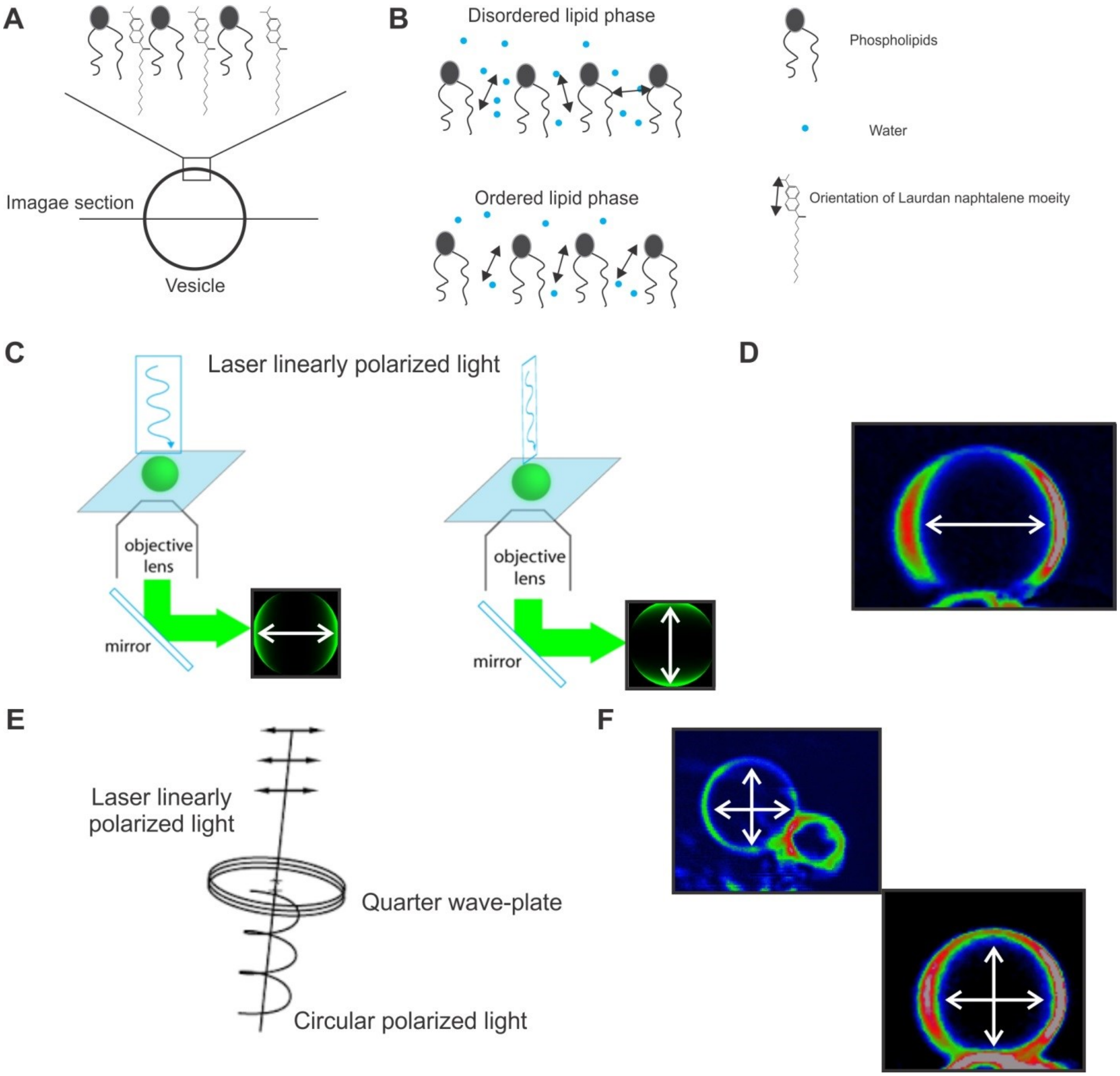

Figure 70. Compensation for the photoselective effect in vesicles. A. Schematic demonstrating the photoselective effect in Laurdan-labeled vesicles when using linear polarized light. **B.** Schematic demonstrating the possible orientations of Laurdan in disordered lipid phase and ordered lipid phases. **C.** Scheme showing the photoselection effect observed in the fluorescence images of vesicles when using linearly polarized light. White arrow is parallel to excitation electric field. **D.** Two photon Laurdan fluorescence images of vesicles that were excited with linearly polarized light. White arrow is parallel to excitation electric field. **E.** A depiction of how we can transform a linearly polarized light into circular polarized light using quarter wave-plate. **F.** Two photon Laurdan fluorescence images of vesicles that were excited with circularly polarized light. White arrows are parallel to excitation electric field.

After the set-up was configured for Laurdan imaging, I established and tested it on cellular membranes. The cells were treated with β-Cyclodextrin (βCD). βCD is a cyclic molecule consisting of seven sugar units and is able to bind hydrophobic molecules in the cavity of its ring-like structure [134]. Thereby, it can extracts cholesterol from the plasma membrane, resulting in a more fluidic and less stacked membrane composition. This control experiment would allow us to verify our sample preparation protocol for vesicle imaging and fixed cell imaging. I tested the approach using HEK293 cells and isolated GPMVs. Using Laurdan imaging and GP image analysis. I could demonstrate a significant decrease in the GP index of GPMVs isolated from βCD-treated HEK293 cells and of intact βCD-treated cells compared to control GPMVs or cells (Figure 71). Both conditions showed regions of high GP that were localized to the outer membranes and regions of low GP values located to inner membranes (Figure 71G). As a consequence the GP histogram consisted of two peaks distribution, which were fitted to a Gaussian that allowed us to estimate the average of both regions (Figure 71H). However, the average GP value of experiments that were performed on different days was varying tremendously (Figure 71C-D). Thus, only measurements obtained on same day and using the same conditions were compared. The next step was to apply this method to analyze dermal fibroblasts.

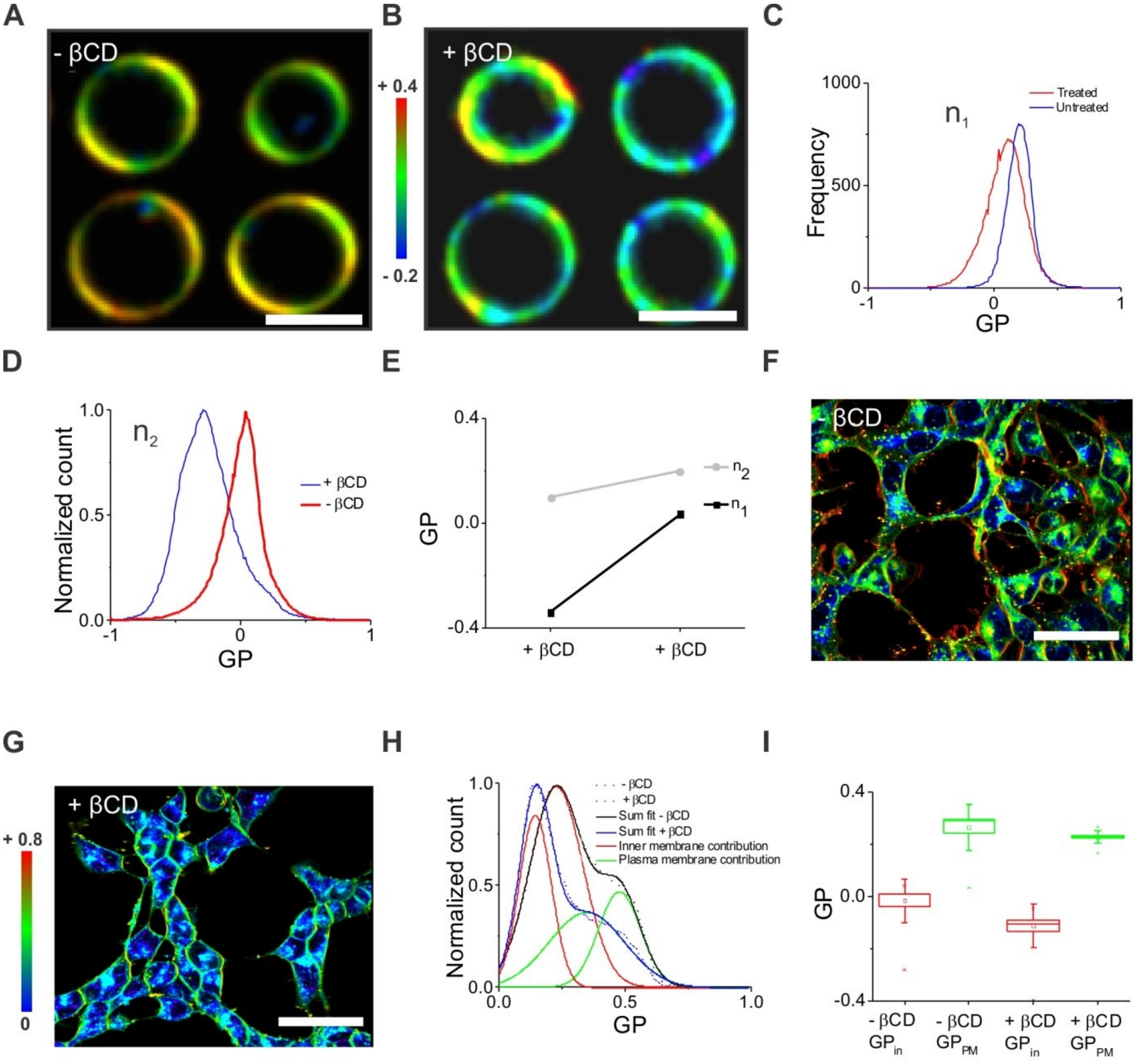

Figure 71. Establishing of GPMV imaging. **A.** GP image of vesicles from untreated HEK293 cells that were. **B.** GP image of vesicles from HEK293 cells that were treated with 10 mM βCD. **C.** Average GP histogram across all pixels obtained from one experiment. Treated histogram is shown in red while untreated histogram is shown in blue. **D.** Average GP histogram across all pixels obtained on a different day from another experiment. Treated histogram is shown in red while untreated histogram is shown in blue. **E.** Plot shows the variation in GP values between the two experiments and between treated and untreated conditions. **F.** RGB GP image of untreated HEK293 cells. **G.** RGB GP image of HEK293 cells treated with 10 mM βCD. **H.** Average GP histograms with two peak distributions for the treated and untreated cells. **I.** Quantification of GP values from 2 experiments. GP_{in} (red) denotes the GP value associated with the inner membranes while GP_{PM} (green) denotes the GP value associated with plasma membrane. Scale bar vesicles: 10 µm, Cells: 20 µm.

I used two photon microscopy to image WT-fibroblasts, WT-fibroblasts treated with 2 µM NBD-NJ and GBA2 KO-fibroblasts (Figure 72). Experiments show that cells can be split into two GP regions: one containing the plasma-membrane and cellular protrusions, which is characterized with high GP values, and the other containing the inner membranes, characterized with low GP values (Figure 72C). This verified earlier reports, demonstrating that outer membranes have higher order than inner membranes [135]. This distribution allowed the extraction of two peaks from the GP image histograms (Figure 72C, F). However, there was no significant difference in both GP regions across all the different samples, neither between WT and KO-fibroblasts, nor between NBD-NJ-treated and non-treated WT-fibroblasts. This might be due to the heterogeneity across samples and uncontrolled environmental factors that contributed to the fluctuations.

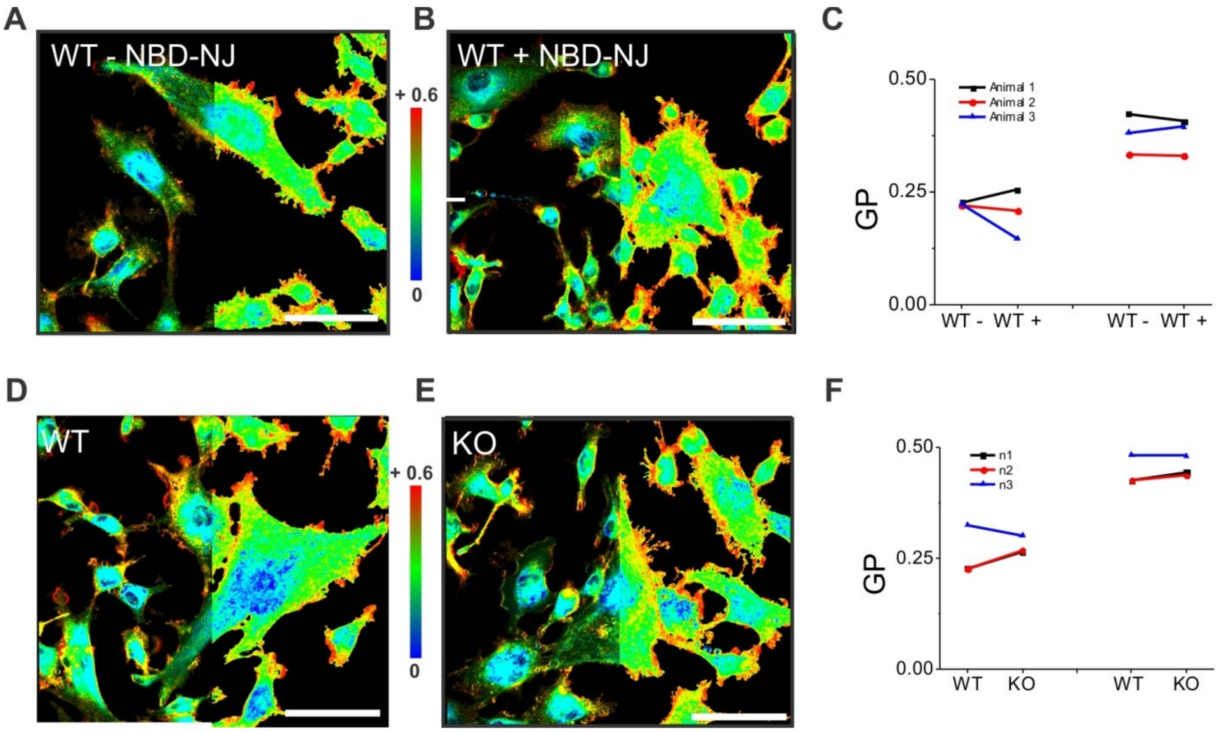

Figure 72. Two photon GP imaging of fibroblasts. A. Intensity-GP merged image (left) and RGB GP image (right) of WT-fibroblasts. **B.** HSB GP image (left) and RGB GP image (right) of WT-fibroblasts treated with 2 µM NBD-NJ. **C.** Plot shows the variation in GP between treated (+) and untreated (-) WT-fibroblasts over the two GP regions (n = 3). **D.** HSB GP image (left) and RGB GP image (right) of WT-fibroblasts. **E.** Intensity-GP merged image (left) and RGB GP image (right) of KO-fibroblasts. **F.** Plot shows the variation in GP between WT-fibroblasts and KO-fibroblasts over the two GP regions (n = 3). Scale bar 20 µm.

5.2. GTPase biosensors

GBA2 KO-fibroblasts showed altered cytoskeletal dynamics [78]. In order to investigate the spatial correlation between cytoskeletal dynamics and membrane stacking, I first established GTPase FRET imaging on a widefield/TIRF setup. Rac1 and Cdc42 were chosen for the study due to their role in lamellopodia and filopodia formations; two structures that were altered in GBA2 KO-fibroblasts [78]. I tested the expression of Rac1 and Cdc42 FRET biosensors in HEK293 cells first, and established a measurement and analysis protocol. To correct for bleedthrough and excitation cross-talk, I expressed individual fluorophores, Cerulean (Figure 73B), and Citrine (Figure 73E) in HEK293 cells. The bleedthrough was measured by either calculating the slope from the colocalization between the respective channel and FRET channel (Figure 73C) or by finding the average ratio of the respective channel and FRET channel (Figure 73D). However both methods gave comparable results. The measured bleedthrough of cerulean into FRET channel was 51 %, while cross-excitation of citrine was 6 % (Figure 73F). Measuring dynamics of GTPase activity requires illuminating the sample for long durations and thereby bleaching the fluorophores. I corrected for this bleaching by fitting the intensity time trace in individual channels to a single exponential and then multiplying the data with the inverse of the fit (Figure 73H). Alternatively, I could rely on the fact that the average FRET ratio does not change with time but rather small local changes occur in the cell. This way, I could fit the FRET ratio time trace to an exponential and use it to correct the FRET movie (Figure 73I). Of note, citrine channel was only monitored to confirm the colocalization and co-expression of FRET pairs of the intermolecular biosensor. It was not used for FRET ratio calculation.

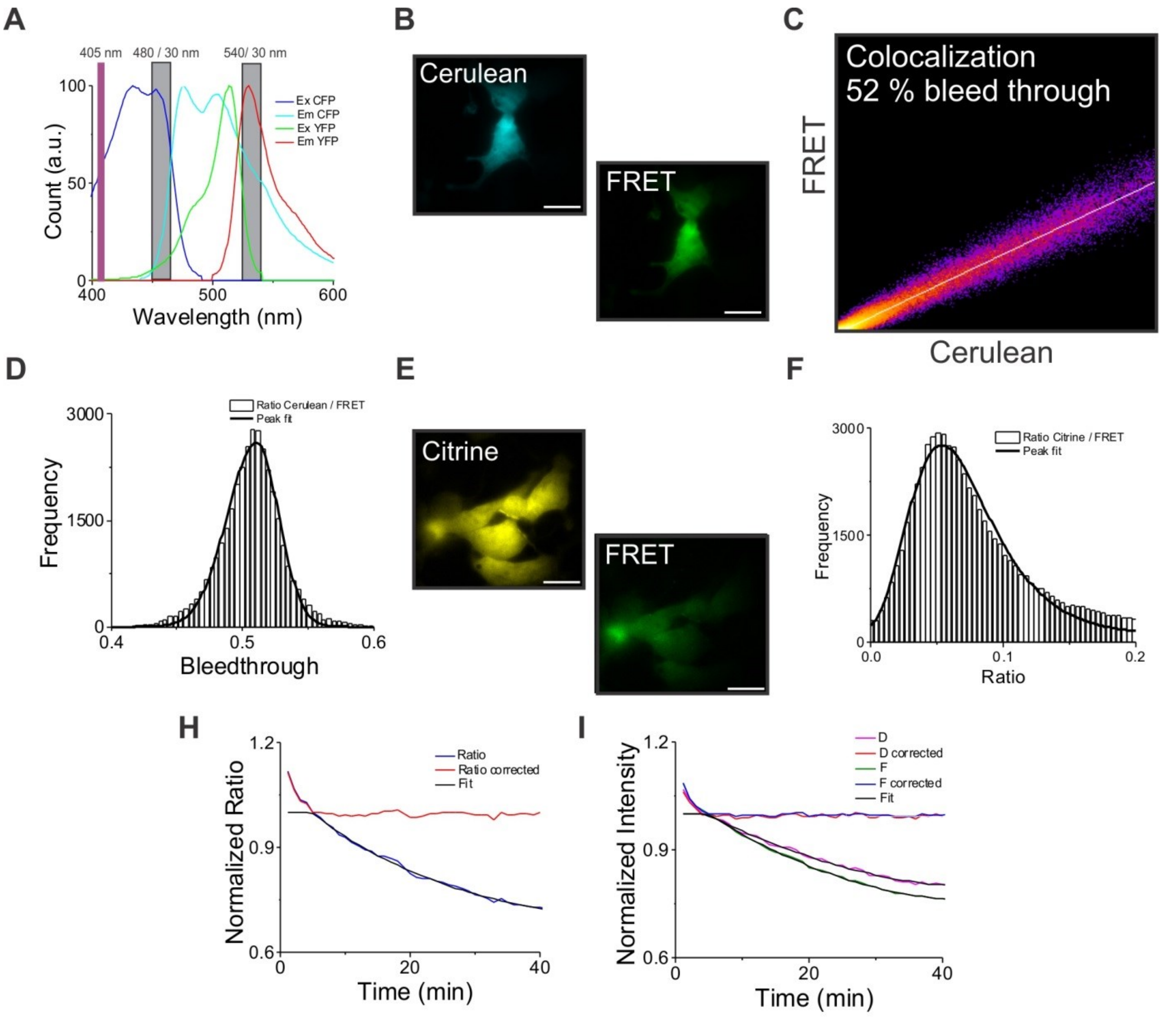

Figure 73. FRET calibration process. A. Excitation and emission spectra of the GTPase FRET biosensors, with donor and acceptor. **B.** Fluorescence images of HEK293 cells expressed with donor only. **C.** Colocalization of FRET and cerulean channels in cells that were expressed with donor only, white line is a straight line fit with a slope of 0.52. **D.** Histogram of the ratio FRET/Cerulean of cells that were expressed with donor only. **E.** Fluorescence images of HEK293 cells expressed with acceptor only. **F.** Histogram of the ratio FRET/acceptor of cells that were expressed with acceptor only. **H.** Time traces of FRET ratio in cells that were expressed with both FRET pairs. The exponential fit was used to correct the overall FRET ratio. **I.** Time traces obtained from fluorescence images of HEK293 cells expressed with both FRET pairs. D denotes time trace of donor channel and F denotes time trace of FRET channel. The exponential fit was used to correct for bleaching in individual channels. Scale bar 10 µm.

I measured the FRET changes with time in HEK293 that expressed the GTPase FRET biosensors. FRET activity map of the Cdc42 biosensor showed a high activity mainly in the protrusions (Figure 74A). The kymograph from the FRET data (Figure 74B) showed Cdc42 activation and deactivation at the protrusions while Cdc42 remained inactive at the basal cell body. The same was seen with Rac1 biosensor in HEK293 cells (Figure 74C-D). These observations are in line with what has been reported on Cdc42 and Rac1 activity in cells [136].

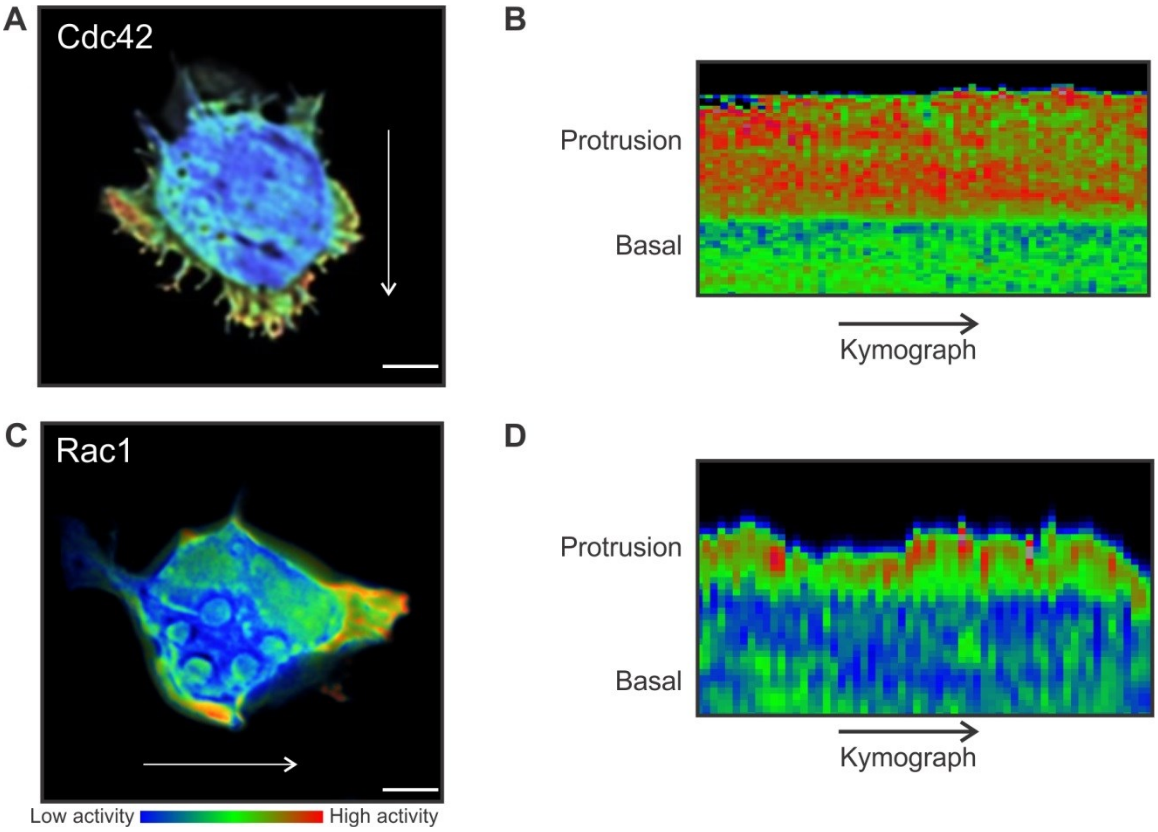

Figure 74. GTPase biosensor test in HEK cells. A. Cdc42 activity map. FRET ratio was RGB-color coded and applied on the deconvolution of the intensity image which resulted in HSB FRET image. Arrow shows the possible direction of movement. **B.** Kymograph taken at the cell edge, showing high Cdc42 activity at the protrusions and low activity at the basal cell body. **C.** Rac1 activity map. FRET ratio was RGB-color coded and applied on the deconvolution of the intensity image which resulted in HSB FRET image. Arrow shows the possible direction of movement. **D.** Kymograph taken at the cell edge, showing high Rac1 activity at the protrusions and low activity at the basal cell body. Scale bar 10 µm.

5.3. Outlook – currently in progress

5.3.1. Correlation of GTPase activity and GlcCer accumulation

Now that we have established the expression and GTPase temporal and spatial mapping in HEK293 cells. I moved to primary fibroblast which is more difficult to transfect. Unlike HEK293 cells, only electroporation method gave sufficient expression levels to map GTPase activity in fibroblasts. FRET images showed high Rac1 activity at the protrusion sites in WT-fibroblast relative to the basal cell body (Figure 75A). This high activity correlates spatially with the high GP values or in other words high membrane stacking (Figure 75B). In order to study this correlation in WT and KO-fibroblasts in a more systematic way we will need to work on a new method that can multiplex GP and FRET imaging. In this case we might be able to decrease fluctuation in GP values between samples by focusing on and comparing only areas of interests, where GP and GTPase activity show high correlations. Laurdan cannot be used for this purpose because its spectrum overlaps with the donor/FRET emissions (Figure 75C). However, di-4-aneppsdhq could replace Laurdan and provide a possibility to multiplex FRET and GP measurements (Figure 75D). This dye could be measured in ratiometric mode, similar to Laurdan [82]. Moreover, fluorescence lifetime microcopy and second harmonic generation imaging in single channel can also be used to investigate membranes using this dye [137].

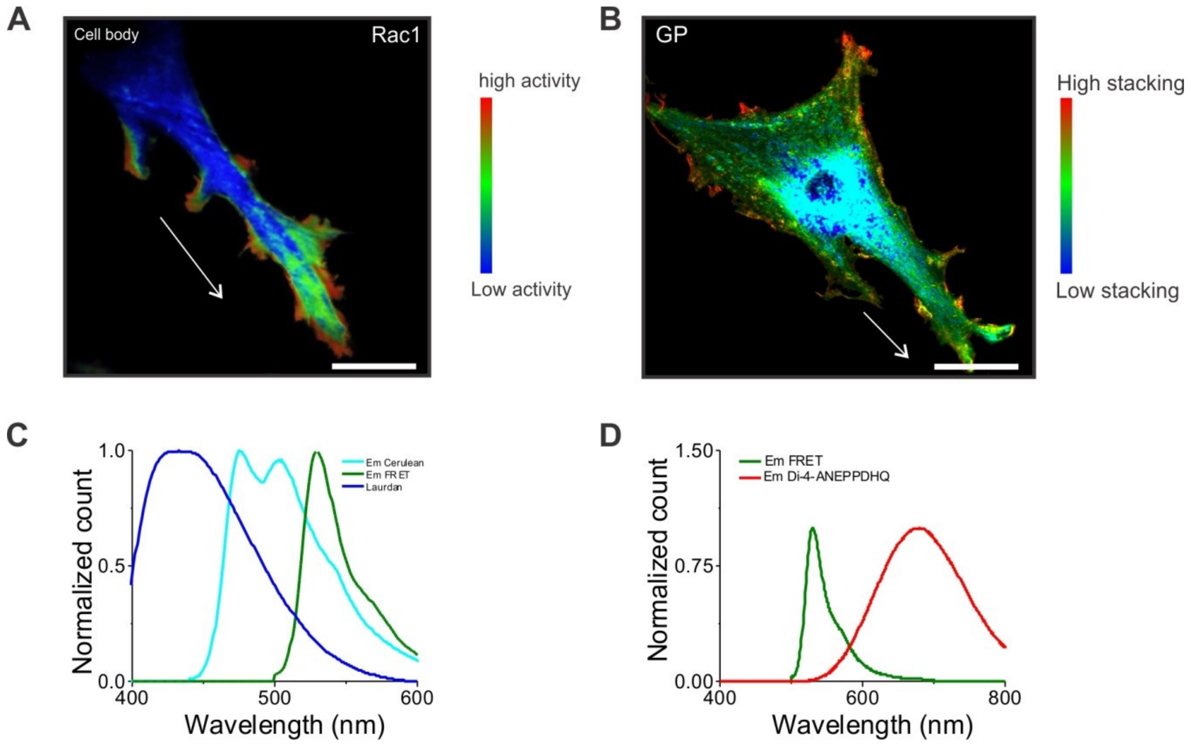

Figure 75. GTPase activity and membrane stacking in fibroblasts. A. Rac1 activity map of WT-primary fibroblast. FRET ratio was RGB-color coded and applied on the deconvolution of the intensity image which resulted in HSB FRET image. Arrow shows the possible direction of movement. **B.** GP map of primary WT-fibroblast. GP was RGB-color coded and applied on the intensity image which resulted in HSB FRET image. Arrow shows the possible direction of movement. **C.** Emission spectra of FRET pair and Laurdan. **D.** Emission spectrum of acceptor and di-4-annepsdhq. Scale bar FRET: 10 µm, GP: 20 µm.

5.3.2. Investigating membrane stacking in cerebellar primary neurons

In addition to the role in spermatogenesis, GBA2 enzyme might play a role in the brain. Recently, it has been reported that patients carrying a mutation in *GBA2* gene suffer from cerebellar ataxia and severe spastic paraplegia with varying degrees of cerebellar and corpus callosum atrophies [138,139]. Studies performed by my colleagues (Marina Woeste and Carina Marx) showed that muscle strength in GBA2-KO mice is severely impaired with a high expression of GBA2 enzyme revealed in the cerebellum but not in muscles. Therefore, we hypothesized that accumulation of GlcCer alters the membrane properties of neurons as well, which in turn affect cytoskeletal dynamics leading to the phenotypes associated with the lack of GBA2. To test this hypothesis I extended the GP analysis to primary cerebellar neurons.

Similarly to fibroblasts, primary cerebellar neurons from isolated WT mice were treated with 2 μM NBD-NJ for 48 hours before two photon GP imaging (Figure 76A-B). The average histogram of GP values showed a shift to higher GP values for the treated condition (Figure 76C). This was also observed with isolated vesicles from the fibroblasts where treated condition had higher GP values. Moreover, primary cerebellar neurons from GBA2-KO mice were treated similarly to neurons from WT mice and then imaged. The average histogram of GP values did not show any variation (Figure 76F), suggesting that the GBA2 inhibitor did not lead to a change in the membrane composition of the neurons and in turn had no effect on GBA2-KO mice due to the lack of the enzyme. Since the GP average fluctuated between animals, I only compared experiments done on the same animal and in case of WT versus KO, only experiments done on same day were compared. In conclusion, GP analysis of neurons from 5 WT and 4 GBA2-KO animals showed a trend of GP change towards higher values after NBD-NJ treatment for WT animals (Figure 76H). However, when we compare GP values between neurons obtained from WT and GBA2-KO animals, we do not see a clear difference (Figure 76I) which could be due to the membrane heterogeneities between animals.

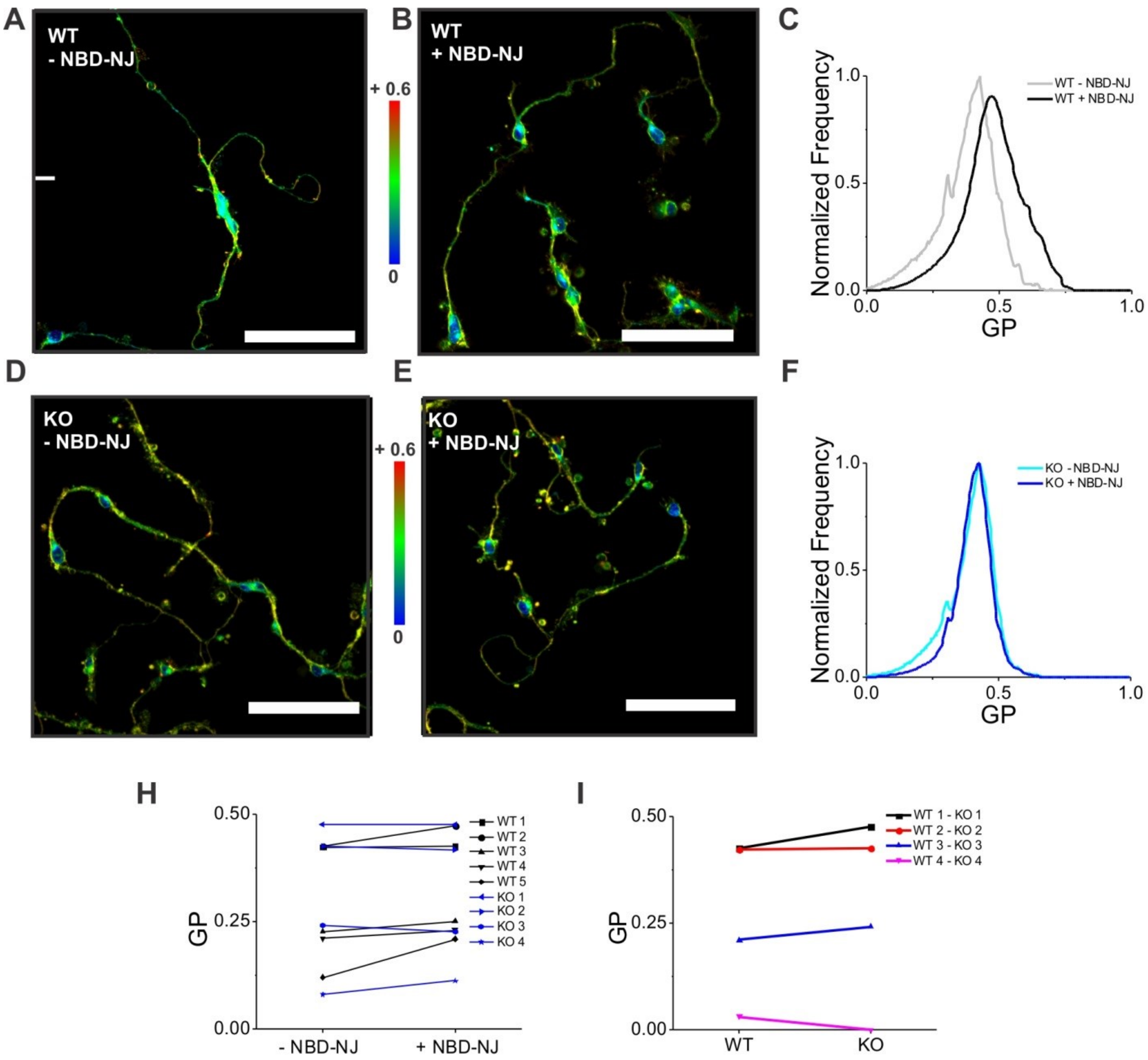

Figure 76. GP imaging on cerebellar primary neurons. A. GP image of untreated primary cerebellar neurons from WT mice. **B.** GP image of primary cerebellar neurons from WT mice that were treated with 2 µM of NBD-NJ. **C.** Average GP histogram across all pixels from treated and untreated WT cells. **D.** GP image of untreated primary cerebellar neurons from GBA2-KO mice. **E.** GP image of primary cerebellar neurons from GBA2-KO mice that were treated with 2 µM of NB-DNJ. **F.** GP histogram across all pixels from treated and untreated GBA2-KO cells. **H.** Plot shows the variation of GP between treated and non-treated neurons of same animal. **I.** Plot shows variation of GP values between WT and GBA2-KO neurons from experiments that were done on same day. Scale bar: 20 µm.

VI. Discussion

In my thesis, I addressed different aspects of sperm physiology. First, using reverse opto-chemical engineering (ROCE), my results provided a quantitative description of the molecular events underlying the binding of one resact molecule to sea urchin sperm. Second, I established an *in vivo* assay to measure cGMP dynamics, which provided insights into PDE activity and cGMP hydrolysis in sea urchin sperm. Third, I developed a new labeling strategy to tag the chemoreceptor in sea urchin sperm and elucidate its supramolecular organization. In mammals, and in particular in human sperm, the "chemoreceptor" is CatSper, the principal Ca^{2+} channel controlling sperm motility. Using super-resolution microscopy, my results demonstrated a quadrilateral arrangement of CatSper in mouse and in human sperm. Last but not least, I established methods to study the effect of lipid environments on cytoskeletal dynamics to reveal the physiological function of GBA2 during sperm development.

1. What is the molecular mechanism underlying single-molecule sensitivity and cGMP dynamics in sea urchin sperm?

Caged compound-based ROCE demonstrated that the binding of a single resact molecule produces on average 6 to 9 cGMP molecules, resulting in a unitary voltage response of about 2 mV. Earlier studies reported the synthesis of 11 cGMP molecules per activated GC, which is in line with our results [4]. In rod photoreceptors the large enzymatic amplification allows the transduction of a single-photon absorption into a measurable macroscopic response [18]. There is no large enzymatic amplification in sperm, therefore, how can sperm transduce a single binding event into a voltage response without relying on a similarly large enzymatic amplification? The answer lies in the exquisite sensitivity of CNGK and CatSper channels to minute changes in cGMP and pH_i. The CNGK channel is exquisitely sensitive to cGMP in a non-cooperative fashion with $K_{1/2}$ = 26 nM and a hill coefficient of unity [4]. Thus, binding of one cGMP molecule can open a single channel. In contrast, the CNG of rods is non-selective, 1000-fold less sensitive to cGMP, and opens upon cooperative binding of more than one cGMP molecule. Upon a single-molecule response, 9 cGMP molecules are synthesized by a GC, thereby increasing the cGMP concentration by 9 nM (assuming flagellar volume of 1.6 fl). At this low concentration, cooperative binding of several cGMP molecules to a single CNGK channel would impair rather than enhance the sensitivity in sea urchin sperm. Instead, CNGK channels evolved to work at extremely low ligand concentration. How can such a low number of cGMP molecules result in a measurable elementary voltage response? We do not know how many of the 9 cGMP molecules bind to CNGK channels and how many are hydrolyzed by the PDE, before they can reach a channel. Nevertheless, due to the large input resistance of sea urchin sperm, even the opening of a single CNGK channel might be sufficient to produce an elementary voltage response of 2 mV. This is in contrast to photoreceptors, where a single-photon response of 1 mV requires the closure of several hundreds of CNG channels [25]. How is the single-molecule Ca^{2+} response generated? CatSper in sea urchin sperm is activated by the combination of two steps: alkalization shifts the voltage dependence by -30 mV, allowing CatSper to open during depolarization. The pH dependence of CatSper is very steep with a hill coefficient of ca. 11 [6]. This allows CatSper to accurately relay the elementary changes in pH_i and V_m into Ca^{2+} signals. Consequently, high amplification might not be needed to produce a macroscopic measurable Ca^{2+} response. It is important to note that the single-molecule Ca^{2+} response measured from a sperm population represents the ensemble average of unitary responses. Therefore, we are currently working on a mathematical model that allows us to extract the single-molecule response of a single cell from the population measurements. Alternatively, single-molecule Ca^{2+} responses are being recorded in single cells with fluorescence microscopy and the unitary response will be compared with the one derived from the population measurements. Spontaneous activation of GC might result in a Ca^{2+} signal that resembles a single-molecule response and, thereby, compromises precision in single-molecule regime. Ca^{2+} imaging in non-stimulated single cells will allow us to estimate the spontaneous inactivation rate of a GC, which is crucial for single-molecule detection. Preliminary results in our group suggest that the GC has a very low spontaneous activation rate. Eventually, unraveling the single-molecule response in single cells would allow us to answer a very important question: Is the single-molecule response uniform between trials? Until now, only rod photoreceptors are known to have a highly reproducible single-photon response [18]. Similar to rhodopsin in rods, the GC has a very low spontaneous activation rate and its inactivation occurs via a multi-stage auto-dephosphorylation, which could allow for precise lifetime control and, thereby, reduction of ‘molecule noise’ that limits the ability to register single molecules [12].

A cGMP-signalling pathway mediates the Ca^{2+} response that controls chemotactic swimming behaviour of sperm. The Ca^{2+} signal is evoked by a transient hyperpolarization; during recovery from the hyperpolarizing peak, CatSper channels open and Ca^{2+} enters the cell. The mechanism that controls the recovery of the membrane voltage after hyperpolarization is ill-defined. Two mechanisms may contribute to recovery: 1) closure of CNGK channels due to PDE activity, resulting in cGMP hydrolysis, and 2) opening of HCN channels upon hyperpolarization, resulting in a Na^+ inward current that depolarizes the cell membrane. The HCN channel is well characterized in heterologous cell systems [5] but its contribution *in vivo* is not known. Moreover, the regulation of PDE activity is not well understood. To isolate the contribution of cGMP hydrolysis by the PDE from HCN activity during the recovery phase, we designed an *in vivo* assay for CNGK activity. In the presence of 100 mM K^+ in the external medium, the reversal potential V_{rev} for a K^+-selective channel is -36.7 mV, i.e. more positive than the resting voltage V_{rest} of about -50 mV. Thus, activating CNGK by cGMP should produce a depolarization rather than hyperpolarization, and the recorded changes in voltage are solely due to binding and dissociation of cGMP to CNGK channels, while HCN channels are mostly closed [5]. The data suggest that after a stimulus, the hydrolysis of cGMP by the PDE mediates the recovery at a significantly slower rate than the recovery due to opening of HCN channels. Therefore, upon stimulation, both depolarization carried by HCN channels and cGMP hydrolysis by the PDE contribute to the recovery at different rates. However, it is not known whether the PDE is constantly active or if it is regulated by e.g. cGMP, pH, or Ca^{2+}. At -36.7 mV, the sNHE is inactive and no changes in pH will occur, therefore, CatSper is not activated and no Ca^{2+} influx occurs. The PDE hydrolyses cGMP even when the membrane potential is at -36.7 mV, suggesting that pH and Ca^{2+} do not activate the PDE. The PDE that hydrolyses cGMP in sea urchin sperm is PDE5 [140]. PDE5 has two GAF domains that constitute potential allosteric binding sites for cGMP. PDE5 in mammals was shown to be directly activated by cGMP [141]. However, it remains to be established whether PDE5 in sea urchin sperm is constitutively active or is activated by cGMP.

1.1. How do sperm transduce periodic changes in chemoattractant concentration into periodic swimming?

Due to the circular movement in a gradient, sperm are periodically exposed to higher and lower chemoattractant concentration. Thus, periodic movement results in a periodic stimulation followed by cytosolic Ca^{2+} oscillations that initiate a periodic change in the asymmetry of the flagellar beat, resulting in periodic variations of curvature and torsion of the path [125]. A quantitative theory of this chemotactic steering by [125] describes navigation along periodic paths: a cellular signaling system transforms the periodic stimulation $s(t)$ (chemoattractant binding) into a periodic intracellular signal $i(t)$ (Ca^{2+} bursts) that, in turn, modulates the swimming path curvature $\kappa_{\mathrm{p}}(t)$ (equation VI.1). The phase shift between $s(t)$ and $\kappa_{\mathrm{p}}(t)$, representing the latency of the Ca^{2+} signal, determines the directed drift of circles up or down a 2D chemical gradient. I validated this quantitative theory and showed that sperm were able to transduce periodic stimulations as fast as 5 Hz. Our results suggest that sperm generate periodic Ca^{2+} oscillations that are phase-locked to the stimulus with a fixed phase shift. The phase shift is due to the delay between the sequence of events separating the release of cGMP and the influx of Ca^{2+}. Because, recovery from stimulation due to PDE activity is too slow to allow pacing of fast Ca^{2+} oscillations, HCN could be the "pacemaker", pacing the fast Ca^{2+} oscillations. In neurons and in the sinoatrial node of the heart, HCN channels plays a similar role by controlling rhythmic electrical activity, and are therefore called pacemaker channels [142].

The single-molecule Ca^{2+} response shows that Ca^{2+} signal need more than 5 seconds to recover to resting levels, while the angular frequency of the sperm 2D circular swimming path is ca. 1 Hz. Then, how is the sperm able to follow stimulations as fast as 1 Hz and what is the underlying signaling pathway that produces fast Ca^{2+} oscillations? Two signaling components are responsible for the fast rise and drop in Ca^{2+} , CatSper channel and Na^+/Ca^{2+}-K^+ exchanger (NCKX). At resting membrane potentials the NCKX is active, thereby keeping $[Ca^2]_i$ at low levels. Upon stimulation, the Ca^{2+} influx is evoked by a transient hyperpolarization; during recovery from the hyperpolarizing peak, which is initiated by HCN, CatSper channels open and Ca^{2+} enters the cell. The subsequent stimulation hyperpolarizes the cell membrane thereby closing CatSper channels. A shift to more negative membrane potentials caused by the hyperpolarization enhances the activity of NCKX and Ca^{2+} is rapidly extruded from the cell, thereby $[Ca^{2+}]_i$ returns to resting values and prepares the cell for the next stimulation. The alternating activation/deactivation of CatSper and modulation of NCKX activity allows the sperm to produce periodic Ca^{2+} oscillation. Finally, the sinusoidal waveform $(\sin(2\pi f t) + b)$, used to uncage cGMP and produce a periodic stimulation, results in a cGMP concentration G(t) that is proportional to the integral of the light waveform $(\int(\sin(2\pi f t) + b)) \propto (\cos(2\pi f t) + bt)$, which is a cosine function (Figure 26). Interestingly, sperm respond with voltage that is proportional to the first derivative of G (t), where $V_m(t) \propto \frac{dG(t)}{dt} \propto \sin(2\pi f t)$ and Ca^{2+} signal C (t) follows the voltage waveform with the addition of a phase shift φ where $C(t) \propto \sin(2\pi f t + \varphi)$; therefore, V_m and Ca^{2+} do not show a cumulative response. The PDE activity can accommodate the cumulative rise in cGMP concentration and thereby could be the reason why sperm respond only to changes rather than a steady increase in [cGMP], while HCN paces the fast oscillations. In conclusion, sperm transduce only rapid changes in stimulus and somehow ignore steady stimulation. In conclusion, $[Ca^{2+}]_i$ oscillations is phase-locked with the time derivative of G (t), and the time derivative of $[Ca^{2+}]_i$ controls the curvature of swimming path (k_p) (equation VI.1) [143]. This result suggests that sperm acts as a differentiator.

$$k_p(t) = k_1 + \beta \frac{d[Ca^{2+}]}{dt} \qquad \text{(VI.1)}$$

Where k_p denotes the curvature of the swimming path, k_1 denotes the basal curvature, and β is a proportionality factor.

When subjected to discrete stimulation, sperm are able to integrate and count cGMP molecules within 200 ms; after that, integration is incomplete. It was suggested that the sampling time is related to the inactivation time of the GC, which is around 300 ms [124]. The concept of sampling period was first introduced by [126], suggesting that sperm sample resact molecules impinging on the flagellum for 200-600 ms before they produce a response. This allows sperm to measure changes in the chemoattractant concentration at different time points [126]. However, the observed Ca^{2+} periodic oscillations that are phase-locked to the periodic stimuli show that sperm continuously sample the impinging chemoattractant concentration and continuously convey the temporal changes in concentration into a temporally varying Ca^{2+} signal, which, in turn, elicits a periodic swimming behavior.

2. Supra-molecular arrangement of sensory molecules in sperm

Sensory receptors often form highly organized supramolecular complexes. For instance, chemoreceptors in bacteria are organized in a hexagonal array, that confers high sensitivity [57]. The visual pigment rhodopsin is organized in densely packed rows of dimers in the disk membrane of mammalian rod photoreceptors [20]. Rhodopsin organization has been proposed to provide a structural platform that binds signalling molecules and coordinate their spatio-temporal interaction. The principal Ca^{2+} channel CatSper forms a quadrilateral arrangement along the flagellum of mouse sperm [34], thereby building a platform for structurally distinct Ca^{2+} signaling domains. Using STORM, I verified the CatSper organization in mouse sperm and revealed that CatSper organization in human sperm is similar. However, the supramolecular arrangement of the GC receptor in sea urchin sperm is not known. Finally, the GC in sea urchin sperm is one of the most densely packed membrane receptors, and solving its supramolecular organization could reveal the structural platform underlying single-molecule detection. Therefore, I developed a new labelling strategy to tag the GC and elucidate its organization using STORM imaging.

2.1. How to elucidate the supra-molecular arrangement of the chemoreceptor?

Sperm from different species not only use diverse repertoires of sperm-specific signaling molecules, but also possess different morphology. For instance, sea urchin sperm flagella do not contain cytoskeleton elements around the axoneme. Thus, the sea urchin sperm flagellum has a smaller diameter compared to mammalian sperm, rendering STORM imaging using antibodies impossible to resolve a potential GC supra-molecular organization.

In an attempt to minimize the offset between the GC and the fluorescent label - caused by the finite size of antibodies, resact was modified with a photo-crosslinker for covalent coupling with the receptor and alkyne groups for direct dye-labeling using click chemistry. The resact analogue is called photoresact and its affinity is not compromised by the modification. However, SDS-PAGE analysis of sperm protein lysates crosslinked to photoresact and clicked to a dye revealed a prominent dye-labeled band at 60-70 kDa. The band was competed with an excess of resact but not speract, suggesting high specificity of photoresact binding. Surprisingly, the estimated Molecular weight (MW) of the protein does not correspond to the MW of the GC at ca. 130 kDa, which has been identified earlier as the resact receptor using chemical crosslinking [131]. Here, the band showed a mobility shift upon addition of resact, indicating dephosphorylation and suggesting deactivation upon resact binding. Based on this evidence, the GC has been proposed to be the resact receptor. I used photo-crosslinking to covalently couple resact to the receptor while in the literature they used chemical crosslinking [131]. Therefore, I tried to reproduce the results from the literature using a resact analogue and chemical crosslinking. However, the results again did not show a predominant band at the expected MW of the GC, but rather at a lower molecular weight. Interestingly, a similar approach in *S. purpuratus* and *L. pictus* sea urchin sperm resulted in a predominant band at 75-80 kDa and two minor bands at 137 and 215 kDa [130]. I verified the results from *S. purpuratus* sea urchin sperm with photo-crosslinking and my results were in line with the literature. Therefore, the data suggests the presence of an apparent speract receptor other than the GC in *S. purpuratus*. Two questions arise: Is this a crosslinking artifact or do sea urchin sperm from different species have different receptors, despite the fact that they share all other signaling motifs and components? And why the crosslinking approaches in *A. punctulata* does not agree with results from earlier crosslinking approaches? In the study that identified the resact receptor in *A. punctulata,* the data was not conclusive and the authors left the identity of the actual receptor, as opposed to a closely associated protein, open for discussion [131]. In the study to identify the speract receptor in *S. purpuratus*, the authors suggested that the putative receptor could be associated with proteins, which are not accessible by the cross-linker [130]. If the receptor is not accessible to chemical crosslinking, using a bifunctional group with different arm lengths could prove to be successful in probing the receptor identity. Nevertheless, both, resact and speract cause elevations of cGMP in intact sperm cells and activation of GC in sperm lysates from *A. punctulata* and *S. purpuratus,* respectively. Therefore, regardless of the identity of the binding proteins, both appear to be coupled to GC [144].

Recently, our research group determined the GC organization using cryo-EM. The GC is organized as a stripe of dimers, which regularly coils as a helix around the flagellum, resulting in coverage of 25 % of the flagellar surface. This architecture may indicate a physiological role for the exquisite sensitivity of sperm to the chemoattractant. For instance, the GC density is uniform along the flagellum, resulting in a high capture probability throughout the entire flagellum. As a consequence, the flagellum is an isotropic sensor, which does not show compartmentalization regarding chemoreceptor organization. Finally, the supra-molecular arrangement of CNGK, CatSper, and other signaling components are still not known. STORM imaging could be combined with expansion microscopy [145] to provide a structure resolution capable to probe and elucidate the supra-molecular organizations of all the signaling components in sea urchin sperm.

2.2. What is the function of the CatSper quadrilateral domain in human sperm?

The principal Ca^{2+}-channel in mouse sperm forms a quadrilateral arrangement along the flagellum [34], organizing a structurally distinct Ca^{2+} signaling domain. The integrity of the Ca^{2+}-signaling domains is crucial for hyperactivated motility and rheotaxis [33]. My results demonstrate that CatSper in human sperm is also organized in quadrilateral domains, which was also shown in a recent publication [133]. However, it is not known yet, whether CatSper also organizes the Ca^{2+} signaling domains in human sperm. Although mouse and human sperm share the same CatSper organization, the function of this organization in human sperm has yet to be determined. The CatSper organization in human sperm that lack any of the CatSper subunits have to be revealed and the organization of its Ca^{2+} signaling domains have to be uncovered before we can elucidate the function of the CatSper organization. Should a functional role of the CatSper domain be discovered, STORM imaging of CatSper in human sperm could serve as a diagnostic tool to probe the molecular structures behind the associated behavioral observations.

3. What is the underlying mechanism behind the dysregulation in cytoskeletal dynamics in cells lacking GBA2 enzyme?

During spermatogesis, sperm develop from a round cell into an elongated cell with a head and a tail. This morphogenesis is driven by complex interactions between germ and Sertoli cells and is controlled by the cytoskeleton. Our results show that the glycosphingolipid GlcCer accumulates in the membrane due to the lack of GBA2. In turn, GlcCer accumulation induces actin polymerization and microtubule persistence, which has been suggested to underlie the development of globozoospermia and male infertility [78]. So far, only ceramide - the building block of GlcCer, has been proposed to promote actin polymerization in mouse embryonic stem cells (ESCs) through protein kinase C activation and focal adhesion kinase/paxillin-dependent-N-WASP/Cdc42/Arp2/3 complex formation, thereby increasing cell migration [146]. It is possible that the increase in ceramide levels result in an increase in GlcCer levels, which, in turn affects, actin polymerization. Also other lipids have been shown to regulate actin polymerization. For instance, the phospholipid PIP_2 controls actin dynamics in highly polarized cells like immune T cells and neurons. PIP_2 accumulates in membrane microdomains, which regulate protein function and form signaling complexes at the plasma membrane [147]. Also other glycosphingolipids accumulate in microdomains called lipid rafts [148]. Lipid rafts compartmentalize in the plasma membrane through lipid-lipid, lipid-protein, and membrane-cytoskeletal interactions [149]. Laurdan measurements using GPMVs demonstrated that accumulation of GlcCer in the absence of GBA2 activity results in a more ordered lipid packaging of the plasma membrane. However, this data does not reveal the cellular localization of this accumulation. Thus, I established laurdan GP imaging in cells. Unfortunately, there was no significant difference between WT and GBA2-KO cells due to the high variability between cells and the difficulty to separate the plasma membrane from inner membranes that are also labeled. However, the membranes of cellular protrusions like fillopodia or lamellipodia displayed a highly ordered lipid environment compared to the rest of the cell. GBA2 knockout-cells display a higher number of filopodia and lamellipodia, which is probably due to an increase in actin polymerization at the protrusion site. Members of the Rho family of GTPases, such as Cdc42 and Rac1, have been shown to regulate cytoskeletal dynamics [76,77] and, in particular, the formation of filopodia and lamellipodia, respectively. Therefore, GlcCer accumulation in the plasma membrane could affect the function of proteins like Cdc42 and Rac1, thereby, dysregulating cytoskeletal dynamics. To measure Cdc42 and Rac1 activity in WT and GBA2-KO cells, I established FRET imaging in live cells using Cdc42 and Rac1 intermolecular biosensors. Preliminary results revealed a high activity of both GTPases at the protrusions site, which correlate with high lipid ordering observed with laurdan GP imaging. I am now working on multiplexing the two imaging methods to explore the relationship between plasma membrane microenviroment and GTPase activity in GBA2-KO cells. But, how GlcCer accumulation dysregulates GTPase activity and, thereby, results in defects during spermatogenesis? During spermatogenesis, the polarized Sertoli cells are connected to germ cells via the ES at the apical end. This connection allows the exchange of proteins and lipids between the two cells, which is crucial for sperm development. GlcCer might accumulate at the junction between the germ and Sertoli cells and disrupt the exchange and the activity of membrane-associated proteins, such as

Cdc42 and Rac1. The two GTPases play a role in regulating the cytoskeletal dynamics that are responsible for sperm-head shaping. It has been shown that accumulation of PIP_2 in other polarized cells, such as T cells, results in microdomains at the immunological synapse. Upon antigen binding to the T cell receptors, lipids in the membrane reorganize, resulting in the clustering of the receptors with lipids, thereby, forming the immunological synapse [128]. Adhesion molecules and junctional proteins are then recruited to the synapse, which include proteins that control the actin cytoskeleton, such as talin, vinculin, and ERM proteins. This recruitment initiates lymphocyte migration [150,151] and dysregulation of the lipid environment at the immunological synapse could alter the control of cytoskeleton and thereby alter lymphocyte migration. Our group reported that F-actin hoops in the ES and the microtubule manchette in spermatids were disrupted in GBA2-knockout testis: F-actin structures were misaligned around developing sperm heads and the microtubule manchette was more elongated compared to that observed in WT [78]. Both cytoskeletal structures are crucial for shaping the sperm head and disrupting them could result in globozoospermia.

To summarize, our results suggest a novel role for GlcCer as a key regulator for cytoskeletal dynamics. The role of GlcCer could be important in sperm development as well as in neuronal development, since our group have recently revealed a high expression level of GBA2 enzyme in the brain. The multiplexing of lipid environment and GTPase activity imaging would allow us to establish the direct link between GlcCer accumulation and dysregulation of cytoskeletal dynamics.

VII. Bibliography

[1] U.B. Kaupp, T. Strünker, Trends Cell Biol. 27 (2017) 101–109.

[2] U.B. Kaupp, J. Gen. Physiol. 140 (2012) 583–586.

[3] D. Wachten, J.F. Jikeli, U.B. Kaupp, Cold Spring Harb. Perspect. Biol. (2017) a028225.

[4] W. Bönigk, A. Loogen, R. Seifert, N. Kashikar, C. Klemm, E. Krause, V. Hagen, E. Kremmer, T. Strünker, U.B. Kaupp, Sci. Signal. 2 (2009) ra68.

[5] R. Gauss, R. Seifert, U.B. Kaupp, Nature 393 (1998) 583–7.

[6] R. Seifert, M. Flick, W. Bönigk, L. Alvarez, C. Trötschel, A. Poetsch, A. Müller, N. Goodwin, P. Pelzer, N.D. Kashikar, E. Kremmer, J. Jikeli, B. Timmermann, H. Kuhl, D. Fridman, F. Windler, U.B. Kaupp, T. Strünker, EMBO J. 34 (2015) 379–92.

[7] B.J. Wainger, M. DeGennaro, B. Santoro, S.A. Siegelbaum, G.R. Tibbs, Nature 411 (2001) 805–810.

[8] L.R. Potter, Cell. Signal. 23 (2011) 1921–1926.

[9] M. Pichlo, S. Bungert-Plümke, I. Weyand, R. Seifert, W. Bönigk, T. Strünker, N.D. Kashikar, N. Goodwin, A. Müller, H.G. Körschen, U. Collienne, P. Pelzer, Q. Van, J. Enderlein, C. Klemm, E. Krause, C. Trötschel, A. Poetsch, E. Kremmer, U.B. Kaupp, J. Cell Biol. 206 (2014) 541 LP-557.

[10] G.E. Ward, V.D. Vacquier, Proc. Natl. Acad. Sci. U. S. A. 80 (1983) 5578–82.

[11] N. Suzuki, D.L. Garbers, Biol. Reprod. 30 (1984) 1167–1174.

[12] T. Strünker, L. Alvarez, U. Kaupp, Curr. Opin. Neurobiol. 34 (2015) 110–116.

[13] M.E. Burns, E.N. Pugh, Jr., Physiology (Bethesda). 25 (2010) 72–84.

[14] R.D. Hamer, S.C. Nicholas, D. Tranchina, P.A. Liebman, T.D. Lamb, J. Gen. Physiol. 122 (2003) 419–444.

[15] U.B. Kaupp, R. Seifert, Physiol. Rev. 82 (2002) 769–824.

[16] Y. Wang, J.W. Meyer, M. Ashraf, G.E. Shull, Circ. Res. 93 (2003) 776–782.

[17] B.E. Galindo, A.T. Neill, V.D. Vacquier, Biochem. Biophys. Res. Commun. 334 (2005) 96–101.

[18] F. Rieke, D. Baylor, Rev. Mod. Phys. 70 (1998) 1027–1036.

[19] E.N. Pugh, T.D. Lamb, Biochim. Biophys. Acta 1141 (1993) 111–49.

[20] M. Gunkel, J. Schöneberg, W. Alkhaldi, S. Irsen, F. Noé, U.B. Kaupp, A. Al-Amoudi,

Structure 23 (2015) 628–638.

[21] V.Y. Arshavsky, T.G. Wensel, C. CK, B. RB, A. VY, S. E., Investig. Opthalmology Vis. Sci. 54 (2013) 7725.

[22] V.Y. Arshavsky, M.E. Burns, J. Biol. Chem. 287 (2012) 1620–1626.

[23] I.B. Leskov, V.A. Klenchin, J.W. Handy, G.G. Whitlock, V.I. Govardovskii, M.D. Bownds, T.D. Lamb, E.N. Pugh, V.Y. Arshavsky, Neuron 27 (2000) 525–37.

[24] M. Ruiz, R.L. Brown, Y. He, T.L. Haley, J.W. Karpen, Biochemistry 38 (1999) 10642–10648.

[25] K.W. Yau, D.A. Baylor, Annu. Rev. Neurosci. 12 (1989) 289–327.

[26] D.A. Baylor, G. Matthews, K.W. Yau, J. Physiol. 309 (1980) 591–621.

[27] D.A. Baylor, B.J. Nunn, J.L. Schnapf, J. Physiol. 357 (1984) 575–607.

[28] P. Ala-Laurila, K. Donner, A. Koskelainen, Biophys J 86 (2004) 3653–3662.

[29] F. Rieke, D.A. Baylor, Biophys. J. 71 (1996) 2553–2572.

[30] S.S. Suarez, Hum. Reprod. Update 14 (2008) 647–657.

[31] D. Ren, B. Navarro, G. Perez, A.C. Jackson, S. Hsu, Q. Shi, J.L. Tilly, D.E. Clapham, Nature 413 (2001) 603–609.

[32] T.A. Quill, D. Ren, D.E. Clapham, D.L. Garbers, Proc. Natl. Acad. Sci. 98 (2001) 12527–12531.

[33] J.-J. Chung, K. Miki, D. Kim, S.-H. Shim, H.F. Shi, J.Y. Hwang, X. Cai, Y. Iseri, X. Zhuang, D.E. Clapham, Elife 6 (2017).

[34] J.-J. Chung, S.-H. Shim, R.A. Everley, S.P. Gygi, X. Zhuang, D.E. Clapham, Cell 157 (2014) 808–822.

[35] Y. Kirichok, B. Navarro, D.E. Clapham, Nature 439 (2006) 737–740.

[36] P. V. Lishko, Y. Kirichok, J. Physiol. 588 (2010) 4667–4672.

[37] P. V. Lishko, I.L. Botchkina, Y. Kirichok, Nature 471 (2011) 387–391.

[38] C. Schiffer, A. Muller, D.L. Egeberg, L. Alvarez, C. Brenker, A. Rehfeld, H. Frederiksen, B. Waschle, U.B. Kaupp, M. Balbach, D. Wachten, N.E. Skakkebaek, K. Almstrup, T. Strunker, EMBO Rep. 15 (2014) 758–765.

[39] C. Brenker, N. Goodwin, I. Weyand, N.D. Kashikar, M. Naruse, M. Krähling, A. Müller, U.B. Kaupp, T. Strünker, EMBO J. 31 (2012) 1654–1665.

[40] M.R. Miller, N. Mannowetz, A.T. Iavarone, R. Safavi, E.O. Gracheva, J.F. Smith, R.Z.

Hill, D.M. Bautista, Y. Kirichok, P. V. Lishko, Science (80-.). 352 (2016) 555–559.

[41] Z. Zhang, J. Liu, J. Meriano, C. Ru, S. Xie, J. Luo, Y. Sun, Sci. Rep. 6 (2016) 23553.

[42] K. Miki, D.E. Clapham, S. Nielsen, Y.C. Ruan, H.Y. Wong, Y.C. Lu, J.H. Guo, Y.W. Chung, P.B. Huang, H.F. Huang, et al., Curr. Biol. 23 (2013) 443–52.

[43] S.-Y. Lee, J.A. Letts, R. MacKinnon, Proc. Natl. Acad. Sci. 105 (2008) 7692–7695.

[44] Y. Okamura, J. Physiol. 588 (2010) 1803–4.

[45] T.K. Berger, D.M. Fußhöller, N. Goodwin, W. Bönigk, A. Müller, N. Dokani Khesroshahi, C. Brenker, D. Wachten, E. Krause, U.B. Kaupp, T. Strünker, J. Physiol. 595 (2017) 1533–1546.

[46] E. Miyazaki, M. Sakaguchi, S. Wakabayashi, M. Shigekawa, K. Mihara, J. Biol. Chem. 276 (2001) 49221–49227.

[47] D. Wang, S.M. King, T.A. Quill, L.K. Doolittle, D.L. Garbers, Nat. Cell Biol. 5 (2003) 1117–1122.

[48] S.-R. Chen, M. Chen, S.-L. Deng, X.-X. Hao, X.-X. Wang, Y.-X. Liu, Cell Death Dis. 7 (2016) e2152.

[49] M.S. Wuttke, J. Buck, L.R. Levin, JOP 2 (2001) 154–8.

[50] F. Xie, M.A. Garcia, A.E. Carlson, S.M. Schuh, D.F. Babcock, B.S. Jaiswal, J.A. Gossen, G. Esposito, M. van Duin, M. Conti, Dev. Biol. 296 (2006) 353–362.

[51] T. Nishigaki, O. José, A.L. González-Cota, F. Romero, C.L. Treviño, A. Darszon, Biochem. Biophys. Res. Commun. 450 (2014) 1149–1158.

[52] X.-H. Zeng, C. Yang, S.T. Kim, C.J. Lingle, X.-M. Xia, Proc. Natl. Acad. Sci. U. S. A. 108 (2011) 5879–84.

[53] C.M. Santi, P. Martínez-López, J.L. de la Vega-Beltrán, A. Butler, A. Alisio, A. Darszon, L. Salkoff, FEBS Lett. 584 (2010) 1041–1046.

[54] C. Brenker, Y. Zhou, A. Müller, F.A. Echeverry, C. Trötschel, A. Poetsch, X.-M. Xia, W. Bönigk, C.J. Lingle, U.B. Kaupp, T. Strünker, Elife 3 (2014).

[55] C. Yang, X.-H. Zeng, Y. Zhou, X.-M. Xia, C.J. Lingle, Proc. Natl. Acad. Sci. U. S. A. 108 (2011) 19419–24.

[56] X.-H. Zeng, C. Yang, X.-M. Xia, M. Liu, C.J. Lingle, Proc. Natl. Acad. Sci. 112 (2015) 2599–2604.

[57] A. Briegel, D.R. Ortega, E.I. Tocheva, K. Wuichet, Z. Li, S. Chen, A. Müller, C. V Iancu,

G.E. Murphy, M.J. Dobro, I.B. Zhulin, G.J. Jensen, Proc. Natl. Acad. Sci. U. S. A. 106 (2009) 17181–6.

[58] G.L. Hazelbauer, J.J. Falke, J.S. Parkinson, Trends Biochem. Sci. 33 (2008) 9–19.

[59] G. Van Meer, J. Wolthoorn, S. Degroote, (2003).

[60] M. de Graaf, I.C. van Veen, I.H. van der Meulen-Muileman, W.R. Gerritsen, H.M. Pinedo, H.J. Haisma, Biochem. J. 356 (2001) 907–10.

[61] B. Henrissat, Biochem. J. (1991) 309–16.

[62] A.J. Day, M.S. DuPont, S. Ridley, M. Rhodes, M.J. Rhodes, M.R. Morgan, G. Williamson, FEBS Lett. 436 (1998) 71–5.

[63] S. van Weely, M. Brandsma, A. Strijland, J.M. Tager, J.M. Aerts, Biochim. Biophys. Acta 1181 (1993) 55–62.

[64] Y. Hayashi, N. Okino, Y. Kakuta, T. Shikanai, M. Tani, H. Narimatsu, M. Ito, J. Biol. Chem. 282 (2007) 30889–900.

[65] R. Jennemann, R. Sandhoff, L. Langbein, S. Kaden, U. Rothermel, H. Gallala, K. Sandhoff, H. Wiegandt, H.-J. Gröne, J. Biol. Chem. 282 (2007) 3083–94.

[66] A. Schwarz, A.H. Futerman, J. Neurosci. 17 (1997) 2929–38.

[67] H.S. Overkleeft, G.H. Renkema, J. Neele, P. Vianello, I.O. Hung, A. Strijland, A.M. van der Burg, G.J. Koomen, U.K. Pandit, J.M. Aerts, J. Biol. Chem. 273 (1998) 26522–7.

[68] H.G. Korschen, Y. Yildiz, D.N. Raju, S. Schonauer, W. Bonigk, V. Jansen, E. Kremmer, U.B. Kaupp, D. Wachten, J. Biol. Chem. 288 (2013) 3381–3393.

[69] Y. Yildiz, H. Matern, B. Thompson, J.C. Allegood, R.L. Warren, D.M.O. Ramirez, R.E. Hammer, F.K. Hamra, S. Matern, D.W. Russell, J. Clin. Invest. 116 (2006) 2985–94.

[70] E. Martin, R. Schüle, K. Smets, A. Rastetter, A. Boukhris, J.L. Loureiro, M.A. Gonzalez, E. Mundwiller, T. Deconinck, M. Wessner, L. Jornea, A.C. Oteyza, A. Durr, J.-J. Martin, L. Schöls, C. Mhiri, F. Lamari, S. Züchner, P. De Jonghe, E. Kabashi, A. Brice, G. Stevanin, Am. J. Hum. Genet. 92 (2013) 238–44.

[71] H.H.N. Yan, D.D. Mruk, W.M. Lee, C.Y. Cheng, Bioessays 29 (2007) 36–48.

[72] F. Francavilla, R. Santucci, A. Barbonetti, S. Francavilla, Front. Biosci. 12 (2007) 2890–911.

[73] G.B. Dooher, D. Bennett, J. Embryol. Exp. Morphol. 32 (1974) 749–61.

[74] A. Cole, M.L. Meistrich, L.M. Cherry, P.K. Trostle-Weige, Biol. Reprod. 38 (1988) 385–

401.

[75] A.L. Kierszenbaum, L.L. Tres, Arch. Histol. Cytol. 67 (2004) 271–84.

[76] A. Hall, Science 279 (1998) 509–14.

[77] A.J. Ridley, A. Hall, Cell 70 (1992) 389–99.

[78] D. Raju, S. Schonauer, H. Hamzeh, K.C. Flynn, F. Bradke, K. vom Dorp, P. Dörmann, Y. Yildiz, C. Trötschel, A. Poetsch, B. Breiden, K. Sandhoff, H.G. Körschen, D. Wachten, PLOS Genet. 11 (2015) e1005063.

[79] Y.-L. Huang, A.S. Walker, E.W. Miller, J. Am. Chem. Soc. 137 (2015) 10767–10776.

[80] K.R. Gee, K.A. Brown, W.-N.U. Chen, J. Bishop-Stewart, D. Gray, I. Johnson, Cell Calcium 27 (2000) 97–106.

[81] R.Y. Tsien, Nature 290 (1981) 527–528.

[82] D.M. Owen, C. Rentero, A. Magenau, A. Abu-Siniyeh, K. Gaus, Nat. Protoc. 7 (2011) 24–35.

[83] E. Sezgin, H.-J. Kaiser, T. Baumgart, P. Schwille, K. Simons, I. Levental, Nat. Protoc. 7 (2012) 1042–51.

[84] L. Palmer, Physiol. Zool. 10 (1937) 352–367.

[85] M. Suchanek, A. Radzikowska, C. Thiele, Nat. Methods 2 (2005) 261–268.

[86] S.A. Sanchez, M.A. Tricerri, G. Gunther, E. Gratton, Mod. Res. Educ. Top. Microsc. 2 (2007) 1007–1014.

[87] K.A. Johnson, Methods Enzymol. 134 (1986) 677–705.

[88] J. Solzin, A. Helbig, Q. Van, J.E. Brown, E. Hildebrand, I. Weyand, U.B. Kaupp, J. Gen. Physiol. 124 (2004) 115–24.

[89] S.W. Hell, J. Wichmann, Opt. Lett. 19 (1994) 780–2.

[90] M.G.L. Gustafsson, Proc. Natl. Acad. Sci. 102 (2005) 13081–13086.

[91] S. Bretschneider, C. Eggeling, S.W. Hell, Phys. Rev. Lett. 98 (2007) 218103.

[92] T. Dertinger, R. Colyer, G. Iyer, S. Weiss, J. Enderlein, Proc. Natl. Acad. Sci. 106 (2009) 22287–22292.

[93] S. Cox, E. Rosten, J. Monypenny, T. Jovanovic-Talisman, D.T. Burnette, J. Lippincott-Schwartz, G.E. Jones, R. Heintzmann, Nat. Methods 9 (2011) 195–200.

[94] N. Gustafsson, S. Culley, G. Ashdown, D.M. Owen, P.M. Pereira, R. Henriques, Nat. Commun. 7 (2016) 12471.

[95] M.J. Rust, M. Bates, X. Zhuang, Nat. Methods 3 (2006) 793–796.

[96] M. Heilemann, S. van de Linde, M. Schüttpelz, R. Kasper, B. Seefeldt, A. Mukherjee, P. Tinnefeld, M. Sauer, Angew. Chemie Int. Ed. 47 (2008) 6172–6176.

[97] E. Betzig, G.H. Patterson, R. Sougrat, O.W. Lindwasser, S. Olenych, J.S. Bonifacino, M.W. Davidson, J. Lippincott-Schwartz, H.F. Hess, Science (80-.). 313 (2006) 1642–1645.

[98] G.T. Dempsey, J.C. Vaughan, K.H. Chen, M. Bates, X. Zhuang, Nat. Methods 8 (2011) 1027–1036.

[99] R. Kaufmann, J. Piontek, F. Grüll, M. Kirchgessner, J. Rossa, H. Wolburg, I.E. Blasig, C. Cremer, PLoS One 7 (2012) e31128.

[100] R.E. Thompson, D.R. Larson, W.W. Webb, Biophys. J. 82 (2002) 2775–83.

[101] C.A. Karatsuba, Integr. Transform. Spec. Funct. 1 (1993) 269–276.

[102] A. Santos, I.T. Young, Appl. Opt. 39 (2000) 2948–58.

[103] M. Ovesny, P. K i ek, J. Borkovec, Z. vindrych, G.M. Hagen, Bioinformatics 30 (2014) 2389–2390.

[104] M.S. Robbins, B.J. Hadwen, IEEE Trans. Electron Devices 50 (2003) 1227–1232.

[105] B. Huang, W. Wang, M. Bates, X. Zhuang, Science (80-.). 319 (2008) 810–813.

[106] L. Barna, B. Dudok, V. Miczán, A. Horváth, Z.I. László, I. Katona, Nat. Protoc. 11 (2015) 163–183.

[107] L. Carlini, S.J. Holden, K.M. Douglass, S. Manley, PLoS One 10 (2015) e0142949.

[108] Y. Tang, X. Wang, X. Zhang, J. Li, L. Dai, Opt. Lett. 39 (2014) 5685–8.

[109] M. El Beheiry, M. Dahan, Nat. Methods 10 (2013) 689–690.

[110] P. Sengupta, T. Jovanovic-Talisman, J. Lippincott-Schwartz, Nat. Protoc. 8 (2013) 345–354.

[111] S.L. Veatch, B.B. Machta, S.A. Shelby, E.N. Chiang, D.A. Holowka, B.A. Baird, PLoS One 7 (2012) 1–13.

[112] T. Pengo, S.J. Holden, S. Manley, Bioinformatics 31 (2015) 797–8.

[113] S. Malkusch, U. Endesfelder, J. Mondry, M. Gelléri, P.J. Verveer, M. Heilemann, Histochem. Cell Biol. 137 (2012) 1–10.

[114] R.P.J. Nieuwenhuizen, K.A. Lidke, M. Bates, D.L. Puig, D. Grünwald, S. Stallinga, B. Rieger, Nat. Methods 10 (2013) 557–562.

[115] U. Endesfelder, S. Malkusch, F. Fricke, M. Heilemann, Histochem. Cell Biol. 141 (2014) 629–638.

[116] V. Venkataramani, F. Herrmannsdörfer, M. Heilemann, T. Kuner, Nat. Methods 13 (2016) 319–321.

[117] M. Tokunaga, N. Imamoto, K. Sakata-Sogawa, Nat. Methods 5 (2008) 159–161.

[118] N. Olivier, D. Keller, P. Gönczy, S. Manley, PLoS One 8 (2013) 1–9.

[119] M.J. Mlodzianoski, J.M. Schreiner, S.P. Callahan, K. Smolková, A. Dlasková, J. Šantorová, P. Ježek, J. Bewersdorf, P. Je, Opt. Express 19 (2011) 15009.

[120] B. Hebert, S. Costantino, P.W. Wiseman, Biophys. J. 88 (2005) 3601–3614.

[121] T. Strünker, I. Weyand, W. Bönigk, Q. Van, A. Loogen, J.E. Brown, N. Kashikar, V. Hagen, E. Krause, U.B. Kaupp, Nat. Cell Biol. 8 (2006) 1149–1154.

[122] N.D. Kashikar, L. Alvarez, R. Seifert, I. Gregor, O. Jäckle, M. Beyermann, E. Krause, U.B. Kaupp, J. Cell Biol. 198 (2012) 1075–91.

[123] J.F. Jikeli, L. Alvarez, B.M. Friedrich, L.G. Wilson, R. Pascal, R. Colin, M. Pichlo, A. Rennhack, C. Brenker, U.B. Kaupp, Nat. Commun. 6 (2015) 7985.

[124] U.B. Kaupp, N.D. Kashikar, I. Weyand, Annu. Rev. Physiol. 70 (2008) 93–117.

[125] B.M. Friedrich, F. Jülicher, Proc. Natl. Acad. Sci. U. S. A. 104 (2007) 13256–61.

[126] M. Böhmer, Q. Van, I. Weyand, V. Hagen, M. Beyermann, M. Matsumoto, M. Hoshi, E. Hildebrand, U.B. Kaupp, EMBO J. 24 (2005) 2741–2752.

[127] J. Ries, C. Kaplan, E. Platonova, H. Eghlidi, H. Ewers, Nat Meth 9 (2012) 582–584.

[128] V. Hong, N.F. Steinmetz, M. Manchester, M.G. Finn, Bioconjug. Chem. 21 (2010) 1912–1916.

[129] L.D. Hughes, R.J. Rawle, S.G. Boxer, PLoS One 9 (2014) e87649.

[130] L.J. Dangott, D.L. Garbers, J. Biol. Chem. 259 (1984) 13712–13716.

[131] H. Shimomura, L.J. Dangott, D.L. Garbers, J. Biol. Chem. 261 (1986) 15778–15782.

[132] J.C. Vaughan, S. Jia, X. Zhuang, Nat. Methods 9 (2012) 1181–4.

[133] J.-J. Chung, K. Miki, D. Kim, S.-H. Shim, H.F. Shi, J.Y. Hwang, X. Cai, Y. Iseri, X. Zhuang, D.E. Clapham, Elife 6 (2017).

[134] R. Zidovetzki, I. Levitan, Biochim. Biophys. Acta 1768 (2007) 1311–24.

[135] M.M. Dodes Traian, F.L. González Flecha, V. Levi, J. Lipid Res. 53 (2012) 609–16.

[136] M. Machacek, L. Hodgson, C. Welch, H. Elliott, O. Pertz, P. Nalbant, A. Abell, G.L.

Johnson, K.M. Hahn, G. Danuser, Nature 461 (2009) 99–103.

[137] M.Y. Berezin, S. Achilefu, Chem. Rev. 110 (2010) 2641–84.

[138] C. Votsi, E. Zamba-Papanicolaou, L.T. Middleton, M. Pantzaris, K. Christodoulou, Ann. Hum. Genet. 78 (2014) 13–22.

[139] S. Sultana, J. Reichbauer, R. Schüle, F. Mochel, M. Synofzik, A.C. van der Spoel, Biochem. Biophys. Res. Commun. 465 (2015) 35–40.

[140] Y.-H. Su, V.D. Vacquier, Mol. Biol. Cell 17 (2005) 114–121.

[141] F. Mullershausen, A. Friebe, R. Feil, W.J. Thompson, F. Hofmann, D. Koesling, J. Cell Biol. 160 (2003) 719–727.

[142] S. Herrmann, F. Hofmann, J. Stieber, A. Ludwig, Br. J. Pharmacol. 166 (2012) 501–509.

[143] L. Alvarez, L. Dai, B.M. Friedrich, N.D. Kashikar, I. Gregor, R. Pascal, U.B. Kaupp, J. Cell Biol. 196 (2012) 653–663.

[144] D.L. Garbers, J. Biol. Chem. 264 (1989) 9103–9106.

[145] F. Chen, P.W. Tillberg, E.S. Boyden, Science (80-.). 347 (2015).

[146] S.S. Park, M.O. Kim, S.P. Yun, J.M. Ryu, J.H. Park, B.N. Seo, J.H. Jeon, H.J. Han, Biochim. Biophys. Acta - Mol. Cell Biol. Lipids 1831 (2013) 350–360.

[147] Y. Sun, R.D. Dandekar, Y.S. Mao, H.L. Yin, C. Wülfing, PLoS One 6 (2011) e27227.

[148] K. Simons, D. Toomre, Nat. Rev. Mol. Cell Biol. 1 (2000) 31–39.

[149] J. a Allen, R. a Halverson-Tamboli, M.M. Rasenick, Nat. Rev. Neurosci. 8 (2007) 128–140.

[150] B.P. Head, H.H. Patel, P.A. Insel, Biochim. Biophys. Acta - Biomembr. 1838 (2014) 532–545.

[151] A. Viola, N. Gupta, Nat. Rev. Immunol. 7 (2007) 889–896.

Acknowledgement

I am thankful that I was given the opportunity to move from applied physics into basic research at Caesar and to work in a multidisciplinary environment. I was fortunate to have received the guidance of **Prof. Dagmar Wachten** and **Prof. U.B. Kaupp** throughout my doctoral work and for that I would like to express my sincere gratitude for their patience, motivation and immense multidisciplinary knowledge that was placed at my disposal.

Prof. Dagmar Wachten guidance helped me in all the time of research and writing of this thesis. I always knew I could rely on her support and brilliant mind. She taught me a lot of topics and provided me with a new perspective to look at problems.

I consider myself privileged and fortunate to have worked with Prof. U.B. Kaupp at the MBL in Woods Hole, USA. It was a great learning experience for me. I had lots of fun and I experienced the true meaning of “the pleasure of finding things out”. I highly appreciate our valuable discussions while I was writing my thesis.

I would like to thank my PhD committee member, **Prof. Thorsten Lang** for his critical advice and discussions throughout my doctoral work.

Moreover, I also thank the International Helmholtz Research School of Biophysics and Soft Matter (IHRS*BioSoft*) for support. Special thanks to **Dr. Thorsten Auth** for organizing the courses and meetings.

When I first joined Caesar, I received valuable support from **Dr. Jan Jikeli**, a PhD student at the time. His knowledge and critical mind was always at my disposal. Many discussions with him over coffee or beer will remain a treasure. He was the first person to buy me a Kölsch beer after I have moved to Germany.

Dr. Andreas Rennhack, the brilliant chemist in our group and my office mate, contributed greatly to my work. He helped us in the design and synthesis of compounds and peptides that I used in my thesis work. Moreover, I would like to thank him for his help in the German abstract. I also would like to thank our second office mate **Dr. Christian Schiffer** for great intellectual discussions and moments together.

I would like to thank **Dr. Luis Alvarez** for his insights during many discussions that we had. I appreciate the critical advices and new perspectives that he always provided. My gratitude goes to **Dr. Reinhard Seifert** for his support in Woods Hole and his input while I was at Caesar. I greatly appreciate the support from **Frau Heike Krause** with administrative paper work. I also would like to thank everybody at Caesar that I worked with for the great working environment that we help create. A special thanks to colleagues and friends for stimulating discussions, for the sleepless nights we were working together and for all the fun we had.

I also would like to thank **Dr. Darine** and **Dr. Fadi** for hosting me in Paris for many Christmas dinners and occasions in the last four years of my PhD.

Last but not least, I would like to thank my mother, my sisters and brothers for their support to this day. I would not have been able to pursue my goals without their help. I thank my brother Ghassan for his financial support during my studies in Beirut and Paris. My sister Sarah had always motivated my curiosity in science and my drive to understand the world around us, and for her memory I dedicate this thesis.